Mars at No Charge:

Active Neutron Spectroscopy for Magma Evolution, Clay Hydration, and Amorphous Composition in Gale Crater, Mars

by

Sean Czarnecki

A Dissertation Presented in Partial Fulfillment
of the Requirements for the Degree
Doctor of Philosophy

Approved July 2023 by the
Graduate Supervisory Committee:

Craig Hardgrove, Chair
Mark Robinson
Patrick Gasda
Steve Ruff
Jim Bell

ARIZONA STATE UNIVERSITY

December 2023

ABSTRACT

Neutron spectroscopy is used to determine bulk water abundances in the near surface of planetary bodies. The Dynamic Albedo of Neutrons (DAN) instrument on the Mars Science Laboratory (MSL) rover, Curiosity, is able to determine the depth distribution of water and neutron absorbers in the top ~50 cm of the subsurface. In this dissertation, I focus on answering significant geologic questions by interpreting DAN results in the geologic context provided by other MSL and orbital datasets. This approach enabled me to investigate significant outstanding questions in Gale crater geology, with implications for the evolution and habitability of Mars.

I mapped an extensive silicic volcaniclastic layer in the subsurface, the first identified and mapped on Mars. This layer served as a silica source for other silica-rich features. But unlike those features, this layer contains abundant rhyolitic glass, indicating an evolved volcanic origin. Similar material on Earth is produced by plate tectonics, so this layer has important implications for the evolution of Mars, which has no evidence of plate tectonics.

One of the primary motivations for exploring Gale crater is a distinct clay mineral signature from orbital data of the Compact Reconnaissance Imaging Spectrometer at Mars (CRISM), which has also identified a corresponding hydration signature. I compared DAN and CRISM hydration results and found that CRISM hydration results are biased by the presence of regolith, indicating that this regolith is either more hydrated or has a different grain size texture than bedrock.

Clay minerals are primary binding sites for organics on Earth, and most organic-mineral binding mechanisms involve either water or hydroxyl. This makes hydrated clays the most efficient hosts for organic preservation, but clays are normally dehydrated when measured by MSL. However, my DAN-derived water abundances are greater in the most clay-rich unit of Gale crater, suggesting that clay

minerals may be hydrated in the subsurface. I developed a new amorphous component analysis method that simultaneously constrains clay mineral hydration and abundances of various hydrated amorphous phases. I found a strong correlation between "excess" water and smectites (expandable clay minerals), indicating that these clay minerals are hydrated in the subsurface.

I dedicate this dissertation to my family. But I will give special mention to my mom and dad, Cheryl and Jim Czarnecki, who both completed college degrees as adults, inspiring me to complete my education even after a 10-year "break". I probably wouldn't have spent the last 6 years using neutrons to study rocks if they hadn't encouraged me be both nerdy (for the neutrons) and outdoorsy (for the rocks). Mom and Dad, I couldn't have done this without your support.

ACKNOWLEDGMENTS

Nobody completes a PhD alone. Here's a short list of people who have helped along the way to creating what you hold in your hands.

My PhD advisor, Craig Hardgrove took a chance on a non-traditional student whose only planetary science experience was a single introductory level class. Craig's enthusiasm for Mars geology is infectious. His support with everything from science to disagreeable scientists, was truly above and beyond reasonable expectations. I must also thank Travis Gabriel, who taught me the ropes when Craig was building spacecraft in the other room. I also benefitted from the guidance of Patrick Gasda, who mentored me during two summer internships (and in between!). Patrick ended up giving me a job too, so thanks for the $$$! To my other committee members, Mark Robinson, Steve Ruff, and Jim Bell, thank you for putting in the time, effort, and occasionally crucial advice to help me reach this point.

The Mars Science Laboratory (MSL) team has been indispensable to the research in this dissertation. The team is incredibly collaborative and full of brilliant people producing amazing science that revolutionizes our understanding of Mars. Thank you for helping me make sure my work is the best it can be. Individual thanks are due to my collaborators Ray Arvidson, Mason Starr, Melissa Rice, Liz Rampe, Mariek Schmidt, Thomas Henley, Fred Calef, Hallie Gengl, Maddie Hughes, Lucy Thompson, Suzanne Nowicki, Jack Lightholder, Luz Maria Martinez Sierra, Insoo Jun, Sergei Nikiforov, Denis Lisov, Maxim Litvak, Jens Frydenvang, Roger Wiens, William Rapin, Horton Newsom, and Igor Mitrofanov. Thanks also to Marion Nachon, Abigail Fraeman, Vivian Sun, Kathryn Powell, Scott VanBommel, and Dan Sullivan.

My admission to ASU was due in no small part to my undergraduate advisors. David Bixler, my department chair at Angelo State University, didn't laugh at me when I told him I wanted to major in geology, physics, and math. Without his

encouragement and logistical support, I couldn't have solved the jigsaw puzzle of 3 degrees in 4 years. I had amazing undergraduate research opportunities thanks to Joe Satterfield in geology and Scott Williams in physics. Thanks to them, I applied to grad school with many conference presentations and four peer-review publications already under my belt. I also know more than any sane person would want to about Bremsstrahlung radiation and the Sand Springs Range in west-central Nevada.

Over the last 6 years I have relied on many friends. Travis Gabriel has already been mentioned, but he belongs here too. Aishwarya Iyer, Dan Sullivan, and Tyler Ryburn suffered through grad school stress with me from start to finish (except Tyler, who had the gall to graduate a year before the rest of us, but then moved just up the road so we forgave her anyway). I love you; expect cookies. Grace Carlson was amazingly supportive during the dark days of COVID, and Debarati Das was a long-distance lifeline at the same time. Morgan Shusterman taught me that you can be successful in grad school without always loving it (a valuable lesson in times of high stress). Thanks also to Foteine Dimitracopoulos, because sometimes I needed a break from science to talk books or anything and everything else (and sometimes science too). There are so many more, but I'm out of space, so I'll just say to the ASU Hardgrove group, past and present: May the group ever remain acronym-less.

My PhD was funded through the MSL Participating Scientist grant (NNN12AA01C) of my advisor, Craig Hardgrove. I also had two summer internships funded by the Center for the Study of Earth and Space at Los Alamos National Laboratory. ASU's Resource Computing provided HPC and storage.

As a student of ASU, I acknowledge that the Tempe campus sits on the ancestral homelands of those American Indian tribes that have inhabited this place for (many) centuries, including the Akimel O'odham (Pima) and Pee Posh (Maricopa) peoples. This land is a treasure and I hope I have treated it well in my time here.

TABLE OF CONTENTS

Page

CHAPTER Page

APPENDIX Page

LIST OF TABLES

LIST OF FIGURES

Figure Page

LIST OF ACRONYMS AND ABBREVIATIONS

Σ_{abs} – Macroscopic Thermal Neutron Absorption Cross Section

Σ_{sct} – Macroscopic Neutron Scattering Cross Section

APXS – Alpha-Particle X-ray Spectrometer (MSL instrument)

BDI – Integrated Band Index (integrated area between continuum and spectral data)

CCD – Charge-Coupled Device (a component of many cameras)

ChemCam – Chemistry and Camera (MSL instrument suite)

CheMin – Chemistry and Mineralogy (MSL instrument suite)

CIA – Chemical Index of Alteration (100 x $Al_2O_3/(Al_2O_3+CaO+Na_2O+K_2O)$)

CRISM – Compact Reconnaissance Imaging Spectrometer at Mars (MRO instrument)

CTN – Counter of Total Neutrons (DAN detector)

DAN - Dynamic Albedo of Neutrons (MSL instrument)

DRT – Dust Removal Tool (MSL tool)

EGA – Evolved Gas Analysis (SAM instrument technique)

fm. - Formation

FOV – Field-Of-View

FULLPAT – FULL Pattern Fitting Program for XRD Analysis

Ga – 10^9 Years Old (from the Greek *γίγας*, 'giant', and the Latin *annum*, 'year')

GCR - Galactic Cosmic Ray (interstellar radiation composed primarily of protons)

Gm – Glasgow Member (geologic unit, Carolyn Shoemaker fm., Gale crater)

GP – Greenheugh Pediment (geomorphic feature in Gale crater)

GT – Glen Torridon (geomorphic feature in Gale crater)

HiRISE – High Resolution Imaging Science Experiment (MRO instrument)

I/F - Interface

Jm – Jura Member (geologic unit, Murray fm., Gale crater)

KHm – Knockfarril Hill Member (geologic unit, Carolyn Shoemaker fm., Gale crater)

LIBS – Laser-Induced Breakdown Spectroscopy (ChemCam instrument technique)

Ma – 10^6 Years (from the Greek *μέγας*, 'great', and the Latin *annum*, 'year')

MAHLI – MArs Hand Lens Imager (MSL instrument)

MARDI – MARs Descent Imager (MSL instrument)

Mastcam – Mast Cameras (MSL instrument suite)

MCMC – Markov-Chain Monte-Carlo

MCNP6 – Monte-Carlo N-Particle 6 (program to simulate neutron transport histories)

MEP – Mars Exploration Program (NASA's Mars science program)

MER – Mars Exploration Rovers (NASA mission, the Spirit and Opportunity rovers)

mnt/sap – Mixed-Layer Montmorillonite/Saponite (smectite clay minerals)

MONS – Mars Odyssey Neutron Spectrometer (Mars Odyssey spacecraft instrument)

MRO – Mars Reconnaissance Orbiter (NASA mission)

MSL - Mars Science Laboratory (NASA mission, the Curiosity rover)

MSR – Mars Sample Return (NASA program within MEP, including Mars 2020)

n – "Neutron" or "Number" (as in number of waters pfu), depending on context

NASEM – National Academies of Sciences, Engineering, and Medicine

nnt - Nontronite (a smectite clay mineral)

NS – Neutron spectrometer (or neutron spectroscopy)

opal-A – Amorphous Opal (as opposed to paracrystalline opal-CT)

opal-CT – Paracrystalline Opal with Microdomains (as opposed to amorphous opal-A)

p-value – Probability Value (probability of the null hypothesis, i.e., no correlation)

PDS – Planetary Data System (open-source online data repository used by NASA)

pfu – Per Formula Unit

PNG - Pulsed Neutron Generator (DAN neutron source)

PPm – Pettegrove Point Member (geologic unit, Murray fm., Gale crater)

Q_1, Q_2, Q_3 – Quartiles 1, 2, 3 (the 25^{th}, 50^{th}, and 75^{th} percentiles of a distribution)

r^2 – Pearson Correlation Coefficient Squared (measure of linear association strength)

RAD – Radiation Assessment Detector (MSL instrument)

REMS – Rover Environmental Monitoring Station (MSL instrument suite)

RMI – Remote Micro-Imager (ChemCam instrument)

SAM – Sample Analysis at Mars (MSL instrument suite)

sap – Saponite (a smectite clay mineral)

SNR – Signal-to-Noise Ratio

SSA – Single Scattering Albedo

st.dev. – Standard Deviation

uncert. - Uncertainty

VRR – Vera Rubin Ridge (geomorphic feature in Gale crater)

WEH - Water-Equivalent Hydrogen (water abundance assuming all H is in H_2O)

XRD – X-Ray Diffraction (CheMin instrument technique)

LIST OF MSL SAMPLE ACRONYMS

AL – Aberlady

AV - Avanavero

BD - Bardou

BK – Buckskin

BS – Big Sky

CA - Canaima

CB – Cumberland

CH – Confidence Hills

DU – Duluth

EB – Edinburgh

GB - Gobabeb

GE – Glen Etive 1 & 2

GG - Glasgow

GH -Greenhorn

GR - Groken

HF – Highfield

HU - Hutton

JC – John Klein and Cumberland

JK – John Klein

KM - Kilmarie

LB – Lubango

MA – Mary Anning 1 & 3

MB – Marimba

MG – Maria Gordon

MJ – Mojave

NT - Nontron

OG – Ogunquit Beach

OK – Okoruso

OU – Oudam

PT - Pontours

QL – Quela

RH – Rock Hall

RN - Rocknest

SB – Sebina

ST – Stoer

TC – Tapo Caparo

TP – Telegraph Peak

WJ – Windjana

ZS - Zechstein

CHAPTER 1

INTRODUCTION

Planetary science is a relatively young discipline. Only in the 1960s did we begin studying another planetary body in detail with the Apollo program and the missions preceding it. Much of what we know today about lunar science came directly from the Apollo missions and analysis of the Apollo samples. But remote sensing missions in the decades since Apollo have greatly expanded lunar science, especially for the lunar farside, polar regions, and the lunar subsurface and interior.

Today, much of planetary science is driven by the need to understand volatile abundances, transport, and sequestration/preservation. Several planetary missions, including to the Moon and Mars, have included neutron spectrometers (NS) capable of sensing hydrogen (i.e., water) up to a meter deep in the subsurface; but only one mission has included an active NS on a roving platform. The Mars Science Laboratory (MSL) Curiosity rover carries the Dynamic Albedo of Neutrons (DAN) instrument. Most DAN science to date has focused on determining water abundances from many locations to track hydration trends along the Curiosity traverse. In contrast, my research focus for this dissertation is putting my DAN-derived hydration results into a broader context to answer specific questions related to the geologic history and habitability of Mars. By doing so, I also demonstrate the utility of active neutron spectroscopy for answering a variety of planetary science questions.

1.1. Planetary Neutron Spectroscopy and DAN

Orbital NS are used to map the abundance of water in the subsurface. They measure the neutron flux from the surface that is due to galactic cosmic rays (GCRs), which bombard planetary surfaces and release neutrons from subsurface nuclei. Neutron detectors use a variety of materials and techniques to count neutrons by measuring the ionization energy produced by neutrons in a detection volume. He-

3 proportional counters are a type of neutron detector using He-3, which has a large probability of an absorption reaction. When an incident neutron is absorbed, or captured, by a He-3 nucleus, it releases ionizing radiation into the surrounding He-3 and produces an electrical signal. Proportional counters therefore record each neutron absorption reaction as a distinct signal with energy proportional to that of the absorbed neutron. But because the probability of neutron absorption is much higher for low energy (or "thermal") neutrons, detection volumes are often surrounded by a neutron moderator material, which reduces the kinetic energy of (i.e., "thermalizes") neutrons by nuclear scattering reactions before they reach the detection volume, thereby increasing thermal neutron count rates.

Missions with NS have flown to several planetary bodies, including the MESSENGER Gamma-Ray and Neutron Spectrometers (GRNS) to Mercury (Goldsten et al., 2007), the Lunar Prospector GRNS (Feldman et al., 1998), the Mars Odyssey Neutron Spectrometer (MONS) (Boynton et al., 2004), and the DAWN GRaND (Gamma-Ray and Neutron Detector) to asteroids Vesta and Ceres (Prettyman et al., 2011). These are typically paired with gamma-ray detectors which measure other subsurface elemental abundances. Active neutron spectroscopy is an alternate technique using an active neutron source. Active sources are only useful on landed surface platforms because they only irradiate a small area. Orbital NS measure neutron flux from very large areas (pixels tens or hundreds of km wide) and are useful for mapping entire planetary surfaces, while active methods are useful for detailed geologic investigations of a particular site.

Active NS have some other differences from passive methods. By using a pulsed neutron generator (PNG), neutron count rates can be increased by orders of magnitude over natural GCR production ($<10^2$ neutrons per second vs. 10^4 – 10^5 neutrons per second), which allows measurements to be obtained in a matter of

minutes, rather than requiring many orbits over a particular measurement area. A PNG 'pulse' accelerates deuterium ions into a tritium target causing a nuclear reaction which emits 14.1 MeV neutrons, and many pulses are used for a single measurement. Neutrons counts are binned by time elapsed since the last PNG pulse and summed over many pulses, producing a neutron "die-away" curve. The shape of this die-away curve is dependent on the physical characteristics of the material being measured, including its composition.

DAN is a NS with a PNG and two He-3 neutron detectors (Mitrofanov et al. 2012), which can operate in active and passive modes. In active mode, a typical measurement pulses the PNG at 10 Hz, producing 10^7 14.1 MeV neutrons per pulse, emitted isotropically. Some of these enter the subsurface, are thermalized by scattering reactions, and return from the top ~50 cm of the subsurface to be counted by the detectors. DAN measures the "albedo" of neutrons which are returned from the subsurface dynamically (i.e., after multiple scattering reactions). One detector is coated in Cd, a thermal neutron absorber, which only counts epithermal neutrons (0.4 eV < n < 100 keV). The other detector counts both thermal (n < 0.4 eV) and epithermal neutrons. By subtracting the first detector's count rate from the second detector's count rate, a thermal count rate is determined.

NS like DAN are sensitive to macroscopic neutron scattering cross section (Σ_{sct}, a measure of the probability of a neutron scattering off of a target nucleus) and macroscopic thermal neutron absorption cross section (Σ_{abs}, a measure of the probability of a thermal neutron being absorbed by a target nucleus) (e.g., Lawrence et al. 2011). Σ_{sct} and Σ_{abs} are units of area within which the number of reactions (dependent on reaction probability) equals the number of incident neutrons multiplied by the number of target nuclei. Σ_{sct} and Σ_{abs} are dependent on the probability of the specific reaction. Hydrogen has a large Σ_{sct} and reduces neutron

kinetic energy by up to 50% per scattering reaction. Σ_{sct} results are often reported as WEH (water-equivalent hydrogen), derived by dividing H abundance by the mass fraction of H in H_2O, which converts H abundance to a corresponding H_2O abundance. Although the vast the majority of neutron scattering reactions are due to H and H reduces energy more per reaction, other light elements such as B or C can also contribute to neutron moderation. Other elements (e.g., Fe, Cl, B, Mn) have large Σ_{abs}, reducing the number of neutrons that return to the detectors to be counted (Hardgrove et al., 2011). So NS are sensitive to both H (which increases thermal neutron counts) and Fe, Cl, B, Mn, etc. (which decrease thermal neutron counts).

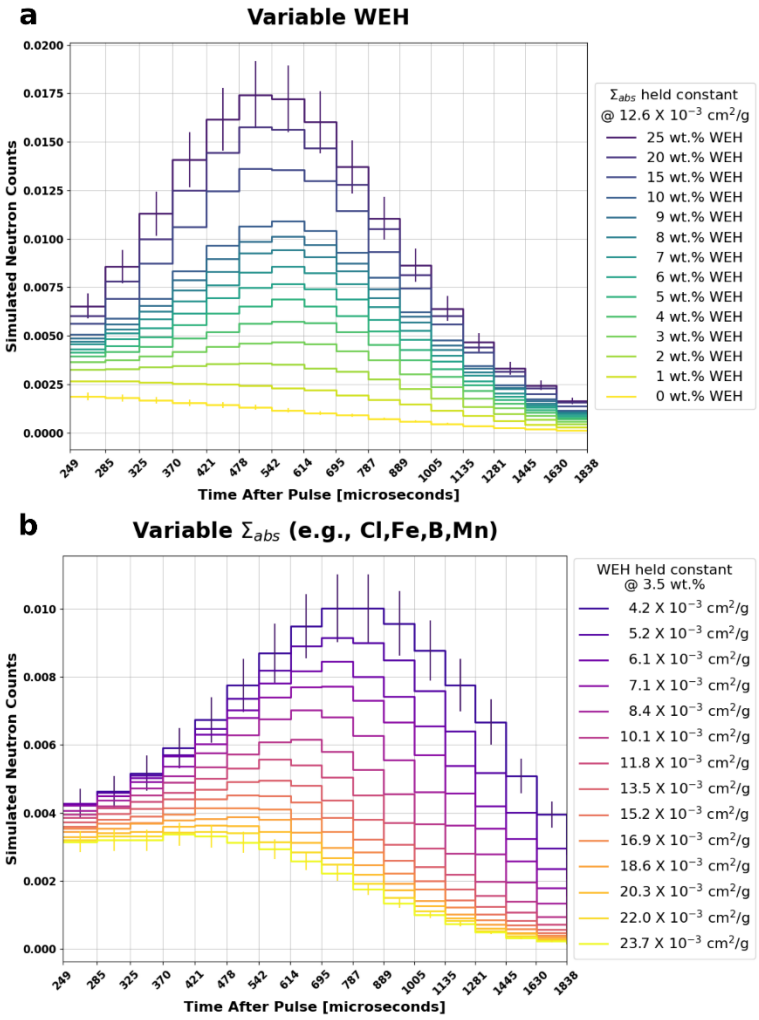

Figure 1.1. Monte Carlo N-Particle 6 (MCNP6) simulated data showing neutron die-away curves for (a) variable WEH (constant Σ_{abs}) and (b) variable Σ_{abs} (constant WEH). WEH increases neutron counts, while Σ_{abs} reduces neutron counts, but the shape of the curve changes differently with variations in these two parameters.

Passive neutron spectroscopy produces a single thermal neutron count rate and cannot independently measure both H and neutron absorber abundances. Active NS with a PNG, on the other hand, measure several neutron count rates at different times after the PNG pulse (e.g., Mitrofanov et al., 2012). As shown in Figure 1.1, the count rates in DAN active die-away curves increase both with increasing H and with decreasing Σ_{abs}, but the shape changes differently with increasing H vs. decreasing Σ_{abs}. Comparing DAN active data to simulations with H and Σ_{abs} as independent parameters, each can be determined. Another advantage of active neutron spectroscopy is the ability to determine WEH and Σ_{abs} as functions of depth below the surface by comparing active data to simulation data generated using multiple subsurface layers with different compositions.

1.2. Evidence for Water and Habitability on Mars Prior to MSL

Aside from Earth, Mars is probably the most intensely studied planet in the last several decades, surpassing any other for number and diversity of missions. Mars is of interest because the geologic record over billions of years is exposed at the surface and there are abundant fluvial and lacustrine surface features, as summarized in recent years by Ehlmann et al. (2016) and the last planetary decadal survey (NASEM, 2022). These features suggest ancient Mars was wetter and warmer than today, and could perhaps have once supported life. NASA's focus on Mars has been driven by the search for life or habitable environments where life could have existed. NS, including DAN, play an important role in this architecture because they measure bulk subsurface water, a necessity for life.

MSL, which hosts the DAN instrument, is the result of a long succession of increasingly ambitious Mars missions, starting with the Mariner missions in the 1960's. The Mariner program included flyby and orbiter spacecraft that investigated atmospheric and surface characteristics, as well as mapping the surface from mid- to

equatorial-latitudes (Steinbacher & Haynes, 1973). Hartmann & Raper (1974) is a great reference for the state of Mars science before and after the Mariner missions. Mariner was followed in the 1970's by the Viking missions with one orbiter and one lander each, giving us our first close look at the martian surface. The Viking orbiters provided more detail on surface cratering and volcanic, fluvial, glaciation, and flood features, while the landers characterized the present and past surface and atmospheric conditions and also had life detection experiments (Soffen & Snyder, 1976). The Viking goals reflect the primary motivations of today's Mars Exploration Program, to characterize the evolution of Mars as a planetary body, and to search for present or past conditions suitable for life.

But one great limitation of the Viking landers was their immobility. In the 1990's and 2000's, the Sojourner, Spirit, and Opportunity rovers revolutionized not just Mars science, but planetary science as a discipline. While Sojourner, of the NASA Pathfinder mission (Golombek et al., 1997), was only able to traverse a small area near the lander, it observed many rocks in the area to be rounded, possibly by water. Similar to the Viking sites, the Pathfinder landing site shows signs of catastrophic flooding and evidence of secondary minerals formed by water-rock interactions. The NASA Mars Exploration Rovers (MER; Crisp et al., 2003) Spirit and Opportunity each travelled many km across the martian surface over several years. The science results of these far-ranging rovers revealed a larger diversity of Mars surface materials (e.g., Morris et al., 2010; Ruff et al., 2011; Squyres et al., 2012). In 50+ km of traverse over 14+ years, the MER rovers showed that Mars was a geologically active planet, including aqueous activity at the surface and in the subsurface that is recorded in present-day rocks.

While the Viking, Pathfinder, and MER landed missions were advancing Mars surface science, a fleet of orbiters was characterizing the atmosphere,

magnetosphere, and surface characteristics using visible, infrared, ultraviolet, and gamma ray wavelengths as well as neutron data. These missions include the NASA orbiters Mars Global Surveyor, Mars Odyssey, Mars Reconnaissance Orbiter (MRO), and MAVEN, and the European Space Agency missions Mars Express and Trace Gas Orbiter. Mars Odyssey included a NS (MONS) (Boynton et al., 2004) that was used to map global WEH values (e.g., Feldman et al., 2004; Wilson et al., 2018). MONS results show hydration as high as several wt.% WEH in equatorial locations, and significantly higher near the poles.

Orbital missions have played a key role in many areas of Mars planetary geology, but they also have been invaluable for surface missions like MSL. Orbital mapping is used to determine landing sites for surface missions and to provide additional science observations of these landing areas and rover traverses. MRO includes the High-Resolution Imaging Science Experiment (HiRISE; McEwen et al., 2007) and the hyperspectral Compact Reconnaissance Imaging Spectrometer at Mars (CRISM; Murchie et al., 2007). HiRISE image mosaics are often used as basemaps by the MSL science team, and have been used to create geomorphic maps of Mars at many scales, including the area of the MSL traverse (e.g., Hughes, 2022). CRISM detects light in a wavelength range that encompasses many important spectral absorption features due to specific molecular compounds or minerals. These absorptions include, e.g., the 3.0 μm hydration band (e.g., He et al., 2022) and the 2.3 μm phyllosilicate metal-OH band (e.g., Milliken et al., 2010; Fraeman et al., 2016). CRISM results have been used to map the mineralogy of the entire MSL traverse from orbit and these results were important in selecting the MSL landing site, Gale crater (Golombek et al., 2012).

1.3. The Mars Science Laboratory: Searching for Habitability

The combination of results from the MER rovers and orbital instruments led to the development of a more ambitious rover with several advances in instrumentation and science objectives (Grotzinger & Milliken, 2012). The NASA Mars Exploration Program had evolved to search for habitable environments and organic matter on a planet that was more active in the past. The MSL rover, Curiosity, was designed as a mobile laboratory with the ability to collect rock samples and deliver them to internal instruments that quantify mineral and volatile abundances. Curiosity has instruments for determining rock geochemistry and hydration, atmospheric characteristics, and the radiation environment, in addition to many cameras for imaging and spectroscopic science. Curiosity is about the size of a sport utility vehicle, with a mast housing navigation, multispectral, and long-distance camera systems and a robotic arm with the drill mechanism, a spectrometer, a high-magnification camera, and a dust-removal tool (DRT) to brush dust from rock surfaces.

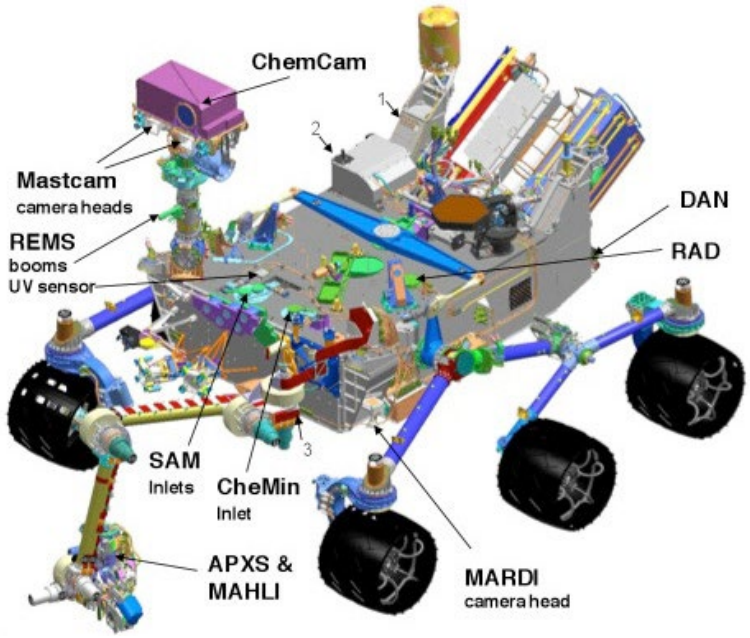

Figure 1.2. Schematic diagram showing DAN and the other science instruments on the MSL rover, Curiosity. The 'DAN' label points to the DAN electronics and detectors. The DAN PNG is in the same location on the opposite side of the rover (not visible). Credit: NASA/JPL-Caltech.

1.3.1. MSL Instruments

The following subsections provide brief overviews of MSL science instruments (Figure 1.2) which appear in the following chapters. In addition to these instruments, MSL has the Mast Cameras (Mastcam; Malin et al., 2017), Mars Hand Lens Imager (MAHLI; Edgett et al., 2012), and Mars Descent Imager (MARDI; Malin et al., 2017) color cameras. Mastcam is a multispectral instrument which is mounted to the rover's mast and has two lenses for stereo imaging and filters wheels for multispectral use. MAHLI is a high-resolution camera mounted to the rover's arm for close up imaging of targets. MARDI acquires images from beneath the rover. Curiosity also has two environmental monitoring stations, REMS (Gomez-Elvira et al., 2012) and RAD (Hassler et al., 2012) which have collected continuous records of atmospheric characteristics and the radiation environment in Gale crater for over 10 years. The many MSL cameras designed for navigation (Maki et al., 2012) are also used for science such as dust devil and cloud surveys.

1.3.1.1. The Alpha-Particle X-ray Spectrometer (APXS)

APXS builds on the heritage of similar instruments on the Pathfinder and MER missions (Foley et al., 2003; Squyres et al., 2003). It uses an active Co source to induce the emission of X-rays characteristic of the constituent elements in rock and soil surfaces. APXS quantifies many major, minor, and trace elements: Na, Mg, Al, Si, P, S, Cl, K, Ca, Ti, Cr, Mn, Fe, Ni, Zn, Br, Rb, Sr, and Y (Campbell et al., 2012). The APXS sensing area is a few cm wide and is placed in contact with target materials, deriving mean surficial compositions of materials in this sensing area. Most science target areas studied by MSL have a few APXS measurements. Drill sites receive additional APXS analyses of the undisturbed drill target, the brushed (i.e., most dust removed by the DRT) drill target, the drill tailings, and the unused drill powder which is dumped on a nearby rock surface after powdered portions have

been delivered to other instruments. APXS data from drill tailings are most representative of material sampled from a drill target.

1.3.1.2. The Chemistry and Camera Instrument (ChemCam)

ChemCam is an instrument that compliments, extends, and enhances geochemistry results for MSL (Maurice et al., 2012; Wiens et al., 2012). Unlike APXS, which is limited to targets within reach of Curiosity's arm, ChemCam determines elemental chemistry using laser-induced breakdown spectroscopy (LIBS) which can focus to measure target chemistry up to seven meters from Curiosity's mast, where the laser is housed. LIBS creates a plasma at the target which emits photons characteristic of the elemental constituents which are analyzed by three spectrometers housed in the rover body. ChemCam quantifies many elements including H, Li, B, Na, Mg, Al, Si, K, Ca, Ti, Mn, Fe, Rb, Sr, and Ba (Lanza et al., 2014; Clegg et al., 2017; Gasda et al., 2017; Payré et al., 2017; Rapin et al., 2017). New elements are calibrated on a regular basis, with P (Dimitracopoulos et al., 2023), S, and Cl set to be calibrated in the future. Typical ChemCam LIBS measurements are rasters of 5 or 10 points on a target with 30 laser shots on each point. Spot sizes are 150 – 500 μm wide, so small features like pebbles or diagenetic nodules and veins can be targeted. ChemCam LIBS is also capable of removing dust without the DRT by vaporizing dust from the rock surface with the first few laser shots. Subsequent shots measure the dust-free target chemistry. Many targets in an area can be used together to approximate the mean chemistry of an area similar to the mean chemistry measured by APXS.

The ChemCam spectrometers also operate in passive mode, enabling spectral investigations of more distant targets or the atmosphere. The black-and-white remote micro-imager (RMI) takes high-resolution images of distant targets for photogeologic interpretation. RMI context images are also collected for LIBS targets.

1.3.1.3. The Chemistry and Mineralogy Instrument (CheMin)

Drilled/powdered rock samples and scooped soil samples acquired by Curiosity are portioned to CheMin for mineralogical analysis. CheMin is an X-ray diffraction and X-ray fluorescence instrument (Blake et al, 2012). It uses transparent Kapton cells to hold sample material while being exposed to X-rays from one side while a charge-coupled device (CCD) records a 2D image on the other side. X-rays are diffracted in crystal lattices as they pass through the sample material and produce the image. This image is converted to a 1D diffraction pattern for comparison against mineral standards. A technique called Rietveld refinement is used to quantify abundances and chemistry of minerals > 1 wt.% of the bulk sample (Morrison et al., 2018), and the full pattern fitting program FULLPAT is used to quantify the phyllosilicate and amorphous fractions (Chipera & Bish, 2013).

Phyllosilicates have non-unique basal spacing between silicate sheets. So CheMin is not always able to conclusively determine the specific phyllosilicate in a sample. But CheMin does provide constraints on phyllosilicate phases, and with Sample Analysis at Mars (SAM) dehydration/dehydroxylation temperatures (see below), a best candidate phyllosilicate phase can usually be indentified.

Amorphous material is even more difficult to identify. In diffraction patterns, it manifests as a broad hump with few or no distinguishing features. SAM data is able to identify certain phases (see below), however neither CheMin nor SAM are able to quantify the abundance of any individual amorphous phase. Because Rietveld refinement quantifies the abundance and crystal chemistry of minerals, and FULLPAT quantifies the abundance of the amorphous fraction, the crystal chemistry (weighted by the crystalline fraction) can be subtracted from the bulk chemistry measured by APXS drill tailings in order to determine the amorphous chemistry of each sample (e.g., Smith et al., 2021). This provides the best insight into the composition of the

amorphous fraction, but what amorphous phases are present is still mostly undetermined throughout Gale crater.

1.3.1.4. The Sample Analysis at Mars Instrument (SAM)

The SAM instrument package (Mahaffy et al., 2012) consists of a quadrupole mass spectrometer, gas chromatograph, and tunable laser spectrometer. In a process called evolved gas analysis (EGA), SAM bakes powdered rock samples up to ~900 °C, releasing volatiles to the mass spectrometer. Gases measured by SAM (e.g., H_2O, CO_2, SO_2) are evolved from minerals, amorphous material, or organics, and the temperature releases of these gases indicate which material(s) they evolved from. For instance, H_2O temperature releases can indicate whether water is being evolved from adsorbed water, hydrated phyllosilicates, hydrated sulfates, etc.

Different phyllosilicate phases release interlayer water or structural hydroxyl at different temperatures. SAM is therefore able to constrain what phyllosilicate phases are present in a sample based on H_2O temperature release profiles. In conjunction with phyllosilicate phase constraints from CheMin, a best candidate phase is usually determined. SAM EGA is also able to identify some individual amorphous phases based on temperature release profiles of volatiles like H_2O or SO_2. But SAM is not able to quantify the abundances of these amorphous phases.

1.3.2. MSL in Geologic Context: Gale Crater

The several hundred-meter-thick stratigraphic succession investigated by MSL in Gale crater is the best-studied sedimentary section outside of Earth (e.g., Milliken et al., 2010; Grotzinger et al., 2014; Sutter et al., 2017; Bedford et al., 2019; Rampe et al., 2020b; Smith et al., 2021; Tu et al., 2021; Vasavada, 2022). Gale crater is an ~150 km equatorial sedimentary basin with an ~5 km tall central mound, Aeolis Mons (informally "Mt. Sharp"). Gale crater sedimentary units are ~3.8 - 3.6 Ga (Thomson et al., 2011), with fluvial resurfacing up to ~1.1 Ga (Le Deit et

al., 2013). Curiosity has traversed tens of km across the crater floor and up the slopes of Aeolis Mons (Figure 1.3a), covering several hundred meters of stratigraphy (Figure 1.3b). One major goal of MSL, the identification of habitable environments, was first accomplished at "Yellowknife Bay", the oldest unit investigated by Curiosity (Grotzinger et al., 2014). Since then, habitability has been established in other areas of the traverse as well (e.g., Grotzinger et al., 2015). Most of the MSL traverse has been through the "Murray" formation on Mt. Sharp. The Murray is primarily lacustrine mudstones with some sandstone intervals, and has a dip of ~3° northwest in the region of Curiosity's traverse (e.g., Kite et al., 2013). Above the Murray is the "Carolyn Shoemaker" formation, which marks a transition from primarily mudstones to primarily sandstones. The "Stimson" formation, an aeolian sandstone, of the "Siccar Point" group unconformably overlies parts of the Murray and Carolyn Shoemaker formations. Several drill samples have been obtained from each formation (Figure 1.3) for analysis by CheMin and SAM. In addition to these samples, three scooped samples of modern windblown sand have also been collected.

Some of the stratigraphically higher geologic units in Figure 1.3b can also be grouped by CRISM spectral signatures identified prior to the MSL landing. As mentioned above, distinct phyllosilicate signatures were observed in CRISM spectra from Gale crater. This signature corresponds to a geomorphic sloped trough-like feature called "Glen Torridon". Although almost all units in Gale crater below Glen Torridon contain phyllosilicates (Vaniman et al., 2014; Rampe et al., 2017; Bristow et al., 2018; Rampe et al., 2020a), CheMin analysis of samples from Glen Torridon have confirmed that this is the most phyllosilicate rich interval investigated by MSL (Thorpe et al., 2022). The units immediately below Glen Torridon also correspond to distinct CRISM spectral features (associated with hematite) and a geomorphic ridge feature called the "Vera Rubin ridge" (e.g., Fraeman et al., 2020). Despite the CRISM

hematite signature, ChemCam and APXS did not observe an increase in Fe on the ridge and DAN did not observe an increase in Σ_{abs} that would correspond to an increase in Fe. However, as I show in Chapter 3 below, there is a distinct increase in WEH between Vera Rubin ridge and Glen Torridon, and this is most likely associated with phyllosilicate hydration (Chapter 4, below).

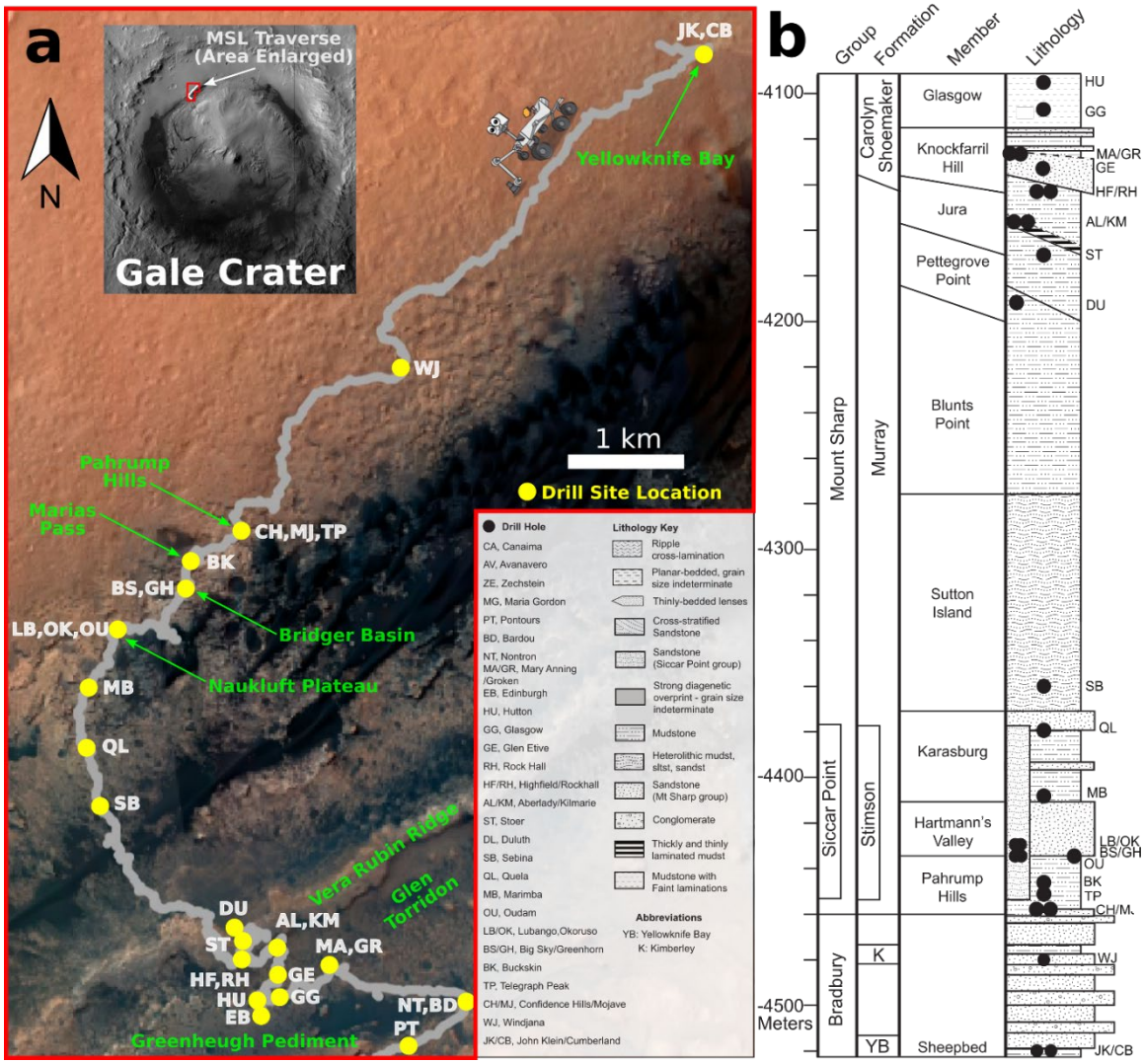

Figure 1.3. (a) Map of the Curiosity traverse up to Sol ~3200. Drill sites are marked by yellow dots with target name acronyms. Selected locations are labeled in green. Inset is a locator map of Gale crater showing the MSL traverse. HiRISE basemap credit: NASA/JPL-Caltech. (b) Partial stratigraphic column compiled by the MSL science team showing unit lithologies and drill targets.

Above the stratigraphic section shown in Figure 1.3b lies the "sulfate unit", which has distinct absorptions in CRISM spectra related to mono-and poly-hydrated magnesium sulfates. The Stimson formation mentioned above also unconformably overlies the sulfate unit. Curiosity has recently begun exploring these strata and CheMin results show a decrease in phyllosilicate abundances compared to Glen Torridon, and eventually are absent from samples entirely. The "Canaima" drill sample in the sulfate unit represents the first sample with crystalline Mg-sulfate in the form of kieserite (Vaniman, 2012; Chipera et al., submitted).

1.4. Outstanding Mars Geology Questions Addressed in This Dissertation

1.4.1. Evolved Igneous Lithologies on Mars

The surface of Mars is primarily mafic, as shown by orbital and surface investigations (e.g., Singer et al., 1979; Mustard et al., 2005; Taylor et al., 2010; McSween et al., 2015). But felsic lithologies have also been observed (Christensen et al., 2005; Carter & Poulet, 2013; Wray et al., 2013; Cousin et al., 2017). Felsic rocks are very common on Earth, where plate tectonics provide a mechanism for crustal recycling which leads to evolved igneous rocks. But evidence of plate tectonics has not been found on Mars, leaving the origin of these evolved felsic lithologies poorly understood. Processes of magma evolution are intimately linked with internal planetary dynamics, so understanding the origin of evolved rocks on Mars is important for planetary evolution models.

The discovery of tridymite, a high-temperature, low-pressure silica polymorph at "Marias Pass" in Gale crater (Figure 1.3a; Morris et al., 2016) provided an opportunity to study an evolved igneous material in detail. This material is thought to be a source for silica-rich fracture halos at "Bridger Basin" and "Naukluft Plateau" in the unconformably overlying Stimson formation (Frydenvang et al., 2017), but the tridymite-bearing drill sample was obtained from the conformable Murray bedrock.

High-silica Murray material was only observed at the surface in a relatively small area within Marias Pass, but DAN's depth sensitivity and the very low Fe content of this silica-rich material allow DAN to detect this material where MSL's geochemical instruments (ChemCam and APXS) cannot.

Alternate theories for the origin of the tridymite have persisted (Yen et al., 2021). But if this material is igneous, it is the only approximately datable (based on the age of Gale sediments referenced above) evolved igneous lithology on Mars, and therefore an important clue for martian planetary evolution. Chapter 2 of this dissertation presents the results of my DAN active data analysis within Marias Pass. These DAN results are combined with results from ChemCam, APXS, CheMin, Mastcam, and CRISM, and interpreted as evidence for a widespread silicic volcaniclastic tridymite-bearing layer that is conformable within the Murray formation and exposed at Marias Pass.

1.4.2. Preservation of Martian Organics in Clay Minerals

The CRISM 2.3 μm metal-OH band is diagnostic of phyllosilicates (clay minerals). There is a distinct absorption at this wavelength in the Glen Torridon region of Gale crater, and abundant clay minerals (up to 34 wt.%) in this region were confirmed in CheMin samples (Thorpe et al., 2022). Hydrated clay minerals also have absorptions at the 3.0 μm hydration band, which has contributions from both water and hydroxyl, and Glen Torridon also has deep 3.0 μm absorptions relative to geologic units stratigraphically below it.

Almost all clay minerals identified in Gale crater are collapsed (i.e., dehydrated) when measured by CheMin (e.g., Rampe et al., 2020b). Rapin et al. (2018) showed evidence of sample dehydration prior to CheMin analysis, and clay minerals could also dehydrate during sample acquisition and handling. Additionally, DAN measures hydration from depths of ~50 cm, while CheMin measures drilled

samples from depths of < 6 cm. If clay minerals are hydrated at depth, DAN WEH results should include contributions from them.

Clay minerals are well known to efficiently preserve organics (Shen et al., 1999; Kennedy et al., 2002; Ehlmann et al., 2008; Fiorito et al., 2008; Broz, 2020), and sorption of organics can be enhanced by hydroxyl or water (Keil & Mayer, 2014), so hydrated clays are the best candidate materials for organic preservation on Mars. Organic matter has been identified by SAM in Gale crater samples (e.g., Sutter et al., 2017), but the Mars surface radiation environment should break down most organics at the MSL sample depth over geologic time (Hassler et al., 2014). Organics at greater depths (e.g., the DAN depth of sensitivity, ~50 cm) should be broken down more slowly due to greater radiation shielding of overlying material, so organic abundances measured by SAM are lower bounds. In Chapter 3, I show that WEH is elevated in the most clay-rich units in Gale crater (Glen Torridon), where CRISM also records a significant increase in the 3.0 μm absorption band. This serves as the motivation for Chapter 4 in which I use DAN WEH results with mineralogy and chemistry from sample sites across the traverse to demonstrate a correlation between abundances of clay minerals and modeled WEH.

1.4.3. The Composition of X-ray Amorphous Material

X-ray amorphous phases are ubiquitous in Gale crater, comprising 20 – 56 wt.% of all drilled samples (Vaniman et al., 2014; Rampe et al., 2017; Bristow et al., 2018; Rampe et al., 2020a; Thorpe et al., 2022). The presence of significant abundances of amorphous material in > 3.5 Ga rocks is surprising because amorphous material tends to crystallize over time in the presence of water, and as discussed above, there is abundant evidence of surface water on ancient Mars. The persistence of these amorphous materials is an indication of infrequent and low

water-rock interactions in the syn- and post-depositional history of Gale crater (Rampe et al., 2020b; McLennan et al., 2019; Smith et al., 2021).

CheMin X-ray diffraction data are able to quantify the overall abundance of amorphous material, but because these materials appear in diffraction patterns as broad humps with crystalline mineral peaks superimposed on them, individual phases cannot be well constrained. Several candidate amorphous phases have been proposed for Gale crater or elsewhere on Mars including volcanic or impact glass, amorphous sulfates, opal-A, allophane, hisingerite, and ferrihydrite (e.g., Dehouck et al., 2014; McLennan et al., 2019; Achilles et al., 2020; Rampe et al., 2020b; Smith et al., 2021). These phases are important indicators of depositional environment characteristics and environmental changes (e.g., Hurowitz et al., 2017). In Chapter 4, I model abundances of these amorphous phases simultaneously with "excess" WEH that is likely bound to clay minerals, as described above.

CHAPTER 2

IDENTIFICATION AND DESCRIPTION OF A SILICIC VOLCANICLASTIC LAYER IN GALE CRATER, MARS, USING ACTIVE NEUTRON INTERROGATION

Abstract

The Dynamic Albedo of Neutrons instrument aboard the Mars Science Laboratory rover, Curiosity, has been used to map a stratigraphically conformable layer of high-SiO_2 material in Gale crater. Previous work has shown that this material contains tridymite, a high-temperature/low-pressure felsic mineral, interpreted to have a volcanic source rock. We describe several characteristics including orientation, extent, hydration, and geochemistry, consistent with a volcaniclastic material conformably deposited within a lacustrine mudstone succession. Relationships with widely dispersed alteration features and orbital detections of hydrated SiO_2 suggest that this high-SiO_2 layer extends at least 17 km laterally.

Mineralogical abundances previously reported for this high-SiO_2 material indicated that hydrous species were restricted to the amorphous (non-crystalline) fraction, which is dominated by SiO_2. The low mean bulk hydration of this high-SiO_2 layer (1.85 ± 0.13 wt.% water-equivalent hydrogen) is consistent with silicic glass in addition to opal-A and opal-CT. Persistent volcanic glass and tridymite in addition to opal in an ancient sedimentary unit indicates that the conversion to more ordered forms of crystalline SiO_2 has not proceeded to completion and that this material has had only limited exposure to water since it originally erupted, despite having been transported in a fluviolacustrine system. Our results, including the conformable nature, large areal extent, and presence of volcanic glass, indicate that this high-SiO2 material is derived from the product of evolved magma on Mars. This is the first identification of a silicic volcaniclastic layer on another planet and has important implications for magma evolution mechanisms on single-plate planets.

Plain Language Summary

Using the Dynamic Albedo of Neutrons instrument aboard the Mars Science Laboratory rover, Curiosity, we mapped a silica-rich layer throughout a small region in Gale crater known as Marias Pass. Previous work has shown that some rocks in Marias Pass contain minerals formed in explosive volcanic eruptions. We determined several key characteristics including orientation, extent, hydration, and elemental composition, which are consistent with material derived from a volcanic deposit. This layer is likely related to nearby silica-rich material deposited by groundwater along subsurface fractures, and geometric relationships to hydrated silica identified from orbit suggest that this high-silica layer extends over at least 17 km. Mineralogical data from previous work indicates the crystalline fraction is anhydrous. As such, we interpret the low hydration of this material, attributable to the amorphous (non-crystalline) fraction, as being consistent with a significant abundance of volcanic glass in addition to other hydrated phases. The presence of volcanic glass indicates that this material has had limited exposure to water since its formation, because glasses tend to preferentially weather. Our results show that this layer is parallel to surrounding rocks, covers a large area, and contains volcanic glass, indicating that it derived from an explosive volcanic product.

Key Points

- A > 1 m thick SiO_2- and tridymite-rich layer in Gale crater likely extends over several kilometers.
- This layer is stratigraphically conformable, with low water content consistent with significant volcanic glass.
- This material is consistent with an evolved igneous material deposited in a lacustrine environment.

2.1. Introduction

Orbital and surface investigations as well as meteorites analyses have shown that the surface of Mars is dominantly basalt (e.g., Agee et al., 2013; McSween, 1984; McSween et al., 2006; McSween, 2015; Mustard et al., 2005; Singer et al., 1979; Taylor et al., 2010), though felsic (e.g., Carter & Poulet, 2013; Christensen et al., 2005; Cousin et al., 2017; Gross & Filiberto, 2014; Humayun et al., 2013; Mangold et al., 2016) compositions have also been identified. Silicic igneous lithologies in various regions of the Martian southern highlands (e.g., Christensen et al., 2005; Wray et al., 2013) support evolved igneous lithologies on early Mars. Felsic compositions are common on Earth where plate tectonics is a mechanism for magma evolution, but there is no evidence for plate tectonics on Mars, requiring other formation mechanisms (Bandfield et al., 2000; Wyatt & McSween Jr., 2002).

Recent results from the Mars Science Laboratory (MSL) Curiosity rover have shown evidence for a large diversity of igneous materials in Gale crater, including SiO_2-rich rocks. One such SiO_2-rich deposit is at a location known as "Marias Pass" where Curiosity detected SiO_2 abundances >80 wt.% (Frydenvang et al., 2017) as well as tridymite, a high-temperature/low-pressure SiO_2 polymorph formed in silicic volcanic eruptions (Morris et al., 2016). Hardgrove et al. (2011) demonstrated that high-SiO_2 material in the near subsurface (<50 cm), if it is associated with depleted levels of iron, would have a significant effect on the neutron flux measured by the MSL Dynamic Albedo of Neutrons (DAN) instrument. We use *in situ* neutron spectroscopy provided by the DAN instrument in conjunction with *in situ* geochemical, *in situ* multispectral, and mineralogical results to characterize the extent and hydration of this material in Marias Pass. We also incorporate other surface and orbital observations to map the layer's extent outside Marias Pass and to investigate the implications for its origin.

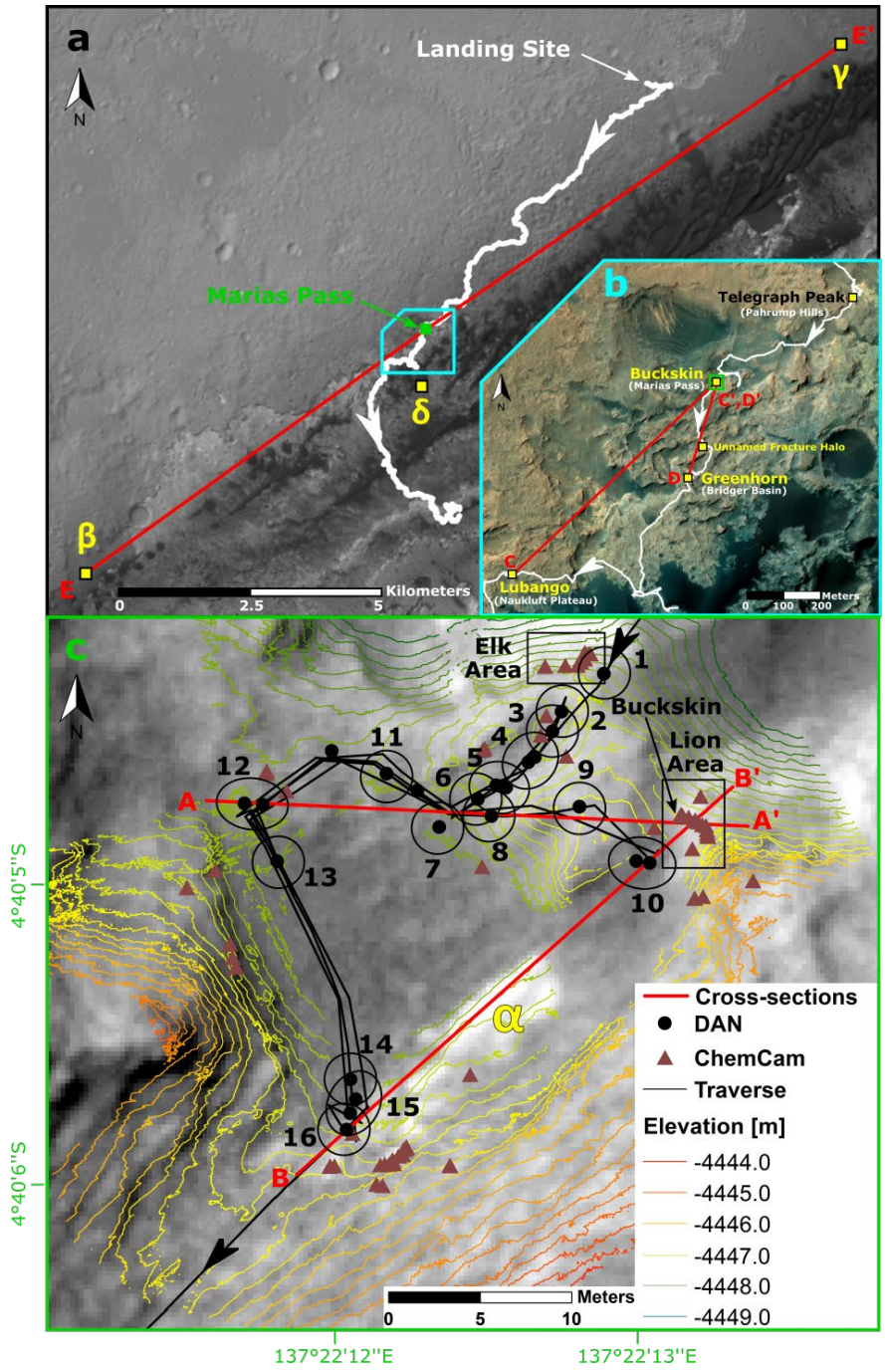

Figure 2.1. Maps on MRO HiRISE image mosaics from Calef III & Parker (2016). (a) Map of the MSL traverse showing the location of cross section E-E' (Figure 2.8e) and CRISM detections of hydrated SiO_2 (β, γ, δ). (b) Map of a traverse section showing drill locations, an unnamed fracture alteration halo, and cross sections C-C' and D-D' (Figures 2.8c,d). Location shown in (a). (c) Map of Marias Pass showing DAN and Chemistry and Camera instrument (ChemCam) measurement locations and cross sections A-A' and B-B' (Figures 2.8a,b). Location shown in (b). DAN surface footprints for analyzed sites are shown as numbered black ellipses. The location of the Site α Mast Camera (Mastcam) multispectral image is marked by a yellow α.

2.1.1. Geologic Setting

Since landing in August 2012, Curiosity has been exploring Gale crater, an ~150 km diameter sedimentary basin on Mars. Curiosity has conducted detailed geologic investigations while traversing the crater floor and up the slopes of the ~5 km tall central peak, Aeolis Mons (informally Mount Sharp; Figure 2.1a). The data returned are used to interpret the depositional environments of geologic units, which include lacustrine, fluvial, and aeolian deposits of primarily basaltic material (Grotzinger et al., 2015). Some of these depositional environments have been interpreted as habitable (Grotzinger et al., 2014) with sedimentary sequences deposited ~3.8–3.6 Ga (Thomson et al., 2011), and possibly as late as ~3.46 Ga with fluvial resurfacing up to ~1.10 Ga (Le Deit et al., 2013).

While traversing up the slopes of Mount Sharp, Curiosity has encountered several rock units including those of the Bradbury group, the Murray formation of the Mount Sharp group, and the Stimson formation of the Siccar Point group (Figure 2.2). The Murray, which this study focuses on, has a regional dip of ~3° to the northwest (Lewis & Turner, 2019; Kite et al., 2013), away from Mount Sharp. The Murray formation is primarily a lacustrine mudstone (Fedo et al., 2017), though it also contains sandstones and conglomerates (Grotzinger et al., 2015). As of January 2020, over 350 m of Murray stratigraphy has been observed. The lowest exposed unit of the Murray formation is the Pahrump Hills member, a laminated lacustrine mudstone with layers and lenses of cross-stratified fluvial sandstone (Grotzinger et al., 2015; Stack et al., 2019). As shown in Figure 2.2, the Pahrump Hills member is stratigraphically overlain by the Hartmann's Valley member of the Murray formation and unconformably overlain by the Stimson formation, an aeolian sandstone (Banham et al., 2018; Fraeman et al., 2016).

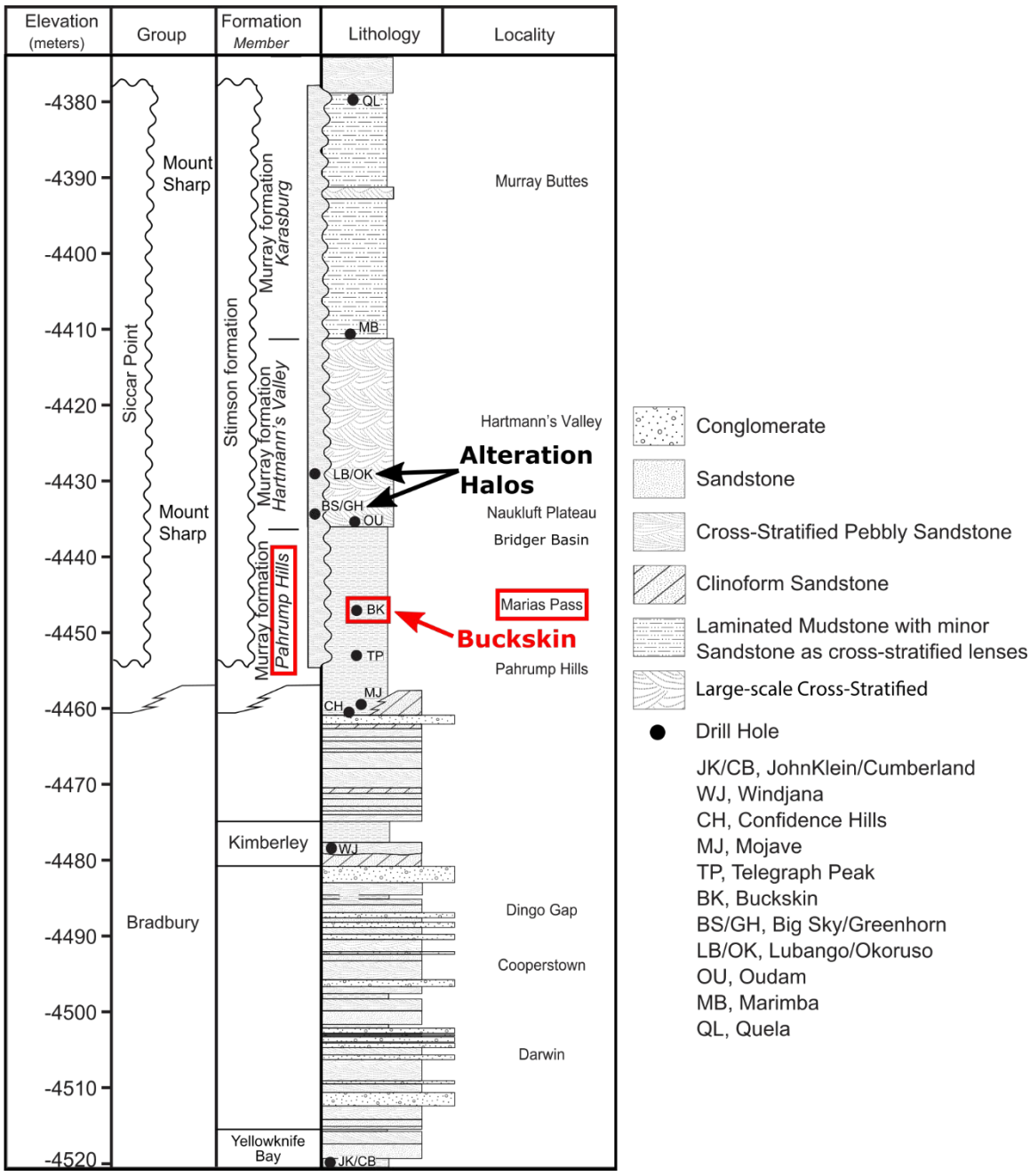

Figure 2.2. Stratigraphic column showing geologic units defined by the MSL team for the lowest ~145 m of stratigraphy investigated by Curiosity. The Buckskin drill target in Marias Pass is located at about the midpoint of the ~23 m thick Pahrump Hills member, which is primarily composed of laminated lacustrine mudstone.

2.1.2. Marias Pass

"Pahrump Hills" is the location (Figure 2.1b) where the geologic member of the same name was first described in detail (Grotzinger et al., 2015), and where the

"Telegraph Peak" mudstone drill sample was obtained. Marias Pass, a 20–30 m wide shallow topographic depression, is ~500 m to the southwest (Figure 2.1b), and 6 m above (Figure 2.2) Pahrump Hills. Curiosity entered Marias Pass on sol (Martian day) 991 after landing. Marias Pass is located at the approximate midpoint of the Pahrump Hills member stratigraphy (~−4448 to −4445 m; Figure 2.2).

Calcium sulfate veins are present throughout the lower Pahrump Hills member (Nachon et al., 2017) as well as in Marias Pass and indicate a post-depositional history of aqueous alteration. Intact calcium sulfate veins present in the Stimson at Marias Pass indicate that alteration continued after the deposition of the Stimson. Crosscutting relationships between calcium sulfate veins and high-SiO_2 fracture alteration halos, which we discuss further in section 2.1.3, indicate that the calcium sulfate veins continued to form during and possibly after alteration halo formation (Frydenvang et al., 2017; Yen et al., 2017).

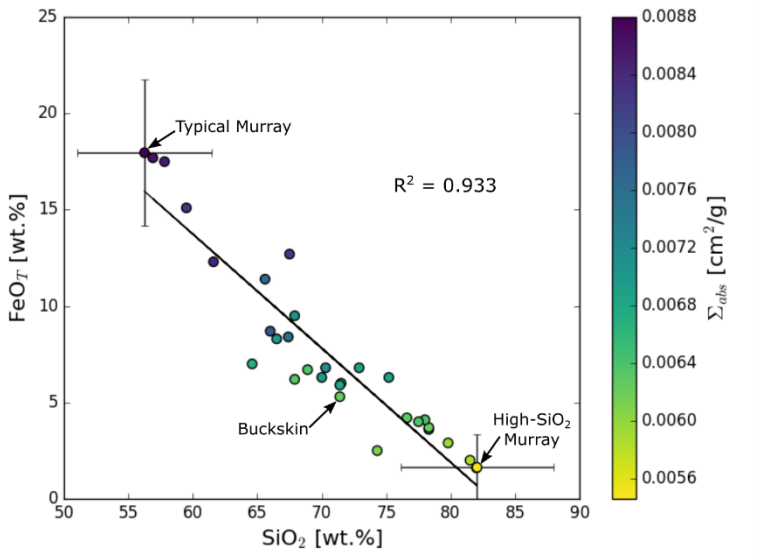

Figure 2.3. Plot of SiO_2 versus FeO_T for ChemCam targets of Murray mudstone within Marias Pass. Labeled data points are reference geochemistries used in simulations (Table 2.1). Colors represent macroscopic neutron absorption cross section (Σ_{abs}) for each target. This strong SiO_2-FeO_T anticorrelation demonstrates that low-Σ_{abs} (low-FeO_T) compositions in Marias Pass can be interpreted as having high-SiO_2 abundances. These data were first reported by Frydenvang et al. (2017). Representative error bars are provided for end-member compositions.

Table 2.1. Bulk mineralogy, SiO_2, FeO_T, and Cl of modeled geochemistries

	Baseline Marias Pass Murray Bedrock[a]	High-SiO_2 Murray Bedrock[b]	Buckskin[c]	Telegraph Peak[d]
SiO_2[e]	56.3 ± 5.2	82.0 ± 5.9	71.0 ± 5.4	51.4 ± 5.0
FeO_T[e]	18.0 ± 3.8	1.63 ± 1.70	5.60 ± 2.10	18.7 ± 3.9
Cl[f]	0.34 ± 0.01	0.34 ± 0.01	0.34 ± 0.01	0.34 ± 0.01
Σ_{abs}[g]	0.0088 ± 0.0011	0.0055 ± 0.0007	0.0065 ± 0.0007	0.0086 ± 0.0009
Plagioclase	-	-	17.1 ± 1.2	27.1 ± 2.8
Sanidine	-	-	3.4 ± 0.7	5.2 ± 2.2
Magnetite	-	-	2.8 ± 0.3	8.2 ± 0.9
Hematite	-	-	-	1.1 ± 0.5
Quartz	-	-	-	0.9 ± 0.4
Anhydrite	-	-	0.7 ± 0.2	-
Tridymite	-	-	13.6 ± 0.8	-
Cristobalite	-	-	2.4 ± 0.3	7.3 ± 1.7
Other[h]	-	-	-	12.1 ± 3.6
Opal-CT	-	-	6.0	10.9
Amorphous	-	-	54	27.2 ± 15

Note. Oxide, elemental, and mineral abundances are listed in wt.%.
[a]SiO_2 and FeO_T averaged from "Mission," "Piegan," and "Fisch_Scale," representative low-SiO_2 endmember ChemCam targets in Marias Pass and Bridger Basin. Cl abundance from APXS of Telegraph Peak drill tailings. No drill sample taken for mineralogical analysis.
[b]SiO_2 and FeO_T averaged from high-SiO_2 endmember ChemCam targets in the "Lion," "Elk," and "Meeteetse" areas in Marias Pass and Bridger Basin. Cl abundance from APXS of Buckskin drill tailings. No drill sample taken for mineralogical analysis.
[c]SiO_2 and FeO_T from "Blind_Gulch" ChemCam target at the Buckskin drill hole. Cl abundance from APXS of Buckskin drill tailings. Mineralogy from Morris et al. (2016).
[d]SiO_2 and FeO_T from "Telegraph_Peak_ccam" ChemCam target. Cl abundance from APXS of Telegraph Peak drill tailings. Mineralogy from Rampe et al. (2017).
[e]SiO_2 and FeO_T reported with accuracy uncertainties from ChemCam.
[f]Cl reported with precision uncertainties from APXS.
[g]Macroscopic thermal neutron absorption cross section (Σ_{abs}) is a measure of the probability that a material will absorb thermal neutrons, reported in cm^2/g.
[h]Other crystalline components include forsterite, pigeonite, orthopyroxene, and fluorapatite. See Rampe et al. (2017) for abundances.

The goal of our work is to map and characterize high-SiO_2/low-FeO_T material observed in Marias Pass to determine the origin of this anomalous material. The lower ~100 m of Murray stratigraphy (including the Pahrump Hills member) has a mean SiO_2 abundance of 54.4 ± 7.0 wt.% (1σ) and FeO_T abundance of 17.8 ± 5.2 wt.% (1σ) as measured by the MSL Chemistry and Camera (ChemCam) instrument (Bedford et al., 2019). As reported previously by Frydenvang et al. (2017), SiO_2 abundances ranging from 57 – 82 wt.% and FeO_T abundances ranging from 2 – 18

wt.% were observed in the Murray mudstone at Marias Pass. SiO_2 and FeO_T are anticorrelated throughout the Murray (Bedford et al., 2019), including in Marias Pass (Figure 2.3), where the highest-SiO_2/lowest-FeO_T material was measured in the Murray "Elk" and "Lion" areas exposed on the northern slope of Marias Pass (Figure 2.1c).

Elevated thermal neutron counts in DAN data were observed at several locations in Marias Pass. This suggested that the subsurface is enriched in hydrogen, depleted in neutron absorbing elements (e.g., iron), or both (these effects are discussed in section 2.2.1). A drill sample was obtained from the high-SiO_2 target "Buckskin" on sol 1060 (Figures 2.1 and 2.3, and Table 2.1). X-ray diffraction (XRD) experiments with the MSL Chemistry and Mineralogy (CheMin) instrument have shown that Buckskin contains 17.1 ± 1.0 wt.% tridymite and 3.0 ± 0.4 wt.% cristobalite, high-temperature/low-pressure SiO_2 polymorphs commonly formed in felsic-intermediate volcanic eruptions (e.g., Morris et al., 2016; Rampe et al., 2017).

The absence of high-SiO_2 mudstone just above the Lion area suggests that this material is confined to a stratigraphic layer, as suggested by Frydenvang et al. (2017). The DAN instrument is sensitive to differences in the depth distribution of hydrogen and neutron absorbers such as iron in the top ~50 cm of the subsurface, allowing us to determine the depth distribution of the high-SiO_2/ low-FeO_T material in Marias Pass and map its extent and relationship to other SiO_2-rich deposits in the Murray and Stimson formations.

2.1.3. Fracture Alteration Halos

A rare exposure of the Murray/Stimson unconformity is at the southern end of Marias Pass (Banham et al., 2018). Several light-toned alteration zones surrounding fractures have been discovered in Gale crater, including in the Stimson just above the exposed unconformity in Marias Pass (Figure 2.4). Upsection from Marias Pass,

drill samples were taken from fracture alteration halo targets and nearby unaltered bedrock targets in the Stimson. The alteration halo target "Greenhorn" is located in "Bridger Basin" ~300 m south of and ~10 m above Marias Pass, and the alteration halo target "Lubango" is located in "Naukluft Plateau" ~640 m southwest of and ~5 m above Bridger Basin (Figure 2.1b). Geochemical analyses of sample drill tailings show that these alteration halos have elevated SiO_2 content (53 – 60 wt.%) relative to nearby unaltered bedrock targets (43 – 45 wt.%) (Yen et al., 2017). Unlike Buckskin, these high-SiO_2 alteration halo samples did not contain tridymite. The association of these alteration halos with fractures indicates their formation is a result of aqueous alteration that post-dated the lithification of the Stimson formation (Frydenvang et al., 2017; Yen et al., 2017). Other light-toned fracture alteration halos have been observed elsewhere in the Stimson formation (Banham et al., 2018), in the Murray formation (Frydenvang et al., 2017; Gasda et al., 2016; Yen et al., 2017), and in the Bradbury group.

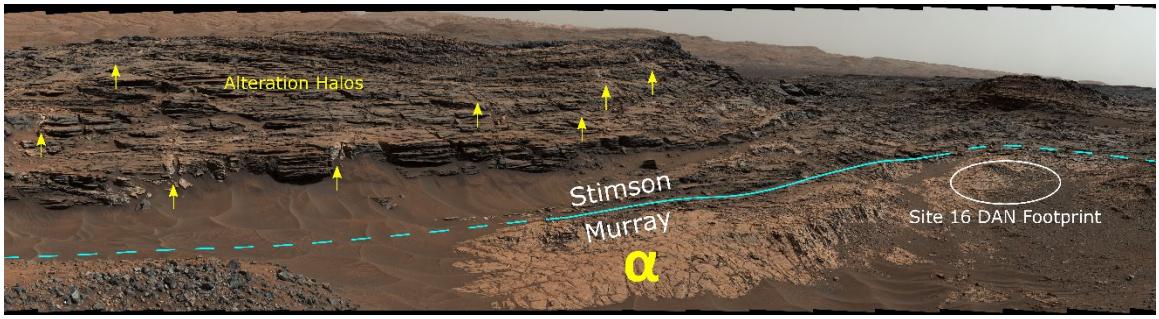

Figure 2.4. Portion of Mastcam mosaic mcam04395 looking south, showing the southeastern area of Marias Pass including Sites 16 and α. Light-toned fracture alteration halos are visible in the overlying Stimson sandstone. Similar light-toned Stimson alteration halos were analyzed upsection at "Greenhorn" and "Lubango" and are enriched in SiO_2. Mastcam image IDs are listed in Appendix Text A.1.

The SiO_2 enrichment mechanism which formed these alteration halos has been debated in the literature and hypotheses include both passive enrichment through acid leaching and active enrichment through SiO_2 sintering. Yen et al. (2017) argued that the Stimson alteration halos were passively enriched in SiO_2

through an acid leaching process in which acidic fluids preferentially remove some geochemical species, leaving relatively more SiO_2 behind. This is consistent with some geochemical differences observed between the altered and unaltered Stimson samples. Evolved Gas Analysis (EGA) by the MSL Sample Analysis at Mars (SAM) instrument of the Greenhorn sample has shown reduced nitrate and oxychlorine abundances relative to nearby unaltered Stimson material (Sutter et al., 2017). This is also consistent with an acid leaching event during the formation of the Stimson alteration halos. Alternatively, it has been suggested that the Stimson high-SiO_2 alteration halos were actively enriched in SiO_2 via mobilization from an underlying source in the Murray formation (Frydenvang et al., 2017; Yen et al., 2017). This helps explain the large SiO_2 enrichment observed in the Stimson halos, which is unlikely to be entirely due to acid leaching, and it is possible that both passive and active enrichment occurred in multiple diagenetic (post-depositional alteration) stages (Yen et al., 2017). Additionally, CO_2 releases detected by the SAM instrument from the Greenhorn drill sample are consistent with the presence of minor carbonates, which in turn would indicate that alkaline alteration occurred after acidic alteration in this halo (Sutter et al., 2017). The most likely source for the SiO_2 mobilized into the Stimson alteration halos is the tridymite-bearing material observed in Marias Pass that underlies the Stimson (Frydenvang et al., 2017).

2.2. Methods

We determined the layered geochemical structure and hydration of 16 sites covering the area of Curiosity's traverse in Marias Pass and identified another location consistent with a high-SiO_2/low-FeO_T composition. This involved integrating compositional data from the DAN, ChemCam, Alpha Particle X-ray Spectrometer (APXS), and Mast Camera (Mastcam) instruments aboard the Curiosity rover.

2.2.1. Instruments

DAN is a neutron spectrometer with passive and active modes, which is composed of a pulsed neutron generator (PNG) and two He-3 neutron detectors. In passive mode, DAN detects neutrons created by galactic cosmic ray spallation in the Martian subsurface. These data are gathered while the rover is stationary as well as during rover mobility (Jun et al., 2013). In active mode, the PNG produces 14.1 MeV neutrons over a typical measurement duration of 20 min. The time-of-flight and energy of neutrons, which return to the detectors, are dependent on the subsurface composition, primarily hydrogen (which efficiently scatters neutrons, reducing kinetic energy) and elements like iron and chlorine which increase the macroscopic thermal neutron absorption cross section (Σ_{abs}), a measure of the probability that a material will absorb thermal neutrons. DAN detects neutrons scattered within the top ~50 cm. Since both hydrogen and iron are very efficient at thermalizing and absorbing neutrons, respectively, DAN is sensitive to abundances of these species in the Martian subsurface (e.g., Hardgrove et al., 2011; Mitrofanov et al., 2012; Sears, 1992) as well as their depth distribution (e.g., Gabriel et al., 2018). Further details on the DAN instrument and its operation can be found in the literature (Litvak et al., 2008; Mitrofanov et al., 2012).

To derive results from DAN, we compare DAN data to simulation data, which incorporates in situ geochemical abundances from the ChemCam and APXS instruments. ChemCam uses Laser-Induced Breakdown Spectroscopy (LIBS), which ablates material from a target up to 7 m away and records the spectrum of the resulting plasma over the 240 – 905 nm wavelength range (Clegg et al., 2017; Maurice et al., 2012; Wiens et al., 2012). Typically, a raster of several LIBS target points (e.g., 5×1 or 3×3) is performed and 30 LIBS shots are taken per point, with each point being 300 – 500 μm in diameter. The first five shots are removed from

analyses due to surficial target dust contamination. The APXS sensor head is located on the rover arm and can be placed in contact with selected targets. Curiosity is equipped with a dust removal tool to minimize the effect of dust cover for APXS surface measurements. Further details on the APXS instrument can be found in the literature (e.g., Campbell et al., 2014). Several elements, such as silicon and iron are quantified by both ChemCam and APXS. Since the geochemistry varies considerably in Marias Pass, we primarily use ChemCam-derived geochemistries because the small ChemCam spot size and larger data set captures more geochemical variability. But because ChemCam does not typically quantify chlorine abundance, we use chlorine abundances determined by APXS from nearby and geochemically similar targets in our analyses.

The Mastcam instrument is a pair of charge-coupled device cameras with fixed focal lengths (34 mm in the left camera and 100 mm in the right camera) mounted roughly 2 m above the surface on the rover's mast (Malin et al., 2017). Each camera obtains images through a Bayer pattern of red, green, and blue filters and telecentric microlenses bonded onto the charge-coupled device and an eight-position narrowband filter wheel that provides the ability to obtain spectra in 12 unique wavelengths between 445 and 1013 nm (Bell III et al., 2017).

2.2.2. DAN Active Data Analysis

After each pulse from the DAN PNG, neutrons from each detector are counted and recorded in 64 lognormal time bins totaling 0.1 s. Total counts for each bin are summed over all pulses for a given measurement, resulting in what is known as a neutron "die-away" curve because the neutron signal first increases then decreases back to the background level. We subtract the background galactic cosmic ray-induced neutron count rate, weighted by bin width, from each time bin as in Gabriel et al. (2018). See Gabriel et al. (2018) for further DAN active preprocessing details.

To improve the statistical precision of data from those DAN active measurements with a signal-to-noise ratio (SNR) less than 5, we coadded (summed the neutron counts on a bin-by-bin basis) multiple such measurements together as performed in Gabriel et al. (2018). Measurements are only coadded if they are proximal both laterally (within 2 – 3 m) and topographically (within 2 – 3 cm vertically), and there is no significant visible change in the material exposed at the surface, determined using rover camera imagery (Abercrombie et al., 2019). Die-away curves for each coadded measurement are also compared to ensure thermal neutron peak location, relative peak height, etc., are similar. DAN active measurements that had an SNR less than 5 for any time bin used in our analysis and could not be coadded to improve SNR, were not included in our final results. Figure 2.5 is an example showing the individual die-away curves of the two DAN active measurements coadded for Site 4, as well as the coadded die-away curve. Appendix Text A.2 describes the process of DAN active collocation and coaddition used in this work.

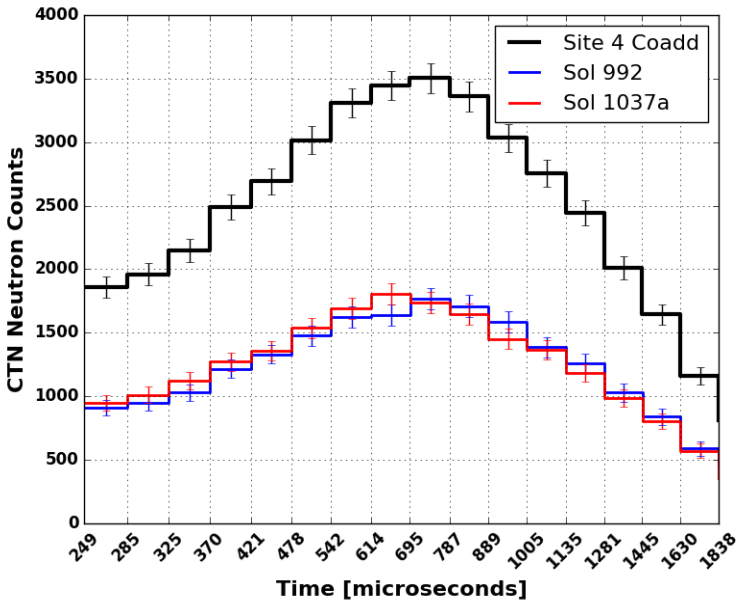

Figure 2.5. Example of coadded DAN active measurements. Shown are DAN CTN (thermal neutron) data for sols 992 and 1037a, which were coadded for Site 4, plotted along with the coadded data. Measurements are only coadded if they are spatially proximal and exhibit similar die-away curves. Because measurement uncertainty is statistical, the coadded measurement has better precision than either constituent measurement.

To estimate the subsurface geochemical composition, we use a forward modeling scheme where the thermal neutron die-away data measured with DAN is compared to synthetic die-away data produced in simulations using the Monte Carlo N-Particle 6 (MCNP6) particle transport code (Werner et al., 2017). These simulations model a 3-dimensional environment, which includes the DAN PNG and detectors, a rover model, the Martian atmosphere, and various subsurface geochemistries. We achieved a relative statistical uncertainty <5% for neutron counts in each analyzed time bin in every simulation used for this study. We use the same MCNP6 input file as that used by Gabriel et al. (2018) with subsurface geochemical abundances from ChemCam and chlorine from APXS. Table 2.1 lists the SiO_2, FeO_T, Cl, Σ_{abs}, and mineralogy for the two *in situ* geochemistries used in our models ("Baseline Marias Pass Murray Bedrock" and "High-SiO_2 Murray Bedrock") along with the Buckskin and Telegraph Peak geochemistries for reference. The SiO_2, FeO_T, and Σ_{abs} are derived from ChemCam data of specific targets (listed in the table notes) and Cl values are from relevant APXS targets (listed in the table notes). The APXS target "Wallace" is the nearest APXS measurement to the Marias Pass ChemCam targets used to generate the Baseline Marias Pass Murray Bedrock geochemistry. The Wallace Σ_{abs} of 0.0092 ± 0.0001 cm^2/g agrees with the Baseline Marias Pass Murray Bedrock value of 0.0088 ± 0.0011 cm^2/g. No APXS measurements were taken at the locations of the Marias Pass ChemCam measurements used to create the High-SiO_2 Murray Bedrock geochemistry. The APXS Buckskin drill tailings Σ_{abs} value of 0.0060 ± 0.0001 cm^2/g agrees with the ChemCam Buckskin value of 0.0065 ± 0.0007 cm^2/g and the APXS Telegraph Peak drill tailings Σ_{abs} value of 0.0089 ± 0.0001 cm^2/g agrees with the ChemCam Telegraph Peak value of 0.0086 ± 0.0009 cm^2/g. We conducted simulations to test the effect of calcium sulfate veins on derived DAN results since these veins are present

throughout the Murray stratigraphy (Vaniman et al., 2018). In Appendix Text A.3 we demonstrate that these veins are not in sufficient volumetric abundance in the subsurface to have a measurable effect on our analysis of data in this region.

Depending on the type of model, we vary several parameters including layer thickness/depth, hydrogen abundance, and Σ_{abs}. The parameters spanned by our "grids" of models are listed in Table 2.2. Our initial simulations for each site used a one-layer subsurface model grid in which individual models varied both hydrogen abundance (reported as water-equivalent hydrogen or WEH) as well as iron and chlorine (as proxies for Σ_{abs}) in a homogeneous subsurface. In order to span the range of Σ_{abs} observed in Gale crater, our one-layer models vary iron between 0.48 and 14.22 wt.% and chlorine between 0.1 and 3.0 wt.%. Most sites in Marias Pass fit best with lower Σ_{abs} values than the Σ_{abs} of Baseline Marias Pass Murray Bedrock (Table 2.1). Sites that had significant sand/rubble cover within the DAN field of view (FOV), or with a surface bedrock geochemistry that was inconsistent with the Σ_{abs} of the best fit one-layer models, were analyzed using one or both of the two-layer model grids. All two-layer models used in this study varied hydrogen abundance and depth for each layer. Model Grid 2A varied the bottom layer geochemistry with the top layer set to the Baseline Marias Pass Murray Bedrock geochemistry, and Model Grid 2B varied the top layer geochemistry with the bottom layer set to the High-SiO_2 Murray Bedrock geochemistry (Table 2.2). Chlorine abundances measured by APXS of drill tailings from the Telegraph Peak and Buckskin samples are both 0.34 ± 0.01 wt.% (Table 2.1), indicating that chlorine does not vary significantly between the high-SiO_2 Buckskin material and the Murray immediately down section, which was sampled at Telegraph Peak. No other elements measured by ChemCam and APXS contribute enough to the Σ_{abs} of these samples to be responsible for significant variations in Σ_{abs}. The low Σ_{abs} determined for most DAN active measurements

analyzed in this work (see section 2.3) do not allow for significant abundances of other efficient neutron absorbers, which are not measured by ChemCam or APXS, without requiring Fe or Cl to have nonphysical negative abundances. For the above reasons, we take the variations observed in Σ_{abs} to be the result of variable FeO_T, following the trend seen in Figure 2.3. Appendix Text A.4 describes the process of model generation and implementation for the modeling grids used in this work.

Table 2.2. Parameter ranges for model grids used in Markov-Chain Monte Carlo (MCMC) analyses

Model grid	WEH range [wt.%]	Σ_{abs} range [cm^2/g]	Depth range [cm]
1	0.2 – 6.0	0.0042 – 0.0237	-
2A	Top: 1.4 – 3.8 Bottom: 0.2-3.0	Top: 0.0088 Bottom: 0.0055 – 0.0086	5 – 25
2B	Top: 1.8 – 3.4 Bottom: 1.2 – 2.8	Top: 0.0063 – 0.0101 Bottom: 0.0055	5 - 25

To compare DAN data to MCNP6 simulation data, we analyze the time bins with the most dynamic thermal neutron count rates (from 249 – 1838 μs after the pulse). At ~249 μs, the PNG-induced epithermal neutron count rate falls to background levels, so the background-subtracted neutron count rate is due to only thermal neutrons. The area under the die-away curve in this range is normalized for both the DAN data and the simulation data (Gabriel et al., 2018). Using the data processing and analysis pipeline from Gabriel et al. (2018), a Markov-Chain Monte Carlo (MCMC) analysis is performed to evaluate the active DAN data across the modeled grid of simulations. See Appendix Text A.5, Gabriel et al. (2018), and Foreman-Mackey et al. (2013) for further details concerning MCMC analyses.

2.2.3. Mastcam Multispectral Data Analysis

Mastcam multispectral observations (Appendix Table A.1) were acquired at Marias Pass and at nearby fracture alteration halos with elevated SiO_2 and low FeO_T. Spectra from the high-SiO_2/low-FeO_T targets were compared to those from other observations of Murray rocks to determine spectral characteristics that distinguish

high-SiO_2/low-FeO_T materials in Mastcam spectra. Spectra from additional Marias Pass targets (at Site α) were then evaluated for these characteristics. See Appendix Text A.6 for further details concerning our Mastcam multispectral analysis.

2.3. Results

The results of MCMC analyses for each investigated DAN active site are listed in Table 2.3. WEH is a unit that represents the water abundance if all measured hydrogen is in the form H_2O, and Σ_{abs} is the macroscopic thermal neutron absorption cross section. Sites 1 – 10 are located in northeastern Marias Pass, and DAN results show that all but one of these sites have relatively low Σ_{abs}, which is consistent with a high-SiO_2/low-FeO_T composition (Figure 2.3). DAN results show that Sites 5, 6, 8, and 10 contain > 10 cm of unconsolidated material covering low-Σ_{abs} bedrock consistent with a high-SiO_2/low-FeO_T composition. Sites 15 and 16, in southern Marias Pass, also are shown to contain relatively low-Σ_{abs} material beneath > 10 cm of Baseline Marias Pass Murray Bedrock (Figure 2.1). Results from Sites 2 (northeastern Marias Pass), 11 – 13 (northwestern Marias Pass), and 14 (southern Marias Pass) are not consistent with low-Σ_{abs} material, likely due to unconsolidated bedrock fragments and/or windblown sand in the top ~50 cm. The hydration of subsurface low-Σ_{abs} material in Marias Pass ranges from 0.94 – 2.74 wt.% WEH.

Plots showing the results of our DAN active MCMC analyses are available in Appendix Figures A.1 – A.16. An example plot is shown in Figure 2.6 for Site 16. Site 16, on the south side of Marias Pass, is ~25 m southwest of the high-SiO_2 material exposed at the Lion area (Figures 2.1c and 2.4). MCMC analysis shows that a low-Σ_{abs} material is buried beneath surface bedrock. This low-Σ_{abs} material does not match the geochemistry of the bedrock exposed at the surface, but is consistent with the highest-SiO_2/lowest-FeO_T material present in the Lion area.

Table 2.3. Results from MCMC analyses of Sites 1 – 16

Site	Sol[a]	WEH [wt.%][b]	Σ_{abs} [cm^2/g][b]	Depth [cm][c]	Model Grid
1	991	1.88 ± 0.29	0.0053 ± 0.0003	—	1
2	1037c	2.08 ± 0.38	0.0080 ± 0.0004	—	1
3	1037b	2.59 ± 0.32	0.0058 ± 0.0003	—	1
4	992, 1037a	2.74 ± 0.32	0.0056 ± 0.0003	—	1
5	1035d, 1042a	2.03 ± 0.37	0.0055d	12.0 ± 4.6	2B
6	1035c	1.92 ± 0.41	0.0055d	12.1 ± 4.5	2B
7	1035b	2.01 ± 0.32	0.0055 ± 0.0003	—	1
8	1049	1.54 ± 0.52	0.0055d	14.3 ± 4.0	2B
9	1051	1.54 ± 0.25	0.0046 ± 0.0003	—	1
10	1053, 1056	1.76 ± 0.41	0.0055d	12.4 ± 4.3	2B
11	1042b	2.03 ± 0.46	0.0126 ± 0.0009	—	1
12	1044a, 1066	1.22 ± 0.31	0.0110 ± 0.0007	—	1
13	1044b	0.92 ± 0.23	0.0090 ± 0.0005	—	1
14	995	0.93 ± 0.25	0.0074 ± 0.0005	—	1
15	1030, 1067	0.94 ± 0.37	0.0061 ± 0.0005	10.3 ± 5.1	2A
16	997 - 1028	1.36 ± 0.38	0.0060 ± 0.0004	10.2 ± 4.7	2A

Note. Both one- and two-layer models were used in Marias Pass, with two-layer models only being used when the surface geochemistry did not agree with one-layer-model Σ_{abs} fit values.

[a]A sol number including a, b, c, or d refers to the first, second, third, or fourth measurement taken on that sol, respectively. Measurements with multiple sols listed have been coadded (see section 2.2.2). Site 16 is coadded from all six measurements in the listed sol range.

[b]Reported WEH and Σ_{abs} are bulk values for one-layer models and high-SiO_2 layer values for multiple-layer models.

[c]Burial depth of high-SiO_2 material in the bottom layer of a two-layer model

[d]Bottom layer geochemistry set to High-SiO_2 Murray Bedrock geochemistry (Table 2.1) based on preliminary one-layer model results (see Appendix Text A.4).

We also find that trends in DAN passive data in the Marias Pass region are consistent with our DAN active results above. In the vicinity of Sites 1 – 8, the mean passive count rate is relatively high (61.9 neutrons per second), suggesting elevated hydrogen content and/or lower neutron absorber content. Lower mean passive count rates in the vicinity of Sites 11 – 13 (29.7 neutrons per second) and moderate mean passive count rates near Sites 14 – 16 (37.6 neutrons per second) suggest a lower level of hydration and/or higher neutron absorber content near these sites. These DAN passive count rate trends are consistent with a high abundance of high-SiO_2/low-FeO_T material near sites 1 – 8, a lower abundance of high-SiO_2/low-FeO_T material near sites 14 – 16, and no high-SiO_2/low-FeO_T material near sites 11 – 13.

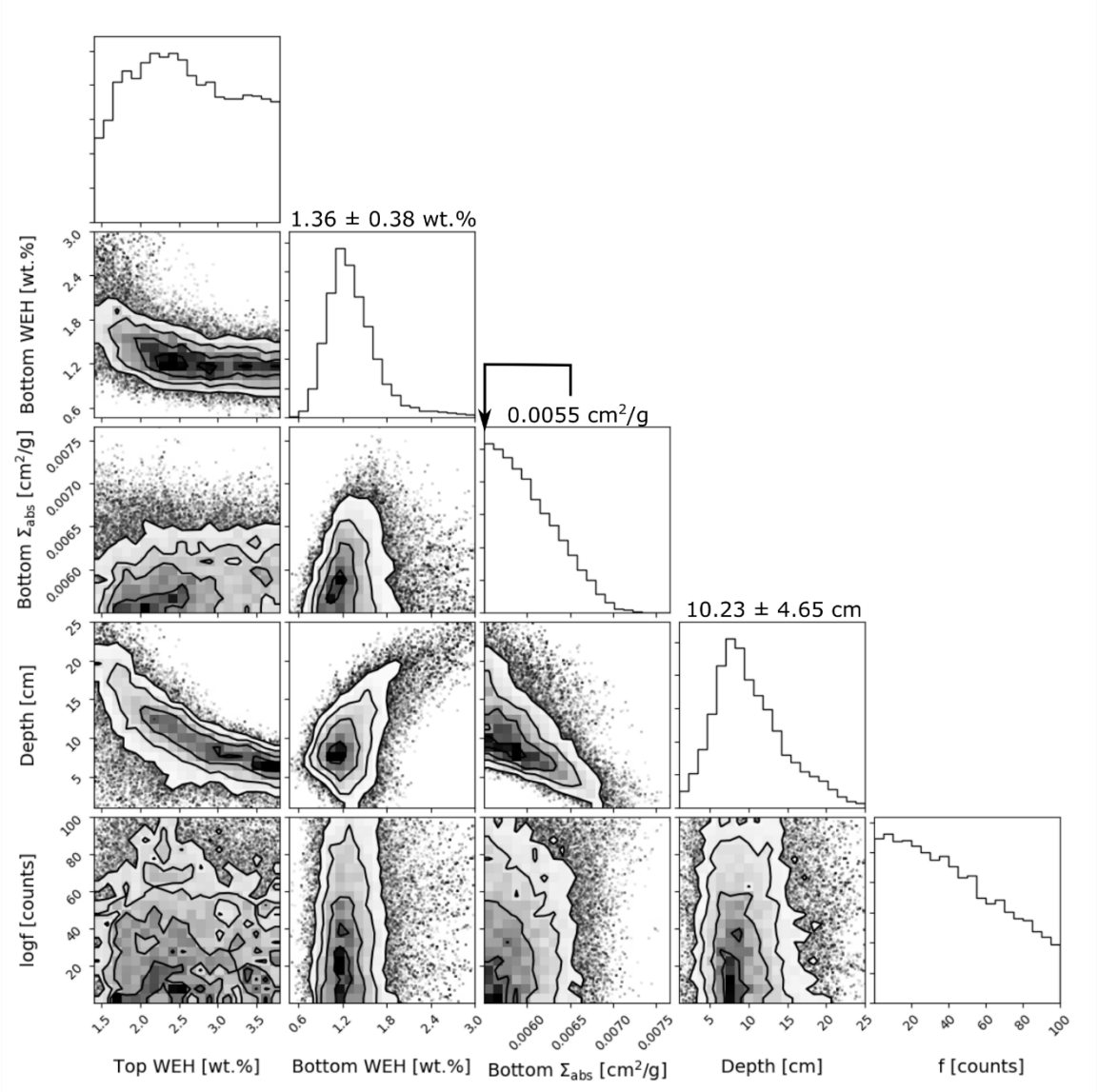

Figure 2.6. Corner plot showing MCMC free parameter posterior distributions of models at Site 16 (Figures 2.1c and 2.4). Nondiagonal frames represent 2-D posterior distributions and are used to understand instrument response to multiple parameters and the measurement degeneracy. The diagonal frames represent the 1-D (marginalized) posterior distribution and are used to determine the optimized value of the free parameters (shown above the frames). This analysis most strongly discriminates the value of the lower layer water content (1.36 ± 0.38 wt.%) and the depth to the bottom layer (10.23 ± 4.65 cm). The top layer water content is not strongly constrained by this analysis, likely due to the fact that it is thin (as shown by the depth result). The lower layer contains a low-Σ_{abs} material consistent with the lowest-Σ_{abs} material observed in Marias Pass (0.0055 barns). The "f" parameter parameterizes underestimated uncertainty. See Appendix Figures A.1 – A.16 for corner plots of each site.

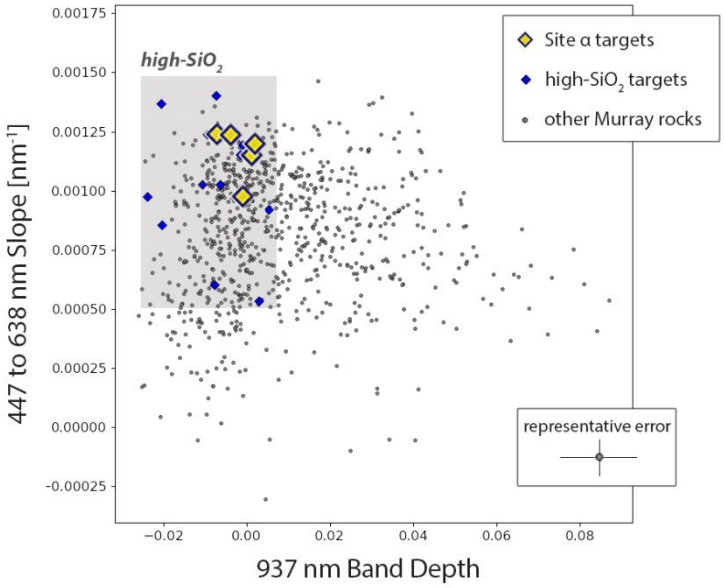

Figure 2.7. Mastcam parameter-space plot comparing spectra of high-SiO_2/low-FeO_T targets to spectra of other rock targets in the Murray formation. The shaded region indicates a Mastcam-based spectral characterization of the high-SiO_2/low-FeO_T targets at Marias Pass and nearby fracture alteration halos (observations listed in Appendix Table A.1): high values of the blue-to-red slope (447 – 638 nm) and small to negative values of the 937 nm band depth (measured beneath a continuum line with shoulder positions at 805 and 1013 nm). Representative error bars for each parameter are calculated from uncertainties in the relative band-to-band reflectance. Spectra from Site α share the same spectral characteristics of known high-SiO_2/low-FeO_T targets. This is consistent with the prediction, based on DAN active analysis, that Site α exposes high-SiO_2/low-FeO_T bedrock. See Figures 2.1c and 2.4 for Site α location.

In Mastcam spectra, the high-SiO_2/low-FeO_T targets from the observations listed in Appendix Table A.1 exhibited small 937 nm band depths and steep blue-to-red (447 – 638 nm) slopes compared to other Murray bedrock (Figure 2.7). 937 nm band depth is defined as the percent drop in R* at 937 nm beneath a continuum line with shoulder positions at 805 and 1013 nm, and indicates the presence of the broad Fe^{2+} absorption in iron-bearing primary minerals (e.g., Clark et al., 1990). The absence of this absorption (negative band depth values) can be an indicator of iron depletion. The blue-to-red slope is an indicator of the overall "redness" of the visible spectrum and is strongly influenced by nanophase iron oxide in Mars' ubiquitous red surface dust, which exhibits a steep ~400 – 600 nm iron-oxygen charger transfer

absorption edge. Light-toned rocks are more easily "reddened" by a thin layer of surface dust than are dark-toned mafic rocks. Therefore, high blue-to-red slope values can indicate bright but otherwise spectrally bland materials, as would be expected for the spectra of high-SiO_2/low-FeO_T targets (e.g., Smith et al., 2013). SiO_2-rich rocks observed by the Mars Exploration Rover Spirit's Panoramic Cameras (Pancam, a multispectral camera system similar to Mastcam) at Gusev crater were also characterized by large blue-to-red spectral slopes (Rice et al., 2010).

Although these spectral characteristics are not unique to the high-SiO_2/ low-FeO_T targets, they are consistent among this compositional class and can be used to determine whether other surface targets are spectrally similar. Figure 2.7 shows that Mastcam spectra of rocks at Site α (from the "Red Horn" and "Red Sheep" targets) fall within the same region of this parameter space as all other known high-SiO_2/low-FeO_T targets. The specific bounds on these parameters (gray box in Figure 2.7) exclude 70% of the other 832 rock spectra from the Murray formation analyzed here.

2.4. Discussion

2.4.1. Orientation and Extent of High-SiO_2 Layer

2.4.1.1. Subsurface Expression in Marias Pass

Sites 1, 3 – 10, 15, and 16 contain material in the subsurface with Σ_{abs} values consistent with high-SiO_2/low-FeO_T material measured by ChemCam and APXS in the Elk and Lion areas ("Hi-SiO_2 Murray" and "Buckskin" in Figure 2.3 and Table 2.1). Mastcam multispectral analysis (Figure 2.7) of Site α is also consistent with this high-SiO_2/low-FeO_T material. Sites 2 and 11 – 14 do not contain high-SiO_2/low-FeO_T material within the DAN FOV, suggesting that the top ~50 cm of the subsurface is detrital material transported from another location and filling an eroded volume. This is supported by rover imagery showing a heterogeneous mixture of rock fragments and sand at the surface in this area (see Appendix Text A.4).

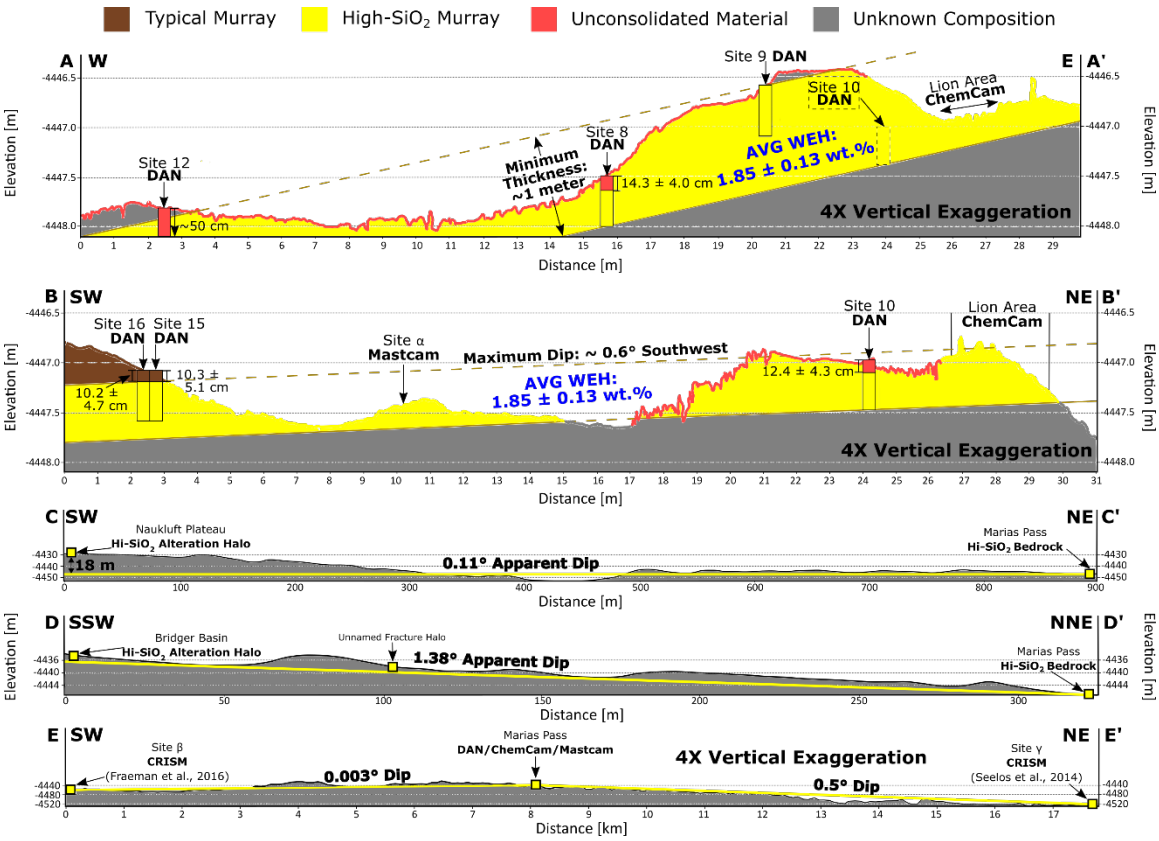

Figure 2.8. Topographic cross sections (locations shown in Figure 2.1). A-A' and B-B' show interpreted subsurface compositions based on DAN-derived Σ_{abs} values and surface compositions from ChemCam/Mastcam analyses. (a) Cross section from Site 12 to the Lion area, 4X vertical exaggeration. One possible high-SiO_2/low-FeO_T layer dip is shown, but the dip component in this direction is not constrained. The minimum thickness of the high-SiO_2/low-FeO_T layer is constrained by DAN results from Sites 8 – 10. Site 10 bedrock (dashed, located about 2 m south of A-A') is projected from its measured elevation. Site 9 is covered by a thin (<5 cm) veneer of sand but was modeled as a single layer to reduce simulation complexity (see Appendix Text A.4). (b) Cross section from Site 16 to the Lion area, 4X vertical exaggeration. Relationships shown here constrain the maximum dip of the high-SiO_2/low-FeO_T layer in this direction. (c, d) Cross sections from Marias Pass to Naukluft Plateau (location of the Lubango fracture alteration halo) and Bridger Basin (location of the Greenhorn fracture alteration halo). The projected apparent dip of the high-SiO_2/low-FeO_T layer, based on a true regional dip of 3° northwest (Kite et al., 2013; Lewis & Turner, 2019) is 0.11° and 1.38° from Marias Pass to Lubango and Greenhorn, respectively. This places the high-SiO_2/low-FeO_T layer ~18 m below Lubango, ~2 m below Greenhorn, and ~1.5 m below an unnamed alteration halo. These vertical proximities support the hypothesis that the high-SiO_2/low-FeO_T bedrock was a source for the SiO_2 enrichment of the overlying alteration halos. (e) Cross section passing through Marias Pass and hydrated SiO_2 deposits observed by CRISM (Fraeman et al., 2016; Seelos et al., 2014), 4X vertical exaggeration. <0.5° dips are required for stratigraphic equivalence between Marias Pass and Sites β and γ, consistent with a 3° regional dip to the northwest.

A single sub-horizontal layer can project through all high-SiO_2/low-FeO_T material observed in Marias Pass. Our depth results constrain the orientation and thickness of this layer. Figures 2.8a,b are cross sections in Marias Pass, locations of which are shown in Figure 2.1c. Relationships shown in Figure 2.8a require a layer ≥ 1 m thick. The Lion area, Sites 5 – 10, and Site 12 are approximately colinear (for clarity, Figure 2.8a only shows Site 8 near the center of the cross section). Since upper and lower contacts of the high-SiO_2/low-FeO_T layer are not observed within the DAN FOV at these sites, the east-west dip (stratigraphic layer orientation relative to horizontal) is unknown, but we note that a smaller or larger dip angle than that shown in Figure 2.8a requires a thicker high-SiO_2/low-FeO_T layer. The dip from the Lion area to the top of the high-SiO_2/low-FeO_T material at Site 16 is at most 0.6° southwest (Figure 2.8b). The Murray has a regional dip of ~3° northwest (Kite et al., 2013; Lewis & Turner, 2019), and the orientation of the high-SiO_2/low-FeO_T layer in Marias Pass is consistent with a minor local variation of this dip.

2.4.1.2. Relationship to High-SiO_2 Fracture Alteration Halos

Mass balance calculations using the amorphous (non-crystalline) phase fraction, relative crystalline phase abundances, and absolute geochemical abundances of drill samples indicate that the amorphous component of the Buckskin high-SiO_2 bedrock (Morris et al., 2016) and Greenhorn and Lubango high-SiO_2 fracture alteration halos (Yen et al., 2017) contain little or no Al_2O_3. Other oxides including SiO_2, FeO_T, MgO, Na_2O, and P_2O_5 all have similar abundances in the high-SiO_2 bedrock and alteration halos. Exceptions include TiO_2, CaO, and SO_3. CaO and SO_3 abundances in the alteration are due to abundant crystalline calcium sulfates and amorphous sulfate phases, which likely were precipitated at least in part after the SiO_2 enrichment diagenetic event (Frydenvang et al., 2017; Yen et al., 2017). TiO_2 is generally immobile during diagenesis (e.g., Yen et al., 2017), and the reduced

abundance of TiO_2 in the alteration halos could be due to passive reduction as other oxides such as SiO_2 are added to the halo. Similar geochemical trends were observed with ChemCam and APXS on an unnamed alteration halo (Figures 2.1b and 2.8d) in the Murray formation near Bridger Basin (Banham et al., 2018). These geochemical similarities are consistent with these materials being part of a shared diagenetic system during amorphous phase formation.

Using the Murray formation's 3° northwest regional dip (Kite et al., 2013; Lewis & Turner, 2019), we extrapolated the elevation of the Marias Pass high-SiO_2/low-FeO_T bedrock to the locations of the Stimson alteration halos Lubango (in Naukluft Plateau, Figure 2.8c) as well as Greenhorn and an unnamed alteration halo (in/near Bridger Basin, Figure 2.8d). We find that the high-SiO_2/low-FeO_T bedrock projects ~18 m below Lubango, ~2 m below Greenhorn, and ~1.5 m below the unnamed alteration halo. The close proximity of these alteration halos to the underlying high-SiO_2/low-FeO_T bedrock supports the hypothesis that this bedrock layer is the source of SiO_2 enrichment for the alteration halos (Frydenvang et al., 2017). If the alteration halos are in fact genetically related to the high-SiO_2/low-FeO_T bedrock, this implies that the high-SiO_2/low-FeO_T bedrock layer extends throughout the area spanned by Marias Pass, Bridger Basin, and Naukluft Plateau (about 1 km, Figure 2.1b).

Alteration halos were also observed earlier in the traverse, ~53 – 55 m below and ~4.9 km northeast of Marias Pass in the Bradbury group. In this area, between sols 383 and 409, anomalously low Σ_{abs} were detected by several DAN active measurements, consistent with high-SiO_2/low-FeO_T material. These alteration halos lie ~11 m below the elevation to which the high-SiO_2/low-FeO_T bedrock projects from Marias Pass, given the regional dip of the Murray formation. The Bradbury group could either underlie the Murray formation or be coeval (deposited at the same time)

with it (Grotzinger et al., 2015); so the relationship between these alteration halos and those in the Murray formation above Marias Pass is unknown. If the Bradbury group underlies the Murray formation stratigraphy, then the presence of these alteration halos at their observed location could indicate (1) a change in structural dip direction or magnitude between Marias Pass and these alteration halos, (2) the mobilization of SiO_2 down section instead of upsection as with the Murray/Stimson alteration halos, or (3) the presence of a distinct high-SiO_2 reservoir underlying these Bradbury group alteration halos. If the Bradbury group is coeval with the Murray formation and represents a more proximal environment than the distal lacustrine Murray (Grotzinger et al., 2015), then the presence of these alteration halos below the projected elevation of Marias Pass suggests that they are related to a distinct, underlying high-SiO_2 reservoir.

2.4.1.3. Relationship to Orbital Detections of Hydrated SiO_2

Seelos et al. (2014) and Fraeman et al. (2016) used the orbital Compact Reconnaissance Imaging Spectrometer for Mars (CRISM) hyperspectral instrument to identify three locations (Sites β, γ, and δ in Figure 2.1a) near the MSL traverse which exhibit spectral signatures consistent with hydrated SiO_2. These detections are based on absorptions at 1.4 μm (OH), 1.9 μm (H_2O), and 2.2 μm (Si-OH), which are consistent with either hydrated SiO_2 glass or opal (Mustard et al., 2008; Rapin et al., 2018). Site β is ~8 km southwest of Marias Pass, Site γ is ~9.5 km northeast of Marias Pass, and Site δ is about 1 km south of Marias Pass (Figure 2.1a). Marias Pass and Sites β and γ are approximately colinear from southwest to northeast (azimuth 054). Since the Murray formation has a northwest regional dip (Kite et al., 2013; Lewis & Turner, 2019) that is nearly perpendicular to this line, these deposits may be bedrock exposures of the high-SiO_2/low-FeO_T layer discovered in Marias Pass. Marias Pass lies ~20 m above Site β and ~80 m above Site γ (Figure 2.8e). If these sites

share a common stratigraphic layer with Marias Pass, the maximum regional dip of this layer along this azimuth is constrained to <0.5° to the southwest or northeast, in agreement with the regional northwest dip direction. A similar analysis shows that Site δ and Marias Pass would lie on the same stratigraphic horizon with a regional dip ~3.5° northwest, also in good agreement with the ~3° northwest regional dip. These orbital detections expand the observed extent of high-SiO_2 bedrock over an area at least 17.5 km wide, which strongly favors a stratigraphically conformable relationship within the Murray formation, and a depositional origin.

2.4.2. Hydration of High-SiO_2 Material

2.4.2.1. Comparison to Other Data Sets

ChemCam also can determine hydrogen abundances, though the LIBS spot size is significantly smaller than the DAN FOV. Hydrogen abundances measured by ChemCam are typically reported as H_2O, calculated in the same way as DAN WEH values. The mean hydration of 14 high-SiO_2 targets measured by ChemCam in the Lion area is 4.0 ± 1.2 wt.% H_2O. No DAN measurements were taken in this exact location, but the 1.85 ± 0.13 wt.% mean WEH measured by DAN in Marias Pass indicates that this ChemCam result is not representative of average Marias Pass high-SiO_2/low-FeO_T material. In contrast, DAN active measurements centered over the Lubango fracture alteration halo show a bulk halo hydration (~5.1 ± 1.0 wt.% WEH) that agrees well with ChemCam results from within the Lubango drill sample (4.0 ± 1.2 wt.% H_2O) (Rapin et al., 2018).

The much smaller FOV for individual ChemCam targets is potentially responsible for the discrepancy between DAN and ChemCam results in Marias Pass. The DAN FOV is a volume bounded by an ~1.5 m radius footprint on the surface and extends to a depth of ~50 cm. ChemCam, on the other hand, ablates material from points 350 – 550 μm in diameter to a depth of <600 μm (Wiens et al., 2012).

Unfortunately, no DAN active measurement was taken in coincidence with ChemCam targets in the Lion area. But given that the 14 high-SiO_2 ChemCam targets in the Lion area were within a 1.5 m radius, it is likely that the ChemCam results are representative of this area, comparable in size to a DAN FOV. Thus, while the bulk H_2O of the 3 m wide Lion area is well represented by ChemCam results, DAN WEH results represent a bulk view spanning Marias Pass over a few tens of meters.

The SAM tunable mass spectrometer aboard Curiosity also measures water content (sourced from both H_2O and OH) via EGA (Sutter et al., 2017). SAM measured 1.8 ± 0.9 wt.% H_2O from the Buckskin sample, which agrees well with our results. However, possible partial dehydration prior to SAM analysis (Rapin et al., 2018) could indicate that the Buckskin sample was significantly more hydrated prior to sample handling, consistent with the ChemCam H_2O results for high-SiO_2 Murray targets in the Lion area. SAM EGA data can also be used to understand the hydrated phases present in a sample. The Buckskin sample shows three evolved water temperature peaks. The first, at <400 °C, is likely due to H_2O evolved from opal-A; the second is from an unidentified source that could be jarosite (though in abundance below the CheMin detection limit); and the third, broadest peak, above ~500 °C is attributed to inclusion water in the amorphous fraction, which is likely to be a volcanic glass component based on CheMin XRD analysis (Sutter et al., 2017). As we demonstrate in the following section, significant contributions to evolved water from both opal-A and glass are consistent with our conclusion that both amorphous phases contain a significant fraction of the WEH measured by DAN. Sutter et al. (2017) also reports EGA results for H_2 and H_2S from the Buckskin sample, but these species (each <0.01 wt.%) do not make significant contributions to the WEH measured by DAN.

2.4.2.2. Constraints on Amorphous SiO_2 Phase Abundances

Due to a lack of hydrous crystalline phases in the Buckskin drill sample, the water content of the high-SiO_2 Murray material is contained in the amorphous phase (Rapin et al., 2018). The Buckskin drill sample contained 60 wt.% amorphous material, which had a SiO_2 abundance of 77 wt.%, based on CheMin and APXS mineralogical and geochemical analyses (Morris et al., 2016). The broad XRD amorphous peak in Buckskin is consistent with a mixture of ~6 wt.% opal-CT and ~33 wt.% opal-A and/or rhyolitic glass in the bulk sample (Morris et al., 2016; Rampe et al., 2017), which accounts for the large SiO_2 abundance of the amorphous fraction. Based on the presence of opal-CT, Morris et al. (2016) argue that the volcanic glass has been altered wholly or in part to opal-A.

The irregular structure of amorphous SiO_2 phases provides sites for H_2O and OH to bind and fill voids, which are lacking in microcrystalline (e.g., chalcedony) and macrocrystalline (quartz) phases (Smith et al., 2013). Most terrestrial opals contain 4 – 9 wt.% water (Segnit et al., 1965), whereas SiO_2 glasses on Earth only hold up to 3 wt.% H_2O (Graetsch et al., 1994; Newman et al., 1986; Rapin et al., 2018). Rapin et al. (2018) describes a correlation between hydrogen and SiO_2 abundances in the high-SiO_2 Murray material at Marias Pass. Using a ChemCam-derived hydration of 4.0 ± 1.3 wt.% H_2O for Buckskin, they predict that the measured hydrogen resides in opal-A and conclude that the Buckskin opal-A has a maximum hydration of 8.0 ± 2.6 wt.% H_2O. But our significantly lower DAN-derived WEH value suggests there may be a significant volcanic glass component in Marias Pass.

Using the mean bulk hydration measured by DAN (1.85 ± 0.13 wt.% WEH) and other geochemical and mineralogical constraints, we can calculate a minimum abundance of SiO_2 glass in the high-SiO_2/low-FeO_T material at Marias Pass. In a

system of n hydrated phases, we calculate the abundance of the *i*th hydrated phase by solving

$$\sum_{i=1}^{n}[WEH]_i[i] = [WEH]_{bulk} \tag{2.1}$$

where $[WEH]_i$ ≡ wt. fraction WEH of the *i*th phase and [i] ≡ bulk abundance of the *i*th phase. To obtain the minimum abundance of SiO_2 glass we assume a maximum hydration of 3 wt.% WEH in the glass (Graetsch et al., 1994; Newman et al., 1986; Rapin et al., 2018), a ferrihydrite hydration of 4.0 wt.% WEH (Gabriel et al., 2018), and an opal hydration of 7.4 ± 1.6 wt.% H_2O reported by Rapin et al. (2018) for the opal-A in high-SiO_2 fracture alteration halos that was shown to be consistent with targeted DAN experiments of those features. Rapin et al. (2018) has shown that hydrogen abundance is correlated with SiO_2 abundance in ChemCam high-SiO_2 Murray targets, indicating that only minor water is contained in non-SiO_2 phases. For this reason, we do not include non-SiO_2 hydrous phases except ferrihydrite reported by Morris et al. (2016). Ferrihydrite abundance in the Buckskin drill sample is limited to ~1.7 wt.% (by available FeO_T in the amorphous fraction) and accounts for a maximum of 0.07 wt.% WEH. Given these constraints and assumptions, we find the minimum abundance of SiO_2 glass in the high-SiO_2/low-FeO_T material to be 15.0 ± 13.5 wt.%. The possible presence of other hydrated amorphous phases, such as amorphous sulfates, would reduce the water inventory available for the SiO2 phases and shift the glass-to-opal ratio toward more abundant glass, thus supporting our conclusion that 15.0 ± 13.5 wt.% SiO2 glass is a minimum abundance. The present retention of at least minor SiO2 glass supports the silicic volcaniclastic origin of this material.

2.4.3. SiO2-rich Sediment Origin and Implications for Magmatic History

The presence of silicic glass and opal along with tridymite in a discrete stratigraphic interval in Marias Pass strongly suggests that this material is derived from an evolved igneous protolith. Hydrated SiO_2 has been identified in many locations on Mars in addition to Gale crater (e.g., Glotch et al., 2006; Milliken et al., 2008; Mustard et al., 2008; Squyres et al., 2008; Sun & Milliken, 2015; Weitz et al., 2011). Multiple pathways for SiO_2 enrichment in Martian environments have been proposed, including active enrichment through SiO_2 sintering (Frydenvang et al., 2017; Ruff et al., 2011; Skok et al., 2010), passive enrichment through acid leaching (McAdam et al., 2008; Squyres et al., 2008; Weitz et al., 2011; Yen et al., 2017), and fractional crystallization in an evolved magmatic system (Carter & Poulet, 2013; Christensen et al., 2005; Edwards et al., 2017; McCubbin et al., 2008; Udry et al., 2014, 2018). The crystalline mineralogy of the Buckskin sample is consistent with a silicic volcanic deposit from an evolved source (Morris et al., 2016; Rampe et al., 2017). Alternatively, it has been proposed that tridymite and cristobalite could form in nonvolcanic environments on Earth, but no such mineral deposits have been unambiguously documented. For instance, tridymite and cristobalite were inferred in a terrestrial deep-sea chert by Klasik (1975). This identification was based on a visual resemblance in photomicrographs; however, XRD experiments were unable to detect these minerals, possibly due to low abundances.

Without plate tectonics, other mechanisms must be invoked to produce evolved magma on Mars. One possible mechanism is mantle plumes that "shut off." Hawaiian volcanism provides a terrestrial analog for this mechanism. The Hawaiian-Emperor seamount chain consists of volcanic edifices fed by a mantle plume beneath the overriding Pacific plate. When a volcanic edifice is transported away from its mantle plume source, the magma supply decreases and shallow magma reservoirs

solidify. Deeper magma reservoirs persist but are cut off from the plume source and can produce more evolved magmas through crystal fractionation of the deep magma chambers (Clague & Sherrod, 2014). On Mars, a mantle plume cannot be cut off from an associated volcanic edifice due to plate motion, but mantle plumes do "shut off," possibly resulting in evolved magmas as at terrestrial hot spots that are cut off from their mantle plumes.

But experiments and simulations have shown that it is not necessary to "shut off" a mantle plume to produce evolved magma on Mars. Experiments conducted by McCubbin et al. (2008) demonstrated that a wet basaltic magma (1.67 wt.% water) at the base of a thick Martian crust can be enriched in SiO_2 up to an intermediate igneous composition through a single stage of fractional crystallization. Additionally, experiments have shown that intraplate magmatism can differentiate a tholeiitic basaltic parent melt to a rhyolitic composition (Whitaker et al., 2007), and ChemCam analyses of float rocks and conglomerate clasts in Gale crater (Cousin et al., 2017) follow compositional trends consistent with this magmatic evolution (Edwards et al., 2017). Further, simulations conducted by Udry et al. (2018) demonstrated that these Gale crater felsic compositions are consistent with mantle melting and fractional crystallization in intraplate magmatism.

In the presence of water, opaline SiO_2 is expected to alter to quartz under typical Martian surface conditions in <400 Ma (Tosca & Knoll, 2009) following the typical SiO_2 diagenesis pathway: glass → opal-A → opal-CT → chalcedony → quartz (e.g., Smith et al., 2013; Tosca & Knoll, 2009; Williams et al., 1985). Opaline SiO_2 deposits observed on Mars today have likely experienced only intermittent, if any, contact with liquid water since their formation (Tosca & Knoll, 2009). The presence of opal-CT in the Buckskin drill sample and minor (~1 wt.%) quartz in the Lubango fracture alteration halo indicate that diagenetic alteration of opal-A did occur in these

materials, but the present retention of opal-A in both the bedrock and alteration halos indicates that diagenesis did not proceed to completion and that these materials have been in contact with liquid water for <400 Ma since the formation of secondary amorphous phases (McLennan et al., 2019; Tosca & Knoll, 2009).

Opaline SiO_2 in the Buckskin drill sample could be either detrital (Morris et al., 2016) or a product of tridymite/cristobalite alteration (Hurowitz et al., 2017). Due to the large fraction of detrital igneous sediment and the likelihood that the amorphous component of high-SiO_2 material is a mixture of volcanic glass and its alteration products, Hurowitz et al. (2017) suggests that mudstone sediments in Gale crater are sourced from igneous provinces and are not recycled sediments. This suggests that the high-SiO_2 material in Marias Pass is the product of erosion from a primary SiO_2-rich volcanic source rock in the Gale lake catchment. The fine laminations observed in Marias Pass high-SiO_2 material are consistent with density sorting of sediment in a lacustrine environment, which would carry less dense, SiO_2-rich clasts to more distal sections of the lake (Hurowitz et al., 2017). Edwards et al. (2017) suggested that larger float rocks observed earlier in the MSL traverse were sourced from regions closer to Gale crater than the generally finer-grained mafic mud-stones, but the observation of a high-SiO_2/low-FeO_T mudstone layer suggests that more distal felsic sources could also have contributed.

A weak correlation exists between ChemCam-derived SiO_2 abundance and chemical index of alteration (CIA) in the Murray formation (Bedford et al., 2019). CIA is a measure of how chemically altered a sample is. Due to the post-depositional alteration of the high-SiO_2 Murray in Marias Pass (see section 2.1.3), Bedford et al. (2019) did not include these data in their CIA analyses. This correlation is not significant enough to explain the variations in SiO_2 observed within the Murray formation, suggesting that SiO_2 abundance in the Murray is likely a result of source

region geochemistry. Based on larger CIA values, higher-SiO_2 abundances, and the presence of cristobalite (in the Telegraph Peak and Buckskin drill samples) and tridymite (in the Buckskin drill sample), Bedford et al. (2019) argue that the Murray formation records a detrital contribution from a more evolved magmatic source that is not present in the Bradbury group. As Bedford et al. (2019) discusses, the higher Murray CIA values could be a result of the felsic mineralogy produced by an evolved magmatic source.

The SiO_2 abundance in Marias Pass is significantly larger than in the Murray stratigraphy above or below it, suggesting a temporal evolution of source region during Murray deposition. The low density of tridymite and cristobalite allows these minerals to remain entrained in fluviolacustrine systems longer than basaltic sediments. Therefore, the source of these minerals could be relatively distant from the Murray formation (Bedford et al., 2019). The nitrate and oxychlorine contents of the Buckskin sample are greater than other Murray samples analyzed by SAM EGA, also suggesting an alternate (or additional) source for this material (Sutter et al., 2017), possibly due to an evolving fluvial catchment feeding Gale lake.

The tridymite and SiO_2-rich glass in Marias Pass could also have been deposited as sediment derived from impact melt. However, the high abundance of tridymite and SiO_2 in Marias Pass would require a significant sedimentary fractionation by relative density if the tridymite-bearing impact melt formed in typical Martian basaltic crust. Alternatively, the impact melt could have been enriched in SiO_2 at the time of formation, but this would likely require an impact into a region of preexisting high-SiO_2 material, requiring another SiO_2 enrichment mechanism preceding the impact, though compositional segregation of impact melt is also possible (Bouska & Bell III, 1993). Terrestrial and lunar impact melts are typically

enriched in Al and depleted in Si (Bouska & Bell III, 1993), inconsistent with the SiO_2-rich, Al_2O_3-poor material in Marias Pass.

Palucis et al. (2014) mapped a >1000 km^2 catchment outside of Gale crater that fed Peace Vallis, an 80 km^2 alluvial fan between the Curiosity traverse and the Gale crater rim to the northwest. Like the Murray formation, the Peace Vallis fan was deposited in the Late Noachian/Early Hesperian (Palucis et al., 2014). If the drainage network that fed Peace Vallis was active during the deposition of the Murray formation, it would have provided an evolving sediment source as the network incised into the plains north of Gale crater. This catchment area may have included ash fall deposits related to volcanic plains further north (Palucis et al., 2014), and this is a possible source of the tridymite-bearing material in Marias Pass. An extensive fluvial network entering Gale crater from the south is another possible sediment source.

The lateral extent, thickness, and conformable expression of the high-SiO_2/low-FeO_T layer mapped throughout Marias Pass, in addition to its genetic relationship to fracture alteration halos up to 1 km away and the orbital detection of likely coeval outcrops over a several kilometer range, all support the hypothesis, originally based on the detection of tridymite in the Buckskin drill sample (Morris et al., 2016), that this material is volcanic in origin and therefore the product of an evolved magma source, rather than being the result of passive or active SiO_2 enrichment during diagenetic alteration like the high-SiO_2 alteration halos upsection. The stratigraphic correlation of Marias Pass with outcrops nearly 10 km away to both the southwest and northeast, as well as an outcrop 1 km to the south, which is consistent with the regional dip of the Murray formation, provides remarkable evidence for a laterally extensive, stratigraphically bound interval of silicic volcaniclastic sediments within the Murray formation.

2.5. Conclusions

Using ChemCam and APXS geochemistry to create subsurface models for DAN simulations, we have identified and mapped a thick layer of high-SiO_2/low-FeO_T material in the Murray formation throughout Marias Pass. Mastcam multispectral analysis of a large outcrop, predicted to be high-SiO_2/low-FeO_T material based on our DAN results, is consistent with a high-SiO_2/low-FeO_T composition and shares spectral characteristics with known high-SiO_2/low-FeO_T material like that exposed in the Lion area. A single sub-horizontal layer can project through all high-SiO_2/low-FeO_T material observed in Marias Pass, and the thickness of this layer is at least 1 m. A probable genetic link between the high-SiO_2/low-FeO_T bedrock in Marias Pass and high-SiO_2 fracture alteration halos is suggested by geochemical similarities and geometric relationships. This genetic link indicates that the high-SiO_2/low-FeO_T bedrock extends throughout the region spanned by Marias Pass and these alteration halos, or about 1 km. Orbital detections from CRISM of hydrated SiO_2 material 1 – 10 km to the south, southwest, and northeast of Marias Pass are approximately stratigraphically equivalent to Marias Pass assuming an ~3° regional dip to the northwest. These outcrops are likely additional exposures of the high-SiO_2/low-FeO_T bedrock investigated in Marias Pass indicating that the high-SiO_2/low-FeO_T material exposed in Marias Pass is laterally extensive over at least a 17.5 km distance.

The DAN-derived WEH for the high-SiO_2/low-FeO_T material is significantly lower than that from ChemCam data in Marias Pass. This is likely due to heterogeneities in opal abundance throughout Marias Pass. The DAN result of 1.85 ± 0.13 wt.% WEH represents the bulk hydration over tens of meters. This hydration suggests that a lower-hydration phase is present in addition to opal-A. SAM EGA temperature release profiles suggest that both rhyolitic glass and opal were present in the Buckskin drill sample. Assuming a maximum SiO_2 glass WEH content of 3

wt.%, we calculate that there is a minimum SiO_2 glass abundance of 15.0 ± 13.5 wt.%.

The Buckskin drill sample from the stratigraphic layer described here contains tridymite. This, along with our determinations of the large areal extent and thickness of this layer, its stratigraphically conformable expression, and its inferred volcanic glass component, indicates that it is a volcaniclastic product derived from felsic igneous rock. Though felsic compositions have been observed in several regions on Mars, it is not well understood how evolved magmas could form. Mechanisms to shut off Martian mantle plumes are not well understood, but would provide a mechanism for the production of evolved magmas on Mars, as seen in intraplate volcanism on Earth. A few other mechanisms have also been suggested that could produce these evolved compositions on Mars. This study is the first example of *in situ* mapping of a silicic volcaniclastic layer and description of its compositional and stratigraphic characteristics on another planet. Similar future applications of this neutron spectroscopy technique on landed missions can help resolve questions that still persist regarding the production of evolved magmatic bodies on Mars.

Acknowledgements

The authors are grateful to JPL for developing and operating the MSL Curiosity rover mission and to the Mars Science Laboratory team for facilitating the multinational collaboration involving scientists from the United States, Denmark, France, Russia, and Canada to synthesize results from several MSL instrument data sets to make this work possible. We also would like to individually thank Marion Nachon, Abigail Fraeman, and Vivian Sun for helpful conversations regarding aspects of this work. This work was supported by the Mars Science Laboratory Participating Scientist Program, the Los Alamos National Laboratory Center for the Study of Earth and Space, the NASA Earth and Space Exploration Fellowship, the Elwha Stipend of

Western Washington University, and the Carlsberg Foundation. The authors acknowledge Research Computing at Arizona State University for providing HPC, storage, etc., resources that have contributed to the research results reported within this paper (URL: http://www.researchcomputing.asu.edu). All data used for this work are available on the NASA Planetary Data System via links on the MSL page (URL: https://pds-geosciences.wustl.edu/missions/msl/).

References

Abercrombie, S. P., Menzies, A., Abarca, H. E., Luo, V. X., Samochina, S., Trautman, M. T., et al. (2019). Multi-platform immersive visualization of planetary, asteroid, and terrestrial analog terrain. *Lunar and Planetary Science L*: 2268.

Agee, C. B., Wilson, N. V., McCubbin, F. M., Ziegler, K., Polyak, V. J., Sharp, Z. D., et al. (2013). Unique meteorite from early Amazonian Mars: Water-rich basaltic breccia Northwest Africa 7034. *Science*, 339: 780–785. https://doi.org/10.1126/science.1228858

Bandfield, J. L., Hamilton, V. E., & Christensen, P. R. (2000). A global view of Martian surface compositions from MGS-TES. *Science*, 287(5458): 1626–1630. https://doi.org/10.1126/science.287.5458.1626

Banham, S. G., Gupta, S., Rubin, D. M., Watkins, J. A., Sumner, D. Y., Edgett, K. S., et al. (2018). Ancient Martian aeolian processes and palaeomorphology reconstructed from the Stimson formation on the lower slope of Aeolis Mons, Gale crater, Mars. *Sedimentology*, 65(4): 993–1042. https://doi.org/10.1111/sed.12469

Bedford, C. C., Bridges, J. C., Schwenzer, S. P., Wiens, R. C., Rampe, E. B., Frydenvang, J., & Gasda, P. J. (2019). Alteration trends and geochemical source region characteristics preserved in the fluviolacustrine sedimentary record of Gale crater, Mars. *Geochimica et Cosmochimica Acta*, 246: 234–266. https://doi.org/10.1016/j.gca.2018.11.031

Bell III, J. F., Godber, A., McNair, S., Caplinger, M. A., Maki, J. N., Lemmon, M. T., et al. (2017). The Mars Science Laboratory Curiosity rover Mastcam instruments: Preflight and in-flight calibration, validation, and data archiving. *Earth and Space Science*, 4(7): 396–452. https://doi.org/10.1002/2016EA000219

Bouska, V. & Bell III, J. F. (1993). Assumptions about the presence of natural glasses on Mars. *Journal of Geophysical Research*, 98(E10): 18,719–18,725. https://doi.org/10.1029/93JE01959

Calef III, F. & Parker, T. (2016). MSL Gale merged orthophoto mosaic. *PDS Annex*, U.S. Geological Survey.

Campbell, J. L., King, P. L., Burkemper, L., Berger, J. A., Gellert, R., Boyd, N. I., et al. (2014). The Mars Science Laboratory APXS calibration target: Comparison of Martian measurements with the terrestrial calibration. *Nuclear Instruments and Methods in Physics Research B*, 323: 49–58. https://doi.org/10.1016/j.nimb.2014.01.011

Carter, J. & Poulet, F. (2013). Ancient plutonic processes on Mars inferred from the detection of possible anorthositic terrains. *Nature Geoscience*, 6: 1008–1012. https://doi.org/10.1038/NGEO1995

Christensen, P. R., McSween Jr., H. Y., Bandfield, J. L., Ruff, S. W., Rogers, A. D., Hamilton, V. E., et al. (2005). Evidence for magmatic evolution and diversity on Mars from infrared observations. *Nature*, 436: 504–509. https://doi.org/10.1038/nature03639

Clague, D. A. & Sherrod, D. R. (2014). Growth and degradation of Hawaiian volcanoes. *U.S. Geological Survey Professional Paper*, 1801: 97–146.

Clark, R. N., King, T. V. V., Klejwa, M., & Swayze, G. A. (1990). High spectral resolution reflectance spectroscopy of minerals. *Journal of Geophysical Research*, 95(B8): 12,653–12,680. https://doi.org/10.1029/JB095iB08p12653

Clegg, S. M., Wiens, R. C., Anderson, R., Forni, O., Frydenvang, J., Lasue, J., et al. (2017). Recalibration of the Mars Science Laboratory ChemCam instrument with an expanded geochemical database. *Spectrochimica Acta Part B: Atomic Spectroscopy*, 129: 64–85. https://doi.org/10.1016/j.sab.2016.12.003

Cousin, A., Sautter, V., Payré, V., Forni, O., Mangold, N., Gasnault, O., et al. (2017). Classification of igneous rocks analyzed by ChemCam at Gale crater, Mars. *Icarus*, 288: 265–283. https://doi.org/10.1016/j.icarus.2017.01.014

Edwards, P. H., Bridges, J. C., Wiens, R., Anderson, R., Dyar, D., Fisk, M., et al. (2017). Basalt-trachybasalt samples in Gale Crater, Mars. *Meteoritics & Planetary Science*, 52(11): 2391–2410. https://doi.org/10.1111/maps.12953

Fedo, C., Grotzinger, J., Gupta, S., Stein, N. T., Watkins, J., Banham, S., et al. (2017). Facies Analysis and Basin Architecture of the Upper Part of the Murray Formation, Gale Crater, Mars. *Lunar and Planetary Science XLVIII*: 1689.

Foreman-Mackey, D., Hogg, D. W., Lang, D., & Goodman, J. (2013). Emcee: The MCMC Hammer. *Publications of the Astronomical Society of the Pacific*, 125(925): 306–312. https://doi.org/10.1086/670067

Fraeman, A. A., Ehlmann, B. L., Arvidson, R. E., Edwards, C. S., Grotzinger, J. P., & Milliken, R. E. (2016). The stratigraphy and evolution of lower Mount Sharp from spectral, morphological, and thermophysical orbital data sets. *Journal of Geophysical Research: Planets*, 121: 1713–1736. https://doi.org/10.1002/2016JE005095

Frydenvang, J., Gasda, P. J., Hurowitz, J. A., Grotzinger, J. P., Wiens, R. C., Newsom, H. E., et al. (2017). Diagenetic silica enrichment and late-stage groundwater activity in Gale crater, Mars. *Geophysical Research Letters*, 44: 4716–4724. https://doi.org/10.1002/2017GL073323

Gabriel, T. S. J, Hardgrove, C., Czarnecki, S., Rampe, E. B., Rapin, W., Achilles, C. N., et al. (2018). Water abundance of dunes in Gale Crater, Mars from active neutron experiments & implications for amorphous phases. *Geophysical Research Letters*, 45, 12,766–12,775. https://doi.org/10.1029/2018GL079045

Gasda, P. J., DeLapp, D. M., Mcinroy, R. E., Wiens, R. C., Bridges, J. C., Edwards, P. H., et al. (2016). Identification of fresh feldspars in Gale Crater using ChemCam. *Lunar and Planetary Science XLVII*: 1604.

Glotch, T. D., Bandfield, J. L., Christensen, P. R., Calvin, W. M., McLennan, S. M., Clark, B. C., et al. (2006). Mineralogy of the light-toned outcrop at Meridiani Planum as seen by the Miniature Thermal Emission Spectrometer and implications for its formation. *Journal of Geophysical Research*, 111: E12S03. https://doi.org/10.1029/2005JE002672

Graetsch, H., Gies, H., & Topalovic', I. (1994). NMR, XRD and IR study on microcrystalline opals. *Physics and Chemistry of Minerals*, 21: 166–175. https://doi.org/10.1007/BF00203147

Gross, J. & Filiberto, J. (2014). Granitic compositions in gabbroic Martian meteorite NWA 6963: Evidence for extreme fractional crystallization of a hydrous magma. *Workshop on Volatiles in the Martian Interior*: 1015.

Grotzinger, J. P., Sumner, D. Y., Kah, L. C., Stack, K., Gupta, S., Edgar, L., Rubin, D., et al. (2014). A habitable fluvio-lacustrine environment at Yellowknife Bay, Gale Crater, Mars. *Science*, 343(6169): 1242777. https://doi.org/10.1126/science.1242777

Grotzinger, J. P., Gupta, S., Malin, M. C., Rubin, D. M., Schieber, J., Siebach, K., et al. (2015). Deposition, exhumation, and paleoclimate of an ancient lake deposit, Gale crater, Mars. *Science*, 350(6257): aac7575. https://doi.org/10.1126/science.aac7575

Hardgrove, C., Moersch, J., & Drake, D. (2011). Effects of geochemical composition on neutron die-away measurements: Implications for Mars Science Laboratory's Dynamic Albedo of Neutrons experiment. *Nuclear Instruments and Methods in Physics Research A*, 659(1): 442–455. https://doi.org/10.1016/j.nima.2011.08.058

Humayun, M., Nemchin, A., Zanda, B., Hewins, R. H., Grange, M., Kennedy, A., et al. (2013). Origin and age of the earliest Martian crust from meteorite NWA 7533. *Nature*, 503: 513–516. https://doi.org/10.1038/nature12764

Hurowitz, J. A., Grotzinger, J. P., Fischer, W. W., McLennan, S. M., Milliken, R. E., Stein, N., et al. (2017). Redox stratification of an ancient lake in Gale crater, Mars. *Science*, 356(6341): eaah6849. https://doi.org/10.1126/science.aah6849

Jun, I., Mitrofanov, I., Litvak, M. L., Sanin, A. B., Kim, W., Behar, A., et al. (2013). Neutron background environment measured by the Mars Science Laboratory's Dynamic Albedo of Neutrons instrument during the first 100 sols. *Journal of Geophysical Research: Planets*, 118: 2400–2412. https://doi.org/10.1002/2013JE004510

Kite, E. S., Lewis, K. W., Lamb, M. P., Newman, C. E., & Richardson, M. I. (2013). Growth and form of the mound in Gale Crater, Mars: Slope wind enhanced erosion and transport. *Geology*, 41(5): 543–546. https://doi.org/10.1130/G33909.1

Klasik, J. A. (1975). High cristobalite and high tridymite in a middle Eocene deep-sea chert. *Science*, 189(4203): 631–632. https://doi.org/10.1126/science.189.4203.631

Le Deit, L., Hauber, E., Fueten, F., Pondrelli, M., Rossi, A. P., & Jaumann, R. (2013). Sequence of infilling events in Gale Crater, Mars: Results from morphology, stratigraphy, and mineralogy. *Journal of Geophysical Research: Planets*, 118: 2439–2473. https://doi.org/10.1002/2012JE004322

Lewis, K. W. & Turner, M. L. (2019). Geologic structure of the Vera Rubin Ridge, Gale Crater, Mars. *Lunar and Planetary Science L*: 2216.

Litvak, M. L., Mitrofanov, I. G., Barmakov, Yu. N., Behar, A., Bitulev, A., Bobrovnitsky, Yu., et al. (2008). The Dynamic Albedo of Neutrons (DAN) experiment for NASA's 2009 Mars Science Laboratory. *Astrobiology*, 8(3): 605–612. https://doi.org/10.1089/ast.2007.0157

Malin, M. C., Ravine, M. A., Caplinger, M. A., Ghaemi, F. T., Schaffner, J. A., Maki, J. N., et al. (2017). The Mars Science Laboratory (MSL) mast cameras and descent imager: Investigation and instrument descriptions. *Earth and Space Science*, 4(8): 506–539. https://doi.org/10.1002/2016EA000252

Mangold, N., Thompson, L. M., Forni, O., Williams, A. J., Fabre, C., Le Deit, L., et al. (2016). Composition of conglomerates analyzed by the Curiosity rover: Implications for Gale Crater crust and sediment sources. *Journal of Geophysical Research: Planets*, 121: 353–387. https://doi.org/10.1002/2015JE004977

Maurice, S., Wiens, R. C., Saccoccio, M., Barraclough, B., Gasnault, O., Forni, O., et al. (2012). The ChemCam instrument suite on the Mars Science Laboratory (MSL) Rover: Science objectives and mast unit description. *Space Science Reviews*, 170: 95–166. https://doi.org/10.1007/s11214-012-9912-2

McAdam, A. C., Zolotov, M. Y., Mironenko, M. V., & Sharp, T. G. (2008). Formation of silica by low-temperature acid alteration of Martian rocks: Physical-chemical constraints. *Journal of Geophysical Research*, 113, E08003. https://doi.org/10.1029/2007JE003056

McCubbin, F. M., Nekvasil, H., Harrington, A. D., Elardo, S. M., & Lindsley, D. H. (2008). Compositional diversity and stratification of the Martian crust: Inferences from crystallization experiments on the picrobasalt Humphrey from Gusev Crater, Mars. *Journal of Geophysical Research*, 113: E11013. https://doi.org/10.1029/2008JE003165

McLennan, S. M., Grotzinger, J. P., Hurowitz, J. A., & Tosca, N. J. (2019). The sedimentary cycle on early Mars. *Annual Review of Earth and Planetary Sciences*, 47: 91–118. https://doi.org/10.1146/annurev-earth-053018-060332

McSween Jr., H. Y. (1984). SNC meteorites: Are they Martian rocks? *Geology*, 12(1): 3–6. https://doi.org/10.1130/0091-7613(1984)12<3:SMATMR>2.0.CO;2

McSween, H. Y., Wyatt, M. B., Gellert, R., Bell III, J. F., Morris, R. V., Herkenhoff, K. E., et al. (2006). Characterization and petrologic interpretation of olivine-rich basalts at Gusev Crater, Mars. *Journal of Geophysical Research*, 111: E02S10. https://doi.org/10.1029/2005JE002477

McSween Jr., H. Y. (2015). Petrology on Mars. *American Mineralogist*, 100(11–12): 2380–2395. https://doi.org/10.2138/am-2015-5257

Milliken, R. E., Swayze, G. A., Arvidson, R. E., Bishop, J. L., Clark, R. N., Ehlmann, B. L., et al. (2008). Opaline silica in young deposits on Mars. *Geology*, 36(11): 847–850. https://doi.org/10.1130/G24967A.1

Mitrofanov, I. G., Litvak, M. L., Varenikov, A. B., Barmakov, Y. N., Behar, A., Bobrovnitsky, Y. I., et al. (2012). Dynamic Albedo of Neutrons (DAN) experiment onboard NASA's Mars Science Laboratory. *Space Science Reviews*, 170: 559–582. https://doi.org/10.1007/s11214-012-9924-y

Morris, R. V., Vaniman, D. T., Blake, D. F., Gellert, R., Chipera, S. J., Rampe, E. B., et al. (2016). Silicic volcanism on Mars evidenced by tridymite in high-SiO_2 sedimentary rock at Gale crater. *Proceedings of the National Academy of Sciences of the United States of America*, 113(26): 7071–7076. https://doi.org/10.1073/pnas.1607098113

Mustard, J. F., Poulet, F., Gendrin, A., Bibring, J.-P., Langevin, Y., Gondet, B., et al. (2005). Olivine and pyroxene diversity in the crust of Mars. *Science*, 307(5715): 1594–1597. https://doi.org/10.1126/science.1109098

Mustard, J. F., Murchie, S. L., Pelkey, S. M., Ehlmann, B. L., Milliken, R. E., Grant, J. A., et al. (2008). Hydrated silicate minerals on Mars observed by the Mars Reconnaissance Orbiter CRISM instrument. *Nature*, 454: 305–309. https://doi.org/10.1038/nature07097

Nachon, M., Mangold, N., Forni, O., Kah, L. C., Cousin, A., Wiens, R. C., et al. (2017). Chemistry of diagenetic features analyzed by ChemCam at Pahrump Hills, Gale crater, Mars. Icarus, 281: 121–136. https://doi.org/10.1016/j.icarus.2016.08.026

Newman, S., Stolper, E. M., & Epstein, S. (1986). Measurement of water in rhyolitic glasses: Calibration of an infrared spectroscopic technique. *American Mineralogist*, 71(11-12): 1527–1541.

Palucis, M. C., Dietrich, W. E., Hayes, A. G., Williams, R. M. E., Gupta, S., Mangold, N., et al. (2014). The origin and evolution of the Peace Vallis fan system that drains to the Curiosity landing area, Gale Crater, Mars. *Journal of Geophysical Research: Planets*, 119: 705–728. https://doi.org/10.1002/2013JE004583

Rampe, E. B., Ming, D. W., Blake, D. F., Bristow, T. F., Chipera, S. J., Grotzinger, J. P., et al. (2017). Mineralogy of an ancient lacustrine mudstone succession from the Murray formation, Gale crater, Mars. *Earth and Planetary Science Letters*, 471: 172–185. https://doi.org/10.1016/j.epsl.2017.04.021

Rapin, W., Chauviré, B., Gabriel, T. S. J., McAdam, A. C., Ehlmann, B. L., Hardgrove, C., et al. (2018). *In situ* analysis of opal in Gale crater, Mars. *Journal of Geophysical Research: Planets*, 123: 1955–1972. https://doi.org/10.1029/2017JE005483

Rice, M. S., Bell III, J. F., Cloutis, E. A., Wang, A., Ruff, S. W., Craig, M. A., et al. (2010). Silica-rich deposits and hydrated minerals at Gusev Crater, Mars: Vis-NIR spectral characterization and regional mapping. *Icarus*, 205(2): 375–395. https://doi.org/10.1016/j.icarus.2009.03.035

Ruff, S. W., Farmer, J. D., Calvin, W. M., Herkenhoff, K. E., Johnson, J. R., Morris, R. V., et al. (2011). Characteristics, distribution, origin, and significance of opaline silica observed by the Spirit rover in Gusev crater, Mars. *Journal of Geophysical Research*, 116: E00F23. https://doi.org/10.1029/2010JE003767

Sears, V. F. (1992). Neutron scattering lengths and cross sections. *Neutron News*, 3(3): 26–37. https://doi.org/10.1080/10448639208218770

Seelos, K. D., Seelos, F. P., Viviano-Beck, C. E., Murchie, S. L., Arvidson, R. E., Ehlmann, B. L., & Fraeman, A. A. (2014). Mineralogy of the MSL Curiosity landing site in Gale crater as observed by MRO/CRISM. *Geophysical Research Letters*, 41: 4880–4887. https://doi.org/10.1002/2014GL060310

Segnit, E. R., Stevens, T. J., & Jones, J. B. (1965). The role of water in opal. *Journal of the Geological Society of Australia*, 12(2): 211–226. https://doi.org/10.1080/00167616508728593

Singer, R. B., McCord, T. B., Clark, R. N., Adams, J. B., & Huguenin, R. L. (1979). Mars surface composition from reflectance spectroscopy: A summary. *Journal of Geophysical Research*, 84(B14): 8415–8426. https://doi.org/10.1029/JB084iB14p08415

Skok, J. R., Mustard, J. F., Ehlmann, B. L., Milliken, R. E., & Murchie, S. L. (2010). Silica deposits in the Nili Patera caldera on the Syrtis Major volcanic complex on Mars. *Nature Geoscience*, 3: 838–841. https://doi.org/10.1038/NGEO990

Smith, M. R., Bandfield, J. L., Cloutis, E. A., & Rice, M. S. (2013). Hydrated silica on Mars: Combined analysis with near-infrared and thermal-infrared spectroscopy. *Icarus*, 223(2): 633–648. https://doi.org/10.1016/j.icarus.2013.01.024

Squyres, S. W., Arvidson, R. E., Ruff, S., Gellert, R., Morris, R. V., Ming, D. W., et al. (2008). Detection of silica-rich deposits on Mars. *Science*, 320(5879): 1063–1067. https://doi.org/10.1126/science.1155429

Stack, K. M., Grotzinger, J. P., Lamb, M. P., Gupta, S., Rubin, D. M., Kah, L. C., et al. (2019). Evidence for plunging river plume deposits in the Pahrump Hills member of the Murray formation, Gale crater, Mars. *Sedimentology*, 66(5): 1768–1802. https://doi.org/10.1111/sed. 12558

Sun, V. Z. & Milliken, R. E. (2015). Ancient and recent clay formation on Mars as revealed from a global survey of hydrous minerals in crater central peaks. *Journal of Geophysical Research: Planets*, 120: 2293–2332. https://doi.org/10.1002/2015JE004918

Sutter, B., McAdam, A. C., Mahaffy, P. R., Ming, D. W., Edgett, K. S., Rampe, E. B., et al. (2017). Evolved gas analyses of sedimentary rocks and eolian sediment in Gale Crater, Mars: Results of the Curiosity rover's sample analysis at Mars instrument from Yellowknife Bay to the Namib Dune. *Journal of Geophysical Research: Planets*, 122: 2574–2609. https://doi.org/10.1002/2016JE005225

Taylor, G. J., Martel, L. M. V., Karunatillake, S., Gasnault, O., & Boynton, W. V. (2010). Mapping Mars geochemically. *Geology*, 38(2): 183–186. https://doi.org/10.1130/G30470.1

Thomson, B. J., Bridges, N. T., Milliken, R., Baldridge, A., Hook, S. J., Crowley, J. K., et al. (2011). Constraints on the origin and evolution of the layered mound in Gale Crater, Mars using Mars Reconnaissance Orbiter data. *Icarus*, 214: 413–432. https://doi.org/10.1016/j.icarus.2011.05.002

Tosca, N. J. & Knoll, A. H. (2009). Juvenile chemical sediments and the long term persistence of water at the surface of Mars. *Earth and Planetary Science Letters*, 286(3-4): 379–386. https://doi.org/10.1016/j.epsl.2009.07.004

Udry, A., Balta, J. B., & McSween Jr., H. Y. (2014). Exploring fractionation models for Martian magmas. *Journal of Geophysical Research: Planets*, 119: 1–18. https://doi.org/10.1002/2013JE004445

Udry, A., Gazel, E., & McSween Jr., H. Y. (2018). Formation of evolved rocks at Gale crater by crystal fractionation and implications for Mars crustal composition. *Journal of Geophysical Research: Planets*, 123: 1525–1540. https://doi.org/10.1029/2018JE005602

Vaniman, D. T., Martínez, G. M., Rampe, E. B., Bristow, T. F., Blake, D. F., Yen, A. S., et al. (2018). Gypsum, bassanite, and anhydrite at Gale crater, Mars. *American Mineralogist*, 103(7): 1011–1020. https://doi.org/10.2138/am-2018-6346

Weitz, C. M., Bishop, J. L., Thollot, P., Mangold, N., & Roach, L. H. (2011). Diverse mineralogies in two troughs of Noctis Labyrinthus, Mars. *Geology*, 39(10): 899–902. https://doi.org/10.1130/G32045.1

Werner, C. J., Armstrong, J., Brown, F. B., Bull, J. S., Casswell, L., Cox, L. J., et al. (2017). MCNP user's manual: Code version 6.2. LA-UR-17-29981.

Whitaker, M. L., Nekvasil, H., Lindsley, D. H., & Difrancesco, N. J. (2007). The role of pressure in producing compositional diversity in intraplate basaltic magmas. *Journal of Petrology*, 48(2): 365–393. https://doi.org/10.1093/petrology/egl063

Wiens, R. C., Maurice, S., Barraclough, B., Saccoccio, M., Barkley, W. C., Bell III, J. F., et al. (2012). The ChemCam instrument suite on the Mars science laboratory (MSL) rover: Body unit and combined system tests. *Space Science Reviews*, 170: 167–227. https://doi.org/10.1007/s11214-012-9902-4

Williams, L. A., Parks, G. A., & Crerar, D. A. (1985). Silica diagenesis, I. Solubility controls. *Journal of Sedimentary Petrology*, 55(3): 301–311. https://doi.org/10.1306/212F86AC-2B24-11D7-8648000102C1865D

Wray, J. J., Hansen, S. T., Dufek, J., Swayze, G. A., Murchie, S. L., & Seelos, F. P. (2013). Prolonged magmatic activity on Mars inferred from the detection of felsic rocks. *Nature Geoscience*, 6: 1013–1017. https://doi.org/10.1038/NGEO1994

Wyatt, M. B. & McSween Jr., H. Y. (2002). Spectral evidence for weathered basalt as an alternative to andesite in the northern lowlands of Mars. *Nature*, 417: 263–266. https://doi.org/10.1038/417263a

Yen, A. S., Ming, D. W., Vaniman, D. T., Gellert, R., Blake, D. F., Morris, R. V., et al. (2017). Multiple stages of aqueous alteration along fractures in mudstone and sandstone strata in Gale Crater, Mars. *Earth and Planetary Science Letters*, 471: 186–198. https://doi.org/10.1016/j.epsl.2017.04.033

CHAPTER 3

HYDRATION OF A CLAY-RICH UNIT ON MARS, COMPARISON OF ORBITAL DATA TO ROVER DATA

Abstract

Glen Torridon (GT) is a geomorphic feature of Aeolis Mons (informally Mt. Sharp) in Gale crater, Mars, variably covered by local regolith and wind-blown basaltic sands. The Mars Reconnaissance Orbiter's Compact Imaging Spectrometer for Mars (CRISM) detected clay minerals in GT, making GT a target of investigation by the Mars Science Laboratory (MSL) rover, Curiosity, which confirmed a large abundance of clays. The MSL Dynamic Albedo of Neutrons (DAN) instrument observed enrichments in bulk subsurface (<50 cm) hydration along the rover traverse compared to lower stratigraphic sections of Mt. Sharp. Here, we investigate the relationship between the CRISM 3 μm hydration index and DAN results, taking into consideration the different spatial scales and effective depths of these two instruments. We show that the elevated hydration observed by CRISM in one area of GT corresponds to elevated DAN-derived hydration, while the lower CRISM hydration in another area of GT does not correspond to a significantly lower DAN-derived hydration. We find that CRISM measured lower hydration in areas with good bedrock exposure or sand cover, while DAN bulk hydration is relatively insensitive to these characteristics. DAN active neutron results also show that the stratigraphically higher section of GT has significantly higher neutron absorption, which could be due to Fe- and Mn-rich diagenetic features. Additionally, DAN results show that GT is enriched in hydrogen with respect to other, less clay-rich units observed throughout the traverse, suggesting that subsurface clay minerals could be a significant reservoir for the hydration measured by DAN in GT.

Plain Language Summary

Glen Torridon (GT) is a region of Mt. Sharp in Gale crater, Mars. The Compact Reconnaissance Imaging Spectrometer for Mars (CRISM), an orbital instrument, detected abundant clay minerals in GT, which the NASA rover, Curiosity, later confirmed. Both CRISM and the DAN instrument on Curiosity (used to measure subsurface water) detected greater hydration in GT than in other rock layers investigated by the rover. CRISM measures hydration of the uppermost surface layer, while DAN measures the subsurface hydration to a depth of ~50 cm. CRISM detected greater surface hydration in northern GT than in southern GT, but DAN sees little difference in the hydration of these two areas. Northern GT has a rougher surface (the bedrock is covered by small rocks and pebbles) than southern GT, which is mostly exposed bedrock. Although northern GT appears to be more hydrated to CRISM, it is probably an effect of the loose surface material boosting the signal. Because DAN is not affected by surface roughness, DAN does not see this enhancement. Instead, DAN sees elevated hydration throughout GT, suggesting that subsurface clays may be more hydrated than previously thought.

Key Points

- The bulk hydration of a clay-rich unit in Gale crater is greater than that of clay-poor units, suggesting hydrated clays are present.
- The bulk hydration of this clay unit corresponds to enhanced spectral features in some, but not all, areas measured from orbit.
- Hydration features in orbital spectra are enhanced for areas with a surface cover of regolith characterized by loose pebbles.

3.1. Introduction

Gale crater, a 154 km crater on Mars, contains a 5 km tall central mound of sedimentary deposits known as Aeolis Mons (informally “Mt. Sharp”). The lower

slopes of Mt. Sharp are mostly sandstones and clay-bearing mudstones and are divided into several stratigraphic members. The Mars Science Laboratory (MSL) rover, Curiosity, has conducted detailed investigations of the chemistry, mineralogy, and hydration of several hundred meters of the exposed stratigraphy (e.g., Grotzinger et al., 2015). MSL investigations of Mt. Sharp have been guided, in part, by orbital observations made prior to and during Curiosity's investigations, including high resolution image data acquired with the Mars Reconnaissance Orbiter's (MRO) High-Resolution Imaging Science Experiment (HiRISE) instrument (McEwen et al., 2007) and the MRO Compact Reconnaissance Imaging Spectrometer for Mars (CRISM) instrument (S. Murchie et al., 2007).

Orbital instruments such as CRISM provide a means of assessing geologic history on a large scale. CRISM spectral data were used to detect the presence of ferric smectites in an area known as Glen Torridon (GT), a broad valley on the slopes of Mt. Sharp (Fraeman et al., 2016; Milliken et al., 2010). Additionally, CRISM detected Mg-sulfate minerals overlying the GT strata. This represents a transition to a more arid environment also found in other regions on Mars (e.g., S. L. Murchie et al., 2009). Gale crater has been viewed as a location that could serve as a reference section for environmental changes around the Noachian/Hesperian boundary (e.g., Grotzinger & Milliken, 2012; Milliken et al., 2010). MSL has been documenting Mt. Sharp's stratigraphy to create such a reference section, but in order to translate these results into characteristics to be usefully applied elsewhere on Mars, we must be able to translate results from landed, detailed, but small-scale data sets to orbital, large-scale data sets.

Results from the MSL Chemistry and Mineralogy instrument (CheMin) are prime examples of tying landed data to orbital data. CheMin data showed that GT bedrock drill samples contain greater smectite mineral abundances (most samples

between 28 and 34 wt.%; Thorpe et al., 2022), than any previous clay-bearing CheMin samples (maximum 28 wt.%; Bristow et al., 2018; Rampe et al., 2020; Rampe et al., 2017; Vaniman et al., 2014). This agreed with CRISM spectra which indicated a significant increase in 2.3 μm band depth in GT that corresponds to smectite minerals. Smectite clay minerals are strong indicators of aqueous activity, but they also have the potential to preserve organics (Summons et al., 2012).

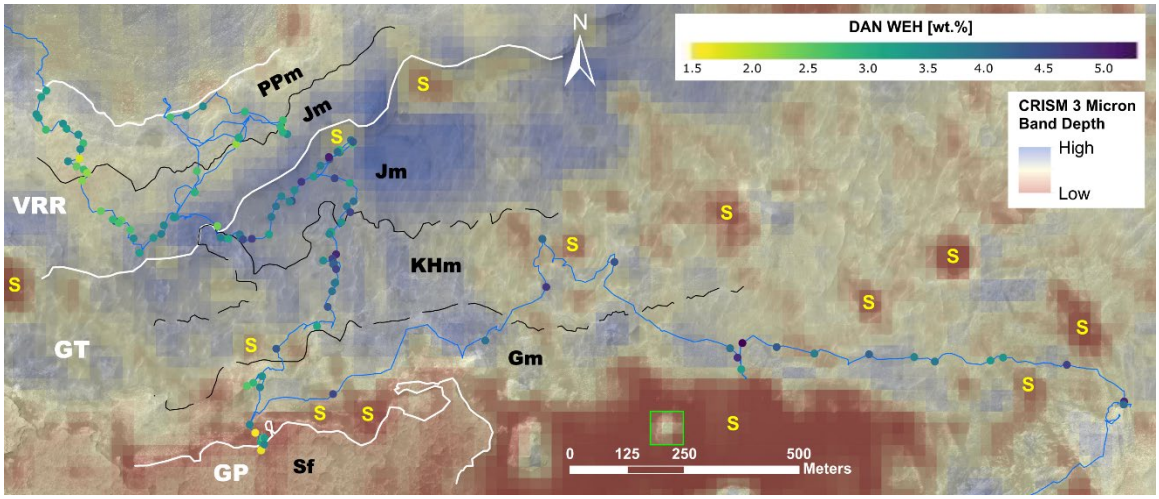

Figure 3.1. Map showing the study area with geomorphic features Vera Rubin ridge (VRR), GT, and Greenheugh pediment (GP) labeled in white, and geologic units (Fedo et al., 2022) "Pettegrove Point" member (PPm), "Jura" member (Jm), "Knockfarril Hill" member (KHm), "Glasgow" member (Gm), and "Stimson" formation (Sf) labeled in black (dashed where inferred). The Jura member spans the VRR-GT boundary. Dynamic Albedo of Neutrons (DAN) active water-equivalent hydrogen (WEH) results are symbolized along the Curiosity traverse (blue line). The basemap is a HiRISE mosaic (Calef III & Parker, 2016). A CRISM 3 μm band depth map is overlain on the HiRISE base. Several of the larger wind-blown sand patches are labeled "S" and correspond to the lowest 3 μm areas. The green box above the scale bar identifies the CRISM pixels shown in Figure 3.6.

Here, we attempt to connect orbital CRISM spectral data of tens of meters scale to data from the MSL Dynamic Albedo of Neutrons (DAN) instrument, which measures the bulk hydration at the meter scale. CRISM spectral data, corrected for atmospheric gases and aerosols and thermal emission, was used to map the depth of the broad 3 μm hydration absorption (He et al., 2022) in GT as well as on the Vera Rubin ridge (VRR) to the north and the Greenheugh pediment (GP) to the south

(Figure 3.1). Curiosity investigated VRR prior to entering GT (e.g., Fraeman et al., 2020). Neutron count rates from DAN are also sensitive to hydration and these data were acquired along the rover traverse through the VRR and GT regions. While these two datasets are both sensitive to hydration, DAN measurement locations are limited to the relatively small fraction of GT through which Curiosity traversed, whereas the CRISM hydration band data cover the entire GT region (Figure 3.1). Additionally, the DAN sensing volume (bulk rock within a few meters surface footprint to a depth of tens of centimeters) is significantly different than the CRISM sensing volume (pixels tens of meters wide and several micrometers deep). In this paper, we investigate the relationship between DAN and CRISM hydration results to understand the bulk hydration of GT and to explore the effects that surface cover and texture have on comparisons of data from these instruments.

3.2. Methods

3.2.1. Dynamic Albedo of Neutrons (DAN)

DAN is a neutron spectrometer with a pulsed neutron generator (PNG) and two He-3 neutron detectors (Litvak et al., 2008; I. G. Mitrofanov et al., 2012). In active mode, the DAN PNG produces 14.1 MeV neutron pulses (fast neutrons) at 10 Hz. A typical measurement lasts 20 min, during which time PNG neutrons are isotropically emitted with each pulse. A fraction of these neutrons enters the martian subsurface below the rover, interact with subsurface nuclei via scattering reactions which reduce kinetic energy (thermalization), and return to the detectors where they are counted. One detector is coated in cadmium, which absorbs neutrons below ~0.3 eV (thermal neutrons) and only counts epithermal neutrons (between 0.3 eV and 100 keV). The second detector counts all thermal and epithermal neutrons. To record thermal neutron count rates, the count rates from the Cd-coated detector are subtracted from those of the uncoated detector. DAN also collects data in passive

mode in which neutrons created by nuclear spallation due to the continuous galactic cosmic ray (GCR) bombardment of the martian surface are counted.

During a DAN active measurement, the time of flight (time after pulse) is recorded for thermal neutrons in 64 lognormal time bins totaling 0.1 s and the counts in each time bin are summed for all pulses. When neutron counts are plotted as a function of time after pulse, the time-resolved counting data are known as a "die-away" curve. The shape of the die-away curve is primarily dependent on the depth and abundance of neutron scatterers (primarily hydrogen) and thermal neutron absorbers including iron, chlorine, boron, and manganese (e.g., Gabriel et al., 2018; Hardgrove et al., 2011; I. G. Mitrofanov et al., 2012; Sears, 1992). In active mode, DAN detects thermal neutrons returning from a lateral distance of up to 1 – 1.5 m, and depths of up to tens of cm in the subsurface.

We determined the bulk water-equivalent hydrogen (WEH, a standard quantity used to report hydrogen abundance as an equivalent water abundance) and thermal neutron absorption cross section (Σ_{abs}, a measure of the probability of thermal neutron absorption) from 123 sites measured by DAN in active mode in VRR, GT, and GP. To be included in our analyses, a DAN active measurement was required to have a signal-to-noise ratio (SNR) of > 5 in each of 16 analyzed time bins (249 - 1838 μs after PNG pulse). SNR is dependent upon the number of fast neutrons produced by the PNG and the fraction that are thermalized before returning to the detectors. Hydrogen thermalizes neutrons and increases signal (Figure 3.2a), while neutron absorbers such as iron and manganese reduce signal (Figure 3.2b) by absorbing thermal neutrons before they return to be counted by DAN's detectors. To achieve an SNR of > 5 in every DAN time bin, we coadded (summed counts in common time bins) thermal neutron counts from DAN active measurements at the same location (Figure 3.3). This was necessary in many locations because of the

reduced PNG neutron production over the lifetime of the DAN instrument. In cases where an SNR of at least 5 was not achieved in each analyzed time bin, the results from those measurements were not included in this study.

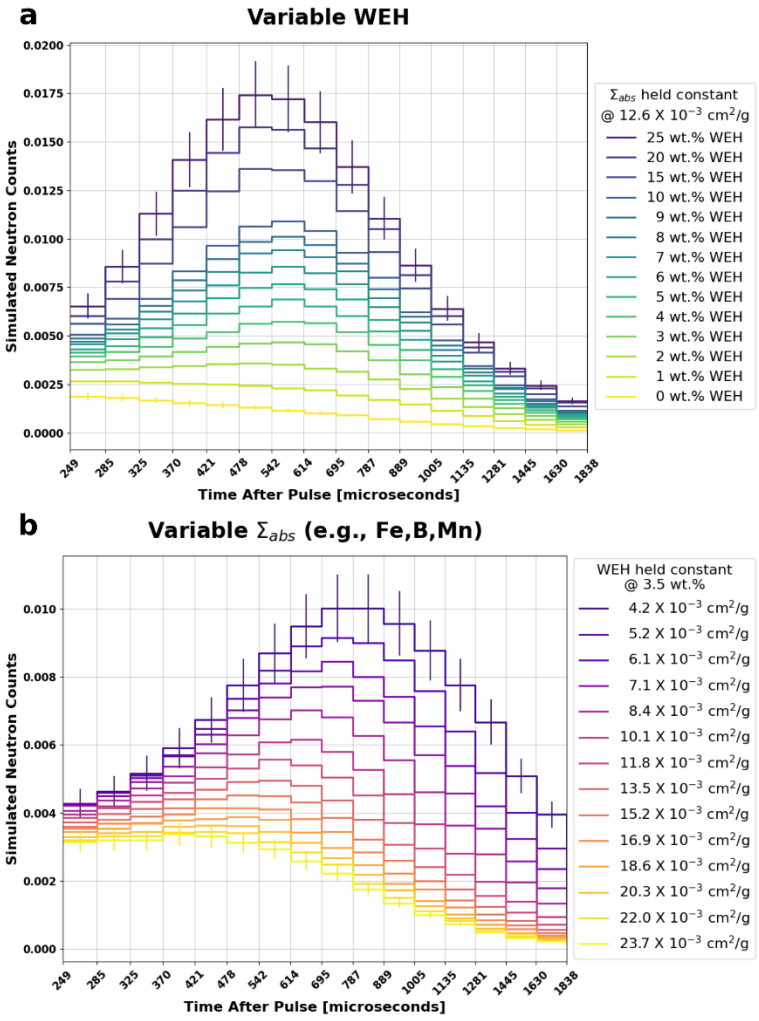

Figure 3.2. (a) Plot of simulated thermal neutron counts using DAN active model geometry with set subsurface neutron absorption cross-section (12.6×10^{-3} cm^2/g) and variable subsurface hydration (in WEH). (b) Plot of simulated thermal neutron counts using the DAN active model geometry with set subsurface hydration (3.5 wt.% WEH) and variable subsurface Σ_{abs}. Statistical uncertainty error bars are shown for the top and bottom curves in each plot.

There are multiple sources of background neutron counts that reduce SNR during DAN active data collection. These include neutrons produced by GCR spallation and neutrons produced by radioactive decay in Curiosity's radioisotope thermoelectric generator. To remove background counts, we subtracted counts from each time bin based on the average count rate in the later time bins, after PNG neutrons have ceased returning to the DAN detectors from the subsurface. In these later time bins, the signal is due only to background sources.

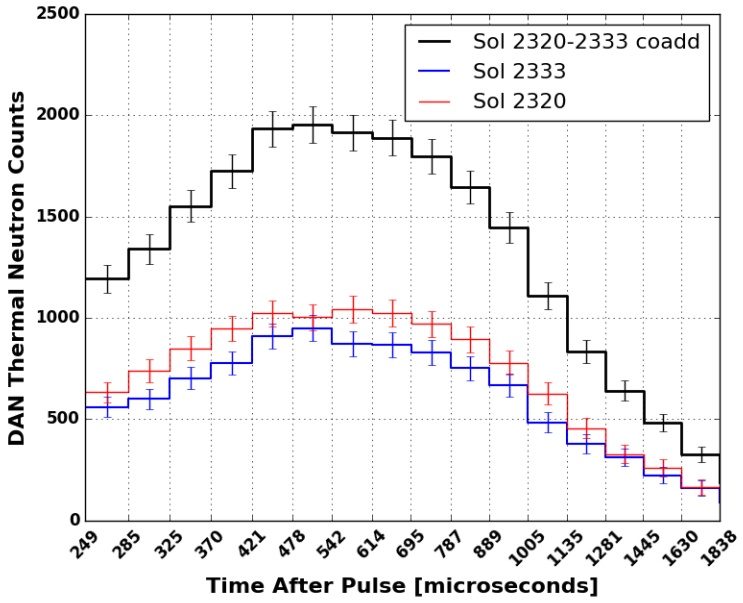

Figure 3.3. Example of DAN data coaddition used in this study. DAN thermal neutron "die-away" curves from measurements taken on sols 2320 and 2333 are plotted with the coadded data from these two measurements. The data from sols 2320 and 2333 were collected at the same location in the Jura member. Note that our analysis does not compare absolute DAN neutron count values to simulated counts. Rather, we compare the shape of the DAN die-away curve to simulated die-away curves by normalizing the DAN and simulated neutron counts to the area under the curve as in Gabriel et al. (2018) and Czarnecki et al. (2020). This allows us to compare the same simulated dataset to individual DAN measurements as well as to data that has been coadded from up to 14 DAN measurements at the same location.

We compared DAN active time spectra to simulated spectra produced using the Monte Carlo N-particle 6 (MCNP6) particle transport code (Werner et al., 2017). MCNP6 simulates neutron transport in a 3-dimensional environment. Our MCNP6 simulations included a detailed rover model (modified from Jun et al., 2013) with the DAN PNG/detectors, martian atmosphere, and variable subsurface compositions. Each MCNP6 subsurface model is assumed to be homogeneous (i.e., laterally and vertically homogeneous within the DAN sensing volume), with a subsurface density of 1.8 g/cm^3 (Gabriel et al., 2018; Lewis et al., 2019; I. G. Mitrofanov et al., 2016). For this study, we used a large grid of subsurface composition models with variable WEH and Σ_{abs}. WEH was varied between 0.1 wt.% and 25 wt.% and Σ_{abs} was varied between 4.2 × 10^{-3} cm^2/g and 23.7 × 10^{-3} cm^2/g (7.6 × 10^{-3} to 42.7 × 10^{-3} cm^{-1} in

density-independent cross section units). This model grid spans the range of Σ_{abs} for geochemistries measured by MSL geochemical instruments in Gale crater. For reference, the geochemical model corresponding to 4.2×10^{-3} cm^2/g includes 0.1 wt.% Cl and 0.48 wt.% Fe, while the model corresponding to 23.7×10^{-3} cm^2/g includes 2.95 wt.% Cl and 14.22 wt.% Fe.

To determine the WEH and Σ_{abs} for each DAN active measurement, we compared the time bins around the thermal neutron peak (249–1838 μs after pulse) from the DAN time spectra (e.g., Figure 3.3) to the grid of MCNP6 simulated spectra (e.g., Figure 3.2) using a Markov-chain Monte Carlo (MCMC) analysis method (Foreman-Mackey et al., 2013). This technique explores the grid space by interpolating between model grid points and calculating the likelihood function of a fit between DAN count rates and simulated count rates in each time bin. This method produces best-fit mean values and uncertainties for the variable parameters in the model grid space. In addition to the known physical parameters (WEH and Σ_{abs}), we also include a term for underestimated uncertainty, the "f" parameter. High values for "f" indicate that either the DAN data or simulation data were noisy, or that the model assumptions did not reflect the physical reality of the DAN measurement (see supplement to Gabriel et al. (2018)). Since we took steps to ensure SNR was above a threshold value (see above), high "f" parameter values in this study indicate that the model assumptions are inaccurate and this is likely due to significant differences in WEH and/or Σ_{abs} with depth. We removed results for which the mean value of the "f" term is greater than 20 counts, because an underestimated uncertainty of more than 20 counts is close to the statistical uncertainties in many of the DAN active time bins used in our analyses. See Gabriel et al. (2018) and associated supplemental material for further detail regarding DAN active data analysis.

We also report trends in DAN passive thermal neutron count rates for the area studied to correlate with DAN active results. We do not derive compositional results from DAN passive data; rather we qualitatively compare DAN passive count rates to DAN active WEH and Σ_{abs} trends.

3.2.2. Compact Reconnaissance Imaging Spectrometer for Mars (CRISM)

CRISM is a hyperspectral imager on the Mars Reconnaissance Orbiter that operates from 0.362 to 3.92 μm with 6.5 nm band spacings (S. Murchie et al., 2007). For this paper, we chose to use an along-track oversampled observation (FRT00021C92) centered over GT. This choice allowed projection of the data at 12 m/pixel using a log maximum likelihood approach for surface reflectance retrieval and regularization as described in He et al. (2019). The Discrete Ordinates Radiative Transport (DISORT) code was used to model atmospheric contributions, including dust and ice aerosols, CO_2, CO, and H_2O gases, and the Hapke surface photometric function (Hapke, 2012) to simulate incidence, emergence, and phase angle effects on the surface single scattering albedo (SSA) for each pixel (e.g., Arvidson et al., 2015). Thermal emission from the surface and atmosphere were also included. Data were processed using a neural network approach to solve the undetermined nature of retrieving surface SSA for wavelengths longer than ~2.65 μm. The underdetermined nature is a consequence of both solar and thermal emittance terms for the long wavelength data, that is, surface kinetic temperature adds an additional unknown quantity. The details of the neural network approach are given in He et al. (2019). The retrieved SSA spectrum for each pixel was then used to generate a series of spectral parameter estimates using the techniques described in Viviano-Beck et al. (2014). One important addition to the standard parameters is a 3 μm integrated band index (BDI). This parameter or index is of crucial importance for comparison of DAN data to CRISM data for this paper. This parameter is associated

with the 3 μm H_2O symmetrical and asymmetrical stretch absorptions, the 6.0 H_2O fundamental bending mode absorption overtone, and the shorter wavelength OH fundamental stretch absorption (e.g., Hawthorne, 1988). It is thus a strong indicator of the presence of H_2O to the several micrometer sampling depth for CRISM observations. The 3 μm BDI was calculated using a continuum line defined between 2.1 and 3.7 μm and then computing the integrated area between the continuum line and actual spectral data from 2.9 to 3.7 μm, employing the actual widths of each spectral band pass.

3.2.3. DAN and CRISM Comparisons

In order to compare DAN and CRISM results, we first registered the map projected CRISM scene to the MRO HiRISE mosaic used by the MSL team for rover traverse planning and locations (Calef III & Parker, 2016). This registration was accomplished by matching common features such as buttes, edges of sand sheets, and distinct albedo boundaries, which are distinct in both CRISM and HiRISE data. Because the CRISM pixels (12 m) are much larger than HiRISE pixels (0.25 m) the registered CRISM data necessarily has location errors of one to two HiRISE pixels, based on detailed examination of sharp albedo boundaries between the two data sets. To reduce the impact of this imperfect registration, the CRISM data were resampled to 24 m/pixel by computing the mean value of the CRISM 3 μm band for each group of four adjacent 12 × 12 m pixels. The surface areas of many, but not all, 24 m CRISM pixels included in our analyses contain multiple DAN active measurements. To compare CRISM 3 μm band depth to DAN WEH for these pixels, we first determined the best-fit WEH and uncertainty for each DAN measurement, then computed the mean value and propagated uncertainty for all DAN measurements within a single CRISM pixel. Appendix Table C.1 identifies DAN measurements that were used to derive mean values in this way.

Because DAN measures the bulk hydration of the top tens of cm beneath the rover, while CRISM measures the hydration of just the top few μm of the surface, we took steps to identify CRISM pixels with surface cover that is not representative of the subsurface measured by DAN. Sand cover is significant in many parts of GT, and sand in Gale crater is known to have a low water content (Gabriel et al., 2018; Sutter et al., 2017). We therefore investigated the effect of sand on CRISM 3 μm band depth. To determine sand cover fraction, we drew polygons around sand patches on a HiRISE basemap in ArcGIS. Because this process uses visual inspection of HiRISE images and it is not always possible to separate sand from bedrock, we determined that a relative uncertainty of 10% is reasonable for these estimated areas. To determine this relative uncertainty, we repeated this method of drawing polygons three times in the area of Figure 3.1 outlined in green. Our best estimate for the area of sand cover within these nine CRISM pixels was 3,100 m^2. A liberal redrawing to include as much sand as possible resulted in an area of 3,290 m^2, or +6%. A conservative redrawing to exclude as much bedrock as possible resulted in an area of 2,732 m^2, or –12%.

Similarly, it is reasonable to expect that dust cover may have a measurable effect on CRISM 3 μm data. To test for such an effect, we analyzed available Mars Hand Lens Imager (MAHLI) high-resolution images taken on VRR and GT. MAHLI is an arm-mounted camera that takes high-resolution images of the surface in front of the rover. Dust cover percentages for MAHLI images throughout VRR and GT were determined using the image analysis software ImageJ (Schmidt et al., 2018; Schneider et al., 2012). Each MAHLI image was matched to the specific CRISM pixel which covered the area of that MAHLI image, and a mean dust cover fraction for each CRISM pixel was determined. Dust coverage within an individual MAHLI image of a horizontal "as is" rock target is generally uniform. Schmidt et al. (2018) found

differences in dust coverages range between 2% and 15% (usually <10%) for different locations within individual images. The presence of very fine dust that cannot be resolved by 15 μm/pixel resolution of 2 cm standoff MAHLI images, may contribute up to ~10% additional uncertainty. Linear or near linear correlations between dust coverage estimates and Alpha-Particle X-ray Spectrometer (APXS) chemistry (Schmidt et al., 2018) suggest these estimates of uncertainty are too high. The overall range of dust coverage in Glen Torridon (~20% – 50%) is relatively restricted compared to the range along the entire rover's traverse (~2% – 80%) (Henley et al., 2021; Schmidt et al., 2018), where lower values are typically associated with eolian dune fields. The length scale of these variations demonstrates relevance to the 12 × 12 m scale of the CRISM pixel. Further details concerning the dust coverage analysis can be found in Schmidt et al. (2018) and the ImageJ software is available free at https://imagej.nih.gov/ij/.

3.3. Results

Appendix Table C.1 lists the mean WEH and Σ_{abs} results with associated uncertainties for each DAN measurement analyzed. In the study area, there are several geologic units as defined in Fedo et al. (2022): the "Pettegrove Point" (PPm) and "Jura" (Jm) members of the "Murray" formation, the "Knockfarril Hill" (KHm) and "Glasgow" (Gm) members of the "Carolyn Shoemaker" formation, and the "Stimson" formation. In this work, the Jm and KHm are further divided between measurements on VRR and in GT due to the significantly different WEH results between these two geomorphic features. Table 3.1 lists the mean DAN active-derived WEH and Σ_{abs} results with associated uncertainties for each of these units (note only two DAN active measurements are included for KHm/VRR). The three GT units have similar WEH results while the VRR units also have similar, but lower, mean WEH values. This

is the case even within the Jm, which spans the same elevation range within VRR and GT, but shows elevated WEH in GT (Figure 3.4).

Table 3.1. MCMC WEH and Σ_{abs} results for geologic units PPm, Jm, KHm, and Gm

Unit	DAN sites	WEH mean	Mean uncertainty [wt.%]	St.dev. of mean	Σ_{abs} mean	Mean uncertainty [10^{-3} cm^2/g]	St.dev. of mean
PPm/VRR	26	3.0	0.6	0.1	11.8	0.7	0.2
Jm/VRR	19	3.0	0.6	0.1	14.5	0.9	0.5
KHm/VRR	2	3.4	0.6	0.3	11.9	0.6	0.3
Jm/GT	29	4.0	0.7	0.1	11.3	0.6	0.1
KHm/GT	19	4.0	0.7	0.1	12.6	0.6	0.3
Gm/GT	26	3.7	0.8	0.2	13.8	0.9	0.4

Note. The mean of individual measurement uncertainties is given as well as the standard deviation of the mean. The number of DAN active measurement locations within each unit is reported as "DAN Sites." MCMC results for individual DAN active measurements are provided in Appendix Table C.1.

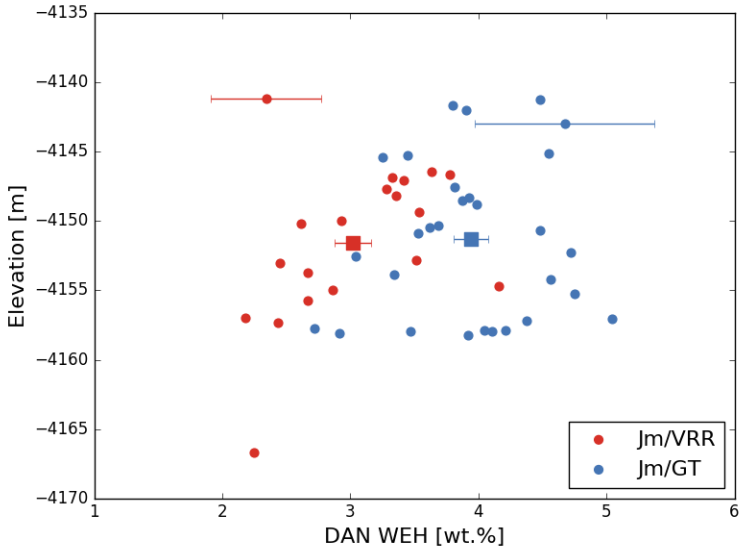

Figure 3.4. Plot of DAN-derived WEH for the Jura geologic unit in both VRR and GT. Representative error bars are included for one measurement in each unit. A square symbol marks the mean WEH for each unit with standard deviation of the mean. The elevation range of the Jura is similar on VRR and in GT, but most Jm/GT WEH values are larger than most Jm/VRR measured WEH values. See also Table 3.1 for mean DAN results and uncertainties and Appendix Table A.1 for individual DAN measurement results and uncertainties.

The map in Figure 3.1 symbolizes each DAN measurement along the rover traverse by WEH over the CRISM 3 μm band depth scene. This map shows that CRISM 3 μm band depth is greater in the Jm/GT compared to the other geologic

units in the map area. Conversely, both Figure 3.1 and Table 3.1 show that while DAN WEH is higher in GT than on VRR, it remains high throughout GT. We will investigate these differences below after examining the effects of sand and dust cover on the data sets.

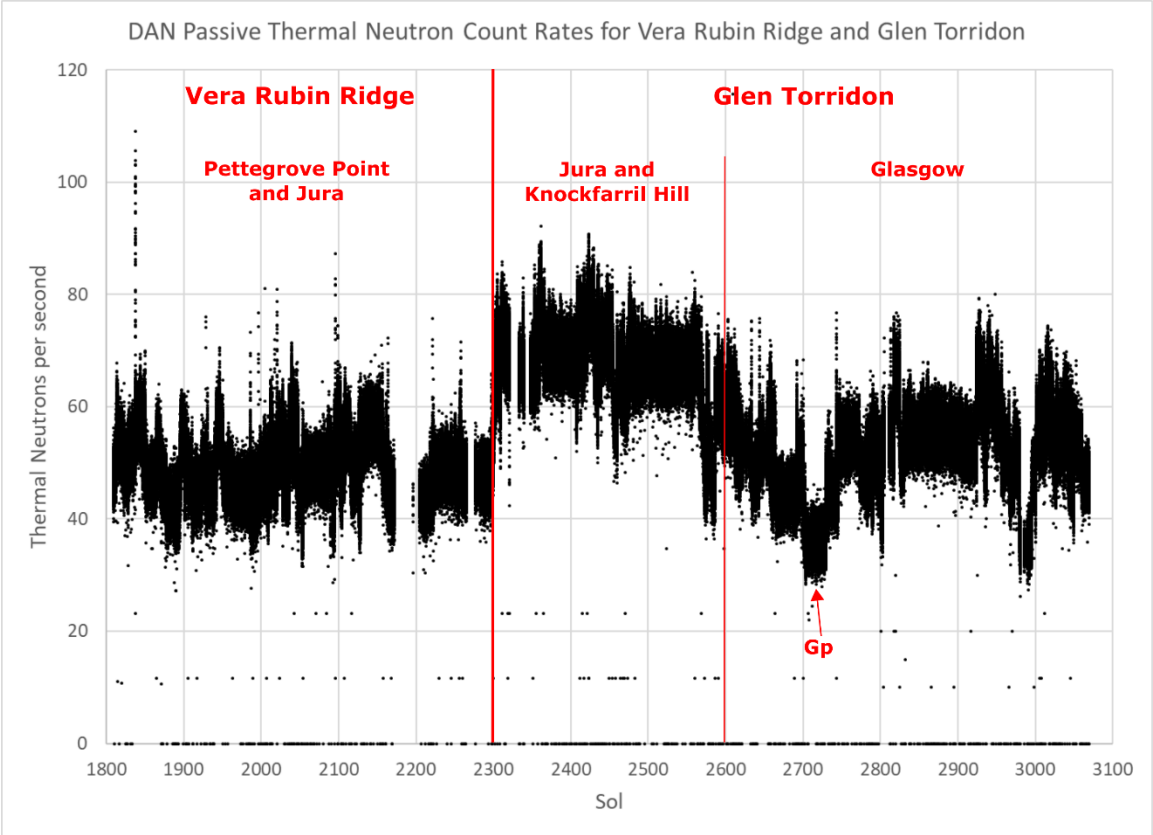

Figure 3.5. DAN passive thermal neutron count rates for the sol range spanning the Mars Science Laboratory (MSL) traverse through VRR and GT. Distinct differences in count rates can be seen between VRR (up to sol 2300), Jm/GT and KHm/GT (sols 2300 – 2600), and Gm/GT (after sol 2600). The increase in count rates at sol 2300 corresponds to the increase in WEH from VRR to GT and the decrease at sol 2600 corresponds to a slight decrease in WEH and a significant increase in Σ_{abs} from KHm/GT to Gm/GT.

Figure 3.5 is a plot of DAN passive thermal neutron count rates over the sol range corresponding to the VRR and GT investigations. As with DAN active measurements, higher DAN passive thermal neutron count rates are consistent with an increase in WEH, a decrease in Σ_{abs}, or both (Jun et al., 2013). The mean DAN passive thermal neutron count rate for VRR is 49.0 neutrons/s (mean uncertainty 2.1

neutrons/s, standard deviation 5.4 neutrons/s). A sharp increase in count rate is seen around sol 2300 which corresponds to the transition from Jm/VRR into Jm/GT. The mean DAN passive thermal neutron count rate for Jm/GT and KHm/GT is 64.2 neutrons/s (mean uncertainty 2.3 neutrons/s, standard deviation 7.9 neutrons/s). A drop in the passive thermal neutron count rate is seen at about sol 2600, which corresponds with the transition from KHm/GT to Gm/GT. The mean DAN passive thermal neutron count rate for Gm/GT is 46.9 neutrons/s (mean uncertainty 5.9 neutrons/s, standard deviation 15.6 neutrons/s).

3.4. Discussion

3.4.1. The Effect of Sand and Dust Cover

Generally, the Curiosity rover does not drive over significant sand patches. As a result, the volume of sand in DAN active measurements is generally low. But windblown sand can be present as (relatively thin) surface cover along the rover traverse. The presence of a very dry material such as sand in the DAN active field of view (FOV) will result in a high "f" parameter value from our MCMC analysis because the simulation results are derived from models with a homogeneous subsurface composition that is not representative of a dry sand layer above more hydrated bedrock. High "f" parameter results have been removed from our analyses (see Section 3.2).

To determine the effect that sand has on CRISM 3 μm band depth, a small area of bedrock surrounded by sand with clear boundaries was identified adjacent to the rover traverse (green box in Figure 3.1). Figure 3.6 is a plot of sand fraction vs. 3 μm BDI for the eight CRISM pixels intersecting this exposed bedrock as well as one adjacent (100% sand cover) CRISM pixel. The strong anti-correlation between sand cover and 3 μm hydration shown in Figure 3.6 (r^2 = 0.74, p-value = 0.003) indicates that the CRISM 3 μm band depth is highly sensitive to the presence of sand.

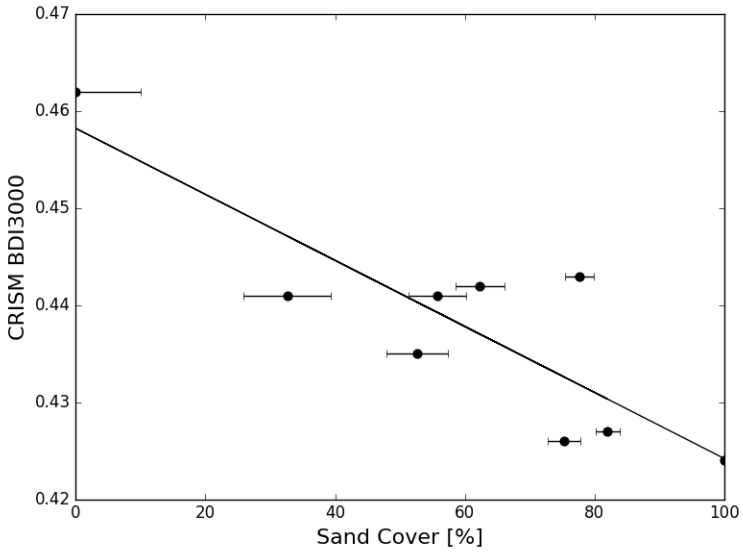

Figure 3.6. Plot of CRISM 3 μm band depth as a function of sand cover for the pixels within the green box in Figure 3.1. The anti-correlation of 3 μm hydration with sand cover indicates that the relative hydration observed by CRISM is significantly biased by the presence of sand cover. r^2 = 0.74, p-value = 0.003.

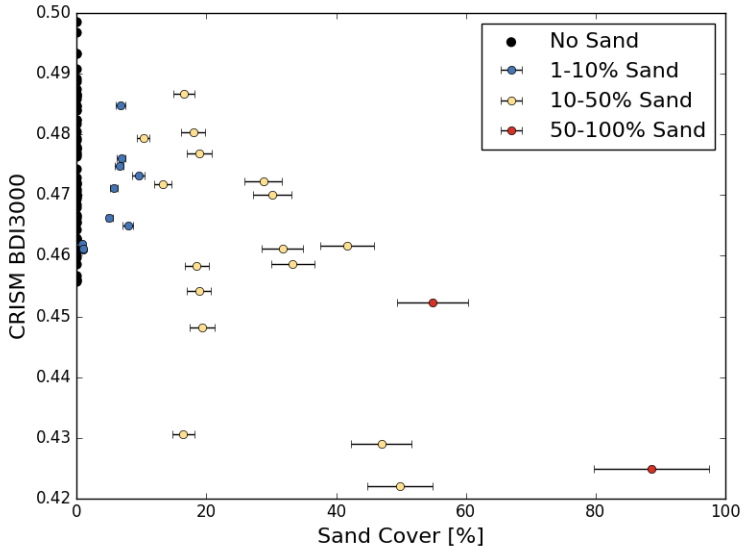

Figure 3.7. Plot of sand cover versus CRISM 3 μm band depth for CRISM pixels containing DAN measurements on VRR and in GT. Pixels with no significant sand cover (black points along y-axis) range from BDI3000 values of 0.455 – 0.500. Data points with between 1% and 10% sand cover (blue points) are also within this range, but data points with >10% sand cover (yellow and red points) are biased to the lower end of this BDI3000 range or are significantly below it. Error bars represent ±10% relative error in sand cover percentages determined by area counting on a HiRISE basemap.

We used the same method of drawing polygons around sand patches to determine the fraction of sand cover for each CRISM pixel containing a DAN measurement. Figure 3.7 is a plot of sand cover vs. CRISM 3 μm BDI. Because sand

does not contribute significantly to our DAN WEH results, and most CRISM pixels with >10% sand cover have lower 3 μm values compared to other pixels with similar DAN-derived WEH values, it is probable that >~10% sand cover biases the measured 3 μm band depth to significantly lower values compared to the unbiased DAN results. However, pixels with 1 – 10% sand cover are not biased to lower 3 μm values compared to other pixels with no obvious sand cover. To remove the bias correlated with >10% sand cover, we removed these CRISM pixels from our analyses.

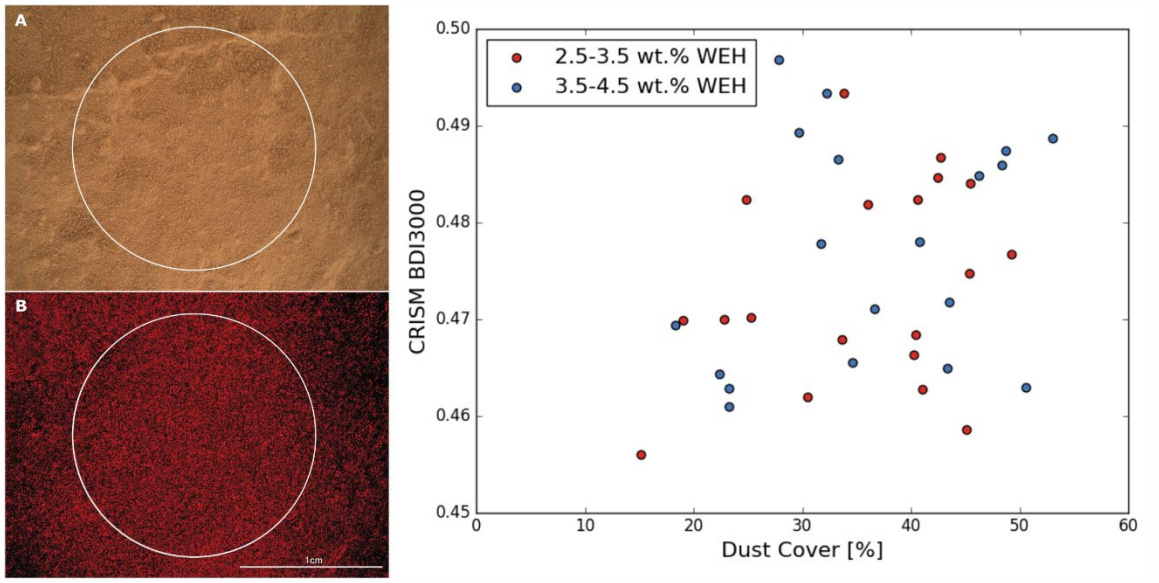

Figure 3.8. (a) MAHLI image (3088MH0001760011101613C00_DXXX) of target Gout Rossignol (Sol 3088). Dust coverage was determined for a centered 17-mm white circle, which represents the APXS FOV for chemical comparisons (Schmidt et al., 2018) and reduces vignetting and lower apparent dust coverage around the edge of the image. (b) Edited MAHLI image where red pixels are dusty and black pixels are dust-free rock surfaces. The dust cover of this image is 41%. (c) Plot of CRISM 3 μm band depth as a function of dust cover for CRISM pixels containing DAN-derived WEH values in two ranges. Pixels containing >10% sand cover are not included. No correlation between dust cover and 3 μm band depth is apparent.

It is possible that surface dust cover would also affect CRISM hydration indices. Because the bulk hydration measured by DAN varies between ~2 – 5 wt.% in the study area, and DAN bulk hydration is not dependent on surficial dust cover, it is important to control for bulk hydration when determining if there is a correlation between CRISM 3 μm band depth and dust cover. Figure 3.8 is a plot of CRISM 3 μm

band depth as a function of dust cover determined using the method described above. It is clear that there is no correlation in either the lower DAN-derived WEH range (2.5 – 3.5 wt.% WEH) nor in the higher WEH range (3.5 – 4.5 wt.% WEH). Because dust cover does not bias CRISM 3 μm band depth in the study area, we do not correct for dust cover in the following analyses.

3.4.2. The Effect of Surface Cover

Figure 3.9 plots of the same DAN WEH vs. CRISM 3 μm data as in Figure 3.7, but with sandy CRISM pixels removed as discussed above. One data point from an active Gale crater sand dune with a previously published DAN-derived hydration (Gabriel et al., 2018) is included for reference. Data points are classified by geologic unit. There are clear distinctions between the CRISM 3 μm BDI of some units. For example, the Jm/GT (yellow) have generally greater 3 μm BDI than the Gm/GT (dark blue), also shown by the mean unit values plotted in Figure 3.9 and listed in Table 3.1. Most of the Jm/GT along the rover traverse is covered in "rubbly" material composed of loose pebbles (Figure 3.10 left), which could promote 3 μm absorption due to either a different grain size or higher water content. Conversely, the Gm/GT unit contains mostly exposed bedrock (Figure 3.10 right). Although sand grain size could also promote multiple scattering, windblown sand in Gale crater contains very low water abundances and does not significantly enhance 3 μm absorption. A comparison of the Jm/GT and Gm/GT data in Figure 3.9 shows the effect of this "rubbly" material on the CRISM 3 μm signal. The rubbly Jm/GT has a significantly enhanced 3 μm signal compared to the bedrock-dominated Gm/GT, even though the average WEH of these two units are similar at 3.9 ± 0.1 and 3.7 ± 0.2 wt.% WEH, respectively. The Gm/GT also shows a positive correlation between DAN-derived bulk WEH and CRISM 3 μm surface hydration (r^2 = 0.40, p-value = 0.038).

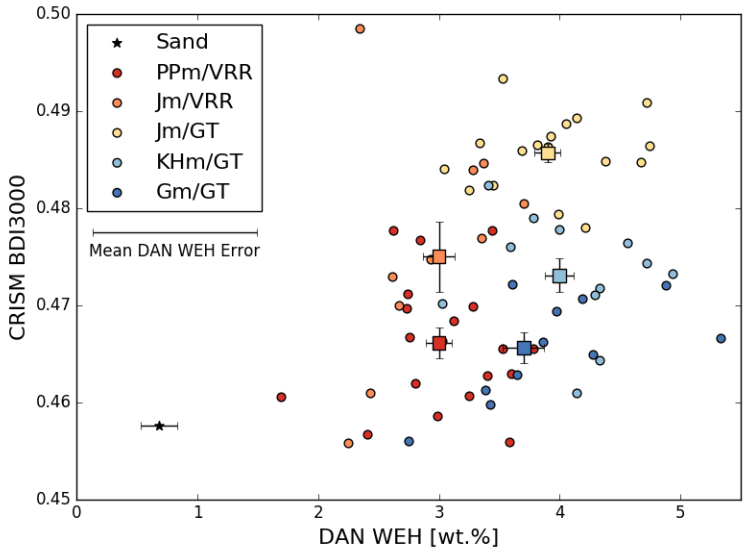

Figure 3.9. Plot of DAN-derived WEH vs. CRISM 3 μm BDI symbolized by geologic unit for pixels containing <10% sand cover. A representative error bar is shown of the mean DAN WEH error for these data. One data point from a previous DAN measurement taken over a sand dune (Gabriel et al., 2018) is included for reference. Mean values for each unit are plotted as square data points with error bars representing standard deviation of the mean.

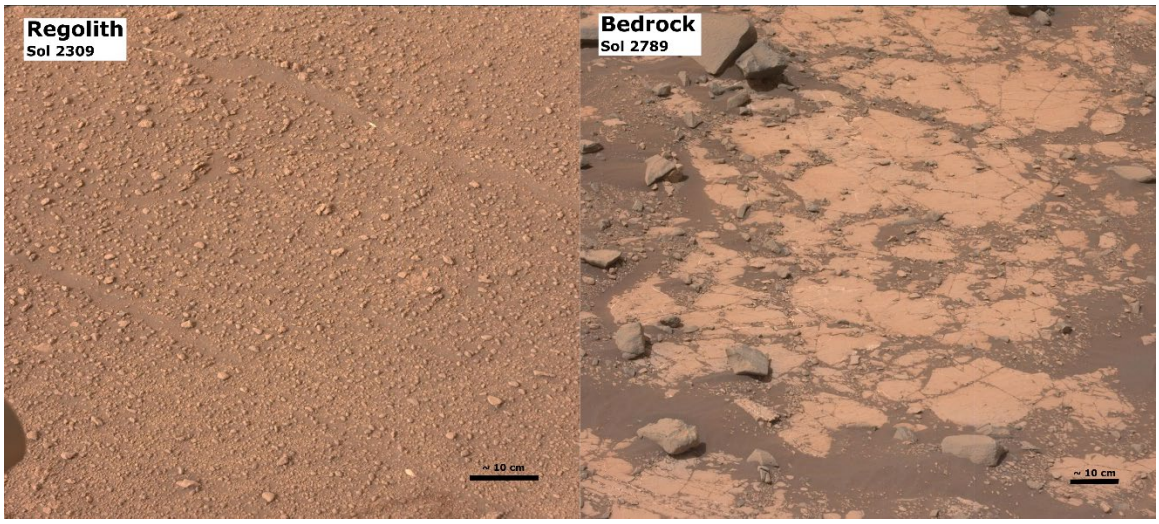

Figure 3.10. (left) This Mast Camera (Mastcam) image (image ID: 2309ML0123340030606013C00, sol 2309, Jm/GT) is a representative location of the "rubbly" material that characterizes the "regolith" surface cover classification. Most (>50%) of the surface area in this class is a mix of loose pebbles and sand. (right) This Mastcam image (image ID: 2789ML0146110880606864C00, sol 2789, Gm/GT) is a representative location of the "bedrock" material that characterizes the surface cover classification of the same name. Most (>50%) of the surface area in this class is exposed in-place bedrock or large broken bedrock blocks.

To examine the effect of surface cover across the entire study region, we classified each CRISM pixel within the study area as either "regolith" (>50% pebble-sized or smaller surface cover; representative location shown in Figure 3.10 left) or "bedrock" (>50% well-exposed bedrock; representative location shown in Figure 3.10 right). The geomorphic units mapped by Hughes (2022) in GT have specific surface characteristics which we used to classify the surface cover of GT units. The Hughes (2022) geomorphic units do not extend onto VRR, so VRR CRISM pixels have been classified based on new examination of HiRISE data (Figure 3.1 basemap).

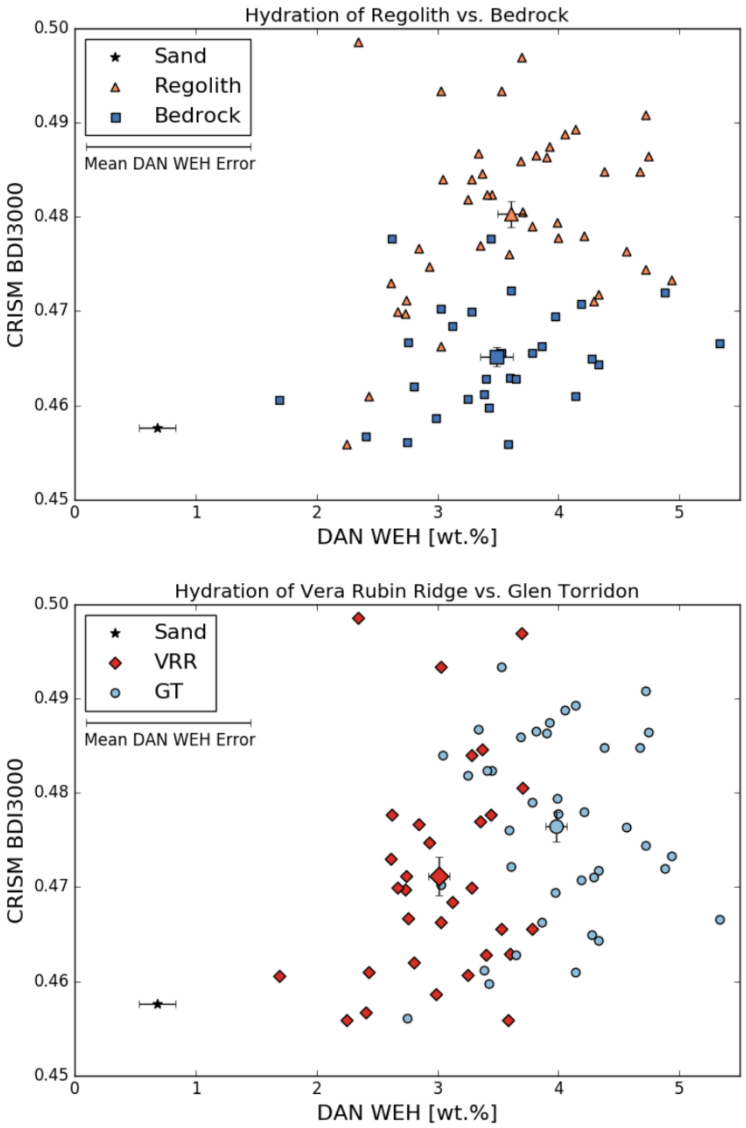

Figure 3.11. DAN-derived WEH vs. CRISM 3 μm BDI symbolized by surface cover (top) and geomorphic region (bottom). The same data are shown in both plots, only the classification scheme differs. CRISM pixels classified as "regolith" are primarily pebble-sized or smaller surface cover, whereas "bedrock" pixels are primarily exposed bedrock. A representative error bar on each plot shows the mean DAN WEH error. One data point from a previous DAN measurement of a sand dune (Gabriel et al., 2018) is included for reference. Mean values are larger points with error bars representing standard deviation of the mean. Regolith pixels have distinctly enhanced 3 μm BDI compared to bedrock pixels (top); and WEH is generally lower on VRR than in GT (bottom).

Figure 3.11 (top) is a plot of DAN WEH versus CRISM 3 μm band depth classified by surface cover, regolith (52 pixels), or bedrock (37 pixels). CRISM 3 μm band depth is enhanced for the regolith pixels (mean 0.480 ± 0.001) compared to bedrock pixels (mean 0.465 ± 0.001). This shows that the regolith surface cover either has a distinct grain size or enhanced hydration compared to underlying bedrock. We see no enhancement of DAN WEH in the regolith material (mean 3.5 ± 0.1 wt.% WEH) compared to the bedrock material (mean 3.5 ± 0.1 wt.% WEH), indicating that if the enhancement of CRISM 3 μm band depth in regolith pixels is due to the hydration of the surface cover, this surface cover must be thin enough that it is not significant within the ~50 cm deep DAN FOV.

3.4.3. Correlation of Surface to Bulk Hydration in Glen Torridon

The r^2 value of DAN WEH versus CRISM 3 μm band depth for the regolith data set plotted in Figure 3.11 (top) is 0.076 and the p-value is 0.08. The r^2 value for the bedrock data set is 0.057 and the p-value is 0.21. In both cases, this indicates that there is not a significant correlation between these two parameters. This may not be surprising given the granularity of a two-category surface cover classification scheme, and the inherent problem of large CRISM pixels and relatively small DAN surface footprints. It is worth noting however, that the same overall data set, when classified by geomorphic region (VRR vs. GT) as in Figure 3.11 (bottom), has much lower r^2 values (0.034 and 0.003 for VRR and GT, respectively). Taken together, this indicates that the variation in these data is better explained by surface cover than by geomorphic region.

3.4.4. Hydration of Glen Torridon Versus Vera Rubin Ridge

Figure 3.11 (bottom) shows that GT data points have higher water values (mean 3.9 ± 0.1 wt.% WEH) than VRR data points (mean 3.0 ± 0.1 wt.% WEH). This is also shown in Table 3.1, which lists the mean WEH for each unit, and in

Figure 3.9, which illustrates the range of WEH values in each unit. The higher WEH abundances measured in Jm/GT and KHm/GT are also reflected in the DAN passive data, where thermal neutron count rates are generally higher for the sol ranges spanned by these units (sols 2302 – 2601 and 2813 – 2948) than sols corresponding to other geologic units (Figure 3.5). The generally lower passive count rates for sols 2602 – 2695, 2734 – 2812, and 2949 – 3069 in the Gm/GT unit are a result of the higher Σ_{abs} seen in DAN active results throughout this unit. The passive count rates in the "Stimson" formation (sols 2696 – 2733) were among the lowest in the study area, which suggests that the Stimson formation of GP may be less hydrated than GT.

3.5. Conclusions

We determined the bulk hydration of multiple geologic units along the Curiosity rover's traverse within the geomorphic features known as VRR and GT using active neutron spectroscopy from the MSL DAN instrument. We found relative agreement between DAN active results and DAN passive neutron counts (i.e., neutrons generated by galactic cosmic rays and the rover radioisotope thermoelectric generator). The bulk hydration in GT (3.9 ± 0.1 wt.% WEH) is greater than in VRR (3.0 ± 0.1 wt.% WEH), broadly in agreement with orbital results from the CRISM instrument, which show a significant enhancement in the 3.0 μm hydration feature in GT (0.476 ± 0.002 band depth) compared to VRR (0.471 ± 0.002 band depth). However, the CRISM 3.0 μm hydration feature is less pronounced in the KHm/ GT (0.473 ± 0.002 band depth) and Gm/GT (0.466 ± 0.002) than in the Jm/GT (0.486 ± 0.001). This trend is not represented in the DAN results, where the Jm/GT and KHm/GT hydration are very similar (3.9 ± 0.1 and 4.0 ± 0.1 wt.% WEH, respectively) and the Gm/GT hydration (3.7 ± 0.2 wt.% WEH) is only slightly reduced (Table 3.1).

CRISM spectral data come from the top few μm of the surface and are susceptible to effects from surface cover (e.g., sand cover as well as regolith vs. bedrock), none of which significantly affect DAN data from the top tens of cm of the subsurface. After removing CRISM pixels with significant sand cover, we found that CRISM pixels in the study area that are predominantly regolith (i.e., primarily pebble-sized or smaller clasts) have significantly greater 3.0 μm absorption (0.480 ± 0.001 band depth) than pixels which are predominantly bedrock (0.465 ± 0.001 band depth). This suggests that the surface cover in GT either has a distinct grain size texture or enhanced hydration compared to the underlying bedrock. Future studies utilizing this spectral feature must account for similar differences in surface cover and the abundance of sand. The mean DAN-derived hydration within CRISM pixels classified as regolith (3.5 ± 0.1 wt.% WEH) is virtually the same as within pixels classified as bedrock (3.5 ± 0.1 wt.% WEH). The similar mean DAN WEH results in areas of regolith surface cover and exposed bedrock indicates that if the enhanced CRISM 3 μm band depth in regolith material is due to enhanced regolith hydration, this regolith material must not be thick enough to be significant in the ~50 cm deep DAN FOV.

CRISM also observed a prominent clay mineral absorption in GT (Fraeman et al., 2016; Milliken et al., 2010), and the presence of clay minerals was confirmed by MSL CheMin instrument X-ray diffraction results. GT contains the most abundant clay minerals yet measured in Gale crater (Thorpe et al., 2022). Clay minerals can contain abundant interlayer H_2O in the subsurface if they are not dehydrated. However, X-ray diffraction results have consistently shown that clays in Gale crater are dehydrated (Bristow et al., 2015, 2018; Rampe et al., 2017, 2020; Vaniman et al., 2014), with the possible exception of one of the two lowest stratigraphic drill samples, "Cumberland" (Bristow et al., 2015; Vaniman et al., 2014) and the "Duluth"

drill sample just north of (and stratigraphically below) VRR (Rampe et al., 2020). Rapin et al. (2018) suggested that drilled samples could dehydrate prior to analysis by the MSL Sample Analysis at Mars (SAM) instrument, and this could also apply to samples analyzed by CheMin. Therefore, although drill sample clay minerals are dehydrated at the time of CheMin analyses, they could have been hydrated before drilling.

Kerner et al. (2020) discuss best-fit model results assuming a homogeneous subsurface distribution of WEH and Σ_{abs} from DAN active measurements up to sol 2080. Here we use the same MCNP6 model assumptions as Kerner et al. (2020) for comparison to DAN active data. Comparing our results from GT to this larger data set shows that GT is among the most hydrated intervals along the MSL traverse (see Figure 10a in Kerner et al., 2020). This result correlates with the relatively large clay abundances measured by CheMin in GT compared to lower stratigraphic units. One previously published result from another clay-rich unit, the "Sutton Island" member of the Murray formation, also demonstrates the usefulness of active neutron spectroscopy for investigating clay-rich units. The CheMin sample "Sebina" from Sutton Island contained 19 ± 4 wt.% clay minerals (Bristow et al., 2018), but CRISM did not detect clay minerals in this area (Milliken et al., 2010). But DAN active analysis of a nearby location in Sutton Island found 4.2 ± 0.51 wt.% WEH (Gabriel et al., 2018), similar to the mean WEH measured in GT. While more work would need to be done in order to determine the specific subsurface distribution of water in GT, the colocation of clay-rich samples in a water-rich region suggests that clay minerals could be a significant subsurface water reservoir.

Data Availability Statement

All data used in this chapter are publicly available on the NASA PDS. Datasets include DAN active and passive neutron data (I. Mitrofanov, 2013), MAHLI image

data (Edgett, 2013), and CRISM spectral data (Seelos, 2016). Simulated neutron data sets used in this work were generated using MCNP6, an export-controlled neutron transport code. Derived DAN WEH results for individual measurement locations are found in Appendix Table C.1 and are available as open-access on Zenodo (Czarnecki et al., 2022).

Acknowledgements

The authors would like to thank Patrick Gasda, Kathryn Powell, Scott VanBommel, and Daniel Sullivan for helpful discussions relating to this work. We are grateful to the Mars Science Laboratory team for facilitating collaborations with groups at several institutions. This work was supported by the Mars Science Laboratory Participating Scientist program Grant NNN12AA01C. The authors acknowledge Research Computing at Arizona State University for providing HPC, storage, etc., resources that have contributed to the results reported here (https://cores.research.asu.edu/research-computing/about).

References

Arvidson, R. E., Bell, J. F., III, Catalano, J. G., Clark, B. C., Fox, V. K., Gellert, R., et al. (2015). Mars Reconnaissance Orbiter and Opportunity observations of the Burns formation: Crater hopping at Meridiani Planum. *Journal of Geophysical Research: Planets*, 120: 429–451. https://doi.org/10.1002/2014JE004686

Bristow, T. F., Bish, D. L., Vaniman, D. T., Morris, R. V., Blake, D. F., Grotzinger, J. P., et al. (2015). The origin and implications of clay minerals from Yellowknife Bay, Gale crater, Mars. *American Mineralogist*, 100(4): 824–836. https://doi.org/10.2138/am-2015-5077CCBYNCND

Bristow, T. F., Rampe, E. B., Achilles, C. N., Blake, D. F., Chipera, P. C., Craig, P., et al. (2018). Clay mineral diversity and abundance in sedimentary rocks of Gale crater, Mars. *Science Advances*, 4(6): eaar3330. https://doi.org/10.1126/sciadv.aar3330

Calef III, F. & Parker, T. (2016). MSL Gale merged orthophoto mosaic. *PDS Annex*, U.S. Geological Survey.

Czarnecki, S., Hardgrove, C., Gasda, P. J., Gabriel, T. S. J., Starr, M., Rice, M., et al. (2020). Identification and description of a silicic volcaniclastic layer in Gale crater, Mars, using active neutron interrogation. *Journal of Geophysical Research: Planets*, 125, e2019JE006180. https://doi.org/10.1029/2019JE006180

Czarnecki, S. Hardgrove, C., Arvidson, R. E., Hughes, M. N., Schmidt, M. E., Henley, T., et al. (2022). "Hydration of a clay-rich unit on Mars, comparison of orbital data to rover data" supplementary data (Version 2). *Zenodo*. https://doi.org/10.5281/ZENODO.7255705

Edgett, K. S. (2013). MSL Mars hand lens imager 4 RDR image v1.0. *NASA Planetary Data System*. https://doi.org/10.17189/1520292

Fedo, C. M., Bryk, A. B., Edgar, L. A., Bennett, K. A., Fox, V. K., Dietrich, W. E., et al. (2022). Geology and stratigraphic correlation of the Murray and Carolyn Shoemaker formations across the Glen Torridon region, Gale crater, Mars. *Journal of Geophysical Research: Planets*, 127(9): e2022JE007408. https://doi.org/10.1029/2022JE007408

Foreman-Mackey, D., Hogg, D. W., Lang, D., & Goodman, J. (2013). Emcee: The MCMC Hammer. *Publications of the Astronomical Society of the Pacific*, 125(925): 306–312. https://doi.org/10.1086/670067

Fraeman, A. A., Ehlmann, B. L., Arvidson, R. E., Edwards, C. S., Grotzinger, J. P., & Milliken, R. E. (2016). The stratigraphy and evolution of lower Mount Sharp from spectral, morphological, and thermophysical orbital data sets. *Journal of Geophysical Research: Planets*, 121: 1713–1736. https://doi.org/10.1002/2016JE005095

Fraeman, A. A., Edgar, L. A., Rampe, E. B., Thompson, L. M., Frydenvang, J., Fedo, C. M., et al. (2020). Evidence for a diagenetic origin of Vera Rubin ridge, Gale crater, Mars: Summary and synthesis of Curiosity's exploration campaign. *Journal of Geophysical Research: Planets*, 125: e2020JE006527. https://doi.org/10.1029/2020JE006527

Gabriel, T. S. J, Hardgrove, C., Czarnecki, S., Rampe, E. B., Rapin, W., Achilles, C. N., et al. (2018). Water abundance of dunes in Gale Crater, Mars from active neutron experiments & implications for amorphous phases. *Geophysical Research Letters*, 45, 12,766–12,775. https://doi.org/10.1029/2018GL079045

Grotzinger, J. P. & Milliken, R. E. (2012). The sedimentary rock record of Mars: Distribution, origins, and global stratigraphy. *Sedimentary Geology of Mars*, 102: 1–48. https://doi.org/10.2110/pec.12.102.0001

Grotzinger, J. P., Gupta, S., Malin, M. C., Rubin, D. M., Schieber, J., Siebach, K., et al. (2015). Deposition, exhumation, and paleoclimate of an ancient lake deposit, Gale crater, Mars. *Science*, 350(6257): aac7575. https://doi.org/10.1126/science.aac7575

Hapke, B. R. (2012). Theory of reflectance and emittance spectroscopy. Cambridge University Press.

Hardgrove, C., Moersch, J., & Drake, D. (2011). Effects of geochemical composition on neutron die-away measurements: Implications for Mars Science Laboratory's Dynamic Albedo of Neutrons experiment. *Nuclear Instruments and Methods in Physics Research A*, 659(1): 442–455. https://doi.org/10.1016/j.nima.2011.08.058

Hawthorne, F. (1988). Spectroscopic methods in mineralogy and geology. *Reviews in Mineralogy* (18). BookCrafters, Inc.

He, L., O'Sullivan, J. A., Politte, D. V., Powell, K. E., & Arvidson, R. E. (2019). Quantitative reconstruction and denoising method HyBER for hyperspectral image data and its application to CRISM. *IEEE Journal of Selected Topics in Applied Earth Observations and Remote Sensing*, 12(4): 1219–1230. https://doi.org/10.1109/JSTARS.2019.2900644

He, L., Arvidson, R. E., O'Sullivan, J. A., Morris, R. V., Condus, T., Hughes, M. N., et al. (2022). Surface kinetic temperatures and nontronite single scattering albedo spectra from Mars Reconnaissance Orbiter CRISM hyperspectral imaging data over Glen Torridon, Gale crater, Mars. *Journal of Geophysical Research: Planets*. 127(9): e2021JE007092. https://doi.org/10.1029/2021JE007092

Henley, T. L. J., Schmidt, M. E., Bray, S. L., & Zheng, J. J. (2021). An update on martian dust coverage and contribution to APXS elemental concentrations for rock targets in Gale crater. *Lunar and Planetary Science Conference VII*, 2241.

Hughes, M. (2022). Geomorphic map of Glen Torridon in Gale crater, Mars. Digital Research Materials (Data & Supplemental files), 95. Retrieved from https://openscholarship.wustl.edu/data/95

Jun, I., Mitrofanov, I., Litvak, M. L., Sanin, A. B., Kim, W., Behar, A., et al. (2013). Neutron background environment measured by the Mars Science Laboratory's Dynamic Albedo of Neutrons instrument during the first 100 sols. *Journal of Geophysical Research: Planets*, 118: 2400–2412. https://doi.org/10.1002/2013JE004510

Kerner, H. R., Hardgrove, C. J., Czarnecki, S., Gabriel, T. S. J., Mitrofanov, I. G., Litvak, M. L., et al. (2020). Analysis of active neutron measurements from the Mars Science Laboratory Dynamic Albedo of Neutrons instrument: Intrinsic variability, outliers, and implications for future investigations. *Journal of Geophysical Research: Planets*, 118. https://doi.org/10.1002/2013JE004510

Lewis, K. W., Peters, S., Gonter, K., Morrison, S., Schmerr, N., Vasavada, A. R., et al. (2019). A surface gravity traverse on Mars indicates low bedrock density at Gale crater. *Science*, 363(6426): 535–537. https://doi.org/10.1126/science.aat0738

Litvak, M. L., Mitrofanov, I. G., Barmakov, Yu. N., Behar, A., Bitulev, A., Bobrovnitsky, Yu., et al. (2008). The Dynamic Albedo of Neutrons (DAN) experiment for NASA's 2009 Mars Science Laboratory. *Astrobiology*, 8(3): 605–612. https://doi.org/10.1089/ast.2007.0157

McEwen, A. S., Eliason, E. M., Bergstrom, J. W., Bridges, N. T., Hansen, C. J., Delamere, W. A., et al. (2007). Mars Reconnaissance Orbiter's High Resolution Imaging Science Experiment (HiRISE). *Journal of Geophysical Research*, 112(5): 1–40. https://doi.org/10.1029/2005JE002605

Milliken, R. E., Grotzinger, J. P., & Thomson, B. J. (2010). Paleoclimate of Mars as captured by the stratigraphic record in Gale crater. *Geophysical Research Letters*, 37(L04201). https://doi.org/10.1029/2009GL041870

Mitrofanov, I. G., Litvak, M. L., Varenikov, A. B., Barmakov, Y. N., Behar, A., Bobrovnitsky, Y. I., et al. (2012). Dynamic Albedo of Neutrons (DAN) experiment onboard NASA's Mars Science Laboratory. *Space Science Reviews*, 170: 559–582. https://doi.org/10.1007/s11214-012-9924-y

Mitrofanov, I. (2013). MSL Dynamic Albedo of Neutrons level 3/4 RDR v1.0. https://doi.org/10.17189/1519502

Mitrofanov, I. G., Kozyrev, A. S., Lisov, D. I., Vostrukhin, A. A., Golovin, D. V., Litvak, M. L., et al. (2016). Active neutron sensing of the martian surface with the DAN experiment onboard the NASA "Curiosity" Mars rover: Two types of soil with different water content in the Gale crater. *Astronomy Letters*, 42(4): 251–259. https://doi.org/10.1134/S1063773716040058

Murchie, S., Arvidson, R., Bedini, P., Beisser, K., Bibring, J.-P., Bishop, J., et al. (2007). Compact Reconnaissance Imaging Spectrometer for Mars (CRISM) on Mars Reconnaissance Orbiter (MRO). *Journal of Geophysical Research*, 112(E05S03). https://doi.org/10.1029/2006JE002682

Murchie, S. L., Mustard, J. F., Ehlmann, B. L., Millikan, R. E., & Bishop, J. L. (2009). A synthesis of Martian aqueous mineralogy after 1 Mars year of observations from the Mars Reconnaissance Orbiter. *Journal of Geophysical Research*, 114(E00D06). https://doi.org/10.1029/2009JE003342

Rampe, E. B., Ming, D. W., Blake, D. F., Bristow, T. F., Chipera, S. J., Grotzinger, J. P., et al. (2017). Mineralogy of an ancient lacustrine mudstone succession from the Murray formation, Gale crater, Mars. *Earth and Planetary Science Letters*, 471: 172–185. https://doi.org/10.1016/j.epsl.2017.04.021

Rampe, E. B., Bristow, T. F., Morris, R. V., Morrison, S. M., Achilles, C. N., Ming, D. W., et al. (2020a). Mineralogy of Vera Rubin ridge from the Mars Science Laboratory CheMin instrument. *Journal of Geophysical Research: Planets*, 125: e2019JE006306. https://doi.org/10.1029/2019JE006306

Rapin, W., Chauviré, B., Gabriel, T. S. J., McAdam, A. C., Ehlmann, B. L., Hardgrove, C., et al. (2018). *In situ* analysis of opal in Gale crater, Mars. *Journal of Geophysical Research: Planets*, 123: 1955–1972. https://doi.org/10.1029/2017JE005483

Schmidt, M. E., Perrett, G. M., Bray, S. L., Bradley, N. J., Lee, R. E., Berger, J. A., et al. (2018). Dusty rocks in Gale crater: Assessing areal coverage and separating dust and rock contributions in APXS analyses. *Journal of Geophysical Research: Planets*, 123: 1649–1673. https://doi.org/10.1029/2018JE005553

Schneider, C. A., Rasband, W. S., & Eliceiri, K. W. (2012). NIH image to ImageJ: 25 years of image analysis. *Nature Methods*, 9(7): 671–675. https://doi.org/10.1038/nmeth.2089

Sears, V. F. (1992). Neutron scattering lengths and cross sections. *Neutron News*, 3(3): 26–37. https://doi.org/10.1080/10448639208218770

Seelos, F. (2016). MRO CRISM map-projected targeted reduced data record v1.0. *NASA Planetary Data System.* https://doi.org/10.17189/1519470

Summons, R. E., Amend, J. P., Bish, D., Buick, R., Cody, G. T., Des Marais, D. J., et al. (2011). Preservation of martian organic and environmental records: Final report of the Mars Biosignature Working Group. *Astrobiology*, 11(2): 157–181. https://doi.org/10.1089/ast.2010.0506

Sutter, B., McAdam, A. C., Mahaffy, P. R., Ming, D. W., Edgett, K. S., Rampe, E. B., et al. (2017). Evolved gas analyses of sedimentary rocks and eolian sediment in Gale Crater, Mars: Results of the Curiosity rover's sample analysis at Mars instrument from Yellowknife Bay to the Namib Dune. *Journal of Geophysical Research: Planets*, 122: 2574–2609. https://doi.org/10.1002/2016JE005225

Thorpe, M. T., Bristow, T. F., Rampe, E. B., Tosca, N. J., Grotzinger, J. P., Bennett, C. N., et al. (2022). Mars Science Laboratory CheMin data from the Glen Torridon region and the significance of lake-groundwater interactions in interpreting mineralogy and sedimentary history. *Journal of Geophysical Research: Planets*, 127(11): e2021JE007099. https://doi.org/10.1029/2021JE007099

Vaniman, D. T., Bish, D. L., Ming, D. W., Bristow, T. F., Morris, R. V., Blake, D. F., et al. (2014). Mineralogy of a mudstone at Yellowknife Bay, Gale crater, Mars. *Science*, 343(3169). https://doi.org/10.1126/science.1243480

Viviano-Beck, C. E., Seelos, F. P., Murchie, S. L., Kahn, E. G., Seelos, K. D., Taylor, H. W., et al. (2014). Revised CRISM spectral parameters and summary products based on the currently detected mineral diversity on Mars. *Journal of Geophysical Research: Planets*, 119: 1403–1431. https://doi.org/10.1002/2014JE004627

Werner, C. J., Armstrong, J., Brown, F. B., Bull, J. S., Casswell, L., Cox, L. J., et al. (2017). MCNP user's manual: Code version 6.2. LA-UR-17-29981.

CHAPTER 4

CONSTRAINING THE HYDRATION OF CLAY MINERALS AND ABUNDANCES OF AMORPHOUS PHASES IN GALE CRATER, MARS

Abstract

Both water and organic matter are required for the development and persistence of life. Phyllosilicates (clay minerals) are high surface area minerals that easily sorb both water and organic matter. The Mars Science Laboratory (MSL) has investigated several hundred meters of stratigraphy in Gale crater, including where clay minerals were detected from orbit. Results from the MSL Dynamic Albedo of Neutrons (DAN) and Chemistry and Mineralogy instruments have suggested that subsurface hydration is greatest in units with the most abundant clay minerals, suggesting that these clay minerals may be hydrated in the subsurface. Organics have also been found throughout Gale crater by the MSL Sample Analysis at Mars instrument (SAM). Smectites are the most common and abundant phyllosilicates in Gale crater samples, and also have the greatest organic sorption capacity because they can expand and sorb water and organics in interlayer sites. The most common organic sorption processes on Earth typically involve water or hydroxyl, so hydrated phyllosilicates are good candidates for organic preservation. Using newly derived DAN subsurface hydration values with previously published mineralogy and geochemistry, we derived modeled constraints on the abundances of hydrated amorphous phases, "excess" water, and "excess" cations. These "excess" phases are not accounted for by published crystalline phase abundances or by amorphous phases constrained here. We found a strong correlation between smectites and "excess" water abundances, indicating that smectites in Gale crater are hydrated. Similar correlations between smectites and "excess" cation abundances suggest that cation bridging could be a mechanism for sorption of organics measured by SAM. Our

results also show the persistence of amorphous sulfates, opal-A, and volcanic or impact glass, which indicate low syn- and post-depositional water-rock interactions. Increased abundances of sulfates and glass in stratigraphically higher samples may indicate lower water availability and environmental aridification during the time these units were being deposited in Gale crater.

4.1. Introduction

For decades, a primary goal of NASA's Mars Exploration Program (MEP) has been the search for present or past life because Mars is known to have had liquid water on the surface in the ancient past (NASEM, 2022). Most MEP surface missions have carried instruments to search for life or its building blocks (i.e., organics) and have investigated regions thought to have supported habitable environments in the past, such as the Mars Science Laboratory (MSL) landing site, Gale crater. Gale, a ~150 km impact basin with a ~5 km tall central mound (informally "Mt. Sharp"), was selected in part due to the Compact Reconnaissance Imaging Spectrometer at Mars (CRISM; Murchie et al., 2007) detection of a significant 2.3 μm spectral absorption corresponding to phyllosilicates (Milliken et al., 2010; Anderson & Bell, 2010). Phyllosilicates (commonly referred to as clay minerals) are sheet silicates common on Earth and Mars. Clay minerals are well known on Earth for their ability to preserve a wide range of organics at high abundances (Shen et al., 1999; Kennedy et al., 2002; Ehlmann et al., 2008; Broz, 2020), and have been studied for the same potential on Mars (Farmer & Des Marais, 1999; Ehlmann et al., 2008; Broz, 2020; Tu et al., 2021). Sorption of organics by clay minerals can be enhanced by the presence of hydroxyl or water (see Section 4.1.3), so clay minerals that remain hydrated today are good candidates for the preservation of organics since their formation. Because clay minerals dehydrate at lower relative humidity, it is important to assess their hydration state prior to sample extraction and handling. The MSL Dynamic

Albedo of Neutrons Instrument (DAN) measures the bulk, undisturbed subsurface hydration from the top ~50 cm including water or hydroxyl bound to clay minerals. Here we use DAN hydration with other results from MSL to constrain the hydration of clay minerals and the abundances of hydrated amorphous phases in Gale crater.

4.1.1. MSL in Gale Crater

CRISM detections of clay minerals in Gale crater were later confirmed by X-ray diffraction analyses of Mt. Sharp drilled samples by the MSL Chemistry and Mineralogy instrument (CheMin). Clay minerals indicate a wet formation environment, and the first CheMin detections (Vaniman et al., 2014) were used as evidence supporting an ancient habitable environment in the area known as "Yellowknife Bay" (Grotzinger et al., 2014) in the "Bradbury" group, the oldest deposits investigated by MSL (Figure 4.1). Clay minerals have since been identified throughout several hundred meters of fluvio-lacustrine mudstone/sandstone stratigraphy of the "Murray" and "Carolyn Shoemaker" formations of the "Mt. Sharp" group on the lower slopes of the central mound (e.g., Rampe et al., 2020b; Thorpe et al., 2022). MSL chemical and mineralogical data clearly show that the sedimentary deposits in Gale crater have experienced significant alteration (e.g., Bridges et al., 2015; Bedford et al., 2019). These alteration products are indicators of environmental change and can constrain the characteristics and duration of habitability in ancient Gale crater (e.g., Hurowitz et al., 2017).

Although Gale sediments are ~3.8 – 3.6 Ga (Thomson et al., 2011) and the radiation environment at Gale should have significantly reduced the abundance of organics at MSL drill depths (~4 - 5 cm) over geologic time (Pavlov et al., 2012; Hassler et al., 2014), organic matter has been identified in all MSL drill samples by the Sample Analysis at Mars instrument (SAM) (e.g., Sutter et al., 2017). Organic abundances measured by SAM may be lower bounds for the bulk rock (NASEM,

2022) because the rate of organic destruction is expected to be ~30% less at 20 cm depth compared to ~2 cm depth (Pavlov et al., 2012), and should be even lower at greater depths (e.g., the DAN depth of sensitivity). Indeed, amino acids could persist for 100 – 500 Ma at half-meter depths (Kminek & Bada, 2006), and the first few MSL samples had cosmic-ray exposure ages in this range (Cohen et al., 2019).

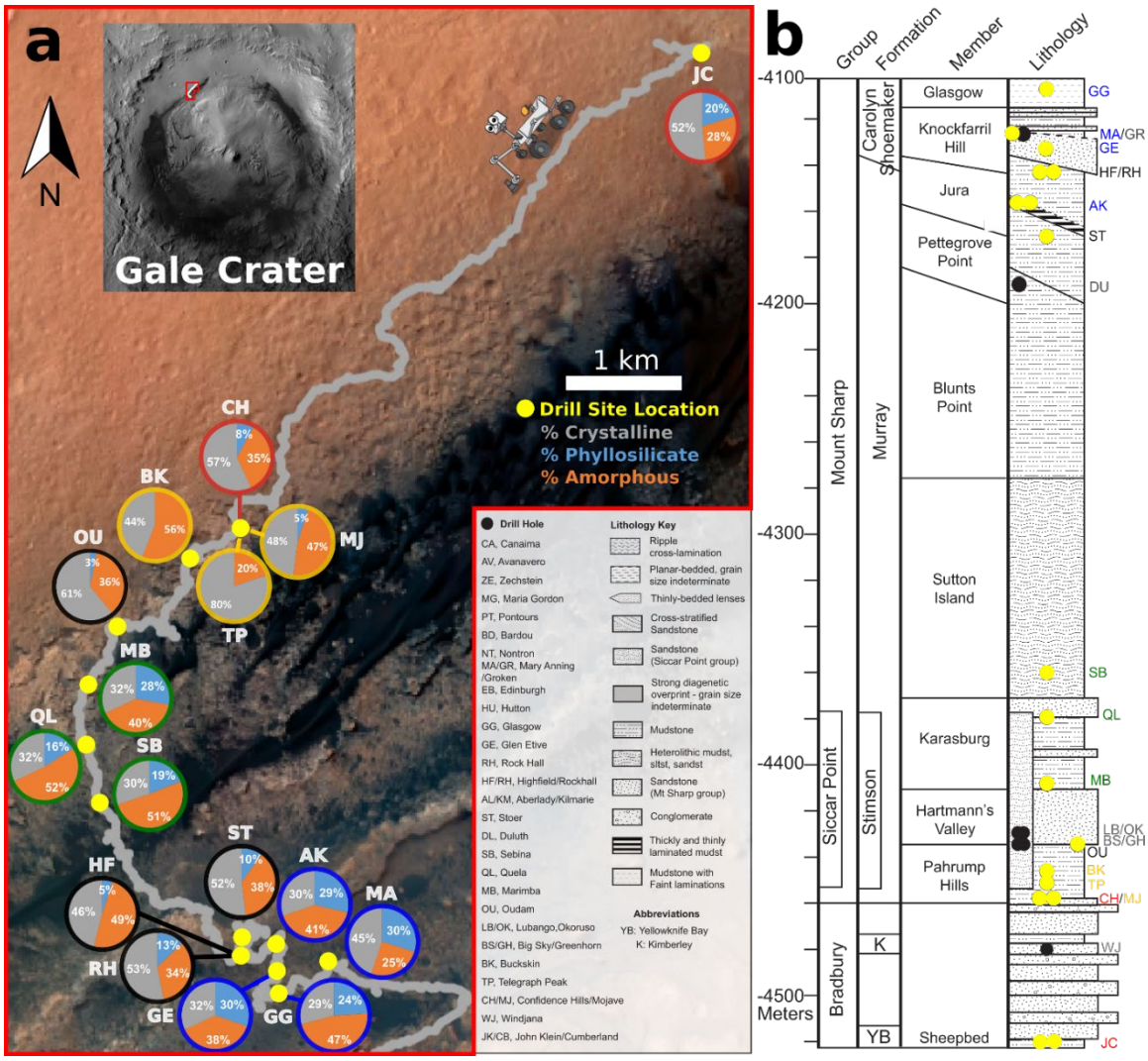

Figure 4.1. (a) Map with MSL drill sites and charts of crystalline, phyllosilicate, and amorphous fractions. Chart borders represent clay minerals: red = saponite, green = mixed-layer montmorillonite/saponite, blue = nontronite, black = ferripyrophyllite, yellow = absent/unknown. Data from Vaniman et al. (2014), Rampe et al. (2017), Bristow et al. (2018), Rampe et al. (2020a), Thorpe et al. (2022). Base map is an MSL localization product. (b) Stratigraphic column modified from MSL team product. Black dots represent additional drill sites not used in this study.

Table 4.1. CheMin samples used in this study with DAN-derived bulk water-equivalent hydrogen (WEH)

Sample		Sol	Xtal[a] [wt.%]	Clay [wt.%]	Amorph. [wt.%]	Clay Mineral[b]	DAN WEH [wt.%]
JC[c]	John Klein, Cumberland	182 279	51.5	20.0	28.5	Sap	2.56
CH[d]	Confidence Hills	759	57.0	8.0	35.0	Sap	2.28
MJ[d]	Mojave	882	48.0	5.0	47.0	N/A	3.04
TP[d]	Telegraph Peak	908	79.9	0.0	20.0	None	2.22
BK[d]	Buckskin	1060	44.0	0.0	56.0	None	1.76
OU[e]	Oudam	1361	61.1	3.0	36.0	Ferri-Prl	4.99
MB[e]	Marimba	1422	31.9	28.0	40.0	Mnt/Sap	3.53
QL[e]	Quela	1464	32.1	16.0	52.0	Mnt/Sap	2.80
SB[e]	Sebina	1495	30.1	19.0	51.0	Mnt/Sap	3.07
ST[f]	Stoer	2136	52.0	10.0	38.0	Ferri-Prl	3.23
HF[f]	Highfield	2224	46.0	5.0	49.0	Ferri-Prl	3.63
RH[f]	Rock Hall	2261	53.1	13.0	34.0	Ferri-Prl	3.75
AK[g]	Aberlady, Kilmarie	2369 2384	29.4	28.9	41.7	Nnt	4.04
GE[g]	Glen Etive 1, Glen Etive 2	2486 2527	32.5	30.0	37.5	Nnt	4.69
GG[g,j]	Glasgow	2754	29.1	24.0	47.0	Nnt	3.90
MA[h]	Mary Anning 1, Mary Anning 3	2838 2870	44.7	29.6	25.7	Nnt	4.22

[a]Opal-CT is included in the crystalline fraction, not in the amorphous fraction.
[b]Sap = saponite, Ferri-Prl = Ferripyrophyllite, Mnt/Sap = mixed-layer montmorillonite/saponite, Nnt = nontronite.
[c]Mineralogy from Vaniman et al. (2014), [d]Mineralogy from Rampe et al. (2017), [e]Mineralogy from Bristow et al. (2018), [f]Mineralogy from Rampe et al. (2020a), [g]Mineralogy from Thorpe et al. (2022)
[h]The DAN active time bin range used for GG is 249 – 1630 μs (see Section 4.2.2).

4.1.2. Clay Minerals in Gale Crater

Clay minerals were first detected in Gale crater by CRISM, but CRISM only identified a strong, continuous phyllosilicate signature on Mt. Sharp in the "Glen Torridon" region, ~300 m above the crater floor deposits. However, the MSL CheMin instrument has detected clay minerals in almost all Bradbury and Mt. Sharp group samples shown in Figure 4.1 and listed in Table 4.1. Clay mineral abundances in these samples range from absent in two samples up to ~30 wt.%, with the greatest abundances in Glen Torridon. Most CheMin and SAM data from these samples are

consistent with the smectite minerals saponite, montmorillonite, or nontronite (Vaniman et al., 2014; Rampe et al., 2017; Bristow et al., 2018; Thorpe et al., 2022), and they likely formed *in situ* (Tu et al., 2021).

During SAM evolved gas analyses (EGA), water evolves from all hydrated material in the sample (including adsorbed water) and different phases evolve water at different temperatures, although there is some overlap. For instance, water evolves from clay minerals and Ca-sulfates at similar temperatures, but Fe- and Mg-sulfates evolve water at higher temperatures (Sutter et al., 2017). Although CheMin has consistently measured clay minerals to be collapsed (dehydrated) in almost all Gale crater samples (e.g., Rampe et al., 2020b), water evolved from SAM EGA could include smectite interlayer water in a few samples (Sutter et al., 2017), and laboratory experiments have demonstrated that smectites should retain some interlayer water under equatorial Mars surface conditions (Bish et al., 2003). But drill powdering increases sample surface area, and the relative humidity inside the CheMin instrument is low (Tu et al., 2021), both of which could contribute to water and/or hydroxyl loss. Similar dehydration has been suggested for opal-A prior to SAM analyses (Rapin et al., 2018). Thus, it is possible that clays may be more hydrated *in situ* than during SAM and CheMin measurements. DAN measures hydrogen abundances in the undisturbed, near-subsurface (depth < ~50 cm). If clay minerals are hydrated in the subsurface, DAN-derived bulk subsurface hydration would include this contribution.

4.1.3. Organic Preservation in Clay Minerals

Clay minerals preserve organics in part because of their large external and internal (for expandable clay minerals like smectites) surface areas where organics can sorb to them (Kennedy et al., 2002; Ehlmann et al., 2008; Summons et al., 2011; Broz, 2020), and because clay minerals remain stable for long periods

(Summons et al., 2011). Certain organics bound to clay minerals are more resistant to pH and temperature changes (Naidja et al., 1997), and certain biomolecules bound to clay minerals can remain bioactive through repeated wet-dry and freeze-thaw cycles (Stotzky et al., 2000). Organics bound to clay minerals are also less likely to be biodegraded (Fiorito et al., 2008), further enhancing organic preservation potential. The large surface areas of clay minerals also make them good candidates for mineral surfaces thought to be involved in the genesis of life on Earth (e.g., Bish et al., 2003; Hazen, 2005, and references therein).

Sorption is the physical or chemical process of binding substances together, and includes absorption and adsorption processes (Pourret et al., 2022). Of the six known mechanisms for organic sorption to mineral surfaces, three (ligand exchange, ion exchange, and cation bridging) typically involve hydroxyl (Keil & Mayer, 2014). Ligand exchange creates very strong bonds (Shen et al., 1999; Lutzow et al., 2006; Keil & Mayer, 2014) and both ligand exchange and cation bridging can preserve organics for long durations (Naidja et al., 1997; Keil & Mayer, 2014). Organics in interlayer sites of clay minerals typically sorb by cation exchange (Kennedy et al., 2002; Ovesen et al., 2001; Keil & Mayer, 2014) or hydrogen bonds with hydroxyl (Lutzow et al., 2006) or water (Sheng et al., 2001). Recent work has shown that the clay mineral-rich Glen Torridon region in Gale crater is correlated with a small increase in mean CRISM 3 μm integrated band depth corresponding to surface hydration, and a large ~30% relative increase in DAN-derived bulk hydration, compared to underlying units (Czarnecki et al., 2023a).

Smectites are the most common clay mineral group in Gale crater (Vaniman et al., 2014; Rampe et al., 2017; Bristow et al., 2018; Thorpe et al., 2022). Smectites are principal binding surfaces for organic matter (Wattel-Koekkoek et al., 2003) and are associated with many of the most organic-rich units on Earth

(Kennedy et al., 2002). Smectites also preserve organic matter even more efficiently and for longer than other clay minerals (Kennedy et al., 2002; Wattel-Koekkoek et al., 2003; Dontsova & Bigham, 2005; Broz, 2020). Nontronite, a dioctahedral smectite identified in the "Glen Torridon" (GT) region of Gale crater (Table 4.1; Thorpe et al., 2022), may have greater organic preservation capacity and longevity than other smectites (Dontsova & Bigham, 2005; dos Santos et al., 2016).

4.1.4. X-ray Amorphous Phases in Gale Crater

Some X-ray amorphous phases are also known to efficiently preserve organics due to high surface area and reactivity, including opal (Nonella & Seeger, 2008; Squyres et al., 2008), allophane (Broz, 2020), and amorphous iron (oxy)hydroxides (e.g., nanophase iron oxides/ferrihydrite; Broz, 2020). Opal in particular has a high organic preservation potential due to its large external surface area, and some modes of organic sorption to opal require water molecules (Costa et al., 2008; Nonella & Seeger, 2008). Opal precipitated from solution is also a mechanism for trapping and preserving microbes (Squyres et al., 2008).

X-ray amorphous phases also preserve clues to syn-depositional and post-depositional environmental conditions and habitability. Many minerals and amorphous phases form under restricted pH, redox conditions, or water-to-rock ratios. Many of these conditions can be constrained by the MSL instrument suite, including CheMin, SAM, the Chemistry and Camera instrument (ChemCam), the Alpha Particle X-ray Spectrometer (APXS), and DAN. The ubiquitous X-ray amorphous component of Gale crater samples, which is 20 – 56 wt.% of all Bradbury and Mt. Sharp group samples (Table 4.1) in the CheMin literature, includes crystalline phases below ~1 wt.% of the bulk sample. But the amorphous phases comprising most of this material remain largely unconstrained.

Several studies have suggested a range of potential amorphous phases for Gale crater or elsewhere on Mars (Dehouck et al., 2014; McLennan et al., 2019; Achilles et al., 2020, Rampe et al., 2020b; Smith et al., 2021), including volcanic or impact glass, amorphous sulfates, and alteration phases such as opal-A, allophane, hisingerite, and ferrihydrite. Each of these proposed phases is supported by other CheMin and SAM studies (e.g., Bish et al., 2013; Morris et al., 2016; Treiman et al., 2016; Achilles et al., 2017; Rampe et al., 2017; Sutter et al., 2017; McAdam et al., 2020; Rampe et al., 2020a; McAdam et al., 2022; Smith et al., 2022; Thorpe et al., 2022). Additional studies of martian materials or martian analogues have also supported the presence of volcanic or impact glasses (Varela et al., 2000; Milliken et al., 2008; Lapotre et al., 2017; Czarnecki et al., 2020), amorphous sulfates (Vaniman et al., 2004; Wang et al., 2009; Hurowitz et al., 2017), opal-A (Glotch et al., 2006; Milliken et al., 2008; Rice et al., 2010; Ruff et al., 2011; Rapin et al., 2018), and hisingerite (Tutolo & Tosca, 2023). The presence or persistence of these phases has implications for the duration of water-rock interactions in syn- and post-depositional environments.

4.1.5. *In Situ* Hydration as an Additional Constraint

MSL studies referenced in Section 4.1.4 have primarily used chemistry and mineralogy to suggest the presence, or provide rough abundances of, amorphous phases. Another previous study, Gabriel et al. (2018), used APXS chemistry, CheMin mineralogy, and the additional parameter of DAN hydration to further constrain amorphous phase abundances for a modern aeolian sand dune in Gale. That study demonstrated the much stricter constraints provided by the addition of the hydration parameter. The present study follows on and modifies the methods of Gabriel et al. (2018) to place constraints on clay mineral hydration and amorphous phase abundances for most MSL drill samples in Gale crater. Although DAN is sensitive to a

much larger subsurface volume (cubic meters) than the samples analyzed by CheMin and APXS (cubic centimeters) , neutron spectroscopy is the only measurement technique available to assess the bulk hydration of the undisturbed subsurface. We employ careful measurement selection criteria, described in Section 4.2.4, to ensure that only the most representative DAN active measurements are used in conjunction with CheMin and APXS drill sample results.

We make a set of compositional assumptions, described in Section 4.2, in large part based on previous work referenced above. Hydration values, reported as water-equivalent hydrogen (WEH, Table 4.1), are derived from new analysis of DAN active data, which is sensitive to elemental hydrogen in both water and hydroxyl. We randomly generate amorphous phase compositions, checking each for consistency with amorphous chemistry and amorphous hydration. Good-fit amorphous phase compositions determine constraints on the abundances of the modeled phases and of clay hydration in Gale crater.

4.2. Instruments and Methods

4.2.1. Dynamic Albedo of Neutrons (DAN)

DAN is a neutron spectrometer with two He-3 neutron detectors and a pulsed neutron generator (PNG; Litvak et al., 2008; Mitrofanov et al., 2012). One detector is coated in Cd to absorb thermal neutrons (<~0.3 eV), and only counts epithermal neutrons (0.3 eV < n < 100 keV). The count rate from this detector can be subtracted from the count rate from the uncoated detector, which detects thermal and epithermal neutrons, to obtain a thermal neutron count rate. In active mode, the PNG produces 14.1 MeV neutrons at 10 Hz, emitted isotropically. Some of these fast neutrons enter the subsurface, are thermalized (energy reduced via moderation) in scattering reactions with subsurface nuclei, and return to be counted by the DAN detectors. Neutron time of flight histograms combine counts generated by many PNG

pulses during a single measurement (12000 in a typical 20-minute active measurement). This histogram is known as a "die-away" curve because after the PNG pulse, neutron counts rise to a peak, then die-away back to background levels before the next pulse (e.g., Figure 4.2). The present study only uses data from DAN active mode, though DAN also operates in passive mode where the neutrons counted are generated by galactic cosmic ray bombardment of the martian subsurface.

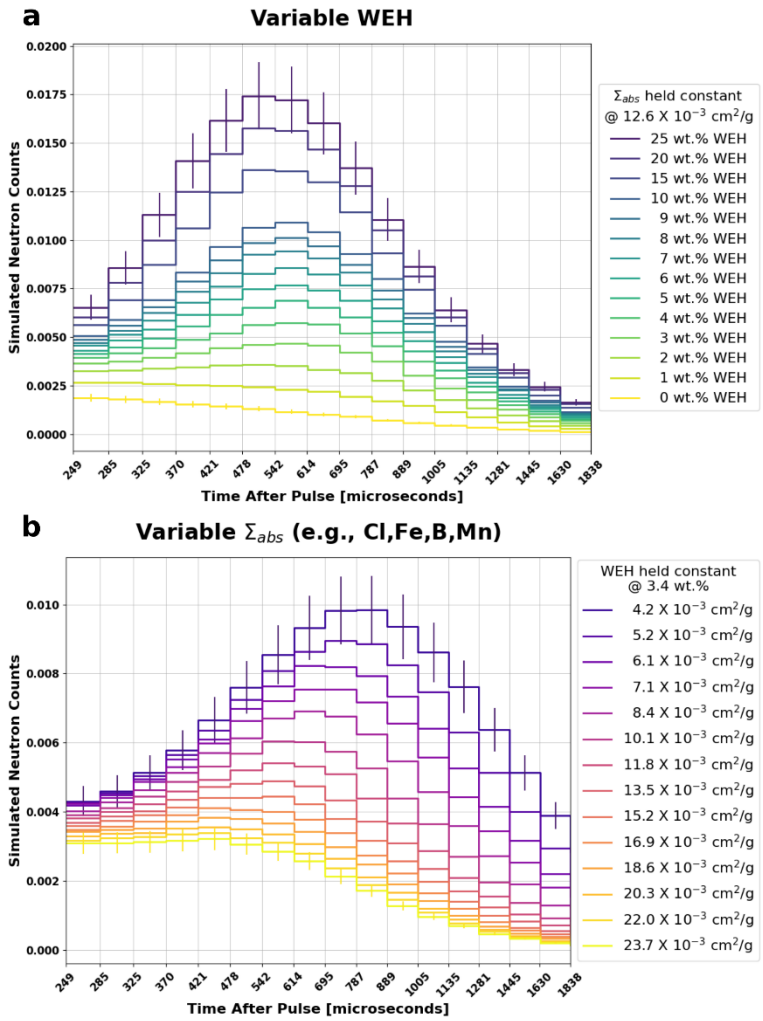

Figure 4.2. Monte Carlo N-Particle 6 (MCNP6) simulated data showing neutron die-away curves for (a) variable WEH (constant Σ_{abs}) and (b) variable Σ_{abs} (constant WEH). WEH increases neutron counts, while macroscopic thermal neutron absorption cross section (Σ_{abs}) reduces neutron counts, but the variations in curve shape shown here (i.e., slope and arrival time) allow us to constrain WEH and Σ_{abs} simultaneously.

The neutron energy and time of flight recorded by DAN are dependent on nuclear interactions in the subsurface. DAN is sensitive to the depth and abundance of efficient neutron scatterers, primarily hydrogen, and efficient thermal neutron absorbers, such as iron, chlorine, and boron (e.g., Sears et al., 1992, Hardgrove et

al., 2011; Mitrofanov et al., 2012; Gabriel et al., 2018). As shown in Figure 4.2, hydrogen (reported as WEH) increases neutron counts (by thermalizing neutrons) while iron, chlorine, boron, etc. reduce neutron counts (by increasing macroscopic thermal neutron absorption cross section, Σ_{abs}, and absorbing thermal neutrons). Die-away curve slope and peak arrival time are dependent on these two parameters, and variations in curve shape with each parameter allow us to vary these parameters independently in simulations to find best-fit parameters.

4.2.2. DAN Data Analysis

To determine bulk WEH and Σ_{abs}, we compare DAN active data to simulated data created using the Monte-Carlo N-Particle transport code (MCNP6) developed at Los Alamos National Lab (Werner et al., 2017). MCNP6 simulates neutron transport histories in a 3D environment which includes a detailed rover model (modified from Jun et al., 2013), martian atmosphere, and variable subsurface composition. We use a simulation grid which varies subsurface WEH from 0.1 wt.% to 25 wt.% and Σ_{abs} from 4.2 x 10^{-3} cm^2/g (equivalent to ~0 Fe and Cl) to 23.7 x 10^{-3} cm^2/g (equivalent to, e.g., ~14 wt.% Fe and ~3 wt.% Cl, or 0 wt.% Fe and ~3.65 wt.% Cl) in a homogeneous subsurface with 1.8 g/cm^3 density (Mitrofanov et al., 2016; Gabriel et al., 2018; Lewis et al., 2019).

WEH and Σ_{abs} results are determined by comparing DAN active data from time bins around the thermal neutron peak (249 – 1838 μs after pulse) to simulated data from the MCNP6 grid using a Markov-Chain Monte-Carlo (MCMC) technique (Foreman-Mackey et al., 2013). MCMC explores the simulation space, interpolating between simulation grid points and calculating likelihood functions of DAN to simulation data. WEH and Σ_{abs} for each interpolation are plotted on histograms (e.g., Figure 4.3). The best-fit mean WEH and Σ_{abs} values and uncertainties are determined from Gaussians fit to these distributions. We also model an "f" parameter

representing underestimated uncertainty. High "f" values indicate either poor model assumptions or noisy data. We ensured that all DAN and simulation data had signal-to-noise ratios (SNR) of ≥ 5 for neutron counts in all time bins analyzed. To achieve this SNR, most DAN active data used in this study is coadded from multiple 20-minute DAN active measurements (see Section 4.2.4). For the "Glasgow" (GG) sample site, the SNR for coadded neutron counts in the 1630 – 1838 μs time bin was insufficient to meet the SNR threshold of 5, so counts from 249 – 1630 μs were used in the MCMC analysis at this site. See Gabriel et al. (2018) for additional detail regarding MCMC analysis of DAN active data.

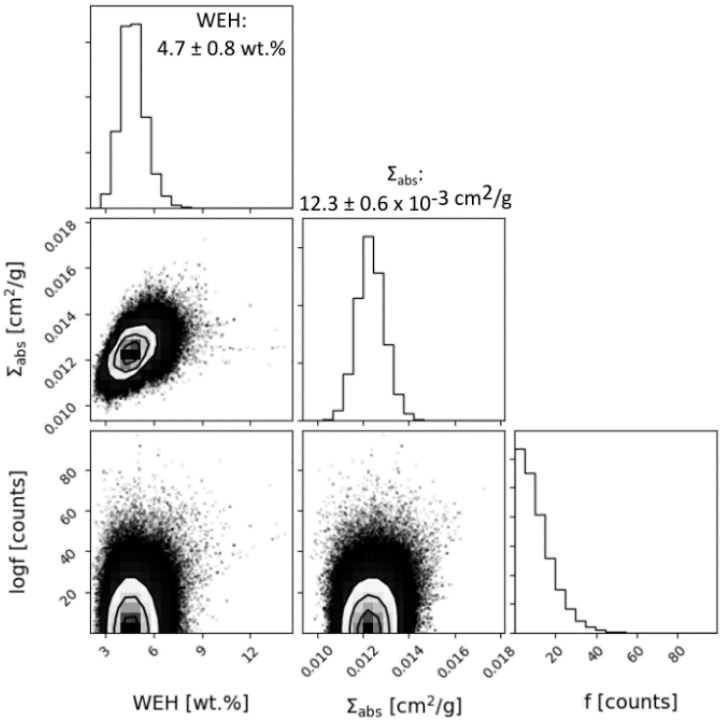

Figure 4.3. Corner plot of MCMC results for the GE sample site (Figure 4.1, Table 4.1). "f" is a free parameter representing underestimated uncertainty. A large "f" value would indicate poor model assumptions or noisy DAN and/or MCNP6 data. Corner plots for all DAN results derived in this work are available in Appendix Figures E.3 – E.23 and are archived online (Czarnecki et al., 2023b).

4.2.3. Other Instruments

Mineralogical abundances used in this work are from previous CheMin analyses of drill samples (Vaniman et al., 2014; Rampe et al., 2017; Bristow et al., 2018; Rampe et al., 2020a; Thorpe et al., 2022). CheMin is an X-ray diffraction (XRD) and X-ray fluorescence (XRF) instrument (Blake et al., 2012). For XRD

analyses, drilled sample powders are delivered to a CheMin sample cell inside the Curiosity rover. A Co source is used to transmit X-rays through powdered samples to a CCD detector which records XRD images that are then converted to diffraction patterns. Rietveld refinement is used to determine abundances and unit-cell parameters of specific minerals >~1 wt.%. X-ray amorphous and poorly crystalline minerals, including phyllosilicates, are quantified using the FULLPAT method which finds a best-fit composition of these materials compared to a library including many X-ray amorphous materials and clay minerals. New laboratory analysis has shown that the previously published uncertainties for X-ray amorphous materials measured by CheMin (50% relative uncertainty) are overestimated (Appendix Text E.1). For amorphous abundances of samples in this study (20 – 60 wt.% amorphous material), FULLPAT relative errors are <5% (Appendix Table E.1 and Figures E.1, E.2), so we use 5% relative uncertainty for amorphous fractions in this study. An overview of Gale crater CheMin mineralogy results and techniques is provided by Rampe et al. (2020b), and Morrison et al. (2018) provides an overview of CheMin crystal chemistry calculations from unit-cell parameters.

Amorphous chemical abundances used in this work are based on APXS amorphous chemistry or bulk chemistry with crystal chemistry provided in the literature (Vaniman et al., 2014; Rampe et al., 2017; Bristow et al., 2018; Rampe et al., 2020a; Thorpe et al., 2022). Amorphous chemistry is calculated by subtracting the weighted crystal chemical abundances based on unit-cell parameters from the bulk chemistry provided by APXS measurements of the drill tailings. APXS measures the abundances of all major rock-forming elements and several minor or trace elements (e.g., Campbell et al., 2014). Although APXS is only sensitive to within the top several microns of the target material for most major elements (Schmidt et al.,

2018), measurements of drill tailings are assumed to be homogenized from the same sample volume as the material delivered to CheMin.

4.2.4. Data and Site Selection

In order to constrain the hydration of clay minerals in Gale crater samples, we pair DAN active measurements with drilled samples. Coordinated measurements are carefully selected, but in all cases we assume that APXS chemistry and CheMin mineralogy results from the drilled volume (cubic centimeters) are representative of the larger DAN sensing volume (cubic meters). The Bradbury and Mt. Sharp groups together represent a >700 m thick fluviolacustrine stratigraphic section. Within this section, MSL has acquired 32 drill samples (and another five from an unconformable aeolian sandstone). In this study, we analyzed 20 samples (Table 4.1) from the lowermost "Sheepbed" member of the Yellowknife Bay formation to the Glasgow member of the Carolyn Shoemaker formation (Figure 4.1). We omitted four samples from this interval. The "Windjana" sample from the "Kimberley" formation was not investigated by DAN. The "Duluth" sample from the Murray formation was taken from a block of bedrock surrounded by aeolian sand that appears to be several cm deep and is very dry (Gabriel et al., 2018), so the ~2 m wide DAN field of view (FOV) is likely not representative of the drilled sample. The "Hutton" drill sample was taken on a relatively steep slope and because the DAN instrument is located ~4 m from drill operations (DAN is at the rear of the rover while the drill mechanism is attached to the arm at the front of the rover), the center of the DAN FOV at this site is tens of cm below the drill site. The "Groken" drill site is within a few meters of the "Mary Anning" and "Mary Anning 3" (MA) drill sites but was selected specifically to investigate unusual diagenetic features. Groken has significant mineralogical and geochemical differences from MA and is thought to be a thin highly altered interval which is not representative of the bulk rock (Gasda et al., 2022; Thorpe et al., 2022;

Treiman et al., in prep). The 20 samples analyzed here appear as 16 sample sites in Table 4.1 because four sample sites contain paired samples as listed in the table. The samples in each of these pairs are within a few meters (the width of the DAN FOV) of each other. For these sites, the mean mineralogy and chemistry were used in our analysis.

For every sample site, the distance from the DAN active measurement(s) used is ≤ ~4 m. In some cases, DAN was centered over the drill hole, and in others DAN data were acquired ~4 m or less from the drill hole. In some of the latter cases, multiple DAN active measurements within ~4 m of the drill hole were coadded together. In all cases, DAN active measurements are only coadded if they are within several meters laterally (and within 4 m of the drill hole), within several cm vertically, and if there is no visible difference in surface characteristics. In one case, the "Buckskin" (BK) sample, we used a previously published DAN WEH value (Czarnecki et al., 2020). See Appendix Table E.2 for a list of DAN measurements used in our analyses.

4.2.5. Amorphous Component Analysis

We employ a new amorphous component analysis code to constrain abundances of several amorphous phases in Gale crater samples. Our modeling is based on the method in Gabriel et al. (2018). We calculate the WEH abundance contained in the crystalline fraction of the sample assuming stoichiometric water and hydroxyl abundances of hydrated crystalline phases and clay mineral structural hydroxyl using the following equation:

$$WEH_{xtal} = \sum WEH_{min_i} * [min_i] \quad (4.1)$$

where WEH_{xtal} ≡ WEH in the crystalline fraction, WEH_{mini} ≡ stoichiometric WEH of the *i*th mineral, and $[min_i]$ ≡ the bulk fractional abundance of the *i*th mineral. The water

or hydroxyl abundances of a few minor phases, which we include in the crystalline fraction for Equation 4.1, are not always well-constrained by CheMin. See Appendix Text E.2 for specific details related to WEH in the crystalline fraction.

With DAN-derived bulk WEH (see Section 4.2.2 and Table 4.1) and the crystalline fraction WEH (Equation 4.1), it is straightforward to calculate the WEH of the amorphous fraction:

$$WEH_{aci} = WEH_{bulk} - WEH_{xtal} \quad (4.2)$$

where WEH_{aci} ≡ WEH of the amorphous fraction plus "excess" WEH, representing sorbed water or hydroxyl not included in other amorphous phases (see below).

We use a Monte-Carlo technique in which we randomly generate candidate amorphous phase compositions from the list of candidate amorphous phases in Table 4.2. We calculate chemical and WEH abundances for each randomly generated candidate amorphous phase composition, and determine if it is a good fit until we have generated 10k good-fits for each sample listed in Table 4.1. A good-fit composition is one which agrees (within propagated uncertainties) with the known sample chemistry and hydration. That is, it meets the criteria of either Equation 4.3, or Equation 4.4, or both, for every oxide listed in Table 4.2, including WEH:

$$\sum[\boldsymbol{Ox_i}] + \boldsymbol{\varphi} * \sqrt{\sum(\boldsymbol{\delta}[\boldsymbol{Ox_i}])^2} \geq [\boldsymbol{Ox_s}] - \boldsymbol{\varphi} * \boldsymbol{\delta}[\boldsymbol{Ox_s}] \quad (4.3)$$

$$\sum[Ox_i] - \varphi * \sqrt{\sum(\delta[Ox_i])^2} \leq [Ox_s] + \varphi * \delta[Ox_s] \quad (4.4)$$

where $[Ox_i]$ ≡ the oxide abundance of the ith candidate phase, $\delta[Ox_i]$ ≡ the oxide abundance uncertainty of the ith candidate phase, $[Ox_s]$ ≡ the oxide abundance of the sample amorphous fraction, $\delta[Ox_s]$ ≡ the oxide abundance uncertainty of the sample amorphous fraction, and φ ≡ an additional uncertainty factor.

Table 4.2. Chemistry and hydration of modeled candidate amorphous phases. Modeled relative uncertainties are discussed in Section 4.2.5.

Modeled Phase	SiO_2	Al_2O_3	FeO_T	MgO	CaO	Na_2O	K_2O	SO_3	WEH
Rhyolitic Glass[a,h]	70.4	16.9	3.3	1.2	1.3	3.6	3.2	0	0.1
Basaltic Glass[b,h]	46.7	11.1	20.3	11.1	8.2	2.5	0.1	0	0.1
Iron Sulfate[c]	0	0	31.4	0	0	0	0	47.3	21.3
Magnesium Sulfate[d]	0	0	0	26.1	0	0	0	51.9	22.0
Opal-A[e]	93.7	0	0	0	0	0	0	0	6.3
Allophane[f,h]	46.1	47.4	0	0	0	0	0	0	6.5
Hisingerite[g,h]	46.6	0	40.3	11.4	1.4	0	0	0	2.6
Ferrihydrite[f,h]	0	0	96.0	0	0	0	0	0	4.0
"Excess" MgO	0	0	0	100.0	0	0	0	0	0
"Excess" CaO	0	0	0	0	100.0	0	0	0	0
"Excess" Na_2O	0	0	0	0	0	100.0	0	0	0
"Excess" K_2O	0	0	0	0	0	0	100.0	0	0
"Excess" WEH	0	0	0	0	0	0	0	0	100.0

[a]Chemistry from Varela et al. (2000)
[b]Chemistry from Filiberto et al. (2008)
[c]Chemistry and hydration from Sklute et al. (2015)
[d]WEH from Vaniman et al. (2004)
[e]WEH from Rapin et al. (2018)
[f]Chemistry from Rampe et al. (2016)
[g]Chemistry from Evans et al. (2017)
[h]WEH from Gabriel et al. (2018)

For most samples, $\varphi = 1$. But for GE ($\varphi = 1.1$), QL ($\varphi = 1.8$), and SB ($\varphi = 1.3$), an additional uncertainty factor was required to obtain good-fit compositions. In practice, this factor inflates the uncertainty in the oxide compositions of the candidate amorphous phases and of the sample. But in reality, $\varphi > 1$ means a broader range of oxide abundances was required for candidate amorphous phases of more variable compositions, such as glasses. Additional details regarding the composition of candidate amorphous phases are described in Appendix Text E.2.

In addition to these amorphous phases, we include "excess" abundances of four cations. These "excess" phases are included because these cations can have variable abundances in crystalline phases and can also be important components in organic sorption to clay minerals. We also include "excess" WEH, which accounts for any sorbed hydration (water or hydroxyl) not already included in other amorphous phases. Because clay minerals are abundant in Gale crater and smectite clays can expand to include a large abundance of WEH, this "excess" WEH component could be present as clay mineral hydration. Several samples contain very little or no abundance of a particular cation. In these cases, we proceed with the analysis described above, but with the absent cation(s) removed from the sample and candidate amorphous phase compositions. See Appendix Text E.2 for more details.

4.3. Results

Table 4.1 includes DAN bulk WEH results for each sample site listed. Corner plots for all WEH results are in Appendix Figures E.3 - E.23 and are archived (Czarnecki et al., 2023b). These results were input quantities in the amorphous component analysis of amorphous phases in Table 4.2. Our results include Gaussian and non-Gaussian distributions. We use quartiles to discuss distribution statistics in an unbiased manner, rather than using other methods (e.g., Gaussian statistics) which assume specific distribution characteristics that are not valid for all results.

4.3.1. "Excess" WEH

Figure 4.4 has modeled "excess" WEH distributions as percentages of the bulk sample for 10k good-fit compositions for each sample site. Each distribution shows the median value (Q_2) and the first (Q_1) and third (Q_3) quartiles. Figure 4.5a shows boxplots of these data for easier comparison. Figure 4.5b are boxplots of modeled "excess" WEH as a percentage of bulk WEH, which shows that the modeled "excess" WEH abundances are a significant percentage of the bulk WEH in many samples.

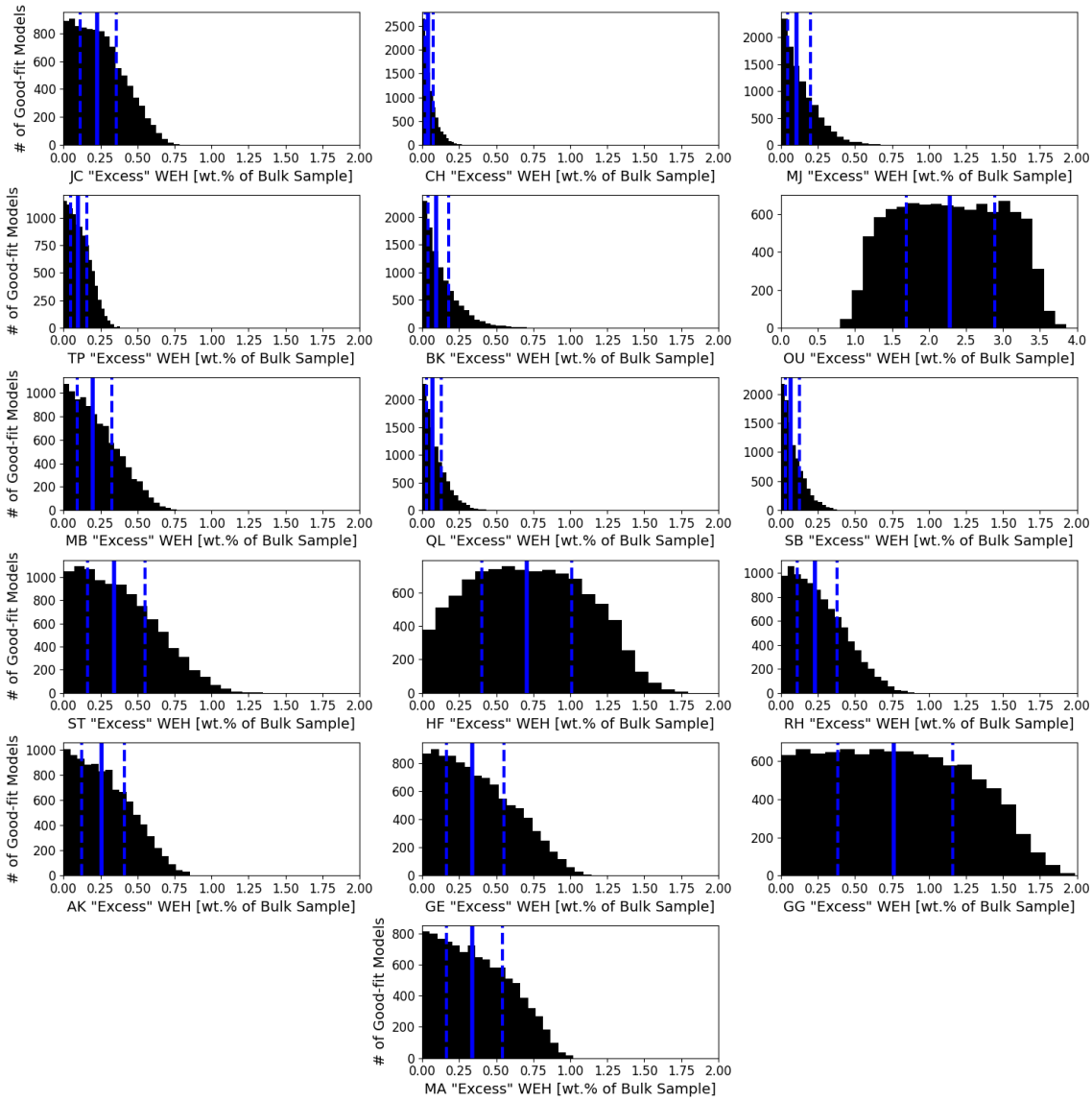

Figure 4.4. Distributions of modeled "excess" WEH as a percentage of the bulk sample. Blue lines denote Q_1, Q_2 (median), and Q_3. Note the larger horizontal axis scale for OU. Vera Rubin ridge and Glen Torridon samples (rows 4 - 6) have greater "excess" WEH than other samples. Data also shown in Figure 4.5a.

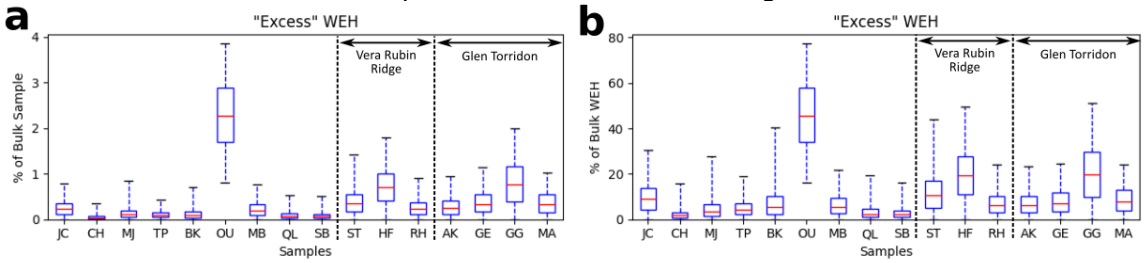

Figure 4.5. Boxplots of modeled "excess" WEH as a percentage of (a) bulk sample, and (b) bulk WEH. Red lines are Q_2 (median), boxes extend from Q_1 to Q_3, and whiskers cover the full distribution. Vera Rubin ridge and Glen Torridon samples have greater "excess" WEH than other samples. Data in (a) also shown in Figure 4.4.

Table 4.3 lists Q_1, Q_2, and Q_3 values for each phase in each sample. There are good-fit modeled compositions for all samples where a significant percentage (> 10 wt.%) of bulk WEH is "excess", but more recent samples from Vera Rubin ridge (VRR) and GT generally have more modeled "excess" WEH than earlier samples, with the notable exception of OU (note the larger WEH scale for OU in Figure 4.4).

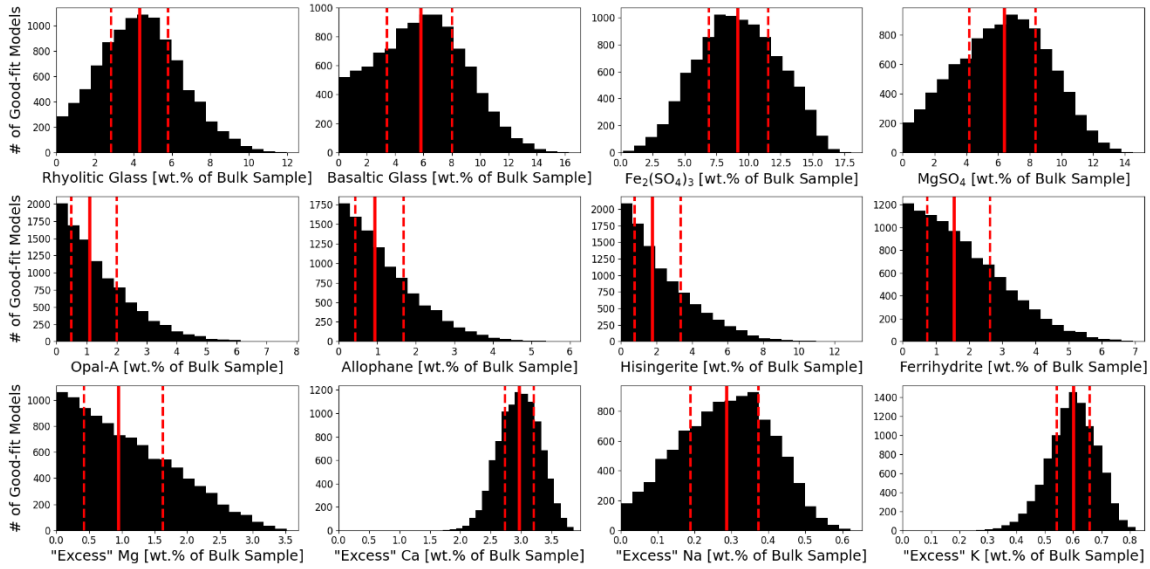

Figure 4.6. Distributions of all candidate phases except "excess" WEH (Figure 4.4) as percentages of the bulk sample for 10k good-fit modeled compositions for the GE sample. Solid red lines denote median values (Q_2) and dashed red lines denote Q_1 and Q_3. Horizontal and vertical axes vary for each distribution. Distributions for all samples are available in Appendix Figures E.24 – E.39 and are archived online (Czarnecki et al., 2023b).

4.3.2. Amorphous Phases and "Excess" Cations

Figure 4.6 shows distributions of all modeled amorphous phases and "excess" cations across the 10k good-fit compositions for the GE sample site as an example. Distributions for all samples are in Appendix Figures E.24 - E.39 and are archived online (Czarnecki et al., 2023b).

Table 4.3. Results for "excess" WEH, amorphous phases, and "excess" cations. Median (Q_2), as well as Q_1 and Q_3 abundances are reported from 10k good-fit modeled compositions.

	"Excess" WEH		Total Glass		Total Amorphous Sulfates[a]		Total Amorphous Alteration Phases[b]		Total "Excess" Cations[c]	
	Q_2	Q_1 Q_3	Q_2	Q_1 Q_3	Q_2	Q_1 Q_3	Q_2	Q_1 Q_3	Q_2	Q_1 Q_3
JC	0.23	0.11 0.36	3.2	2.3 4.1	6.1	5.7 6.5	13.3	12.2 14.3	5.7	5.1 6.3
CH	0.04	0.02 0.07	16.2	14.8 17.5	8.3	8.2 8.5	9.7	8.2 11.2	0.7	0.5 1.0
MJ	0.11	0.05 0.20	17.6	16.1 19.4	9.5	9.3 10.0	17.2	15.2 19.0	2.4	2.1 2.8
TP	0.10	0.05 0.16	2.6	1.8 3.6	3.7	3.6 3.9	12.9	11.9 13.7	0.6	0.5 0.8
BK	0.09	0.04 0.18	38.5	36.5 40.7	7.7	7.4 8.1	8.5	6.1 10.7	1.1	0.7 1.4
OU	2.28	1.70 2.88	4.0	2.5 5.7	0.6	0.5 0.8	25.9	24.3 27.4	4.0	3.7 4.2
MB	0.20	0.09 0.33	5.4	3.7 7.0	5.2	5.1 5.5	27.9	26.4 29.5	1.3	1.1 1.4
QL	0.07	0.03 0.13	25.7	23.0 27.8	10.8	10.7 11.1	11.6	9.5 14.1	3.9	3.3 4.3
SB	0.06	0.03 0.12	22.7	19.9 24.7	8.7	8.5 8.9	16.7	14.8 19.3	2.8	2.5 3.2
ST	0.34	0.16 0.55	11.4	8.8 13.9	6.8	6.5 7.2	15.2	12.8 17.6	4.3	4.0 4.6
HF	0.71	0.40 1.01	14.5	12.2 16.5	2.8	2.5 3.1	28.6	26.6 30.8	2.8	2.5 3.1
RH	0.23	0.11 0.38	10.0	8.3 11.7	14.5	14.3 14.9	7.3	5.7 9.1	1.8	1.6 2.0
AK	0.25	0.12 0.41	21.5	19.2 23.5	9.6	9.3 10.0	7.6	5.8 9.6	3.6	3.1 4.1
GE	0.34	0.16 0.55	10.3	8.3 12.3	15.3	14.8 16.0	6.4	4.7 8.4	4.8	4.2 5.5
GG	0.76	0.38 1.16	21.7	19.2 24.4	7.1	6.8 7.6	14.6	11.9 17.1	3.2	2.7 3.6
MA	0.33	0.16 0.52	1.8	1.3 2.3	11.8	11.3 12.4	8.6	7.5 9.6	3.4	2.8 4.2

Note: All abundances are reported in wt.% of the bulk sample.
[a]Includes amorphous Fe- and Mg- sulfate
[b]Includes opal-A, allophane, hisingerite, and ferrihydrite
[c]Includes "excess" Na, K, Mg, and Ca

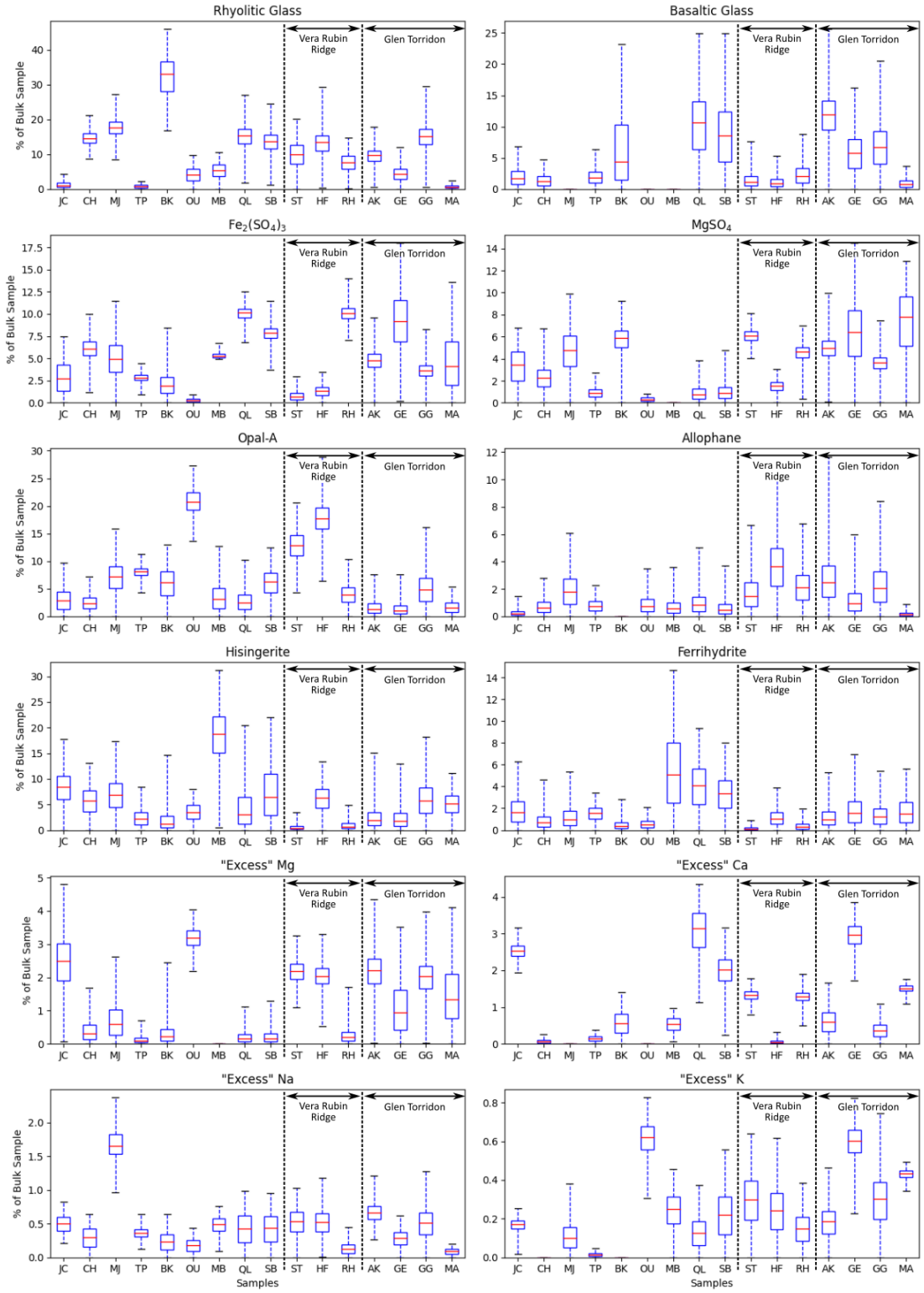

Figure 4.7. Boxplots for each amorphous phase and "excess" cation from 10k good-fit modeled compositions. Red lines denote median values (Q_2), boxes extend from Q_1 to Q_3, and whiskers extend across the entire distribution.

Figure 4.7 shows boxplots for each modeled amorphous phase and "excess" cation. Figure 4.8 shows boxplots with each candidate phase grouped into one of four categories: total glass, total amorphous sulfates, total amorphous alteration phases (opal-A, allophane, hisingerite, and ferrihydrite), and total "excess" cations. Figure 4.8 shows that several samples require significant glass and/or alteration phases to achieve good-fits, and these two categories are generally more abundant than amorphous sulfates and "excess" cations. But note that most samples have median amorphous sulfate values between 5 – 15 wt.%.

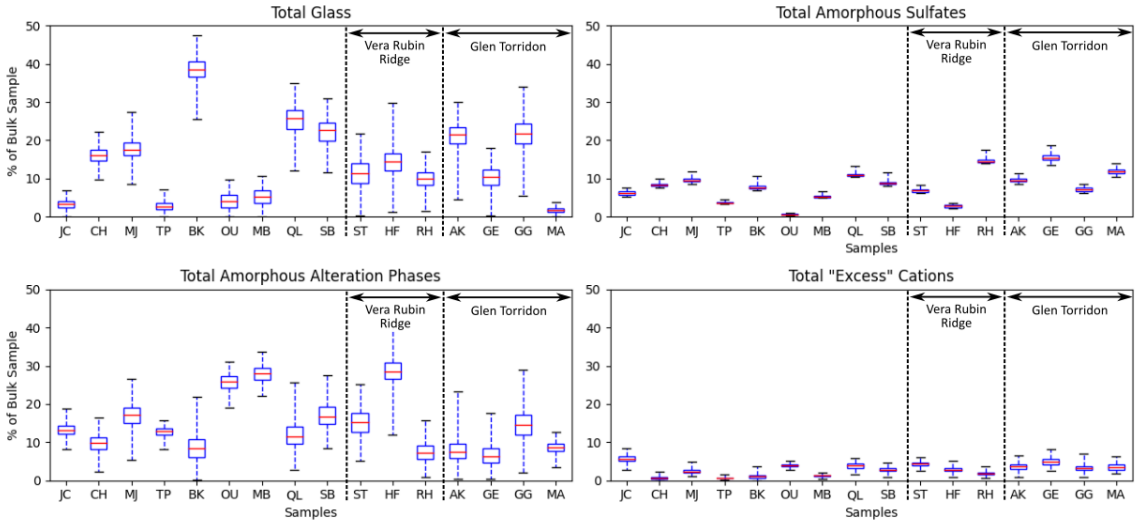

Figure 4.8. Boxplots for three categories of amorphous phases and total "excess" cations from 10k good-fit modeled compositions. Total Amorphous Alteration Phases includes opal-A, allophane, hisingerite, and ferrihydrite. Red lines denote median values (Q_2), boxes extend from Q_1 to Q_3, and whiskers extend across the entire distribution range.

4.4. Discussion

4.4.1. Smectite Hydration

Litvak et al. (2023) noted an increase in bulk WEH for VRR and GT compared to stratigraphically lower units, and Czarnecki et al. (2023a) showed that bulk WEH is greater in GT than on VRR, and proposed that the increase in GT bulk WEH could

correlate with the greater clay mineral abundances in GT samples (Thorpe et al., 2022). Figures 4.4 and 4.5 predict that, with the notable exception of OU, VRR and GT also have more "excess" WEH than stratigraphically lower samples sites. VRR and GT samples have mean "excess" WEH of 0.42 ± 0.09 wt.% and samples below VRR (not including OU as an outlier) have mean "excess" WEH of 0.11 ± ~0.03 wt.%. This again suggests that the clay minerals in this region could be hydrated in the subsurface. Although our models show that OU and the VRR samples ST and HF have some of the greatest "excess" WEH in Gale, these clay minerals have been identified most closely with ferripyrophyllite (Bristow et al., 2018; Rampe et al., 2020a), which has a lower potential to sorb "excess" WEH than smectites because it lacks expandable interlayer regions that are a characteristic of smectites. For this reason, the OU and VRR samples' "excess" WEH is more likely sorbed to amorphous phases such as opal-A (see Section 4.4.3).

We focus here on the subset of samples with identified smectites (Sap, Mnt/Sap, and Nnt in Table 4.1). We also include MJ which may contain smectite (Rampe et al., 2017), and TP and BK, which represent the endmember case of no clay minerals. Figure 4.9 is a plot of smectite abundance vs. modeled "excess" WEH. With the exception of GG, a high "excess" WEH outlier, there is a correlation between median "excess" WEH and smectite abundance (r^2 = 0.60). This strong correlation suggests that most "excess" WEH in these samples is sorbed to smectite clays. The slope of the best-fit line (m = 0.0073 ± 0.0020) indicates that if all the "excess" WEH in these samples is sorbed to smectites, these smectites contain 0.73 ± 0.20 wt.% WEH as interlayer water. One water per formula unit (pfu) of an intermediate saponite or nontronite is ~4 wt.% WEH, so this equates to n = ~0.13 – 0.23 waters pfu in Gale crater smectites. Note that this assumes all "excess" WEH is sorbed to smectites, and therefore is an upper bound.

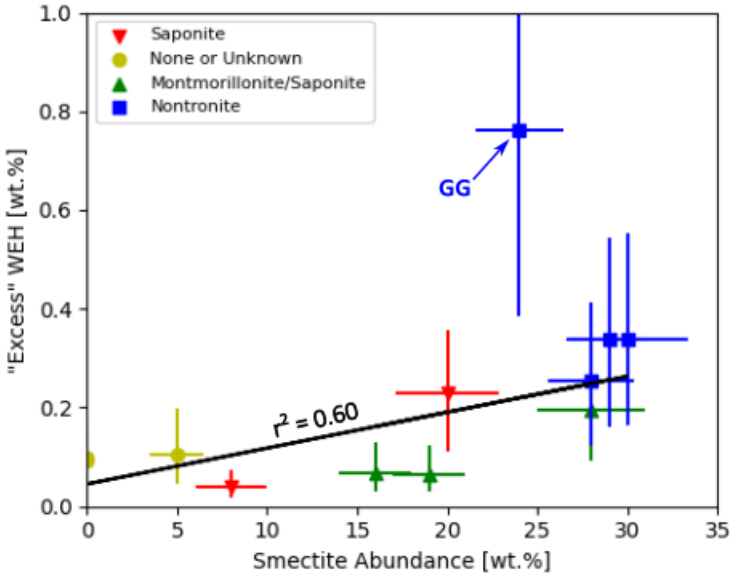

Figure 4.9. Plot of smectite abundance vs. modeled "excess" WEH. The correlation shown here is strong (r^2 = 0.60) when the GG high "excess" WEH outlier is removed. "Excess" WEH error bars extend from Q_1 to Q_3. Samples with ferripyrophyllite are not included.

This result agrees with the suggestion made by Sutter et al. (2017) that water measured by SAM may have contributions from smectite interlayer water, and strengthens the possibility that organics measured by SAM (e.g., Ming et al., 2014; Sutter et al., 2017; Eigenbrode et al., 2018) could be bound to these smectites because the organic sorption to mineral surfaces is commonly through hydroxyl (Lutzow et al., 2006; Keil & Mayer, 2014) or water (Sheng et al., 2001).

There are other potential sources for the "excess" WEH modeled here. One is gypsum, which Vaniman et al. (2018) showed can dehydrate to bassanite (from two waters pfu to one-half water pfu) in the relatively warm and low humidity conditions inside CheMin. If bassanite in samples dehydrated from gypsum during sample handling, then the bassanite measured by CheMin could be in the more hydrated gypsum form in the subsurface when measured by DAN. We compared CheMin bassanite abundances to modeled "excess" WEH (Appendix Figure E.40), and see no correlation, indicating that if gypsum is dehydrating to bassanite prior to CheMin analysis, the change in bulk hydration is not significant.

Another potential explanation for our modeled "excess" WEH is underestimated hydration of the modeled amorphous phases (Table 4.2), which all have variable hydration. We have attempted to mitigate this possibility by using hydration values sourced from either laboratory studies of martian meteorites, Mars analogue work, or a previous study using DAN WEH results to constrain amorphous phase abundances (Gabriel et al., 2018). We also incorporate generous relative uncertainties (30%) for the selected amorphous phase hydration values to simulate some of the natural variation in these phases' hydration. Nevertheless it is possible that amorphous phase hydration is more variable than represented by our modeled phase uncertainties in some cases, including for GG (see e.g., Section 4.4.2).

We also modeled "excess" abundances of four cations. Figure 4.10a shows smectite abundance vs. "excess" monovalent cations (Na and K) and Figure 4.10b shows smectite abundance vs. "excess" divalent cations (Mg and Ca). Divalent cations sorb organics to clay minerals more effectively than monovalent cations do (Dontsova & Bigham, 2005), and "excess" divalent cations are also more abundant than "excess" monovalent cations in Gale crater (Figures 4.7 and 4.10). Additionally, divalent cations can sorb organics through waters of hydration (Dontsova & Bigham, 2005), rather than through clay mineral hydroxyls. As with "excess" WEH discussed above, modeled "excess" monovalent and divalent cations both increase with increasing smectite. Removing one outlier from each Figure 4.10 plot, we find strong correlations for "excess" monovalent cations (remove MJ outlier, $r^2 = 0.75$) and "excess" divalent cations (remove MB outlier, $r^2 = 0.59$). On Earth, cation bridging is a principal mechanism that binds organics to mineral surfaces and can preserve organics for long durations (Naidja et al., 1997; Keil & Mayer, 2014). So these correlations indicate conditions favorable to the binding of organic molecules to smectites and support smectite preservation of organics in Gale crater.

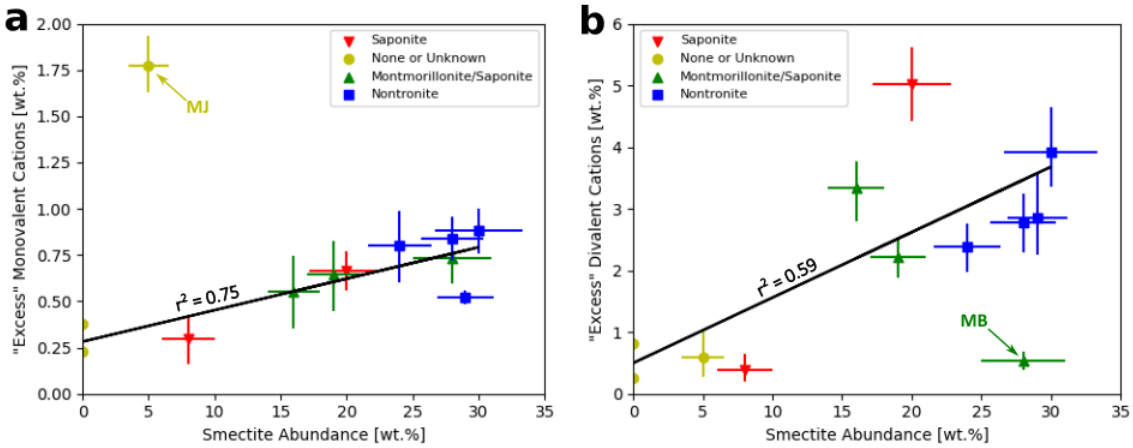

Figure 4.10. Plots of smectite abundance vs. (a) modeled "excess" monovalent cations (Na + K) and (b) divalent cations (Mg + Ca). For monovalent cations the best-fit line (r^2 = 0.75) does not include the MJ outlier and for divalent cations the best-fit line (r^2 = 0.59) does not include the MB outlier. "Excess" cation error bars extend from Q_1 to Q_3. Samples with ferripyrophyllite are not included.

Illite contains more K pfu than smectites contain Na pfu. So the MJ high "excess" monovalent cations model result in Figure 4.10.a supports illite in MJ rather than a smectite. As shown in Figure 4.10.b, MB has low modeled "excess" divalent cation abundances compared to samples with similar smectite abundances. We did not include "excess" Fe in our analyses, but MB has a high Fe abundance in the amorphous fraction (Rampe et al., 2017), some of which may be "excess", which would cause MB to better fit the trend in Figure 4.10.b.

Given the correlation of clay minerals, which enhance organic preservation (see Section 4.1.3), with modeled "excess" WEH and "excess" cations, it is likely that Gale organics are bound to clay minerals. This agrees with conclusions reached in previous work as well (e.g., Ming et al., 2014; Eigenbrode et al., 2018). Additionally, results from the ChemCam instrument have demonstrated that boron is abundant in some sections of Gale stratigraphy that correspond to clay-bearing units (Gasda et al., 2017; Das et al., 2020). Boron is thought to be important in the development of RNA (Gasda et al., 2017) as a requirement for life, and recent work has demonstrated that up to 90 – 110 ppm boron could be sorbed to smectites in Gale

(Nellessen et al., 2023). Borate adsorbs more efficiently in the presence of major cations such as Na and Ca (Nellessen et al., 2023), so boron detections in clay-bearing units where modeled "excess" cations are correlated with smectites supports the sorption of borates to smectites in Gale crater.

4.4.2. Opal-A

Although most samples have good-fit compositions with little to no modeled opal-A, a few samples (OU, ST, and HF) have median opal-A abundances > 10 wt.% (Figure 4.7). OU and HF have good-fit compositions up to > 25 wt.% opal-A. Opal-A often forms from the alteration of basaltic sediment (Rampe et al., 2020b), but does not persist long on Earth, rapidly transforming to opal-CT and then to quartz (e.g., Dehouck et al., 2014) when in contact with water at 0°C for < 400 Ma total (Tosca & Knoll, 2009). The persistence of opal-A indicates relatively little water-rock interaction in syn- and post-depositional history.

Opal-A also has a large surface area and is another potential reservoir for "excess" WEH and "excess" cations in some samples. And as discussed in Section 4.1.4, hydrated opal is another good candidate for organic preservation (Costa et al., 2008; Nonella & Seeger, 2008) and microbe preservation (Squyres et al., 2008). Our models suggest that some of the samples with the greatest "excess" WEH abundances also have large opal-A abundances (Appendix Figure E.41), including the OU, ST, and HF ferripyrophyllite-bearing samples that were not included in the Figure 4.9 and 4.10 smectite analyses. The GG high "excess" WEH outlier in Figure 4.9 also potentially has more opal-A than the other GT samples (Figure 4.8 opal-A boxplot). Opal-A can have a variety of hydration states; for our models we used a value of 6.3 wt.% WEH, the mean value from Rapin et al. (2018). But Rapin et al. (2018) reported larger opal-A WEH values from Gale crater samples as well, and Gabriel et al. (2022) proposed that opal-A in some Gale crater samples (not included in our

analyses) contain > 10 wt.% WEH. Given the high abundance of modeled opal-A in the distributions of OU, ST, and HF, and to a lesser extent in GG, it is likely that a significant amount of the modeled "excess" WEH from these samples is due to underestimated opal-A WEH in our models.

OU was sampled just above BK in the stratigraphic section (Figure 4.1) in a region where other high-silica samples were drilled from opal-rich fracture halos in the unconformable "Stimson" formation (Yen et al., 2017; Gabriel et al., 2022; Rapin et al., 2018). Silica in these samples is primarily opal-A (Rapin et al., 2018) that was likely mobilized from the underlying high-silica material sampled at BK (Frydenvang et al., 2017; Czarnecki et al., 2020), which is glass-rich and opal-A poor (Figures 4.7 and 4.8). Samples from this section of the traverse, including TP, BK, and OU from the Murray formation, and the "Greenhorn" and "Lubango" samples from the overlying unconformable Stimson formation have unique mineralogy, including opal-A, opal-CT, tridymite, and cristobalite. The opal-A hydration of these samples will be the subject of future work.

4.4.3. Hisingerite, Allophane, and Ferrihydrite

Figure 4.7 shows higher modeled abundances of hisingerite earlier in the stratigraphic section (below VRR), where median abundances are generally ≥ 5 wt.%, compared to later in the section (VRR and GT), where median abundances are < ~5 wt.%. Hisingerite is a product of serpentization and produces abundant H_2 (Evans et al., 2017; Tutolo et al., 2019; Tutolo & Tosca, 2023) which is an energy source for life (Amador et al., 2018; Tutolo et al., 2019). H_2 produced by serpentization could be related to the origin of life of Earth and is a compelling reason to search for biosignatures in areas of serpentization (Amador et al., 2018). The presence of hisingerite (in abundances up to 20 wt.% or more in some samples) is another indication of habitability during sediment diagenesis of these units.

Rampe et al. (2020b) and David et al. (2022) concluded that allophane was a minor component of Gale crater samples. This is supported by our results in which all samples have good-fit compositions with little to no allophane (Figure 4.7). In our model results, allophane is somewhat more abundant in samples from the upper section (VRR and GT) where median allophane is generally ~2 – 4 wt.% with good-fit compositions up to 10 – 12 wt.% in HF and AK. In the lower section (below VRR) median allophane is < 2 wt.% with maximum good-fit compositions < 6 wt.%.

Figure 4.7 shows that modeled ferrihydrite is also a relatively minor component of Gale crater samples, but is most abundant in the MB, QL, and SB samples. Median abundances for these samples are between ~4 – 6 wt.%. Achilles et al. (2020) previously suggested that the MB sample likely contains ferrihydrite, and in our analysis this sample has the highest potential ferrihydrite abundance, with good-fit compositions up to > 14 wt.%. All samples other than MB, QL, and SB have median abundances < 2 wt.% with maximum good-fit compositions mostly < 6 wt.%. Rampe et al. (2016) showed that chemisorption of sulfate or phosphate complexes onto ferrihydrite can inhibit its transformation to a crystalline phase. But sulfates are not particularly abundant in these samples, and though phosphorus was not included in our analyses, reported phosphorus abundances in the amorphous fraction of these samples are also not particularly high (Bristow et al., 2018).

4.4.4. Glasses

Previous work using FULLPAT analysis of CheMin data has consistently suggested the presence of remnant volcanic or impact glass (e.g., Rampe et al., 2017; Rampe et al., 2020a; Rampe et al. 2020b). Our modeling has shown a significant remnant glass component in nearly all samples. Median total glass abundances are > 10 wt.% in two-thirds of samples (Figure 4.8), reaching a maximum in BK at ~40 wt.%. The high-silica material sampled at BK contained

tridymite, indicating a silicic volcanic origin (Morris et al., 2016), and the high glass content of BK constrained by our models supports a volcanic origin for this material. Glass is easily altered by water (e.g., Dehouck et al., 2014), and allophane and ferrihydrite are common weathering products of volcanic glass (e.g., Rampe et al., 2016). So the relatively high abundances of glass and low abundances of allophane and ferrihydrite (Figures 4.7 and 4.8) in these samples could indicate low water-rock interaction over the syn- and post-depositional history of Gale crater.

4.4.5. Amorphous Sulfates

Experimental studies have suggested that amorphous sulfates could be abundant on present-day Mars (e.g., Vaniman & Chipera, 2006; Wang et al., 2009; Sklute et al., 2015; Chipera et al., submitted), and polyhydrated Mg-sulfates identified from orbit are consistent with amorphous phases (Wang et al., 2009; Chipera et al., submitted). Amorphous ferric sulfates can form from evaporation of aqueous ferric sulfate solutions at low relative humidity (Xu et al., 2009) or from rapid dehydration of crystalline forms (Wang & Zhou, 2014; Sutter et al., 2017). Amorphous ferric sulfates have been shown to endure diurnal relative humidity variations without recrystallization (Sklute et al., 2015), while amorphous Mg-sulfate quickly alters to crystalline and back depending on water availability (Vaniman et al., 2004). Both Fe- and Mg-sulfates should become amorphous during MSL sample acquisition and handling (Vaniman et al., 2014; Sutter et al., 2017). This suggests that although CheMin and SAM should expect to measure primarily amorphous Fe- and Mg-sulfates, these sulfates could be either amorphous or crystalline in the subsurface.

Various studies have concluded that amorphous sulfates are present in Gale crater samples (e.g., Sutter et al., 2017; McAdam et al., 2020, Rampe et al., 2020a,b; McAdam et al., 2022). Model results in Figure 4.8 show amorphous sulfates

in all samples except OU, which fits best with very little to no amorphous sulfate. David et al. (2022) suggested that amorphous sulfates are the major carrier of soil hydration in Gale. Although our models show generally less total amorphous sulfate than total glass or amorphous alteration phases, the median overall amorphous sulfate abundance (~8 wt.%) with the sulfate hydration in our models (~22 wt.% WEH) indicates that amorphous sulfates contain up to a few wt.% of bulk WEH. Although they are not the major carrier in all samples, amorphous sulfates are certainly a significant overall source of subsurface hydration in Gale crater. Modeled amorphous sulfate abundances are highly variable among the samples analyzed (Figure 4.7), with median abundances from < 1 wt.% for both Fe- and Mg-sulfate up to ~8 wt.% for Mg-sulfate and ~10 wt.% for Fe-sulfate. Overall similar trends are followed across the traverse for these two sulfate species. Only ST requires appreciable amounts of Mg-sulfate for good-fit compositions, but CH, TP, MB, QL, SB, and RH all require some Fe-sulfate for good-fit compositions.

In our models, total amorphous sulfates increase in abundance from the base of the section to the MJ sample, then decrease to the BK and OU samples. Above OU, sulfate abundances increase again up to the QL sample, followed by another steady decrease until the HF sample on VRR. Because sulfates are an indicator of acidic conditions (e.g., Achilles et al., 2020), the correspondence of very low sulfate abundances and very high amorphous silica abundances in the BK and OU samples suggests that these silica abundances are not the result of acid leaching, but rather of a change in sediment source (e.g., Morris et al., 2016; Czarnecki et al., 2020) or passive enrichment as in the fracture halos of the unconformably overlying Stimson formation (Yen et al., 2017; Gabriel et al., 2022, Rapin et al., 2018).

The HF sample has much lower modeled amorphous sulfate (and crystalline Ca-sulfate, Rampe et al., 2020a) than RH at the same stratigraphic level. HF follows

a decreasing amorphous sulfate trend upsection from QL, whereas RH represents the start of an interval of more abundant amorphous sulfates that persists through most GT samples (Figure 4.8). GT lies at the boundary of clay mineral-dominated stratigraphy and sulfate-dominated stratigraphy on the ascent up Mt. Sharp. Samples obtained above GT contain lower and lower clay mineral abundances until clay minerals are entirely absent in the "Zechstein", "Avanavero", and "Canaima" samples (Vaniman, 2012; Chipera et al., submitted). Canaima is also the first sample, measuring from the base of the section, that contains crystalline sulfates. This transition from clay to sulfate mineralogy may have been in evidence first in the VRR and GT samples, which our models show contain, on average, more amorphous sulfates than underlying samples (Figure 4.8). This increase in sulfate abundance represents a transition to a more arid environment that is also evident in other areas of Mars (e.g., Murchie et al., 2009). Future work will extend our analysis to these overlying samples in order to quantify total sulfate abundances for stratigraphy that preserve evidence of the aridification of Gale crater.

4.5. Conclusions

We developed a method of constraining amorphous phase abundances and "excess" water and cations for Gale crater samples by modifying and expanding the modeling techniques of Gabriel et al. (2018). We determined which randomly generated candidate amorphous phase compositions have good-fit chemistry and hydration compared to MSL drill sample amorphous compositions based on CheMin mineralogy, APXS geochemistry, and DAN bulk hydration. Modeled distributions of these phases for all samples are available in Figure 4.4 and Appendix Figures E.24 – E.39. Boxplots in Figures 4.5, 4.7, and 4.8 allow for easy comparison of samples. We have derived four primary conclusions from these results:

1. *Smectites in Gale crater are hydrated.* The correlation shown in Figure 4.9, between modeled "excess" WEH and smectite abundance (r^2 = 0.60) in Gale samples (excepting one smectite-bearing outlier) indicates that these smectites are likely hydrated, though at low abundance (equivalent to n = ~0.2 H_2O pfu) and indicates that organics measured by SAM (e.g., Ming et al., 2014; Sutter et al., 2017; Eigenbrode et al., 2018) could be bound to these smectites through hydroxyl (Lutzow et al., 2006; Keil & Mayer, 2014) or water (Sheng et al., 2001).
2. *Smectites in Gale crater contain bound cations that may act as cation bridges for sorbed water or organics.* Correlations between smectite abundance and modeled "excess" monovalent and divalent cations (excepting one outlier each) are shown in Figure 4.10 (r^2 = 0.75 and 0.59, respectively). These correlations indicate that these "excess" cations are bound to smectites in these samples. Cation bridging is a prevalent mechanism for organic preservation in clay minerals on Earth (Keil & Mayer, 2014), and our results indicate may be prevalent in Gale crater as well.
3. *Amorphous phase abundances indicate low water-rock interactions in the syn- and post-depositional history of Gale crater.* The presence of abundant amorphous material in Gale crater indicates intermittent, low-volume groundwater (Rampe et al., 2020b), and low water-rock interactions (McLennan et al., 2019; Smith et al, 2021) in the syn- and post-depositional history of Gale crater. Our model results support low water-rock interactions, as indicated by the persistence of abundant amorphous sulfates (Chipera et al., submitted), opal-A (Tosca & Knoll, 2009), and glass (Dehouck et al., 2014) (Figures 4.7 and 4.8). Low abundances of modeled allophane and ferrihydrite (Figure 4.7), which are common weathering products of glass (Rampe et al., 2017), also support low water-rock interactions.

4. *Amorphous phase abundances indicate increasing oxidation upsection in the Murray and Carolyn Shoemaker formations.* Prior work has shown abundant evidence of oxidation from low water availability in the upper Gale crater stratigraphic section including increased hematite:magnetite ratios and the switch from trioctahedral smectites (saponite) to dioctahedral smectites (montmorillonite and nontronite) (Tu et al., 2021). This is also supported by our model results indicating increased abundances of amorphous sulfates and glass up-section (Figure 4.8).

This work has demonstrated the diversity of phases that can be modeled by our amorphous component analysis. The method is adaptable to allow, for example, an investigation into the hydration state of a specific phase such as opal-A as suggested in Section 4.4.2. The change from clay mineral stratigraphy to sulfate mineral stratigraphy is discussed in Section 4.4.5, and our method would be a powerful tool to constrain amorphous sulfates in this area as well. Our methods can also be applied to samples currently being collected by NASA's Perseverance rover in Jezero crater for the Mars Sample Return program. These samples will be returned to Earth probably in the 2030s. Neutron spectroscopy can be applied to these samples before they are unsealed in the lab, allowing investigators to measure the bulk hydration and enabling techniques like the amorphous component analysis method developed here.

References

Achilles, C. N., Downs, R. T., Ming, D. W., Rampe, E. B., Morris, R. V., Treiman, A. H., et al. (2017). Mineralogy of an active eolian sediment from the Namib dune, Gale crater, Mars. *Journal of Geophysical Research: Planets*, 122: 2344-2361. https://doi.org/10.1002/2017JE005262

Achilles, C. N., Rampe, E. B., Downs, R. T., Bristow, T. F., Ming, D. W., Morris, R. V., et al. (2020). Evidence for multiple diagenetic episodes in ancient fluvial-lacustrine sedimentary rocks in Gale crater, Mars. *Journal of Geophysical Research: Planets*, 125: e2019JE006295. https://doi.org/10.1029/2019JE006295

Amador, E. S., Bandfield, J. L., & Thomas, N. H. (2018). A search for minerals associated with serpentization across Mars using CRISM spectral data. *Icarus*, 311: 113-134. https://doi.org/10.1016/j.icarus.2018.03.021

Anderson, R. B. & Bell III, J. F. (2010). Geologic mapping and characterization of Gale crater and implications for its potential as a Mars Science Laboratory landing site. *Mars*, 5: 76-128. https://doi.org/10.1555/mars.2010.0004

Bedford, C. C., Bridges, J. C., Schwenzer, S. P., Wiens, R. C., Rampe, E. B., Frydenvang, J., & Gasda, P. J. (2019). Alteration trends and geochemical source region characteristics preserved in the fluviolacustrine sedimentary record of Gale crater, Mars. *Geochimica et Cosmochimica Acta*, 246: 234–266. https://doi.org/10.1016/j.gca.2018.11.031

Bish, D. L., Carey, J. W., Vaniman, D. T., Chipera, S. J. (2003). Stability of hydrous minerals on the martian surface. *Icarus*, 164: 96-103. https://doi.org/10.1016/S0019-1035(03)00140-4

Bish, D. L., Blake, D. F., Vaniman, D. T., Chipera, S. J., Morris, R. V., Ming, D. W., et al. (2013). X-ray diffraction results from Mars Science Laboratory: Mineralogy of Rocknest at Gale crater. *Science*, 341(6153): 1238932-1. https://doi.org/10.1126/science.1238932

Blake, D., Vaniman, D., Achilles, C., Anderson, R., Bish, D., Bristow, T. (2012). Characterization and calibration of the CheMin mineralogical instrument on Mars Science Laboratory. *Space Science Reviews*, 170: 341-399. https://doi.org/10.1007/s11214-012-9905-1

Bridges, J. C., Schwenzer, S. P., Leveille, R., Westall, F., Wiens, R. C., Mangold, N. (2015). Diagenesis and clay mineral formation at Gale crater, Mars. *Journal of Geophysical Research: Planets*, 120: 1-19. https://doi.org/10.1002/2014JE004757

Bristow, T. F., Rampe, E. B., Achilles, C. N., Blake, D. F., Chipera, P. C., Craig, P., et al. (2018). Clay mineral diversity and abundance in sedimentary rocks of Gale crater, Mars. *Science Advances*, 4(6): eaar3330. https://doi.org/10.1126/sciadv.aar3330

Broz, A. P. (2020). Organic matter preservation in ancient soils of Earth and Mars. *Life*, 10(113). https://doi.org/10.3390/life10070113

Campbell, J. L., King, P. L., Burkemper, L., Berger, J. A., Gellert, R., Boyd, N. I., et al. (2014). The Mars Science Laboratory APXS calibration target: Comparison of Martian measurements with the terrestrial calibration. *Nuclear Instruments and Methods in Physics Research B*, 323: 49–58. https://doi.org/10.1016/j.nimb.2014.01.011

Chipera, S. J., Vaniman, D. T., Rampe, E. B., Bristow, T. F., Martinez, G., Tu, V. M., et al. (submitted). Mineralogical investigation of Mg-sulfate at the Canaima drill site, Gale crater, Mars. *Journal of Geophysical Research: Planets*.

Cohen, B. A., Malespin, C. A., Farley, K. A., Martin, P. E., Cho, Y., & Mahaffy, P. R. (2019). *In situ* geochronology on Mars and the development of future instrumentation. *Astrobiology*, 19(11): 1303-1314. https://doi.org/10.1089/ast.2018.1871

Costa, D., Tougerti, A., Tielens, F., Gervais, C., Stievano, L., & Lambert, J. F. (2008). *Physical Chemistry Chemical Physics*, 10: 6360-6368. https://doi.org/10.1016/10.1039/b806501b

Czarnecki, S., Hardgrove, C., Gasda, P. J., Gabriel, T. S. J., Starr, M., Rice, M., et al. (2020). Identification and description of a silicic volcaniclastic layer in Gale crater, Mars, using active neutron interrogation. *Journal of Geophysical Research: Planets*, 125, e2019JE006180. https://doi.org/10.1029/2019JE006180

Czarnecki, S., Hardgrove, C., Arvidson, R. E., Hughes, M. N., Schmidt, M. E., Henley, T., et al. (2023a). Hydration of a clay-rich unit on Mars, comparison of orbital data to rover data. *Journal of Geophysical Research: Planets*, 128: e2021JE007104. https://doi.org/10.1029/2021JE007104

Czarnecki, S., Hardgrove, C., Rampe, E. B., & Gasda, P. J. (2023b). "Constraining the hydration of clay minerals and abundances of amorphous phases in Gale crater, Mars" supplementary information (Version 1). *Zenodo*. https://doi.org/10.5281/zenodo.8136072

Das, D., Gasda, P. J., Wiens, R. C., Berlo, K., Leveille, R. J., Frydenvang, J., et al. (2020). Boron and lithium in calcium sulfate veins: Tracking precipitation of diagenetic materials in Vera Rubin ridge, Gale crater. *Journal of Geophysical Research: Planets*, 125(8): e2019JE006301. https://doi.org/10.1029/2019JE006301

David, G., Dehouck, E., Meslin, P.-Y., Rapin, W., Cousin, A., Forni, O., et al. (2022). Evidence for amorphous sulfates as the main carrier of soil hydration in Gale crater, Mars. *Geophysical Research Letters*, 49: e2022GL098755. https://doi.org/10.1029/2022GL098755

Dehouck, E., McLennan, S. M., Meslin, P.-Y., & Cousin, A. (2014). Constraints on abundance, composition, and nature of X-ray amorphous components of soils and rocks at Gale crater, Mars. *Journal of Geophysical Research: Planets*, 119: 2640-2657. https://doi.org/10.1002/2014JE004716

Dontsova, K. M. & Bigham, J. M. (2005). Anionic polysaccharide sorption by clay minerals. *Soil Science of America Journal*, 69: 1026-1035. https://doi.org/10.2136/sssaj2004.0203

dos Santos, R., Patel, M., Cuadros, J., & Martins, Z. (2016). Influence of mineralogy on the preservation of amino acids under simulated Mars conditions. *Icarus*, 277: 342-353. http://doi.org/10.1016/j.icarus.2016.05.029

Ehlmann, B. L., Mustard, J. F., Fassett, C. I., Schon, S. C., Head III, J. W., Des Marais, D. J., et al. (2008). Clay minerals in delta deposits and organic preservation potential on Mars. *Nature Geoscience*, 1: 355-358. https://doi.org/10.1038/ngeo207

Eigenbrode, J. L., Summons, R. E., Steele, A., Freissinet, C., Millan, M., Navarro-Gonález, R., et al. (2018). *Science*, 360(6393): 1096-1101. https://doi.org/10.1126/science.aas9185

Evans, B. W., Kuehner, S. M., Joswiak, D. J., & Cressey, G. (2017). Serpentine, iron-rich phyllosilicates and fayalite produced by hydration and Mg depletion of peridotite, Duluth complex, Minnesota, USA. *Journal of Petrology*. 58(3): 495-512. https://doi.org/10.1093/petrology/egx024

Farmer, J. D. & Des Marais, D. J. (1999). Exploring for a record of ancient Martian life. *Journal of Geophysical Research*, 104(E11): 26977-26995. https://doi.org/10.1029/1998je000540

Filiberto, J., Treiman, A. H., & Le, L. (2008). Crystallization experiments on a Gusev Adirondack basalt composition. *Meteoritics & Planetary Science*, 43(7): 1137-1146. https://doi.org/10.1111/j.1945-5100.2008.tb01118.x

Fiorito, T. M., Icoz, I., & Stotzky, G. (2008). Adsorption and binding of the transgenic plant proteins, human serum albumin, *β*-glucuronidase, and Cry3Bb1, on montmorillonite and kaolinite: Microbial utilization and enzymatic activity of free and clay-bound proteins. *Applied Clay Science*, 39: 142-150. https://doi.org/10.1016/j.clay.2007.07.006

Foreman-Mackey, D., Hogg, D. W., Lang, D., & Goodman, J. (2013). Emcee: The MCMC Hammer. *Publications of the Astronomical Society of the Pacific*, 125(925): 306–312. https://doi.org/10.1086/670067

Frydenvang, J., Gasda, P. J., Hurowitz, J. A., Grotzinger, J. P., Wiens, R. C., Newsom, H. E., et al. (2017). Diagenetic silica enrichment and late-stage groundwater activity in Gale crater, Mars. *Geophysical Research Letters*, 44: 4716–4724. https://doi.org/10.1002/2017GL073323

Gabriel, T. S. J, Hardgrove, C., Czarnecki, S., Rampe, E. B., Rapin, W., Achilles, C. N., et al. (2018). Water abundance of dunes in Gale Crater, Mars from active neutron experiments & implications for amorphous phases. *Geophysical Research Letters*, 45, 12,766–12,775. https://doi.org/10.1029/2018GL079045

Gabriel, T. S. J., Hardgrove, C., Achilles, C. N., Rampe, E. B., Rapin, W. N., Nowicki, S., et al. (2022). On an extensive late hydrologic event in Gale crater as indicated by water-rich fracture halos. *Journal of Geophysical Research: Planets*, 127: e2020JE006600. https://doi.org/10.1029/2020JE006600

Gasda, P. J., Haldeman, E. B., Wiens, R. C., Rapin, W., Bristow, T. F., Bridges, J. C., et al. (2017). *In situ* detection of boron by ChemCam on Mars. *Geophysical Research Letters*, 44(17): 8739-8748. https://doi.org/10.1002/2017GL074480

Gasda, P. J., Comellas, J., Essunfeld, A., Das, D., Bryk, A. B., Dehouck, E., et al. (2022). Overview of the morphology and chemistry of diagenetic features in the clay-rich Glen Torridon unit of Gale crater, Mars. *Journal of Geophysical Research: Planets*, 127: e2021JE007097. https://doi.org/10.1029/2021JE007097

Glotch, T. D., Bandfield, J. L., Christensen, P. R., Calvin, W. M., McLennan, S. M., Clark, B. C., et al. (2006). Mineralogy of the light-toned outcrop at Meridiani Planum as seen by the Miniature Thermal Emission Spectrometer and implications for its formation. *Journal of Geophysical Research*, 111: E12S03. https://doi.org/10.1029/2005JE002672

Grotzinger, J. P., Sumner, D. Y., Kah, L. C., Stack, K., Gupta, S., Edgar, L., Rubin, D., et al. (2014). A habitable fluvio-lacustrine environment at Yellowknife Bay, Gale Crater, Mars. *Science*, 343(6169): 1242777. https://doi.org/10.1126/science.1242777

Hardgrove, C., Moersch, J., & Drake, D. (2011). Effects of geochemical composition on neutron die-away measurements: Implications for Mars Science Laboratory's Dynamic Albedo of Neutrons experiment. *Nuclear Instruments and Methods in Physics Research A*, 659(1): 442–455. https://doi.org/10.1016/j.nima.2011.08.058

Hassler, D. M., Zeitlin, C., Wimmer-Schweingruber, R. F., Ehresmann, B., Rafkin, S., Eigenbrode, J. L. (2014). Mars' surface radiation environment measured with the Mars Science Laboratory's Curiosity rover. *Science*, 343: 1244797-1. https://doi.org/10.1126/science.1244797

Hazen, R. (2005). Genesis: Rocks, minerals, and the geochemical origin of life. *Elements*, 1(3): 135-137. https://doi.org/10.2113/gselements.1.3.135

Hurowitz, J. A., Grotzinger, J. P., Fischer, W. W., McLennan, S. M., Milliken, R. E., Stein, N., et al. (2017). Redox stratification of an ancient lake in Gale crater, Mars. *Science*, 356(6341): eaah6849. https://doi.org/10.1126/science.aah6849

Jun, I., Mitrofanov, I., Litvak, M. L., Sanin, A. B., Kim, W., Behar, A., et al. (2013). Neutron background environment measured by the Mars Science Laboratory's Dynamic Albedo of Neutrons instrument during the first 100 sols. *Journal of Geophysical Research: Planets*, 118: 2400–2412. https://doi.org/10.1002/2013JE004510

Keil, R. G. & Mayer, L. M. (2014). Mineral matrices and organic matter. *Treatise on Geochemistry 2nd Edition*, 12: 337-359. http://doi.org/10.1016/B978-0-08-095975-7.01024-X

Kennedy, M. J., Pevear, D. R., & Hill, R. J. (2002). Mineral surface control of organic carbon in black shale. *Science*, 295: 657-660. https://doi.org/10.1126/science.1066611

Kminek, G. & Bada, J. L. (2006). The effect of ionizing radiation on the preservation of amino acids on Mars. *Earth and Planetary Science Letters*, 245(1-2): 1-5. https://doi.org/10.1016/j.epsl.2006.03.008

Lapotre, M. G., Ehlmann, B. L., Minson, S. E., Arvidson, R. E., Ayoub, F., Fraeman, A. A., et al. (2017). *Journal of Geophysical Research: Planets*, 122: 2489-2509. https://doi.org/10.1002/2016JE005133

Lewis, K. W., Peters, S., Gonter, K., Morrison, S., Schmerr, N., Vasavada, A. R., et al. (2019). A surface gravity traverse on Mars indicates low bedrock density at Gale crater. *Science*, 363(6426): 535–537. https://doi.org/10.1126/science.aat0738

Litvak, M. L., Mitrofanov, I. G., Barmakov, Yu. N., Behar, A., Bitulev, A., Bobrovnitsky, Yu., et al. (2008). The Dynamic Albedo of Neutrons (DAN) experiment for NASA's 2009 Mars Science Laboratory. *Astrobiology*, 8(3): 605–612. https://doi.org/10.1089/ast.2007.0157

Litvak, M. L., Mitrofanov, I. G., Gellert, R., Djachkova, M. V., Lisov, D. I., Vasavada, A.R., et al. (2023). Depth distribution of chlorine at Gale crater, Mars, as derived from the DAN and APXS experiments onboard the Curiosity rover. *Journal of Geophysical Research: Planets*, 128(5): e2022JE007694. https://doi.org/10.1029/2022JE007694

Lützow, M. V., Kögel-Knabner, I., Ekschmitt, K., Matzner, E., Guggenberger, G., Marschner, B., et al. (2006). Stabilization of organic matter in temperate soils: mechanisms and their relevance under different soil conditions – a review. *European Journal of Soil Science*, 57: 426-445. https://doi.org/10.1111/j.1365-2389.2006.00809.x

McAdam, A. C., Sutter, B., Archer, P. D., Franz, H. B., Wong, G. M., Lewis, J. M. T., et al. (2020). Constraints on the mineralogy and geochemistry of Vera Rubin ridge, Gale crater, Mars from Mars Science Laboratory Sample Analysis at Mars evolved gas analysis. *Journal of Geophysical Research: Planets*, 125: e2019JE006309. https://doi.org/10.1029/2019JE006309

McAdam, A. C., Sutter, B., Archer, P. D., Franz, H. B., Wong, G. M., Lewis, J. M. T., et al. (2022). Evolved gas analyses of sedimentary rocks from the Glen Torridon clay-bearing unit, Gale crater, Mars: Results from the Mars Science Laboratory Sample Analysis at Mars instrument suite. *Journal of Geophysical Research: Planets*, 127: e2022JE007179. https://doi.org/10.1029/2022JE007179

McLennan, S. M., Grotzinger, J. P., Hurowitz, J. A., & Tosca, N. J. (2019). The sedimentary cycle on early Mars. *Annual Review of Earth and Planetary Sciences*, 47: 91–118. https://doi.org/10.1146/annurev-earth-053018-060332

Milliken, R. E., Swayze, G. A., Arvidson, R. E., Bishop, J. L., Clark, R. N., Ehlmann, B. L., et al. (2008). Opaline silica in young deposits on Mars. *Geology*, 36(11): 847–850. https://doi.org/10.1130/G24967A.1

Milliken, R. E., Grotzinger, J. P., & Thomson, B. J. (2010). Paleoclimate of Mars as captured by the stratigraphic record in Gale crater. *Geophysical Research Letters*, 37(L04201). https://doi.org/10.1029/2009GL041870

Ming, D. W., Archer Jr., P. D., Glavin, D. P., Eigenbrode, J. L., Franz, H. B., Sutter, B., et al. (2014). Volatile and organic compositions of sedimentary rocks in Yellowknife Bay, Gale crater, Mars. *Science*, 343(6169). https://doi.org/10.1126/science.1245267

Mitrofanov, I. G., Litvak, M. L., Varenikov, A. B., Barmakov, Y. N., Behar, A., Bobrovnitsky, Y. I., et al. (2012). Dynamic Albedo of Neutrons (DAN) experiment onboard NASA's Mars Science Laboratory. *Space Science Reviews*, 170: 559–582. https://doi.org/10.1007/s11214-012-9924-y

Mitrofanov, I. G., Kozyrev, A. S., Lisov, D. I., Vostrukhin, A. A., Golovin, D. V., Litvak, M. L., et al. (2016). Active neutron sensing of the martian surface with the DAN experiment onboard the NASA "Curiosity" Mars rover: Two types of soil with different water content in the Gale crater. *Astronomy Letters*, 42(4): 251–259. https://doi.org/10.1134/S1063773716040058

Morris, R. V., Vaniman, D. T., Blake, D. F., Gellert, R., Chipera, S. J., Rampe, E. B., et al. (2016). Silicic volcanism on Mars evidenced by tridymite in high-SiO_2 sedimentary rock at Gale crater. *Proceedings of the National Academy of Sciences of the United States of America*, 113(26): 7071–7076. https://doi.org/10.1073/pnas.1607098113

Morrison, S. M., Downs, R. T., Blacke, D. F., Vaniman, D. T., Ming, D. W., Hazen, R. M. (2018). Crystal chemistry of martian minerals from Bradbury Landing through Naukluft plateau, Gale crater, Mars. *American Mineralogist*, 103: 857-871. https://doi.org/10.2138/am-2018-6124

Murchie, S., Arvidson, R., Bedini, P., Beisser, K., Bibring, J.-P., Bishop, J., et al. (2007). Compact Reconnaissance Imaging Spectrometer for Mars (CRISM) on Mars Reconnaissance Orbiter (MRO). *Journal of Geophysical Research*, 112(E05S03). https://doi.org/10.1029/2006JE002682

Murchie, S. L., Mustard, J. F., Ehlmann, B. L., Millikan, R. E., & Bishop, J. L. (2009). A synthesis of Martian aqueous mineralogy after 1 Mars year of observations from the Mars Reconnaissance Orbiter. *Journal of Geophysical Research*, 114(E00D06). https://doi.org/10.1029/2009JE003342

Naidja, A., Huang, P. M., & Bollag, J.-M. (1997). Activity of tyrosinase immobilized on hydroxyaluminum-montmorillonite complexes. *Journal of Molecular Catalysis A: Chemical*, 115: 305-316. https://doi.org/10.1016/S1381-1169(96)00335-4

National Academies of Sciences, Engineering, and Medicine. (2022). Origins, Worlds, and Life: A Decadal Strategy for Planetary Science and Astrobiology 2023-2032. *Washington, DC: The National Academies Press*. https://doi.org/10.17226/26522

Nellessen, M. A., Gasda, P., Crossey, L., Peterson, E., Ali, A., Zhang, J., et al. (2023). Boron adsorption in clay minerals: Implications for martian groundwater chemistry and boron on Mars. *Icarus*, (401): 115372. https://doi.org/10.1016/j.icarus.2023.115599

Nonella, M. & Seeger, S. (2008). Investigating alanine-silica interactions by means of first-principles molecular-dynamics simulations. *ChemPhysChem*, 9: 414-421. https://doi.org/10.1002/cphc.200700546

Ovesen, R. G., Nielsen, J., & Bruun Hansen, H. C. (2011). Biomedicine in the environment: Sorption of the cyclotide kalata B2 to montmorillonite, goethite, and humic acid. *Environmental Toxicology and Chemistry*, 30(8): 1785-1792. https://doi.org/10.1002/etc.579

Pavlov, A. A., Vasilyev, G., Ostryakov, V. M., Pavlov, A. K., & Mahaffy, P. (2012). Degradation of the organic molecules in the shallow subsurface of Mars due to irradiation by cosmic rays. *Geophysical Research Letters*, 39: L13202. https://doi.org/10.1029/2012GL052166

Pourret, O., Bollinger, J.-C., Hursthouse, A., & van Hullebusch, E. D. (2022). Sorption vs adsorption: The words they are a-changin', not the phenomena. *Science of the Total Environment*, 838: 156545. https://doi.org/10.1016/j.scitotenv.2022.156545

Rampe, E. B., Morris, R. V., Archer Jr., P. D., Agresti, D. G., & Ming, D. W. (2016). Recognizing sulfate and phosphate complexes chemisorbed onto nanophase weathering products on Mars using *in-situ* and remote observations. *American Mineralogist*, 101: 678-689. http://doi.org/10.2138/am-2016-5408CCBYNCND

Rampe, E. B., Ming, D. W., Blake, D. F., Bristow, T. F., Chipera, S. J., Grotzinger, J. P., et al. (2017). Mineralogy of an ancient lacustrine mudstone succession from the Murray formation, Gale crater, Mars. *Earth and Planetary Science Letters*, 471: 172–185. https://doi.org/10.1016/j.epsl.2017.04.021

Rampe, E. B., Bristow, T. F., Morris, R. V., Morrison, S. M., Achilles, C. N., Ming, D. W., et al. (2020a). Mineralogy of Vera Rubin ridge from the Mars Science Laboratory CheMin instrument. *Journal of Geophysical Research: Planets*, 125: e2019JE006306. https://doi.org/10.1029/2019JE006306

Rampe, E. B., Blake, D. F., Bristow, T. F., Ming, D. W., Vaniman, D. T., Morris, R. V., et al. (2020b). Mineralogy and geochemistry of sedimentary rocks and eolian sediments in Gale crater, Mars: A review after six Earth years of exploration with *Curiosity*. *Geochemistry*, 80: 125605. https://doi.org/10.1016/j.chemer.2020.125605

Rapin, W., Chauviré, B., Gabriel, T. S. J., McAdam, A. C., Ehlmann, B. L., Hardgrove, C., et al. (2018). *In situ* analysis of opal in Gale crater, Mars. *Journal of Geophysical Research: Planets*, 123: 1955–1972. https://doi.org/10.1029/2017JE005483

Rice, M. S., Bell III, J. F., Cloutis, E. A., Wang, A., Ruff, S. W., Craig, M. A., et al. (2010). Silica-rich deposits and hydrated minerals at Gusev Crater, Mars: Vis-NIR spectral characterization and regional mapping. *Icarus*, 205(2): 375–395. https://doi.org/10.1016/j.icarus.2009.03.035

Ruff, S. W., Farmer, J. D., Calvin, W. M., Herkenhoff, K. E., Johnson, J. R., Morris, R. V., et al. (2011). Characteristics, distribution, origin, and significance of opaline silica observed by the Spirit rover in Gusev crater, Mars. *Journal of Geophysical Research*, 116: E00F23. https://doi.org/10.1029/2010JE003767

Schmidt, M. E., Perrett, G. M., Bray, S. L., Bradley, N. J., Lee, R. E., Berger, J. A., et al. (2018). Dusty rocks in Gale crater: Assessing areal coverage and separating dust and rock contributions in APXS analyses. *Journal of Geophysical Research: Planets*, 123: 1649–1673. https://doi.org/10.1029/2018JE005553

Sears, V. F. (1992). Neutron scattering lengths and cross sections. *Neutron News*, 3(3): 26–37. https://doi.org/10.1080/10448639208218770

Shen, Y.-H. (1999). Sorption of natural dissolved organic matter on soil. *Chemosphere*, 38(7): 1505-1515. https://doi.org/10.1016/S0045-6535(98)00371-3

Sheng, G., Johnston, C. T., Teppen, B. J., & Boyd, S. A. (2001). Potential contributions of smectite clays and organic matter to pesticide retention in soils. *Journal of Agricultural and Food Chemistry*, 49(6): 2899-2907. https://doi.org/10.1021/jf001485d

Sklute, E. C., Jensen, H. B., Rogers, A. D., & Reeder, R. J. (2015). Morphological, structural, and spectral characteristics of amorphous iron sulfates. *Journal of Geophysical Research: Planets*, 120: 809-830. https://doi.org/10.1002/2014JE004784

Smith, R. J., McLennan, S. M., Achilles, C. N., Dehouck, E., Horgan, B. H. N., Mangold, N., et al. (2021). X-ray amorphous components in sedimentary rocks of Gale crater, Mars: Evidence for ancient formation and long-lived aqueous activity. *Journal of Geophysical Research: Planets*, 126: e2020JE006782. https://doi.org/10.1029/2020JE006782

Smith, R. J., McLennan, S. M., Sutter, B., Rampe, E. B., Dehouck, E., Siebach, K. L., et al. (2022). X-ray amorphous sulfur-bearing phases in sedimentary rocks of Gale crater, Mars. *Journal of Geophysical Research: Planets*, 127: e2021JE007128. https://doi.org/10.1029/2021JE007128

Squyres, S. W., Arvidson, R. E., Ruff, S., Gellert, R., Morris, R. V., Ming, D. W., et al. (2008). Detection of silica-rich deposits on Mars. *Science*, 320(5879): 1063–1067. https://doi.org/10.1126/science.1155429

Stotzky, G. (2000). Persistence and biological activity in soil of insecticidal proteins from *Bacillus thuringiensis* and of bacterial DNA bound on clays and humic acids. *Journal of Environmental Quality*, 29(3): 691-705. https://doi.org/10.2134/jeq2000.00472425002900030003x

Summons, R. E., Amend, J. P., Bish, D., Buick, R., Cody, G. T., Des Marais, D. J., et al. (2011). Preservation of martian organic and environmental records: Final report of the Mars Biosignature Working Group. *Astrobiology*, 11(2): 157–181. https://doi.org/10.1089/ast.2010.0506

Sutter, B., McAdam, A. C., Mahaffy, P. R., Ming, D. W., Edgett, K. S., Rampe, E. B., et al. (2017). Evolved gas analyses of sedimentary rocks and eolian sediment in Gale Crater, Mars: Results of the Curiosity rover's sample analysis at Mars instrument from Yellowknife Bay to the Namib Dune. *Journal of Geophysical Research: Planets*, 122: 2574–2609. https://doi.org/10.1002/2016JE005225

Thomson, B. J., Bridges, N. T., Milliken, R., Baldridge, A., Hook, S. J., Crowley, J. K., et al. (2011). Constraints on the origin and evolution of the layered mound in Gale Crater, Mars using Mars Reconnaissance Orbiter data. *Icarus*, 214: 413–432. https://doi.org/10.1016/j.icarus.2011.05.002

Thorpe, M. T., Bristow, T. F., Rampe, E. B., Tosca, N. J., Grotzinger, J. P., Bennett, C. N., et al. (2022). Mars Science Laboratory CheMin data from the Glen Torridon region and the significance of lake-groundwater interactions in interpreting mineralogy and sedimentary history. *Journal of Geophysical Research: Planets*, 127(11): e2021JE007099. https://doi.org/10.1029/2021JE007099

Tosca, N. J. & Knoll, A. H. (2009). Juvenile chemical sediments and the long term persistence of water at the surface of Mars. *Earth and Planetary Science Letters*, 286(3-4): 379–386. https://doi.org/10.1016/j.epsl.2009.07.004

Treiman, A. H., Bish, D. L., Vaniman, D. T., Chipera, S. J., Blake, D. F., Ming, D. W., et al. (2016). Mineralogy, provenance, and diagenesis of a potassic basaltic sandstone on Mars: CheMin X-ray diffraction of the Windjana sample (Kimberley area, Gale crater). *Journal of Geophysical Research: Planets*, 121: 75-106. https://doi.org/10.1002/2015JE004932

Treiman, A. H., Lanza, N., VanBommel, S., Berger, J., Wiens, R. Bristow, T., et al. (in prep). Manganese-iron phosphate nodules at the Groken site, Gale crater, Mars.

Tu, V. M., Rampe, E. B., Bristow, T. F., Thorpe, M. T., Clark, J. V., Castle, N. (2021). A review of the phyllosilicates in Gale crater as detected by the CheMin instrument on the Mars Science Laboratory, Curiosity rover. *Minerals*, 11(847). https://doi.org/10.3390/min11080847

Tutolo, B. M., Evans, B. W., & Kuehner, S. M. (2019). Serpentine-hisingerite solid solution in altered ferroan peridotite and olivine gabbro. *Minerals*, 9(47). https://doi.org/10.3390/min9010047

Tutolo, B. M. & Tosca, N. J. (2023). Observational constraints on the process and products of Martian serpentization. *Science Advances*, 9(5): eadd8472. https://doi.org/10.1126/sciadv.add8472

Vaniman, D. T., Bish, D. L., Chipera, S. J., Fialips, C. L., Carey, J. W., & Feldman, W. C. (2004). Magnesium sulphate salts and the history of water on Mars. *Nature*, 431: 663-665. https://doi.org/10.1038/nature02973

Vaniman, D. T. & Chipera, S. J. (2006). Transformations of Mg- and Ca-sulfate hydrates in Mars regolith. *American Mineralogist*, 91: 1628-1642. https://doi.org/10.2138/am.2006.2092

Vaniman, D., (2012). Mars Science Laboratory Chemistry & Mineralogy RDR Data V1.0. *NASA Planetary Data System*. https://doi.org/10.17189/1519453

Vaniman, D. T., Bish, D. L., Ming, D. W., Bristow, T. F., Morris, R. V., Blake, D. F., et al. (2014). Mineralogy of a mudstone at Yellowknife Bay, Gale crater, Mars. *Science*, 343(3169). https://doi.org/10.1126/science.1243480

Vaniman, D. T., Martínez, G. M., Rampe, E. B., Bristow, T. F., Blake, D. F., Yen, A. S., et al. (2018). Gypsum, bassanite, and anhydrite at Gale crater, Mars. *American Mineralogist*, 103(7): 1011–1020. https://doi.org/10.2138/am-2018-6346

Varela, M. E., Kurat, G., Bonnin-Mosbah, M., Clocchiatti, R., & Massare, D. (2000). Glass-bearing inclusions in olivine of the Chassigny achondrite: Heterogeneous trapping at sub-igneous temperatures. *Meteoritics & Planetary Science*, 35: 39-52. https://doi.org/10.1111/j.1945-5100.2000.tb01972.x

Wang, A., Freeman, J. J., & Jolliff, B. L. (2009). Phase transition pathways of the hydrates of magnesium sulfate in the temperature range 50°C to 5°C: Implications for sulfates on Mars. *Journal of Geophysical Research*, 114: E04010. https://doi.org/10.1029/2008JE003266

Wang, A. A. & Zhou, Y. H. (2014). Experimental comparison of the pathways and rates of the dehydration of Al-, Fe-, Mg- and Ca-sulfates under Mars relevant conditions. *Icarus*, 234: 162–173. https://doi.org/10.1016/j.icarus.2014.02.003

Wattel-Koekkoek, E. J., Buurman, P., van der Plicht, J., Wattel, E., & van Breeman, N. (2003). Mean residence time of soil organic matter associated with kaolinite and smectite. *European Journal of Soil Science*, 54: 269-278. https://doi.org/10.1046/j.1365-2389.2003.00512.x

Werner, C. J., Armstrong, J., Brown, F. B., Bull, J. S., Casswell, L., Cox, L. J., et al. (2017). MCNP user's manual: Code version 6.2. LA-UR-17-29981.

Xu, W., Tosca, N. J., McLennan, S. M., & Parise, J. B. (2009). Humidity-induced phase transitions of ferric sulfate minerals studied by *in situ* and *ex situ* X-ray diffraction. *American Mineralogist*, 94: 1629-1637. https://doi.org/10.2138/am.2009.3182

Yen, A. S., Ming, D. W., Vaniman, D. T., Gellert, R., Blake, D. F., Morris, R. V., et al. (2017). Multiple stages of aqueous alteration along fractures in mudstone and sandstone strata in Gale Crater, Mars. *Earth and Planetary Science Letters*, 471: 186–198. https://doi.org/10.1016/j.epsl.2017.04.033

CHAPTER 5

CONCLUSIONS

5.1. Primary Conclusions of This Dissertation

In Chapter 1, I described three areas of Mars geology that are poorly understood: The origin of evolved magmatic lithologies, specifically in Gale crater at Marias Pass; the hydration of clay minerals; and the composition of the ubiquitous X-ray amorphous material in Gale crater. In Chapters 2 – 4, I investigated these problems using neutron spectroscopy results from the Mars Science Laboratory (MSL) Dynamic Albedo of Neutrons instrument (DAN) in conjunction with several other MSL and orbital instrument data sets and results.

In Chapter 2, I showed that tridymite-bearing, high-silica material in Marias Pass is part of an extensive volcaniclastic unit at least a meter thick and conformable with surrounding Murray stratigraphy. This material has a very low Σ_{abs} consistent with the high-silica chemistry measured by the Chemistry and Camera instrument (ChemCam) at BK. This material is has relatively low hydration (1.85 ± 0.13 wt.% water-equivalent hydrogen, or WEH), unlike high-silica fracture halos in the unconformably overlying Stimson unit (Gabriel et al., 2022). DAN detections of this high-silica material on the NE and SW sides of Marias Pass predicted that high-silica material was present in central Marias Pass (Figure 5.1b). This area was inaccessible to ChemCam and DAN, but Mast Camera (Mastcam) multispectral results placed it in-family with high-silica material measured by ChemCam. By projecting geologic cross sections from Marias Pass to the NE and SW using the regional dip of the Murray formation, I showed that the high-silica layer is a likely source of the silica in Stimson fracture halos as suggested by Frydenvang et al. (2017) (Figure 5.1c,d), and that Compact Reconnaissance Imaging Spectrometer at Mars (CRISM) hydrated

silica observations several km from Marias Pass (Seelos et al., 2014; Fraeman et al., 2016) also reside along this projected stratigraphic horizon (Figure 5.1e).

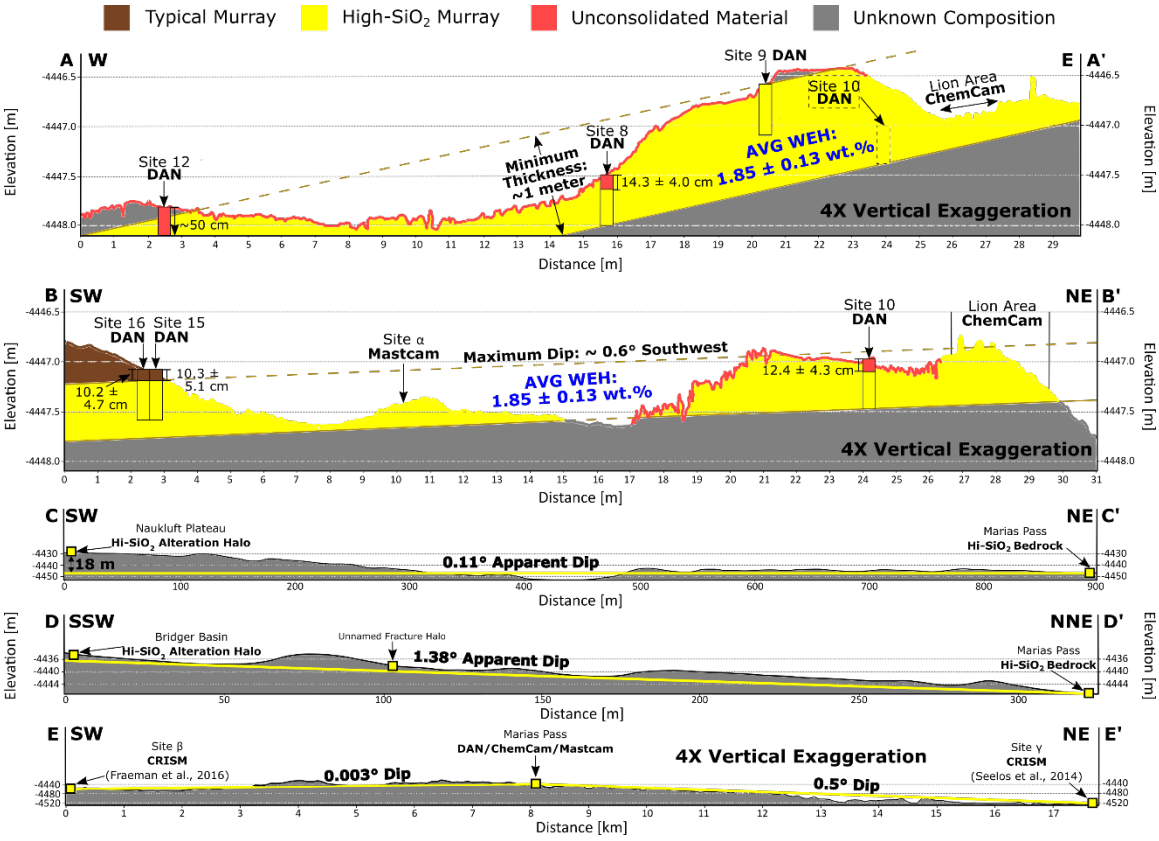

Figure 5.1. Topographic cross sections through Marias Pass. (a) Cross section from Site 12 to the Lion area, 4X vertical exaggeration. One possible high-SiO_2/low-FeO_T layer dip is shown, but the dip component in this direction is not constrained. The minimum thickness of the high-SiO_2/low-FeO_T layer is constrained by DAN results from Sites 8 – 10. Site 10 bedrock (dashed, located about 2 m south of A-A') is projected from its measured elevation. Site 9 is covered by a thin (<5 cm) veneer of sand but was modeled as a single layer to reduce complexity (see Appendix Text A.4). (b) Cross section from Site 16 to the Lion area, 4X vertical exaggeration. Relationships shown here constrain the maximum dip of the high-SiO_2/low-FeO_T layer in this direction. (c, d) Cross sections from Marias Pass to Naukluft Plateau (Lubango fracture alteration halo) and Bridger Basin (Greenhorn fracture alteration halo). The projected apparent dip of the high-SiO_2/low-FeO_T layer, based on a true regional dip of 3° northwest (Kite et al., 2013; Lewis & Turner, 2019) is 0.11° and 1.38° from Marias Pass to Lubango and Greenhorn, respectively. This places the high-SiO_2/low-FeO_T layer ~18 m below Lubango, ~2 m below Greenhorn, and ~1.5 m below an unnamed alteration halo. These vertical proximities support the hypothesis that the high-SiO_2/low-FeO_T bedrock was a source for the SiO_2 enrichment of the overlying alteration halos. (e) Cross section passing through Marias Pass and CRISM hydrated SiO_2 detections (Fraeman et al., 2016; Seelos et al., 2014), 4X vertical exaggeration. <0.5° dips are required for stratigraphic equivalence between Marias Pass and Sites β and γ, consistent with a 3° regional dip to the NW.

DAN was invaluable for mapping the extent of this high-silica layer because although it was only measured at the surface in a small area around the BK drill site, it was shallowly buried within the DAN sensing depth over a larger area in Marias Pass (Figure 5.1a,b). The low hydration of this material is a key piece of evidence that the abundant amorphous silica is not primarily opal-A like the silica-rich Stimson fracture halos (Rapin et al., 2018). Rather, its orientation and hydration indicate that it is a rhyolitic glass-rich deposit sourced from an evolved volcanic material and deposited in the lacustrine Murray succession. This conclusion is also supported by my work in Chapter 4, where I showed that the BK sample from this high-silica layer contains much more rhyolitic glass than opal-A.

In Chapter 3, I presented results for DAN active and passive measurements in Vera Rubin ridge (VRR) and Glen Torridon (GT). VRR samples have lower clay mineral abundances than GT, and VRR contains ferripyrophyllite (Rampe et al., 2020a), a non-expandable clay mineral, whereas GT contains nontronite (Thorpe et al., 2022), an expandable clay mineral that can accommodate water in interlayer sites. So the water capacity of clay minerals in GT is much greater than in VRR. This is reflected in my DAN active results (Figure 5.2b) which show significantly higher mean hydration in GT (3.9 ± 0.1 wt.% WEH) than in VRR (3.0 ± 0.1 wt.% WEH). DAN passive results from this region are consistent with this trend, showing increased thermal neutron counts in GT compared to VRR. CRISM spectral parameter maps originally identified GT as a clay-bearing unit based on the 2.3 μm absorption diagnostic of clay minerals (Milliken et al., 2010; Fraeman et al., 2016). CRISM also shows a small, but significant, increase in the mean 3.0 μm hydration index (He et al., 2022) for GT (0.476 ± 0.002 BDI) compared to VRR (0.471 ± 0.002 BDI).

By classifying CRISM pixels in VRR and GT into 'regolith' and 'bedrock' categories, I found a distinct bias toward greater mean 3.0 μm hydration in regolith

pixels (0.480 ± 0.001 BDI) compared to bedrock pixels (0.465 ± 0.001 BDI) (Figure 5.2a), indicating that the regolith is either more hydrated than the bedrock or has a different grain size texture. In contrast, the mean DAN WEH of regolith pixels (3.5 ± 0.1 wt.% WEH) is indistinguishable from that of bedrock pixels (3.5 ± 0.1 wt.% WEH), indicating that the regolith is not thick and most of the DAN field of view (FOV) contains bedrock. I plotted DAN WEH vs. CRISM 3.0 μm BDI for the unbiased bedrock pixels, but did not find a significant correlation, possibly due to the granularity of the regolith vs. bedrock classification scheme.

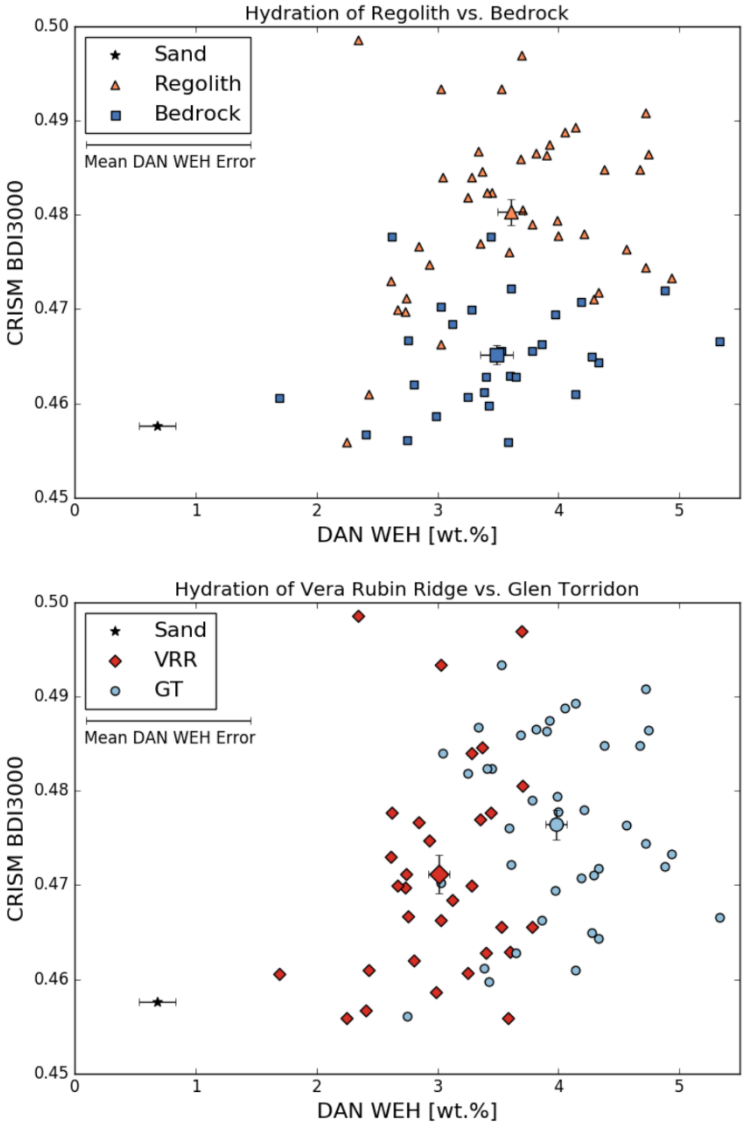

Figure 5.2. DAN-derived WEH vs. CRISM 3 μm BDI symbolized by surface cover (top) and geomorphic region (bottom). The same data are shown in both plots, only the classification scheme differs. CRISM pixels classified as "regolith" are primarily pebble-sized or smaller surface cover, whereas "bedrock" pixels are primarily exposed bedrock. A representative error bar on each plot shows the mean DAN WEH error. One data point from a previous DAN measurement of a sand dune (Gabriel et al., 2018) is included for reference. Mean values are larger points with error bars representing standard deviation of the mean. Regolith pixels have distinctly enhanced 3 μm BDI compared to bedrock pixels (top); and WEH is generally lower on VRR than in GT (bottom).

Chemistry and Mineralogy instrument (CheMin) results from Gale crater samples have shown that clay minerals are consistently collapsed (e.g., Rampe et al., 2020b). But my DAN-derived results from GT, in comparison to VRR, suggest the possibility that expandable clay minerals may be hydrated in the subsurface prior to MSL sample acquisition and handling. This highlights the importance of neutron spectroscopy for measuring the undisturbed, *in situ* bulk hydration of ancient materials. These results also motivate the investigation of clay mineral hydration throughout Gale crater.

In Chapter 4, I developed a method to constrain clay mineral hydration as well as the abundances of candidate amorphous phases in Gale crater samples. Starting with DAN bulk WEH, I subtracted WEH contributions from hydrated crystalline phases to determine the hydration of the amorphous fraction plus "excess" WEH for each sample. CheMin and the Alpha-Particle X-ray Spectrometer (APXS) provide the amorphous fraction chemistry in the literature (Vaniman et al., 2014; Rampe et al., 2017; Bristow et al., 2018; Rampe et al., 2020a; Thorpe et al., 2022). With the amorphous hydration and chemistry, I was able to model 10k good-fit amorphous phase compositions that consist of volcanic or impact glass, Fe- and Mg-sulfates, opal-A, allophane, hisingerite, and ferrihydrite, plus "excess" WEH, Na, Mg, K, and Ca.

I found a strong correlation between smectite abundance and modeled "excess" WEH in Gale crater smectite-bearing samples (Figure 5.3, $r^2 = 0.60$). This result indicates that smectites in Gale crater are hydrated (although only at the equivalent of ~0.2 H_2O per formula unit) and that organics measured by the Sample Analysis at Mars instrument are likely bound to clay minerals through hydroxyl (Lutzow et al., 2006; Keil & Mayer, 2014) or waters of hydration (Sheng et al., 2001). Similar strong correlations between clay minerals and modeled "excess"

monovalent cations (Figure 5.4a, r^2 = 0.75) as well as modeled "excess" divalent cations (Figure 5.4b, r^2 = 0.59) indicate that organics may be primarily bound through cation bridging as on Earth (Keil & Mayer, 2014).

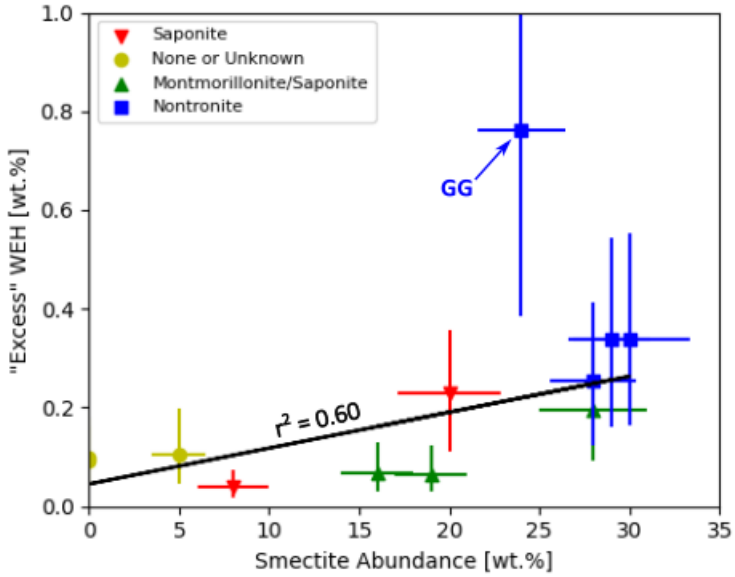

Figure 5.3. Plot of smectite abundance vs. modeled "excess" WEH. The correlation shown here is strong (r^2 = 0.60) when the GG high "excess" WEH outlier is removed. "Excess" WEH error bars extend from Q_1 to Q_3. Samples with ferripyrophyllite are not included.

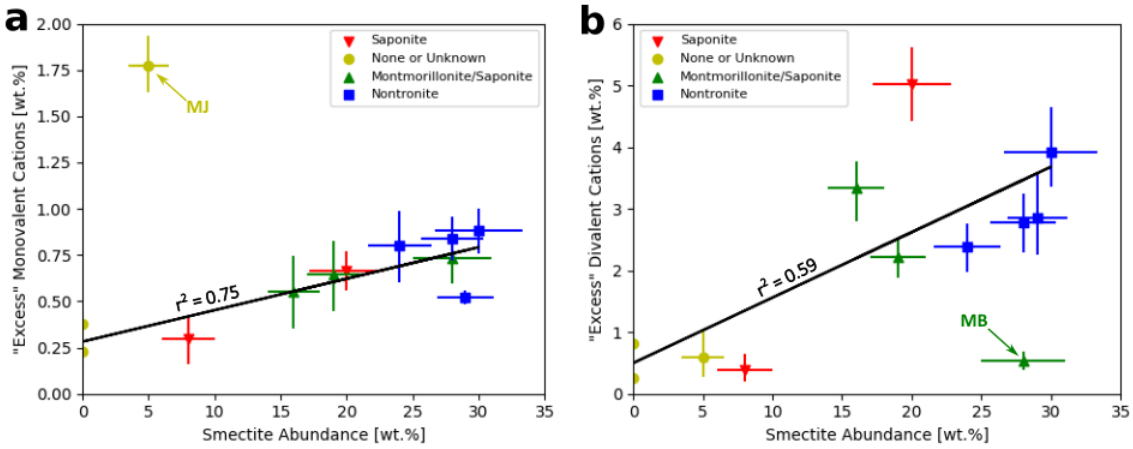

Figure 5.4. Plots of smectite abundance vs. (a) modeled monovalent cations (Na + K) and (b) modeled divalent cations (Mg + Ca). For monovalent cations the best-fit line (r^2 = 0.75) does not include the MJ outlier and for divalent cations the best-fit line (r^2 = 0.59) does not include the MB outlier. "Excess" cation error bars extend from Q_1 to Q_3. Samples with ferripyrophyllite are not included.

The persistence of amorphous sulfates, opal-A, and glass, and low abundances of allophane and ferrihydrite in Gale crater indicate low syn- and post-depositional water-rock interactions, in agreement with previous studies of Gale

crater (McLennan et al., 2019; Rampe et al., 2020b; Smith et al., 2021). Additionally, increased abundances of sulfates and glass upsection indicate increasingly oxidizing environments, also in agreement with previous studies (e.g., Tu et al., 2021).

5.2. Future Applications of the Methods Used in This Dissertation

The amorphous component analysis code I developed in Chapter 4 is a widely applicable technique for neutron spectroscopy in planetary science. Some of the Gale crater samples with the most modeled "excess" WEH contain the non-expandable clay mineral ferripyrophyllite (Bristow et al., 2018; Rampe et al., 2020a). The large modeled opal-A abundances in these samples suggest that the opal-A hydration used in my models (6.3 ± 1.8 wt.% WEH) may not be representative of all Gale crater samples. In a future study, I will modify the code to allow variable opal-A hydration for the TP, BK, OU, ST, and HF samples in the Murray formation and the opal-rich Stimson fracture halo samples GH and LB. Several different processes can form opal-A, and hydration may inform the characteristics of its formation in these samples.

Above GT, samples analyzed by CheMin show steadily decreasing and finally absent clay minerals (Vaniman, 2012) in a region where CRISM spectra show a change from clay-rich mineralogy to sulfate-rich mineralogy (e.g., Fraeman et al., 2016) and where CheMin has detected crystalline sulfates for the first time in the "Canaima" drill sample (Chipera et al., submitted). This clay-to-sulfate transition represents a major change from a wetter environment to a dryer environment, and increasing abundances of amorphous sulfates upsection may indicate the start of this trend. This is another opportunity to use a modified version of the amorphous component analysis code developed in Chapter 4 for samples in this transition region. Properly modified, this code could not only constrain abundances of Fe- and

Mg-sulfates, but potentially their hydration as well, similar to the proposed opal-A study above.

This year I begin a postdoc appointment at Los Alamos National Laboratory. In addition to working on the above projects, a portion of my research funding will be to develop an active neutron spectroscopy laboratory method for returned samples like those from the Mars Sample Return (MSR) program. These samples are already being gathered by the NASA Mars 2020 rover, Perseverance in Jezero crater. Because the bulk hydration of these samples has not been determined (Perseverance does not have a neutron spectrometer, NS), it is important to assess the WEH content and distribution of these samples prior to unsealing them on Earth. The techniques and results in this dissertation show the value of bulk hydration as a constraint in a variety of geologic investigations. The diverse science instruments and techniques available on Earth only enhances the impact that active neutron spectroscopy results will have for MSR.

5.3. Recommended Improvements for Planetary Neutron Spectroscopy

Planetary neutron spectroscopy is at a turning point that began with the development of MSL over a decade ago. The DAN instrument is the first active NS on a planetary science mission, and this dissertation has demonstrated the utility of active NS. DAN has the unique ability to sense hydrogen and neutron absorbers like Fe, Cl, B, Mn, etc. Using appropriate models, DAN can also determine their depth distributions. In addition, my work demonstrated the benefits of coordinated data sets such as ChemCam, APXS, CheMin, Mastcam, and CRISM to the interpretation of DAN results. But determining subsurface hydration with active NS could benefit greatly from some additional instrument subsystems.

In Chapter 1, I used ChemCam and APXS chemistry in MCNP6 simulations to set the Σ_{abs} of one layer in two-layer models. This still involves an assumption that

the ChemCam/APXS chemistry from a thin (≤ 6 cm) upper layer is representative of a layer up to 10 cm or more thick. A more robust technique would be to model subsurface Σ_{abs} using chemical abundances that are measured from the entire DAN subsurface sensing depth. To accomplish this, future active NS should be paired with gamma-ray spectrometers (GRS). GRS coordinates well with active NS because neutron scattering and absorption reactions with a subsurface nucleus also produce characteristic gamma-rays for that element (e.g., Boynton et al., 2004). These gamma-rays are a byproduct of normal DAN active operations (PNG pulsing), but because Curiosity does not carry a GRS, this potential geochemical data is not collected. Bulk subsurface geochemistry would have value not just for DAN active simulations, but for many other science investigations, in the same way that ChemCam/APXS surface and shallow subsurface chemistry is used now.

DAN includes two He-3 neutron detectors so that it can effectively measure thermal and epithermal neutrons. But a fast (high-energy) neutron detector would also be useful for DAN data analysis. The DAN PNG output is reduced over time as the abundance of the radioactive tritium in the PNG decays. Because DAN does not include a fast neutron detector to measure the PNG output of 14.1 MeV neutrons directly, we cannot accurately simulate the PNG production rate in MCNP6 simulations. Instead we simulate enough neutron histories to ensure good SNR in the simulated data (typically 2.5×10^9 neutron histories) and then normalize the area under the curve to the area under the DAN die-away curve for comparison. This allows us to compare relative count rates in the die-away time bins, but we cannot compare absolute simulated count rates to absolute DAN count rates. This also prevents direct comparison of one DAN active die-away curve to another, especially from measurements taken years apart when the PNG output was significantly different (e.g., the early part of the mission to the present day). These limitations

make DAN active data analysis more complicated and computationally intensive than would otherwise be necessary and delays the derivation of results. On a roving platform with many science priorities such as MSL, the longer it takes to produce results, the less useful the instrument is for tactical operations in the nominal planning cycle (3 – 5 tactical plans per week).

Fast neutron detectors have been used with thermal and epithermal neutron detectors on other missions. For example, the Mars Odyssey orbital spacecraft includes a High-Energy Neutron Detector (HEND; Boynton et al., 2004; a subsystem of an instrument suite that also includes the MONS thermal and epithermal neutron detectors as well as a GRS). HEND is shielded from detections of thermal neutrons in the same way as one of the DAN detectors, i.e., it is coated in a thin layer of cadmium, which very efficiently absorbs thermal neutrons below ~0.4 eV. HEND includes three He-3 neutron detectors coated in cadmium with various thicknesses of a polyethylene moderator between the cadmium coating and the He-3 detection volume. Thicker polyethylene reduces neutron energy more, and therefore changes the neutron energy range each detector is most sensitive to. The appropriate polyethylene thickness can effectively select the neutron energy range of interest for a specific instrument or mission.

The addition of a fast neutron detector and GRS to a DAN-like instrument suite with thermal and epithermal detectors and a PNG would add a great deal of science value and allow for a full elemental and hydration characterization of the layered near subsurface environment in detailed geologic studies that can also add value on a tactical timeline for a roving platform like MSL. The NASA Dragonfly helicopter mission to Titan, planned for launch in 2027, will include the Dragonfly Gamma-ray and Neutron Spectrometer (DraGNS; Lawrence et al., 2022) with a PNG, GRS, and thermal, epithermal, and fast neutron detectors. By utilizing the active

neutron spectrometer die-away technique, DraGNS would be capable of similarly detailed investigations as those demonstrated in this dissertation, but in the very different surface environment of Titan. Because DraGNS also includes a GRS and fast neutron detector, the enhancements in data analysis and results discussed in this section can also be applied.

At the start of my PhD six years ago, the focus of most planetary NS publications was reporting water abundances, the original and primary use case for these instruments. Our group at ASU is shifting the focus of NS from quantifying water to using derived water and neutron absorber abundances to answer a broad range of geologic questions. With the increasing frequency of planetary surface missions, instruments like DAN can make significant contributions to the geology of not only Mars, but wherever we may rove.

REFERENCES

Abercrombie, S. P., Menzies, A., Abarca, H. E., Luo, V. X., Samochina, S., Trautman, M. T., et al. (2019). Multi-platform immersive visualization of planetary, asteroid, and terrestrial analog terrain. *Lunar and Planetary Science L*: 2268.

Achilles, C. N., Downs, R. T., Ming, D. W., Rampe, E. B., Morris, R. V., Treiman, A. H., et al. (2017). Mineralogy of an active eolian sediment from the Namib dune, Gale crater, Mars. *Journal of Geophysical Research: Planets*, 122: 2344-2361. https://doi.org/10.1002/2017JE005262

Achilles, C. N., Rampe, E. B., Downs, R. T., Bristow, T. F., Ming, D. W., Morris, R. V., et al. (2020). Evidence for multiple diagenetic episodes in ancient fluvial-lacustrine sedimentary rocks in Gale crater, Mars. *Journal of Geophysical Research: Planets*, 125: e2019JE006295. https://doi.org/10.1029/2019JE006295

Agee, C. B., Wilson, N. V., McCubbin, F. M., Ziegler, K., Polyak, V. J., Sharp, Z. D., et al. (2013). Unique meteorite from early Amazonian Mars: Water-rich basaltic breccia Northwest Africa 7034. *Science*, 339: 780–785. https://doi.org/10.1126/science.1228858

Amador, E. S., Bandfield, J. L., & Thomas, N. H. (2018). A search for minerals associated with serpentization across Mars using CRISM spectral data. *Icarus*, 311: 113-134. https://doi.org/10.1016/j.icarus.2018.03.021

Anderson, R. B. & Bell III, J. F. (2010). Geologic mapping and characterization of Gale crater and implications for its potential as a Mars Science Laboratory landing site. *Mars*, 5: 76-128. https://doi.org/10.1555/mars.2010.0004

Arvidson, R. E., Bell, J. F., III, Catalano, J. G., Clark, B. C., Fox, V. K., Gellert, R., et al. (2015). Mars Reconnaissance Orbiter and Opportunity observations of the Burns formation: Crater hopping at Meridiani Planum. *Journal of Geophysical Research: Planets*, 120: 429–451. https://doi.org/10.1002/2014JE004686

Bandfield, J. L., Hamilton, V. E., & Christensen, P. R. (2000). A global view of Martian surface compositions from MGS-TES. *Science*, 287(5458): 1626–1630. https://doi.org/10.1126/science.287.5458.1626

Banham, S. G., Gupta, S., Rubin, D. M., Watkins, J. A., Sumner, D. Y., Edgett, K. S., et al. (2018). Ancient Martian aeolian processes and palaeomorphology reconstructed from the Stimson formation on the lower slope of Aeolis Mons, Gale crater, Mars. *Sedimentology*, 65(4): 993–1042. https://doi.org/10.1111/sed.12469

Bedford, C. C., Bridges, J. C., Schwenzer, S. P., Wiens, R. C., Rampe, E. B., Frydenvang, J., & Gasda, P. J. (2019). Alteration trends and geochemical source region characteristics preserved in the fluviolacustrine sedimentary record of Gale crater, Mars. *Geochimica et Cosmochimica Acta*, 246: 234–266. https://doi.org/10.1016/j.gca.2018.11.031

Bell III, J. F., Godber, A., McNair, S., Caplinger, M. A., Maki, J. N., Lemmon, M. T., et al. (2017). The Mars Science Laboratory Curiosity rover Mastcam instruments: Preflight and in-flight calibration, validation, and data archiving. *Earth and Space Science*, 4(7): 396–452. https://doi.org/10.1002/2016EA000219

Bish, D. L., Carey, J. W., Vaniman, D. T., Chipera, S. J. (2003). Stability of hydrous minerals on the martian surface. *Icarus*, 164: 96-103. https://doi.org/10.1016/S0019-1035(03)00140-4

Bish, D. L., Blake, D. F., Vaniman, D. T., Chipera, S. J., Morris, R. V., Ming, D. W., et al. (2013). X-ray diffraction results from Mars Science Laboratory: Mineralogy of Rocknest at Gale crater. *Science*, 341(6153): 1238932-1. https://doi.org/10.1126/science.1238932

Blake, D., Vaniman, D., Achilles, C., Anderson, R., Bish, D., Bristow, T. (2012). Characterization and calibration of the CheMin mineralogical instrument on Mars Science Laboratory. *Space Science Reviews*, 170: 341-399. https://doi.org/10.1007/s11214-012-9905-1

Bouska, V. & Bell III, J. F. (1993). Assumptions about the presence of natural glasses on Mars. *Journal of Geophysical Research*, 98(E10): 18,719–18,725. https://doi.org/10.1029/93JE01959

Boynton, W. V., Feldman, W. C., Mitrofanov, I. G., Evans, L. G., Reedy, R. C., Squyres, S. W., et al. (2004). The Mars Odyssey Gamma-ray Spectrometer instrument suite. *Space Science Reviews*, 110: 37-83. https://doi.org/10.1023/B:SPAC.0000021007.76126.15

Bridges, J. C., Schwenzer, S. P., Leveille, R., Westall, F., Wiens, R. C., Mangold, N. (2015). Diagenesis and clay mineral formation at Gale crater, Mars. *Journal of Geophysical Research: Planets*, 120: 1-19. https://doi.org/10.1002/2014JE004757

Bristow, T. F., Bish, D. L., Vaniman, D. T., Morris, R. V., Blake, D. F., Grotzinger, J. P., et al. (2015). The origin and implications of clay minerals from Yellowknife Bay, Gale crater, Mars. *American Mineralogist*, 100(4): 824–836. https://doi.org/10.2138/am-2015-5077CCBYNCND

Bristow, T. F., Rampe, E. B., Achilles, C. N., Blake, D. F., Chipera, P. C., Craig, P., et al. (2018). Clay mineral diversity and abundance in sedimentary rocks of Gale crater, Mars. *Science Advances*, 4(6): eaar3330. https://doi.org/10.1126/sciadv.aar3330

Broz, A. P. (2020). Organic matter preservation in ancient soils of Earth and Mars. *Life*, 10(113). https://doi.org/10.3390/life10070113

Calef III, F. & Parker, T. (2016). MSL Gale merged orthophoto mosaic. *PDS Annex*, U.S. Geological Survey.

Campbell, J. L., Perrett, G. M., Gellert, R., Andrushenko, S. M., Boyd, N. I., Maxwell, J. A., et al. (2012). Calibration of the Mars Science Laboratory Alpha Particle X-ray Spectrometer. *Space Science Reviews*, 170: 319-340. https://doi.org/10.1007/s11214-012-9873-5

Campbell, J. L., King, P. L., Burkemper, L., Berger, J. A., Gellert, R., Boyd, N. I., et al. (2014). The Mars Science Laboratory APXS calibration target: Comparison of Martian measurements with the terrestrial calibration. *Nuclear Instruments and Methods in Physics Research B*, 323: 49–58. https://doi.org/10.1016/j.nimb.2014.01.011

Carter, J. & Poulet, F. (2013). Ancient plutonic processes on Mars inferred from the detection of possible anorthositic terrains. *Nature Geoscience*, 6: 1008–1012. https://doi.org/10.1038/NGEO1995

Chipera, S. J. & Bish, D. L. (2002). FULLPAT: A full-pattern quantitative analysis program for X-ray powder diffraction using measured and calculated patterns. *Journal of Applied Crystallography*, 35: 744-749. https://doi.org/10.1107/S0021889802017405

Chipera, S. J. & Bish, D. L. (2013). Fitting full X-ray diffraction patterns for quantitative analysis: A method for readily quantifying crystalline and disordered phases. *Advances in Materials Physics and Chemistry*, 3(1A): 30340. https://doi.org/10.4236/ampc.2013.31A007

Chipera, S. J., Vaniman, D. T., Rampe, E. B., Bristow, T. F., Martinez, G., Tu, V. M., et al. (submitted). Mineralogical investigation of Mg-sulfate at the Canaima drill site, Gale crater, Mars. *Journal of Geophysical Research: Planets*.

Christensen, P. R., McSween Jr., H. Y., Bandfield, J. L., Ruff, S. W., Rogers, A. D., Hamilton, V. E., et al. (2005). Evidence for magmatic evolution and diversity on Mars from infrared observations. *Nature*, 436: 504–509. https://doi.org/10.1038/nature03639

Clague, D. A. & Sherrod, D. R. (2014). Growth and degradation of Hawaiian volcanoes. *U.S. Geological Survey Professional Paper*, 1801: 97–146.

Clark, R. N., King, T. V. V., Klejwa, M., & Swayze, G. A. (1990). High spectral resolution reflectance spectroscopy of minerals. *Journal of Geophysical Research*, 95(B8): 12,653–12,680. https://doi.org/10.1029/JB095iB08p12653

Clegg, S. M., Wiens, R. C., Anderson, R., Forni, O., Frydenvang, J., Lasue, J., et al. (2017). Recalibration of the Mars Science Laboratory ChemCam instrument with an expanded geochemical database. *Spectrochimica Acta Part B: Atomic Spectroscopy*, 129: 64–85. https://doi.org/10.1016/j.sab.2016.12.003

Cohen, B. A., Malespin, C. A., Farley, K. A., Martin, P. E., Cho, Y., & Mahaffy, P. R. (2019). *In situ* geochronology on Mars and the development of future instrumentation. *Astrobiology*, 19(11): 1303-1314. https://doi.org/10.1089/ast.2018.1871

Costa, D., Tougerti, A., Tielens, F., Gervais, C., Stievano, L., & Lambert, J. F. (2008). *Physical Chemistry Chemical Physics*, 10: 6360-6368. https://doi.org/10.1016/10.1039/b806501b

Cousin, A., Sautter, V., Payré, V., Forni, O., Mangold, N., Gasnault, O., et al. (2017). Classification of igneous rocks analyzed by ChemCam at Gale crater, Mars. *Icarus*, 288: 265–283. https://doi.org/10.1016/j.icarus.2017.01.014

Crisp, J. A., Adler, M., Matijevic, J. R., Squyres, S. W., Arvidson, R. E., & Kass, D. M. (2003). Mars Exploration Rover mission. *Journal of Geophysical Research*, 108(E12): 8061. https://doi.org/10.1029/2002JE002038

Czarnecki, S., Hardgrove, C., Gasda, P. J., Gabriel, T. S. J., Starr, M., Rice, M., et al. (2020). Identification and description of a silicic volcaniclastic layer in Gale crater, Mars, using active neutron interrogation. *Journal of Geophysical Research: Planets*, 125, e2019JE006180. https://doi.org/10.1029/2019JE006180

Czarnecki, S. Hardgrove, C., Arvidson, R. E., Hughes, M. N., Schmidt, M. E., Henley, T., et al. (2022). "Hydration of a clay-rich unit on Mars, comparison of orbital data to rover data" supplementary data (Version 2). *Zenodo*. https://doi.org/10.5281/ZENODO.7255705

Czarnecki, S., Hardgrove, C., Arvidson, R. E., Hughes, M. N., Schmidt, M. E., Henley, T., et al. (2023a). Hydration of a clay-rich unit on Mars, comparison of orbital data to rover data. *Journal of Geophysical Research: Planets*, 128: e2021JE007104. https://doi.org/10.1029/2021JE007104

Czarnecki, S., Hardgrove, C., Rampe, E. B., & Gasda, P. J. (2023b). "Constraining the hydration of clay minerals and abundances of amorphous phases in Gale crater, Mars" supplementary information (Version 1). *Zenodo*. https://doi.org/10.5281/zenodo.8136072

Das, D., Gasda, P. J., Wiens, R. C., Berlo, K., Leveille, R. J., Frydenvang, J., et al. (2020). Boron and lithium in calcium sulfate veins: Tracking precipitation of diagenetic materials in Vera Rubin ridge, Gale crater. *Journal of Geophysical Research: Planets*, 125(8): e2019JE006301. https://doi.org/10.1029/2019JE006301

David, G., Dehouck, E., Meslin, P.-Y., Rapin, W., Cousin, A., Forni, O., et al. (2022). Evidence for amorphous sulfates as the main carrier of soil hydration in Gale crater, Mars. *Geophysical Research Letters*, 49: e2022GL098755. https://doi.org/10.1029/2022GL098755

Dehouck, E., McLennan, S. M., Meslin, P.-Y., & Cousin, A. (2014). Constraints on abundance, composition, and nature of X-ray amorphous components of soils and rocks at Gale crater, Mars. *Journal of Geophysical Research: Planets*, 119: 2640-2657. https://doi.org/10.1002/2014JE004716

Dimitracopoulos, F. D., Newsom, H. E., Gasda, P. J., Meslin, P. Y., Cerrato, J. M., Crossey, L. J., et al. (2023). Laboratory analyses for adsorption experiments of phosphoric acid species and phosphate rock standards for P characterization on Mars by ChemCam. *Lunar and Planetary Science LIV*: 2323.

Dontsova, K. M. & Bigham, J. M. (2005). Anionic polysaccharide sorption by clay minerals. *Soil Science of America Journal*, 69: 1026-1035. https://doi.org/10.2136/sssaj2004.0203

dos Santos, R., Patel, M., Cuadros, J., & Martins, Z. (2016). Influence of mineralogy on the preservation of amino acids under simulated Mars conditions. *Icarus*, 277: 342-353. http://doi.org/10.1016/j.icarus.2016.05.029

Edgett, K. S., Yingst, R. A., Ravine, M. A., Caplinger, M. A., Maki, J. N., Ghaemi, F. T., et al. (2012). Curiosity's Mars Hand Lens Imager (MAHLI) investigation. *Space Science Reviews*, 170: 259-317. https://doi.org/10.1007/s11214-012-9910-4

Edgett, K. S. (2013). MSL Mars hand lens imager 4 RDR image v1.0. *NASA Planetary Data System*. https://doi.org/10.17189/1520292

Edwards, P. H., Bridges, J. C., Wiens, R., Anderson, R., Dyar, D., Fisk, M., et al. (2017). Basalt-trachybasalt samples in Gale Crater, Mars. *Meteoritics & Planetary Science*, 52(11): 2391–2410. https://doi.org/10.1111/maps.12953

Ehlmann, B. L., Mustard, J. F., Fassett, C. I., Schon, S. C., Head III, J. W., Des Marais, D. J., et al. (2008). Clay minerals in delta deposits and organic preservation potential on Mars. *Nature Geoscience*, 1: 355-358. https://doi.org/10.1038/ngeo207

Ehlmann, B. L., Anderson, F. S., Andrews-Hanna, J., Catling, D. C., Christensen, P. R., Cohen, B. A., et al. (2016). The sustainability of habitability on terrestrial planets: Insights, questions, and needed measurements from Mars for understanding the evolution of Earth-like worlds. *Journal of Geophysical Research: Planets*, 121: 1927-1961. https://doi.org/10.1002/2016JE005134

Eigenbrode, J. L., Summons, R. E., Steele, A., Freissinet, C., Millan, M., Navarro-Gonález, R., et al. (2018). *Science*, 360(6393): 1096-1101. https://doi.org/10.1126/science.aas9185

Evans, B. W., Kuehner, S. M., Joswiak, D. J., & Cressey, G. (2017). Serpentine, iron-rich phyllosilicates and fayalite produced by hydration and Mg depletion of peridotite, Duluth complex, Minnesota, USA. *Journal of Petrology*. 58(3): 495-512. https://doi.org/10.1093/petrology/egx024

Farmer, J. D. & Des Marais, D. J. (1999). Exploring for a record of ancient Martian life. *Journal of Geophysical Research*, 104(E11): 26977-26995. https://doi.org/10.1029/1998je000540

Fedo, C., Grotzinger, J., Gupta, S., Stein, N. T., Watkins, J., Banham, S., et al. (2017). Facies Analysis and Basin Architecture of the Upper Part of the Murray Formation, Gale Crater, Mars. *Lunar and Planetary Science XLVIII*: 1689.

Fedo, C. M., Bryk, A. B., Edgar, L. A., Bennett, K. A., Fox, V. K., Dietrich, W. E., et al. (2022). Geology and stratigraphic correlation of the Murray and Carolyn Shoemaker formations across the Glen Torridon region, Gale crater, Mars. *Journal of Geophysical Research: Planets*, 127(9): e2022JE007408. https://doi.org/10.1029/2022JE007408

Feldman, W. C., Maurice, S., Binder, A. B., Barraclough, B. L., Elphic, R. C., & Lawrence, D. J. (1998). Fluxes of fast and epithermal neutrons from Lunar Prospector: Evidence for water ice at the lunar poles. *Science*, 281(5382): 1496-1500.

Feldman, W. C., Prettyman, T. H., Maurice, S., Plaut, J. J., Bish, D. L., Vaniman, D. T., et al. (2004). Global distribution of near-surface hydrogen on Mars. *Journal of Geophysical Research: Planets*, 109(E9): E09006. https://doi.org/10.1029/2003JE002160

Filiberto, J., Treiman, A. H., & Le, L. (2008). Crystallization experiments on a Gusev Adirondack basalt composition. *Meteoritics & Planetary Science*, 43(7): 1137-1146. https://doi.org/10.1111/j.1945-5100.2008.tb01118.x

Fiorito, T. M., Icoz, I., & Stotzky, G. (2008). Adsorption and binding of the transgenic plant proteins, human serum albumin, *β*-glucuronidase, and Cry3Bb1, on montmorillonite and kaolinite: Microbial utilization and enzymatic activity of free and clay-bound proteins. *Applied Clay Science*, 39: 142-150. https://doi.org/10.1016/j.clay.2007.07.006

Foley, C. N., Economou, T. E., & Clayton, R. N. (2003) Final chemical results from the Mars Pathfinder alpha proton X-ray spectrometer. *Journal of Geophysical Research*, 108(8095): https://doi.org/10.1029/2002JE002018

Foreman-Mackey, D. (2013). corner.py: Scatterplot matrices in Python. *The Journal of Open Source Software*, 1(2). https://doi.org/10.21105/joss.00024

Foreman-Mackey, D., Hogg, D. W., Lang, D., & Goodman, J. (2013). Emcee: The MCMC Hammer. *Publications of the Astronomical Society of the Pacific*, 125(925): 306–312. https://doi.org/10.1086/670067

Fraeman, A. A., Ehlmann, B. L., Arvidson, R. E., Edwards, C. S., Grotzinger, J. P., & Milliken, R. E. (2016). The stratigraphy and evolution of lower Mount Sharp from spectral, morphological, and thermophysical orbital data sets. *Journal of Geophysical Research: Planets*, 121: 1713–1736. https://doi.org/10.1002/2016JE005095

Fraeman, A. A., Edgar, L. A., Rampe, E. B., Thompson, L. M., Frydenvang, J., Fedo, C. M., et al. (2020). Evidence for a diagenetic origin of Vera Rubin ridge, Gale crater, Mars: Summary and synthesis of Curiosity's exploration campaign. *Journal of Geophysical Research: Planets*, 125: e2020JE006527. https://doi.org/10.1029/2020JE006527

Frydenvang, J., Gasda, P. J., Hurowitz, J. A., Grotzinger, J. P., Wiens, R. C., Newsom, H. E., et al. (2017). Diagenetic silica enrichment and late-stage groundwater activity in Gale crater, Mars. *Geophysical Research Letters*, 44: 4716–4724. https://doi.org/10.1002/2017GL073323

Gabriel, T. S. J, Hardgrove, C., Czarnecki, S., Rampe, E. B., Rapin, W., Achilles, C. N., et al. (2018). Water abundance of dunes in Gale Crater, Mars from active neutron experiments & implications for amorphous phases. *Geophysical Research Letters*, 45, 12,766–12,775. https://doi.org/10.1029/2018GL079045

Gabriel, T. S. J., Hardgrove, C., Achilles, C. N., Rampe, E. B., Rapin, W. N., Nowicki, S., et al. (2022). On an extensive late hydrologic event in Gale crater as indicated by water-rich fracture halos. *Journal of Geophysical Research: Planets*, 127: e2020JE006600. https://doi.org/10.1029/2020JE006600

Gasda, P. J., DeLapp, D. M., Mcinroy, R. E., Wiens, R. C., Bridges, J. C., Edwards, P. H., et al. (2016). Identification of fresh feldspars in Gale Crater using ChemCam. *Lunar and Planetary Science XLVII*: 1604.

Gasda, P. J., Haldeman, E. B., Wiens, R. C., Rapin, W., Bristow, T. F., Bridges, J. C., et al. (2017). *In situ* detection of boron by ChemCam on Mars. *Geophysical Research Letters*, 44(17): 8739-8748. https://doi.org/10.1002/2017GL074480

Gasda, P. J., Comellas, J., Essunfeld, A., Das, D., Bryk, A. B., Dehouck, E., et al. (2022). Overview of the morphology and chemistry of diagenetic features in the clay-rich Glen Torridon unit of Gale crater, Mars. *Journal of Geophysical Research: Planets*, 127: e2021JE007097. https://doi.org/10.1029/2021JE007097

Glotch, T. D., Bandfield, J. L., Christensen, P. R., Calvin, W. M., McLennan, S. M., Clark, B. C., et al. (2006). Mineralogy of the light-toned outcrop at Meridiani Planum as seen by the Miniature Thermal Emission Spectrometer and implications for its formation. *Journal of Geophysical Research*, 111: E12S03. https://doi.org/10.1029/2005JE002672

Goldsten, J. O., Rhodes, E. A., Boynton, W. V., Feldman, W. C., Lawrence, D. J., Trombka, J. I., et al. (2007). The MESSENGER Gamma-Ray and Neutron Spectrometer. *Space Science Reviews*, 131: 339-391. https://doi.org/10.1007/s11214-007-9262-7

Golombek, M. P., Cook, R. A., Economou, T., Folkner, W. M., Haldemann, A. F. C., Kellemeyn, P. H., et al. (1997). Overview of the Mars Pathfinder mission and assessment of landing site predictions. *Science*, 278(5344): 1743-1748. https://doi.org/10.1126/science.278.5344.1743

Golombek, M., Grant, J., Kipp, D., Vasavada, A., Kirk, R., Fergason, R., et al. (2012). Selection of the Mars Science Laboratory landing site. *Space Science Reviews*, 170: 641-737. https://doi.org/10.1007/s11214-012-9916-y

Gómez-Elvira, J., Armiens, C., Castañer, L., Domínguez, M., Genzer, M., Gómez, F., et al. (2012). REMS: The environmental sensor suite for the Mars Science Laboratory rover. *Space Science Reviews*, 170: 583-640. https://doi.org/10.1007/s11214-012-9921-1

Goodman, J. & Weare, J. (2010). Ensemble samplers with affine invariance. *Communications in Applied Mathematics and Computational Science*, 5(1): 65-80. https://doi.org/10.2140/camcos.2010.5.65

Graetsch, H., Gies, H., & Topalovic', I. (1994). NMR, XRD and IR study on microcrystalline opals. *Physics and Chemistry of Minerals*, 21: 166–175. https://doi.org/10.1007/BF00203147

Gross, J. & Filiberto, J. (2014). Granitic compositions in gabbroic Martian meteorite NWA 6963: Evidence for extreme fractional crystallization of a hydrous magma. *Workshop on Volatiles in the Martian Interior*: 1015.

Grotzinger, J. P. & Milliken, R. E. (2012). The sedimentary rock record of Mars: Distribution, origins, and global stratigraphy. *Sedimentary Geology of Mars*, 102: 1–48. https://doi.org/10.2110/pec.12.102.0001

Grotzinger, J. P., Sumner, D. Y., Kah, L. C., Stack, K., Gupta, S., Edgar, L., Rubin, D., et al. (2014). A habitable fluvio-lacustrine environment at Yellowknife Bay, Gale Crater, Mars. *Science*, 343(6169): 1242777. https://doi.org/10.1126/science.1242777

Grotzinger, J. P., Gupta, S., Malin, M. C., Rubin, D. M., Schieber, J., Siebach, K., et al. (2015). Deposition, exhumation, and paleoclimate of an ancient lake deposit, Gale crater, Mars. *Science*, 350(6257): aac7575. https://doi.org/10.1126/science.aac7575

Hapke, B. R. (2012). Theory of reflectance and emittance spectroscopy. Cambridge University Press.

Hardgrove, C., Moersch, J., & Drake, D. (2011). Effects of geochemical composition on neutron die-away measurements: Implications for Mars Science Laboratory's Dynamic Albedo of Neutrons experiment. *Nuclear Instruments and Methods in Physics Research A*, 659(1): 442–455. https://doi.org/10.1016/j.nima.2011.08.058

Hartmann, W. K. & Raper, O. (1974). The new Mars: The discoveries of Mariner 9. *NASA SP-337*, Washington, D.C.

Hassler, D. M., Zeitlin, C., Wimmer-Schweingruber, R. F., Böttcher, S., Martin, C., Andrews, J., et al. (2012). The Radiation Assessment Detector (RAD) investigation. *Space Science Reviews*, 170: 503-558. https://doi.org/10.1007/s11214-012-9913-1

Hassler, D. M., Zeitlin, C., Wimmer-Schweingruber, R. F., Ehresmann, B., Rafkin, S., Eigenbrode, J. L. (2014). Mars' surface radiation environment measured with the Mars Science Laboratory's Curiosity rover. *Science*, 343: 1244797-1. https://doi.org/10.1126/science.1244797

Hawthorne, F. (1988). Spectroscopic methods in mineralogy and geology. *Reviews in Mineralogy* (18). BookCrafters, Inc.

Hazen, R. (2005). Genesis: Rocks, minerals, and the geochemical origin of life. *Elements*, 1(3): 135-137. https://doi.org/10.2113/gselements.1.3.135

He, L., O'Sullivan, J. A., Politte, D. V., Powell, K. E., & Arvidson, R. E. (2019). Quantitative reconstruction and denoising method HyBER for hyperspectral image data and its application to CRISM. *IEEE Journal of Selected Topics in Applied Earth Observations and Remote Sensing*, 12(4): 1219–1230. https://doi.org/10.1109/JSTARS.2019.2900644

He, L., Arvidson, R. E., O'Sullivan, J. A., Morris, R. V., Condus, T., Hughes, M. N., et al. (2022). Surface kinetic temperatures and nontronite single scattering albedo spectra from Mars Reconnaissance Orbiter CRISM hyperspectral imaging data over Glen Torridon, Gale crater, Mars. *Journal of Geophysical Research: Planets*. 127(9): e2021JE007092. https://doi.org/10.1029/2021JE007092

Henley, T. L. J., Schmidt, M. E., Bray, S. L., & Zheng, J. J. (2021). An update on martian dust coverage and contribution to APXS elemental concentrations for rock targets in Gale crater. *Lunar and Planetary Science Conference VII*, 2241.

Hughes, M. (2022). Geomorphic map of Glen Torridon in Gale crater, Mars. Digital Research Materials (Data & Supplemental files), 95. Retrieved from https://openscholarship.wustl.edu/data/95

Humayun, M., Nemchin, A., Zanda, B., Hewins, R. H., Grange, M., Kennedy, A., et al. (2013). Origin and age of the earliest Martian crust from meteorite NWA 7533. *Nature*, 503: 513–516. https://doi.org/10.1038/nature12764

Hurowitz, J. A., Grotzinger, J. P., Fischer, W. W., McLennan, S. M., Milliken, R. E., Stein, N., et al. (2017). Redox stratification of an ancient lake in Gale crater, Mars. *Science*, 356(6341): eaah6849. https://doi.org/10.1126/science.aah6849

Jun, I., Mitrofanov, I., Litvak, M. L., Sanin, A. B., Kim, W., Behar, A., et al. (2013). Neutron background environment measured by the Mars Science Laboratory's Dynamic Albedo of Neutrons instrument during the first 100 sols. *Journal of Geophysical Research: Planets*, 118: 2400–2412. https://doi.org/10.1002/2013JE004510

Keil, R. G. & Mayer, L. M. (2014). Mineral matrices and organic matter. *Treatise on Geochemistry 2nd Edition*, 12: 337-359. http://doi.org/10.1016/B978-0-08-095975-7.01024-X

Kennedy, M. J., Pevear, D. R., & Hill, R. J. (2002). Mineral surface control of organic carbon in black shale. *Science*, 295: 657-660. https://doi.org/10.1126/science.1066611

Kerner, H. R., Hardgrove, C. J., Czarnecki, S., Gabriel, T. S. J., Mitrofanov, I. G., Litvak, M. L., et al. (2020). Analysis of active neutron measurements from the Mars Science Laboratory Dynamic Albedo of Neutrons instrument: Intrinsic variability, outliers, and implications for future investigations. *Journal of Geophysical Research: Planets*, 118. https://doi.org/10.1002/2013JE004510

Kite, E. S., Lewis, K. W., Lamb, M. P., Newman, C. E., & Richardson, M. I. (2013). Growth and form of the mound in Gale Crater, Mars: Slope wind enhanced erosion and transport. *Geology*, 41(5): 543–546. https://doi.org/10.1130/G33909.1

Klasik, J. A. (1975). High cristobalite and high tridymite in a middle Eocene deep-sea chert. *Science*, 189(4203): 631–632. https://doi.org/10.1126/science.189.4203.631

Kminek, G. & Bada, J. L. (2006). The effect of ionizing radiation on the preservation of amino acids on Mars. *Earth and Planetary Science Letters*, 245(1-2): 1-5. https://doi.org/10.1016/j.epsl.2006.03.008

Lanza, N. L., Fischer, W. W., Wiens, R. C., Grotzinger, J., Ollila, A. M., Cousin, A., et al. (2014). High manganese concentrations in rocks at Gale crater, Mars. *Geophysical Research Letters*, 41(16): 5755-5763. https://doi.org/10.1002/2014JE004620

Lapotre, M. G., Ehlmann, B. L., Minson, S. E., Arvidson, R. E., Ayoub, F., Fraeman, A. A., et al. (2017). *Journal of Geophysical Research: Planets*, 122: 2489-2509. https://doi.org/10.1002/2016JE005133

Lawrence, D. L., Hurley, D. M., Feldman, W. C., Elphic, R. C., Maurice, S., Miller, R. S., et al. (2011). Sensitivity of orbital neutron measurements to the thickness and abundance of surficial lunar water. *Journal of Geophysical Research*, 116: E01002. https://doi.org/10.1029/2010JE003678

Lawrence, D. J., Adams, D., Ames, W. F., Ayllon-Unzueta, M., Bronner, B M., Burks, M. T., et al. (2022). The Dragonfly Gamma-Ray and Neutron Spectrometer (DraGNS): Providing *in-situ* measurements of Titan's elemental composition. *Lunar and Planetary Science LIII*: 1939.

Le Deit, L., Hauber, E., Fueten, F., Pondrelli, M., Rossi, A. P., & Jaumann, R. (2013). Sequence of infilling events in Gale Crater, Mars: Results from morphology, stratigraphy, and mineralogy. *Journal of Geophysical Research: Planets*, 118: 2439–2473. https://doi.org/10.1002/2012JE004322

Lewis, K. W., Peters, S., Gonter, K., Morrison, S., Schmerr, N., Vasavada, A. R., et al. (2019). A surface gravity traverse on Mars indicates low bedrock density at Gale crater. *Science*, 363(6426): 535–537. https://doi.org/10.1126/science.aat0738

Lewis, K. W. & Turner, M. L. (2019). Geologic structure of the Vera Rubin Ridge, Gale Crater, Mars. *Lunar and Planetary Science L*: 2216.

Litvak, M. L., Mitrofanov, I. G., Barmakov, Yu. N., Behar, A., Bitulev, A., Bobrovnitsky, Yu., et al. (2008). The Dynamic Albedo of Neutrons (DAN) experiment for NASA's 2009 Mars Science Laboratory. *Astrobiology*, 8(3): 605–612. https://doi.org/10.1089/ast.2007.0157

Litvak, M. L., Mitrofanov, I. G., Gellert, R., Djachkova, M. V., Lisov, D. I., Vasavada, A.R., et al. (2023). Depth distribution of chlorine at Gale crater, Mars, as derived from the DAN and APXS experiments onboard the Curiosity rover. *Journal of Geophysical Research: Planets*, 128(5): e2022JE007694. https://doi.org/10.1029/2022JE007694

Lützow, M. V., Kögel-Knabner, I., Ekschmitt, K., Matzner, E., Guggenberger, G., Marschner, B., et al. (2006). Stabilization of organic matter in temperate soils: mechanisms and their relevance under different soil conditions – a review. *European Journal of Soil Science*, 57: 426-445. https://doi.org/10.1111/j.1365-2389.2006.00809.x

Mahaffy, P. R., Webster, C. R., Cabane, M., Conrad, P. G., Coll, P., Atreya, S. K., et al. (2012). The Sample Analysis at Mars investigation and instrument suite. *Space Science Reviews*, 170: 401-478. https://doi.org/10.1007/s11214-012-9879-z

Maki, J., Thiessen, D., Pourangi, A., Kobzeff, P., Litwin, T., Scherr, L., et al. (2012). The Mars Science Laboratory engineering cameras. *Space Science Reviews*, 170: 77-93. https://doi.org/10.1007/s11214-012-9882-4

Malin, M. C., Ravine, M. A., Caplinger, M. A., Ghaemi, F. T., Schaffner, J. A., Maki, J. N., et al. (2017). The Mars Science Laboratory (MSL) mast cameras and descent imager: Investigation and instrument descriptions. *Earth and Space Science*, 4(8): 506–539. https://doi.org/10.1002/2016EA000252

Mangold, N., Thompson, L. M., Forni, O., Williams, A. J., Fabre, C., Le Deit, L., et al. (2016). Composition of conglomerates analyzed by the Curiosity rover: Implications for Gale Crater crust and sediment sources. *Journal of Geophysical Research: Planets*, 121: 353–387. https://doi.org/10.1002/2015JE004977

Maurice, S., Wiens, R. C., Saccoccio, M., Barraclough, B., Gasnault, O., Forni, O., et al. (2012). The ChemCam instrument suite on the Mars Science Laboratory (MSL) Rover: Science objectives and mast unit description. *Space Science Reviews*, 170: 95–166. https://doi.org/10.1007/s11214-012-9912-2

McAdam, A. C., Zolotov, M. Y., Mironenko, M. V., & Sharp, T. G. (2008). Formation of silica by low-temperature acid alteration of Martian rocks: Physical-chemical constraints. *Journal of Geophysical Research*, 113, E08003. https://doi.org/10.1029/2007JE003056

McAdam, A. C., Sutter, B., Archer, P. D., Franz, H. B., Wong, G. M., Lewis, J. M. T., et al. (2020). Constraints on the mineralogy and geochemistry of Vera Rubin ridge, Gale crater, Mars from Mars Science Laboratory Sample Analysis at Mars evolved gas analysis. *Journal of Geophysical Research: Planets*, 125: e2019JE006309. https://doi.org/10.1029/2019JE006309

McAdam, A. C., Sutter, B., Archer, P. D., Franz, H. B., Wong, G. M., Lewis, J. M. T., et al. (2022). Evolved gas analyses of sedimentary rocks from the Glen Torridon clay-bearing unit, Gale crater, Mars: Results from the Mars Science Laboratory Sample Analysis at Mars instrument suite. *Journal of Geophysical Research: Planets*, 127: e2022JE007179. https://doi.org/10.1029/2022JE007179

McCubbin, F. M., Nekvasil, H., Harrington, A. D., Elardo, S. M., & Lindsley, D. H. (2008). Compositional diversity and stratification of the Martian crust: Inferences from crystallization experiments on the picrobasalt Humphrey from Gusev Crater, Mars. *Journal of Geophysical Research*, 113: E11013. https://doi.org/10.1029/2008JE003165

McEwen, A. S., Eliason, E. M., Bergstrom, J. W., Bridges, N. T., Hansen, C. J., Delamere, W. A., et al. (2007). Mars Reconnaissance Orbiter's High Resolution Imaging Science Experiment (HiRISE). *Journal of Geophysical Research*, 112(5): 1–40. https://doi.org/10.1029/2005JE002605

McLennan, S. M., Grotzinger, J. P., Hurowitz, J. A., & Tosca, N. J. (2019). The sedimentary cycle on early Mars. *Annual Review of Earth and Planetary Sciences*, 47: 91–118. https://doi.org/10.1146/annurev-earth-053018-060332

McSween Jr., H. Y. (1984). SNC meteorites: Are they Martian rocks? *Geology*, 12(1): 3–6. https://doi.org/10.1130/0091-7613(1984)12<3:SMATMR>2.0.CO;2

McSween, H. Y., Wyatt, M. B., Gellert, R., Bell III, J. F., Morris, R. V., Herkenhoff, K. E., et al. (2006). Characterization and petrologic interpretation of olivine-rich basalts at Gusev Crater, Mars. *Journal of Geophysical Research*, 111: E02S10. https://doi.org/10.1029/2005JE002477

McSween Jr., H. Y. (2015). Petrology on Mars. *American Mineralogist*, 100(11–12): 2380–2395. https://doi.org/10.2138/am-2015-5257

Milliken, R. E., Swayze, G. A., Arvidson, R. E., Bishop, J. L., Clark, R. N., Ehlmann, B. L., et al. (2008). Opaline silica in young deposits on Mars. *Geology*, 36(11): 847–850. https://doi.org/10.1130/G24967A.1

Milliken, R. E., Grotzinger, J. P., & Thomson, B. J. (2010). Paleoclimate of Mars as captured by the stratigraphic record in Gale crater. *Geophysical Research Letters*, 37(L04201). https://doi.org/10.1029/2009GL041870

Ming, D. W., Archer Jr., P. D., Glavin, D. P., Eigenbrode, J. L., Franz, H. B., Sutter, B., et al. (2014). Volatile and organic compositions of sedimentary rocks in Yellowknife Bay, Gale crater, Mars. *Science*, 343(6169). https://doi.org/10.1126/science.1245267

Mitrofanov, I. G., Litvak, M. L., Varenikov, A. B., Barmakov, Y. N., Behar, A., Bobrovnitsky, Y. I., et al. (2012). Dynamic Albedo of Neutrons (DAN) experiment onboard NASA's Mars Science Laboratory. *Space Science Reviews*, 170: 559–582. https://doi.org/10.1007/s11214-012-9924-y

Mitrofanov, I. (2013). MSL Dynamic Albedo of Neutrons level 3/4 RDR v1.0. https://doi.org/10.17189/1519502

Mitrofanov, I. G., Kozyrev, A. S., Lisov, D. I., Vostrukhin, A. A., Golovin, D. V., Litvak, M. L., et al. (2016). Active neutron sensing of the martian surface with the DAN experiment onboard the NASA "Curiosity" Mars rover: Two types of soil with different water content in the Gale crater. *Astronomy Letters*, 42(4): 251–259. https://doi.org/10.1134/S1063773716040058

Morris, R. V., Ruff, S. W., Gellert, R., Ming, D. W., Arvidson, R. E., Clark, B. C., et al. (2010). Identification of carbonate-rich outcrops on Mars by the Spirit rover. *Science*, 329(5990): 421-424. https://doi.org/10.1126/science.1189667

Morris, R. V., Vaniman, D. T., Blake, D. F., Gellert, R., Chipera, S. J., Rampe, E. B., et al. (2016). Silicic volcanism on Mars evidenced by tridymite in high-SiO_2 sedimentary rock at Gale crater. *Proceedings of the National Academy of Sciences of the United States of America*, 113(26): 7071–7076. https://doi.org/10.1073/pnas.1607098113

Morrison, S. M., Downs, R. T., Blacke, D. F., Vaniman, D. T., Ming, D. W., Hazen, R. M. (2018). Crystal chemistry of martian minerals from Bradbury Landing through Naukluft plateau, Gale crater, Mars. *American Mineralogist*, 103: 857-871. https://doi.org/10.2138/am-2018-6124

Murchie, S., Arvidson, R., Bedini, P., Beisser, K., Bibring, J.-P., Bishop, J., et al. (2007). Compact Reconnaissance Imaging Spectrometer for Mars (CRISM) on Mars Reconnaissance Orbiter (MRO). *Journal of Geophysical Research*, 112(E05S03). https://doi.org/10.1029/2006JE002682

Murchie, S. L., Mustard, J. F., Ehlmann, B. L., Millikan, R. E., & Bishop, J. L. (2009). A synthesis of Martian aqueous mineralogy after 1 Mars year of observations from the Mars Reconnaissance Orbiter. *Journal of Geophysical Research*, 114(E00D06). https://doi.org/10.1029/2009JE003342

Mustard, J. F., Poulet, F., Gendrin, A., Bibring, J.-P., Langevin, Y., Gondet, B., et al. (2005). Olivine and pyroxene diversity in the crust of Mars. *Science*, 307(5715): 1594–1597. https://doi.org/10.1126/science.1109098

Mustard, J. F., Murchie, S. L., Pelkey, S. M., Ehlmann, B. L., Milliken, R. E., Grant, J. A., et al. (2008). Hydrated silicate minerals on Mars observed by the Mars Reconnaissance Orbiter CRISM instrument. *Nature*, 454: 305–309. https://doi.org/10.1038/nature07097

Nachon, M., Mangold, N., Forni, O., Kah, L. C., Cousin, A., Wiens, R. C., et al. (2017). Chemistry of diagenetic features analyzed by ChemCam at Pahrump Hills, Gale crater, Mars. Icarus, 281: 121–136. https://doi.org/10.1016/j.icarus.2016.08.026

Naidja, A., Huang, P. M., & Bollag, J.-M. (1997). Activity of tyosinase immobilized on hydroxyaluminum-montmorillonite complexes. *Journal of Molecular Catalysis A: Chemical*, 115: 305-316. https://doi.org/10.1016/S1381-1169(96)00335-4

NASEM: National Academies of Sciences, Engineering, and Medicine. (2022). Origins, Worlds, and Life: A Decadal Strategy for Planetary Science and Astrobiology 2023-2032. *Washington, DC: The National Academies Press*. https://doi.org/10.17226/26522

Nellessen, M. A., Gasda, P., Crossey, L., Peterson, E., Ali, A., Zhang, J., et al. (2023). Boron adsorption in clay minerals: Implications for martian groundwater chemistry and boron on Mars. *Icarus*, (401): 115372. https://doi.org/10.1016/j.icarus.2023.115599

Newman, S., Stolper, E. M., & Epstein, S. (1986). Measurement of water in rhyolitic glasses: Calibration of an infrared spectroscopic technique. *American Mineralogist*, 71(11-12): 1527–1541.

Nonella, M. & Seeger, S. (2008). Investigating alanine-silica interactions by means of first-principles molecular-dynamics simulations. *ChemPhysChem*, 9: 414-421. https://doi.org/10.1002/cphc.200700546

Ovesen, R. G., Nielsen, J., & Bruun Hansen, H. C. (2011). Biomedicine in the environment: Sorption of the cyclotide kalata B2 to montmorillonite, goethite, and humic acid. *Environmental Toxicology and Chemistry*, 30(8): 1785-1792. https://doi.org/10.1002/etc.579

Palucis, M. C., Dietrich, W. E., Hayes, A. G., Williams, R. M. E., Gupta, S., Mangold, N., et al. (2014). The origin and evolution of the Peace Vallis fan system that drains to the Curiosity landing area, Gale Crater, Mars. *Journal of Geophysical Research: Planets*, 119: 705–728. https://doi.org/10.1002/2013JE004583

Pavlov, A. A., Vasilyev, G., Ostryakov, V. M., Pavlov, A. K., & Mahaffy, P. (2012). Degradation of the organic molecules in the shallow subsurface of Mars due to irradiation by cosmic rays. *Geophysical Research Letters*, 39: L13202. https://doi.org/10.1029/2012GL052166

Payré, V., Fabre, C., Cousin, A., Sautter, V., Wiens, R. C., Forni, O., et al. (2017). Alkali trace elements in Gale crater, Mars, with ChemCam: Calibration update and geological implications. *Journal of Geophysical Research: Planets*, 122(3): 650-679. https://doi.org/10.1002/2016JE005201

Pourret, O., Bollinger, J.-C., Hursthouse, A., & van Hullebusch, E. D. (2022). Sorption vs adsorption: The words they are a-changin', not the phenomena. *Science of the Total Environment*, 838: 156545. https://doi.org/10.1016/j.scitotenv.2022.156545

Prettyman, T. H., Feldman, W. C., McSween Jr., H. Y., Dingler, R. D., Enemark, D. C., Patrick, D. E., et al. (2011). Dawn's Gamma Ray and Neutron Detector. *Space Science Reviews*, 163: 371-459. https://doi.org/10.1007/s11214-011-9862-0

Rampe, E. B., Morris, R. V., Archer Jr., P. D., Agresti, D. G., & Ming, D. W. (2016). Recognizing sulfate and phosphate complexes chemisorbed onto nanophase weathering products on Mars using *in-situ* and remote observations. *American Mineralogist*, 101: 678-689. http://doi.org/10.2138/am-2016-5408CCBYNCND

Rampe, E. B., Ming, D. W., Blake, D. F., Bristow, T. F., Chipera, S. J., Grotzinger, J. P., et al. (2017). Mineralogy of an ancient lacustrine mudstone succession from the Murray formation, Gale crater, Mars. *Earth and Planetary Science Letters*, 471: 172–185. https://doi.org/10.1016/j.epsl.2017.04.021

Rampe, E. B., Bristow, T. F., Morris, R. V., Morrison, S. M., Achilles, C. N., Ming, D. W., et al. (2020a). Mineralogy of Vera Rubin ridge from the Mars Science Laboratory CheMin instrument. *Journal of Geophysical Research: Planets*, 125: e2019JE006306. https://doi.org/10.1029/2019JE006306

Rampe, E. B., Blake, D. F., Bristow, T. F., Ming, D. W., Vaniman, D. T., Morris, R. V., et al. (2020b). Mineralogy and geochemistry of sedimentary rocks and eolian sediments in Gale crater, Mars: A review after six Earth years of exploration with *Curiosity*. *Geochemistry*, 80: 125605. https://doi.org/10.1016/j.chemer.2020.125605

Rapin, W., Meslin, P.-Y., Maurice, S., Wiens, R. C., Laporte, D., Chauviré, B., et al. (2017). Quantification of water content by laser induced breakdown spectroscopy on Mars. *Spectrochimica Acta Part B*, 130: 82-100. http://doi.org/10.1016/j.sab.2017.02.007

Rapin, W., Chauviré, B., Gabriel, T. S. J., McAdam, A. C., Ehlmann, B. L., Hardgrove, C., et al. (2018). *In situ* analysis of opal in Gale crater, Mars. *Journal of Geophysical Research: Planets*, 123: 1955–1972. https://doi.org/10.1029/2017JE005483

Rice, M. S., Bell III, J. F., Cloutis, E. A., Wang, A., Ruff, S. W., Craig, M. A., et al. (2010). Silica-rich deposits and hydrated minerals at Gusev Crater, Mars: Vis-NIR spectral characterization and regional mapping. *Icarus*, 205(2): 375–395. https://doi.org/10.1016/j.icarus.2009.03.035

Rice, M. S., Starr, M. S., Hughes, C. M., Seeger, C. H., Fraeman, A. A., Johnson, J. R., et al. (2019). Science results from a comprehensive Mastcam spectral database for Curiosity's traverse*. Lunar and Planetary Science L*: 3030.

Ruff, S. W., Farmer, J. D., Calvin, W. M., Herkenhoff, K. E., Johnson, J. R., Morris, R. V., et al. (2011). Characteristics, distribution, origin, and significance of opaline silica observed by the Spirit rover in Gusev crater, Mars. *Journal of Geophysical Research*, 116: E00F23. https://doi.org/10.1029/2010JE003767

Schmidt, M. E., Perrett, G. M., Bray, S. L., Bradley, N. J., Lee, R. E., Berger, J. A., et al. (2018). Dusty rocks in Gale crater: Assessing areal coverage and separating dust and rock contributions in APXS analyses. *Journal of Geophysical Research: Planets*, 123: 1649–1673. https://doi.org/10.1029/2018JE005553

Schneider, C. A., Rasband, W. S., & Eliceiri, K. W. (2012). NIH image to ImageJ: 25 years of image analysis. *Nature Methods*, 9(7): 671–675. https://doi.org/10.1038/nmeth.2089

Sears, V. F. (1992). Neutron scattering lengths and cross sections. *Neutron News*, 3(3): 26–37. https://doi.org/10.1080/10448639208218770

Seelos, F. (2016). MRO CRISM map-projected targeted reduced data record v1.0. *NASA Planetary Data System.* https://doi.org/10.17189/1519470

Seelos, K. D., Seelos, F. P., Viviano-Beck, C. E., Murchie, S. L., Arvidson, R. E., Ehlmann, B. L., & Fraeman, A. A. (2014). Mineralogy of the MSL Curiosity landing site in Gale crater as observed by MRO/CRISM. *Geophysical Research Letters*, 41: 4880–4887. https://doi.org/10.1002/2014GL060310

Segnit, E. R., Stevens, T. J., & Jones, J. B. (1965). The role of water in opal. *Journal of the Geological Society of Australia*, 12(2): 211–226. https://doi.org/10.1080/00167616508728593

Shen, Y.-H. (1999). Sorption of natural dissolved organic matter on soil. *Chemosphere*, 38(7): 1505-1515. https://doi.org/10.1016/S0045-6535(98)00371-3

Sheng, G., Johnston, C. T., Teppen, B. J., & Boyd, S. A. (2001). Potential contributions of smectite clays and organic matter to pesticide retention in soils. *Journal of Agricultural and Food Chemistry*, 49(6): 2899-2907. https://doi.org/10.1021/jf001485d

Singer, R. B., McCord, T. B., Clark, R. N., Adams, J. B., & Huguenin, R. L. (1979). Mars surface composition from reflectance spectroscopy: A summary. *Journal of Geophysical Research*, 84(B14): 8415–8426. https://doi.org/10.1029/JB084iB14p08415

Sklute, E. C., Jensen, H. B., Rogers, A. D., & Reeder, R. J. (2015). Morphological, structural, and spectral characteristics of amorphous iron sulfates. *Journal of Geophysical Research: Planets*, 120: 809-830. https://doi.org/10.1002/2014JE004784

Skok, J. R., Mustard, J. F., Ehlmann, B. L., Milliken, R. E., & Murchie, S. L. (2010). Silica deposits in the Nili Patera caldera on the Syrtis Major volcanic complex on Mars. *Nature Geoscience*, 3: 838–841. https://doi.org/10.1038/NGEO990

Smith, M. R., Bandfield, J. L., Cloutis, E. A., & Rice, M. S. (2013). Hydrated silica on Mars: Combined analysis with near-infrared and thermal-infrared spectroscopy. *Icarus*, 223(2): 633–648. https://doi.org/10.1016/j.icarus.2013.01.024

Smith, R. J., McLennan, S. M., Achilles, C. N., Dehouck, E., Horgan, B. H. N., Mangold, N., et al. (2021). X-ray amorphous components in sedimentary rocks of Gale crater, Mars: Evidence for ancient formation and long-lived aqueous activity. *Journal of Geophysical Research: Planets*, 126: e2020JE006782. https://doi.org/10.1029/2020JE006782

Smith, R. J., McLennan, S. M., Sutter, B., Rampe, E. B., Dehouck, E., Siebach, K. L., et al. (2022). X-ray amorphous sulfur-bearing phases in sedimentary rocks of Gale crater, Mars. *Journal of Geophysical Research: Planets*, 127: e2021JE007128. https://doi.org/10.1029/2021JE007128

Soffen, G. A. & Snyder, C. W. (1976). The first Viking mission to Mars. *Science*, 193(4255): 759-766. https://doi.org/10.1126/science.193.4255.759

Squyres, S. W., Arvidson, R. E., Baumgartner, E. T., Bell III, J. F., Christensen, P. R., Gorevan, S. (2003). Athena Mars rover science investigation. *Journal of Geophysical Research*, 108(8062). https://doi.org/10.1029/2003JE002121

Squyres, S. W., Arvidson, R. E., Ruff, S., Gellert, R., Morris, R. V., Ming, D. W., et al. (2008). Detection of silica-rich deposits on Mars. *Science*, 320(5879): 1063–1067. https://doi.org/10.1126/science.1155429

Squyres, S. W., Arvidson, R. E., Bell III, J. F., Calef III, F., Clark, B. C., Cohen, B. A., et al. (2012). Ancient impact and aqueous processes at Endeavour crater, Mars. *Science*, 336(6081): 570-576. https://doi.org/10.1126/science.1220476

Stack, K. M., Grotzinger, J. P., Lamb, M. P., Gupta, S., Rubin, D. M., Kah, L. C., et al. (2019). Evidence for plunging river plume deposits in the Pahrump Hills member of the Murray formation, Gale crater, Mars. *Sedimentology*, 66(5): 1768–1802. https://doi.org/10.1111/sed. 12558

Starr, M. S., Rice, M. S., Hughes, C. M., Seeger, C. H., Bell III, J. F., & Wellington, D. F. (2019). Methodology for the creation and analysis of a comprehensive Mastcam multispectral database of Curiosity's traverse. *Lunar and Planetary Science L*: 3087.

Steinbacher, R. H. & Haynes, N. R. (1973) Mariner 9 mission profile and project history. *Icarus*, 18: 64-74. https://doi.org/10.1016/0019-1035(73)90173-5

Stotzky, G. (2000). Persistence and biological activity in soil of insecticidal proteins from *Bacillus thuringiensis* and of bacterial DNA bound on clays and humic acids. *Journal of Environmental Quality*, 29(3): 691-705. https://doi.org/10.2134/jeq2000.00472425002900030003x

Summons, R. E., Amend, J. P., Bish, D., Buick, R., Cody, G. T., Des Marais, D. J., et al. (2011). Preservation of martian organic and environmental records: Final report of the Mars Biosignature Working Group. *Astrobiology*, 11(2): 157–181. https://doi.org/10.1089/ast.2010.0506

Sun, V. Z. & Milliken, R. E. (2015). Ancient and recent clay formation on Mars as revealed from a global survey of hydrous minerals in crater central peaks. *Journal of Geophysical Research: Planets*, 120: 2293–2332. https://doi.org/10.1002/2015JE004918

Sutter, B., McAdam, A. C., Mahaffy, P. R., Ming, D. W., Edgett, K. S., Rampe, E. B., et al. (2017). Evolved gas analyses of sedimentary rocks and eolian sediment in Gale Crater, Mars: Results of the Curiosity rover's sample analysis at Mars instrument from Yellowknife Bay to the Namib Dune. *Journal of Geophysical Research: Planets*, 122: 2574–2609. https://doi.org/10.1002/2016JE005225

Taylor, G. J., Martel, L. M. V., Karunatillake, S., Gasnault, O., & Boynton, W. V. (2010). Mapping Mars geochemically. *Geology*, 38(2): 183–186. https://doi.org/10.1130/G30470.1

Thomson, B. J., Bridges, N. T., Milliken, R., Baldridge, A., Hook, S. J., Crowley, J. K., et al. (2011). Constraints on the origin and evolution of the layered mound in Gale Crater, Mars using Mars Reconnaissance Orbiter data. *Icarus*, 214: 413–432. https://doi.org/10.1016/j.icarus.2011.05.002

Thorpe, M. T., Bristow, T. F., Rampe, E. B., Tosca, N. J., Grotzinger, J. P., Bennett, C. N., et al. (2022). Mars Science Laboratory CheMin data from the Glen Torridon region and the significance of lake-groundwater interactions in interpreting mineralogy and sedimentary history. *Journal of Geophysical Research: Planets*, 127(11): e2021JE007099. https://doi.org/10.1029/2021JE007099

Tosca, N. J. & Knoll, A. H. (2009). Juvenile chemical sediments and the long term persistence of water at the surface of Mars. *Earth and Planetary Science Letters*, 286(3-4): 379–386. https://doi.org/10.1016/j.epsl.2009.07.004

Treiman, A. H., Bish, D. L., Vaniman, D. T., Chipera, S. J., Blake, D. F., Ming, D. W., et al. (2016). Mineralogy, provenance, and diagenesis of a potassic basaltic sandstone on Mars: CheMin X-ray diffraction of the Windjana sample (Kimberley area, Gale crater). *Journal of Geophysical Research: Planets*, 121: 75-106. https://doi.org/10.1002/2015JE004932

Treiman, A. H., Lanza, N., VanBommel, S., Berger, J., Wiens, R. Bristow, T., et al. (in prep). Manganese-iron phosphate nodules at the Groken site, Gale crater, Mars.

Tu, V. M., Rampe, E. B., Bristow, T. F., Thorpe, M. T., Clark, J. V., Castle, N. (2021). A review of the phyllosilicates in Gale crater as detected by the CheMin instrument on the Mars Science Laboratory, Curiosity rover. *Minerals*, 11(847). https://doi.org/10.3390/min11080847

Tutolo, B. M., Evans, B. W., & Kuehner, S. M. (2019). Serpentine-hisingerite solid solution in altered ferroan peridotite and olivine gabbro. *Minerals*, 9(47). https://doi.org/10.3390/min9010047

Tutolo, B. M. & Tosca, N. J. (2023). Observational constraints on the process and products of Martian serpentization. *Science Advances*, 9(5): eadd8472. https://doi.org/10.1126/sciadv.add8472

Udry, A., Balta, J. B., & McSween Jr., H. Y. (2014). Exploring fractionation models for Martian magmas. *Journal of Geophysical Research: Planets*, 119: 1–18. https://doi.org/10.1002/2013JE004445

Udry, A., Gazel, E., & McSween Jr., H. Y. (2018). Formation of evolved rocks at Gale crater by crystal fractionation and implications for Mars crustal composition. *Journal of Geophysical Research: Planets*, 123: 1525–1540. https://doi.org/10.1029/2018JE005602

Vaniman, D. T., Bish, D. L., Chipera, S. J., Fialips, C. L., Carey, J. W., & Feldman, W. C. (2004). Magnesium sulphate salts and the history of water on Mars. *Nature*, 431: 663-665. https://doi.org/10.1038/nature02973

Vaniman, D. T. & Chipera, S. J. (2006). Transformations of Mg- and Ca-sulfate hydrates in Mars regolith. *American Mineralogist*, 91: 1628-1642. https://doi.org/10.2138/am.2006.2092

Vaniman, D., (2012). Mars Science Laboratory Chemistry & Mineralogy RDR Data V1.0. *NASA Planetary Data System*. https://doi.org/10.17189/1519453

Vaniman, D. T., Bish, D. L., Ming, D. W., Bristow, T. F., Morris, R. V., Blake, D. F., et al. (2014). Mineralogy of a mudstone at Yellowknife Bay, Gale crater, Mars. *Science*, 343(3169). https://doi.org/10.1126/science.1243480

Vaniman, D. T., Martínez, G. M., Rampe, E. B., Bristow, T. F., Blake, D. F., Yen, A. S., et al. (2018). Gypsum, bassanite, and anhydrite at Gale crater, Mars. *American Mineralogist*, 103(7): 1011–1020. https://doi.org/10.2138/am-2018-6346

Varela, M. E., Kurat, G., Bonnin-Mosbah, M., Clocchiatti, R., & Massare, D. (2000). Glass-bearing inclusions in olivine of the Chassigny achondrite: Heterogeneous trapping at sub-igneous temperatures. *Meteoritics & Planetary Science*, 35: 39-52. https://doi.org/10.1111/j.1945-5100.2000.tb01972.x

Vasavada, A. R. (2022). Mission overview and scientific contributions from the Mars Science Laboratory Curiosity rover after eight years of surface operations. *Space Science Reviews*, 218(14). https://doi.org/10.1007/s11214-022-00882-7

Viviano-Beck, C. E., Seelos, F. P., Murchie, S. L., Kahn, E. G., Seelos, K. D., Taylor, H. W., et al. (2014). Revised CRISM spectral parameters and summary products based on the currently detected mineral diversity on Mars. *Journal of Geophysical Research: Planets*, 119: 1403–1431. https://doi.org/10.1002/2014JE004627

Wang, A., Freeman, J. J., & Jolliff, B. L. (2009). Phase transition pathways of the hydrates of magnesium sulfate in the temperature range 50°C to 5°C: Implications for sulfates on Mars. *Journal of Geophysical Research*, 114: E04010. https://doi.org/10.1029/2008JE003266

Wang, A. A. & Zhou, Y. H. (2014). Experimental comparison of the pathways and rates of the dehydration of Al-, Fe-, Mg- and Ca-sulfates under Mars relevant conditions. *Icarus*, 234: 162–173. https://doi.org/10.1016/j.icarus.2014.02.003

Wattel-Koekkoek, E. J., Buurman, P., van der Plicht, J., Wattel, E., & van Breeman, N. (2003). Mean residence time of soil organic matter associated with kaolinite and smectite. *European Journal of Soil Science*, 54: 269-278. https://doi.org/10.1046/j.1365-2389.2003.00512.x

Weitz, C. M., Bishop, J. L., Thollot, P., Mangold, N., & Roach, L. H. (2011). Diverse mineralogies in two troughs of Noctis Labyrinthus, Mars. *Geology*, 39(10): 899–902. https://doi.org/10.1130/G32045.1

Werner, C. J., Armstrong, J., Brown, F. B., Bull, J. S., Casswell, L., Cox, L. J., et al. (2017). MCNP user's manual: Code version 6.2. LA-UR-17-29981.

Whitaker, M. L., Nekvasil, H., Lindsley, D. H., & Difrancesco, N. J. (2007). The role of pressure in producing compositional diversity in intraplate basaltic magmas. *Journal of Petrology*, 48(2): 365–393. https://doi.org/10.1093/petrology/egl063

Wiens, R. C., Maurice, S., Barraclough, B., Saccoccio, M., Barkley, W. C., Bell III, J. F., et al. (2012). The ChemCam instrument suite on the Mars science laboratory (MSL) rover: Body unit and combined system tests. *Space Science Reviews*, 170: 167–227. https://doi.org/10.1007/s11214-012-9902-4

Williams, L. A., Parks, G. A., & Crerar, D. A. (1985). Silica diagenesis, I. Solubility controls. *Journal of Sedimentary Petrology*, 55(3): 301–311. https://doi.org/10.1306/212F86AC-2B24-11D7-8648000102C1865D

Wilson, J. T., Eke, V. R., Massey, R. J., Elphic, R. C., Feldman, W. C., Maurice, S., et al. (2018). Equatorial locations of water on Mars: Improved resolution maps based on Mars Odyssey Neutron Spectrometer data. *Icarus*, 299: 148-160. http://doi.org/10.1016/j.icarus.2017.07.028

Wray, J. J., Hansen, S. T., Dufek, J., Swayze, G. A., Murchie, S. L., & Seelos, F. P. (2013). Prolonged magmatic activity on Mars inferred from the detection of felsic rocks. *Nature Geoscience*, 6: 1013–1017. https://doi.org/10.1038/NGEO1994

Wyatt, M. B. & McSween Jr., H. Y. (2002). Spectral evidence for weathered basalt as an alternative to andesite in the northern lowlands of Mars. *Nature*, 417: 263–266. https://doi.org/10.1038/417263a

Xu, W., Tosca, N. J., McLennan, S. M., & Parise, J. B. (2009). Humidity-induced phase transitions of ferric sulfate minerals studied by *in situ* and *ex situ* X-ray diffraction. *American Mineralogist*, 94: 1629-1637. https://doi.org/10.2138/am.2009.3182

Yen, A. S., Ming, D. W., Vaniman, D. T., Gellert, R., Blake, D. F., Morris, R. V., et al. (2017). Multiple stages of aqueous alteration along fractures in mudstone and sandstone strata in Gale Crater, Mars. *Earth and Planetary Science Letters*, 471: 186–198. https://doi.org/10.1016/j.epsl.2017.04.033

Yen, A. S., Morris, R. V., Ming, D. W., Schwenzer, S. P., Sutter, B., Vaniman, D. T., et al. (2021). Formation of tridymite and evidence for a hydrothermal history at Gale crater, Mars. *Journal of Geophysical Research: Planets*, 136(3): e2020JE006569. https://doi.org/10.1029/2020JE006569

APPENDIX A

SUPPLEMENTAL INFORMATION FOR CHAPTER 2: "IDENTIFICATION AND DESCRIPTION OF A SILICIC VOLCANICLASTIC LAYER IN GALE CRATER, MARS, USING ACTIVE NEUTRON INTERROGATION"

Introduction

This Appendix provides additional details on the data, methods, and results in Chapter 2. All raw data used in this work is available on the Planetary Data System (https://pds-geosciences.wustl.edu/missions/msl/).

Text A.1

Figure 2.4 in Chapter 2 is an annotated portion of a color-corrected mosaic which consists of 145 individual Mast Camera (Mastcam) M100 frames taken on sol 993 to document the unconformity between the Pahrump Hills member of the Murray formation and the overlying Stimson formation. The individual frames of the complete mosaic have the following image IDs:
0993MR0043950000503182C00, 0993MR0043950010503183C00, 0993MR0043950020503184C00, 0993MR0043950030503185C00, 0993MR0043950040503186C00, 0993MR0043950050503187C00, 0993MR0043950060503188C00, 0993MR0043950070503189C00, 0993MR0043950080503190C00, 0993MR0043950090503191C00, 0993MR0043950100503192C00, 0993MR0043950110503193C00, 0993MR0043950120503194C00, 0993MR0043950130503195C00, 0993MR0043950140503196C00, 0993MR0043950150503197C00, 0993MR0043950160503198C00, 0993MR0043950170503199C00, 0993MR0043950180503200C00, 0993MR0043950190503201C00, 0993MR0043950200503202C00, 0993MR0043950210503203C00, 0993MR0043950220503204C00, 0993MR0043950230503205C00, 0993MR0043950240503206C00, 0993MR0043950250503207C00, 0993MR0043950260503208C00, 0993MR0043950270503209C00, 0993MR0043950280503210C00, 0993MR0043950290503211C00, 0993MR0043950300503212C00, 0993MR0043950310503213C00, 0993MR0043950320503214C00, 0993MR0043950330503215C00, 0993MR0043950340503216C00, 0993MR0043950350503217C00, 0993MR0043950360503218C00, 0993MR0043950370503219C00, 0993MR0043950380503220C00, 0993MR0043950390503221C00, 0993MR0043950400503222C00, 0993MR0043950410503223C00, 0993MR0043950420503224C00, 0993MR0043950430503225C00, 0993MR0043950440503226C00, 0993MR0043950450503227C00, 0993MR0043950460503228C00, 0993MR0043950470503229C00, 0993MR0043950480503230C00, 0993MR0043950490503231C00, 0993MR0043950500503232C00, 0993MR0043950510503233C00, 0993MR0043950520503234C00, 0993MR0043950530503235C00, 0993MR0043950540503236C00, 0993MR0043950550503237C00, 0993MR0043950560503238C00, 0993MR0043950570503239C00, 0993MR0043950580503240C00, 0993MR0043950590503241C00, 0993MR0043950600503242C00, 0993MR0043950610503243C00, 0993MR0043950620503244C00, 0993MR0043950630503245C00, 0993MR0043950640503246C00, 0993MR0043950650503247C00, 0993MR0043950660503248C00, 0993MR0043950670503249C00, 0993MR0043950680503250C00, 0993MR0043950690503251C00, 0993MR0043950700503252C00, 0993MR0043950710503253C00, 0993MR0043950720503254C00, 0993MR0043950730503255C00, 0993MR0043950740503256C00, 0993MR0043950750503257C00, 0993MR0043950760503258C00, 0993MR0043950770503259C00, 0993MR0043950780503260C00, 0993MR0043950790503261C00, 0993MR0043950800503262C00, 0993MR0043950810503263C00, 0993MR0043950820503264C00, 0993MR0043950830503265C00, 0993MR0043950840503266C00, 0993MR0043950850503267C00, 0993MR0043950860503268C00, 0993MR0043950870503269C00, 0993MR0043950880503270C00, 0993MR0043950890503271C00, 0993MR0043950900503272C00, 0993MR0043950910503273C00, 0993MR0043950920503274C00, 0993MR0043950930503275C00, 0993MR0043950940503276C00, 0993MR0043950950503277C00, 0993MR0043950960503278C00, 0993MR0043950970503279C00, 0993MR0043950980503280C00, 0993MR0043950990503281C00, 0993MR0043951000503282C00, 0993MR0043951010503283C00, 0993MR0043951020503284C00, 0993MR0043951030503285C00, 0993MR0043951040503286C00, 0993MR0043951050503287C00, 0993MR0043951060503288C00, 0993MR0043951070503289C00, 0993MR0043951080503290C00, 0993MR0043951090503291C00, 0993MR0043951100503292C00, 0993MR0043951110503293C00, 0993MR0043951120503294C00, 0993MR0043951130503295C00, 0993MR0043951140503296C00, 0993MR0043951150503297C00, 0993MR0043951160503298C00, 0993MR0043951170503299C00, 0993MR0043951180503300C00, 0993MR0043951190503301C00, 0993MR0043951200503302C00, 0993MR0043951210503303C00, 0993MR0043951220503304C00, 0993MR0043951230503305C00, 0993MR0043951240503306C00, 0993MR0043951250503307C00, 0993MR0043951260503308C00, 0993MR0043951270503309C00, 0993MR0043951280503310C00, 0993MR0043951290503311C00, 0993MR0043951300503312C00, 0993MR0043951310503313C00, 0993MR0043951320503314C00, 0993MR0043951330503315C00, 0993MR0043951340503316C00, 0993MR0043951350503317C00, 0993MR0043951360503318C00, 0993MR0043951370503319C00, 0993MR0043951380503320C00, 0993MR0043951390503321C00, 0993MR0043951400503322C00, 0993MR0043951410503323C00, 0993MR0043951420503324C00, 0993MR0043951430503325C00, 0993MR0043951440503326C00

Text A.2

To ensure that the Dynamic Albedo of Neutrons (DAN) measurements coadded for this work have fields of view (FOV) which are representative of each other, we examined rover camera imagery using OnSight, a multi-platform visualization system developed for the Mars Science Laboratory (MSL) team to explore the surface of Mars in an immersive, full-scale, 3D terrain reconstruction (Abercrombie et al., 2019). OnSight uses an integrated mesh reconstruction of Mars, incorporating rover images overlain on surface topography. Using the OnSight tool, we are able to co-locate DAN active footprints. For this study, measurement data were only coadded when they were proximal both laterally (within 2 - 3 m) and topographically (within 2 - 3 cm vertically), and there is no significant visible change in the material exposed at the surface. Die-away curves for each coadded measurement are also compared to ensure similar thermal neutron peak location, relative peak height, etc. Figure 2.5 in Chapter 2 is an example showing the individual die-away curves of the two DAN active measurements coadded for Site 4, as well as the coadded die-away curve. DAN active measurements that had a signal-to-noise (SNR) ratio less than 5 for any time bin used in our analysis and could not be coadded to improve SNR, were not included in our results. Sites that had significant sand/rubble cover within the DAN FOV, or with a surface bedrock geochemistry that was inconsistent with the macroscopic thermal neutron absorption cross section (Σ_{abs}) of the best-fit one-layer models, were analyzed using one or both of the two-layer model grids (Table 2.2, Chapter 2).

Text A.3

Ca-sulfate veins are present throughout the Murray formation. We calculated the change in Σ_{abs} after adding 5 vol.% Ca-sulfate to the geochemistries in Table 2.1 (Chapter 2). Anhydrite was the only Ca-sulfate phase in the Buckskin sample (Vaniman et al., 2018), so this was the only phase added to the high-SiO_2 geochemistry. The only other Pahrump Hills sample with Ca-sulfate, Telegraph Peak, contained both bassanite and anhydrite (Vaniman et al., 2018), so we added a 50/50 mix of these two phases to the Baseline Marias Pass Murray Bedrock geochemistry. The addition of Ca-sulfate yielded a slight increase in Σ_{abs} for each geochemistry (~0.003 cm^2/g per 5 vol.% Ca-sulfate) that is within 1σ uncertainties of our simulated geochemistries (Table 2.1, Chapter 2) and of our derived results (Table 2.3, Chapter 2). As such, our simulations do not include Ca-sulfate.

Text A.4

DAN acquired a total of 28 active measurements in Marias Pass from sol 991 - 1067. 16 DAN active measurements were coadded into six coadded measurements (Sites 4, 5, 10, 12, 15, and 16) and ten other DAN active measurements met our SNR criteria individually (Sites 1 - 3, 6 - 9, 11, 13, and 14). Results from these sites are included in Table 2.3 (Chapter 2). Two DAN active measurements did not meet the SNR or coaddition requirements and were not further analyzed.

DAN acquired six active measurements at Site 16 on the south side of Marias Pass during the 2015 solar conjunction when the rover was stationary for > 1 month. The Chemistry and Camera (ChemCam) target "Mission" is near the center of the DAN FOV at Site 16 and has a geochemistry representative of the Baseline Marias Pass Murray Bedrock (Table 2.1, Chapter 2), which is well-exposed at this site. Site 16 is located ~25 meters southwest of the high-SiO_2 material exposed at the surface

in the Lion area and is at the same elevation (~-4447 meters). Markov-Chain Monte Carlo (MCMC) optimization of model grid 1 (Table 2.2, Chapter 2) with Site 16 data produced a Σ_{abs} significantly lower than the surface geochemistry of the Mission target. This motivated the creation of a 2-layer model grid (model grid 2A) with a top layer of Baseline Marias Pass Murray Bedrock geochemistry and a bottom layer that varied Σ_{abs} from the lowest-Σ_{abs} bedrock geochemistry in Marias Pass (High-SiO_2 Murray in Table 2.1, Chapter 2) to the highest-Σ_{abs} bedrock geochemistry in Marias Pass (Baseline Marias Pass Murray Bedrock). The parameter ranges of model grid 2A span the reasonable water-equivalent hydrogen (WEH) and Σ_{abs} values for Sites 15 and 16 and were used for MCMC analyses at these sites.

Sites 1 - 10, in northeastern Marias Pass, are covered by sand/rubble of unknown composition. MCMC optimization of model grid 1 with these sites indicated that high-SiO_2/low-FeO_T material was present in the subsurface at all but one of these sites, motivating the creation of a 2-layer model grid (model grid 2B) with low-Σ_{abs} material in the lower layer. The top layer geochemistry of the sand/rubble at these sites was unknown, but it potentially contained not only regional wind-blown sand, but also eroded Murray and Stimson material from the local area. Model grid 2B has a top layer Σ_{abs} variable over a range which encompasses the average Stimson from ChemCam targets in Marias Pass, the Baseline Marias Pass Murray Bedrock from ChemCam targets, and regional wind-blown sand averaged from the Alpha-Particle X-ray Spectrometer (APXS) targets "Kelso" and "Dumont" in the Pahrump Hills area (the closest sand targets to Marias Pass). The bottom layer of this model grid contains the high-SiO_2 composition observed at the surface in the Lion area and consistent with the subsurface at Site 16. The parameter ranges of model grid 2B span the reasonable WEH and Σ_{abs} values for Sites 1 - 10 and were used for MCMC analyses at these sites. MCMC optimization of model grid 2B with Site 5, 6, 8, and 10 data resulted sand/rubble layer thicknesses greater than 10 cm, and this optimization was used in our final analyses at these sites. MCMC optimization of model grid 2B with Sites 1, 3, 4, 7, and 9 data indicated a surface sand/rubble layer thickness of less than 5 cm, so the simpler model grid 1 was used for final analyses at these sites. MCMC optimization of model grid 1 with Site 2 is not consistent with high-SiO_2 material. This site is located in a small topographic depression, which may have accumulated a thick deposit of unconsolidated sand/rubble. Although visual evidence is not conclusive on the thickness of such a surface deposit, the DAN passive count rates and DAN active results from Sites 1 and 3 - 10 indicate high-SiO_2 bedrock underlies surface deposits in this area of Marias Pass.

Sites 11 - 13 in northwestern Marias Pass are also covered by sand/rubble of unknown composition. MCMC optimization of model grid 1 with data from these sites produced high Σ_{abs}, indicating that there is no significant low-Σ_{abs} material in the top 50 cm of the subsurface. An examination of rover imagery via the OnSight tool shows that the northwestern section of Marias Pass contains thick sand with large broken bedrock blocks at various orientations, indicating that this material has been transported. ChemCam compositions from these broken blocks ("Edith", "Scheffer", and "Finley") are consistent with the Stimson target "Ronan drt 2" in Marias Pass, and they are likely remnants of the Stimson transported to fill in a topographic low.

Text A.5

To quantify the mean best-fit parameter values (WEH, Σ_{abs}, and depth) and associated uncertainties for our DAN active measurements, we employ a Markov-Chain Monte Carlo analysis routine as in Gabriel et al. (2018) that utilizes the EMCEE package (Foreman-Mackey et al., 2013) for the Python Programming Language and

the corner plotting package to visualize results (Foreman-Mackey, 2013). Our MCMC analyses compare simulation results with multiple variable parameters to a single (or coadded) DAN active measurement. The likelihood function value (a measure of goodness-of-fit) is computed for each model simulated compared to the DAN active data product. Then 40 "walkers" are created according to *a priori* parameter estimates. The walkers then traverse the parameter space according to the affine-invariant ensemble sampler algorithm (Goodman & Weare, 2010) in an effort to maximize the negative log of the likelihood function. We set the number of iterations (walker steps) to 20000. The walker positions after 18000 iterations are used to eliminate effects from *a priori* or to remove "burn-in" steps. We also performed MCMC optimizations at a greater number of iterations in several cases with insignificant changes to the results.

The results of our MCMC analyses of all DAN active measurements analyzed for this work are provided as corner plots in Figures A.1 – A.16, where Figure A.1 corresponds to Site 1, Figure A.2 corresponds to Site 2, etc. Parameter values sampled by each walker for steps 18001 - 20000 are represented by a point in each scatter plot. In areas with points beyond a density threshold, contour lines are plotted in which the darker pixels represent areas of greater point density. The histogram at the top of each column shows the binned counts for that column's parameter. The f parameter is a measure of underestimated uncertainty. Parameter values with uncertainties in Table 2.3 (Chapter 2) were determined by fitting a Gaussian to the corresponding histogram distribution. Reported uncertainties are one standard deviation from the Gaussian mean. For more details concerning MCMC analysis see Foreman-Mackey et al. (2013) and Gabriel et al. (2018).

Text A.6

Mastcam multispectral images are calibrated based on pre-flight calibration coefficients and calibration target observations. The resulting I/F-calibrated images are converted to relative radiance (also called R*) by dividing by the cosine of solar incidence angle (Bell III et al., 2017). In each observation, representative Mastcam spectra of each lithology in the scene are extracted by manually selecting pixels from common regions of interest (ROIs) in the right and left camera images (Rice et al., 2019; Starr et al., 2019). Spectra from the two cameras are joined by normalizing to the average R* value of the overlapping left- and right-eye bands at 1013 nm. Errors in band parameters calculated from R* values are calculated from uncertainties in the relative band-to-band derived reflectance, which are estimated as 1 - 2% from the pre-flight calibration of the Mastcam instruments (Bell III et al., 2017).

Table A.1. Mastcam observations in Figure 2.7 (Chapter 2)

Location	Target Name	Sol	Sequence ID
Marias Pass (Site *a*)	Red Horn	994	mcam04398
	Red Sleep	994	mcam04399
Marias Pass (Elk area)	Elk	1041	mcam04560
	Lamoose	1041	mcam04561
	Mosquito_Frog	1041	mcam04562
Marias Pass (Lion area)	Buckskin Drill Tailings	1062	mcam04672
	Buckskin Presieve Dump	1066	mcam04689
Bridger Basin (fracture halos)	Greenhorn Full Drill	1138	mcam05095
	Big Sky Post Sieve Pile	1138	mcam05096

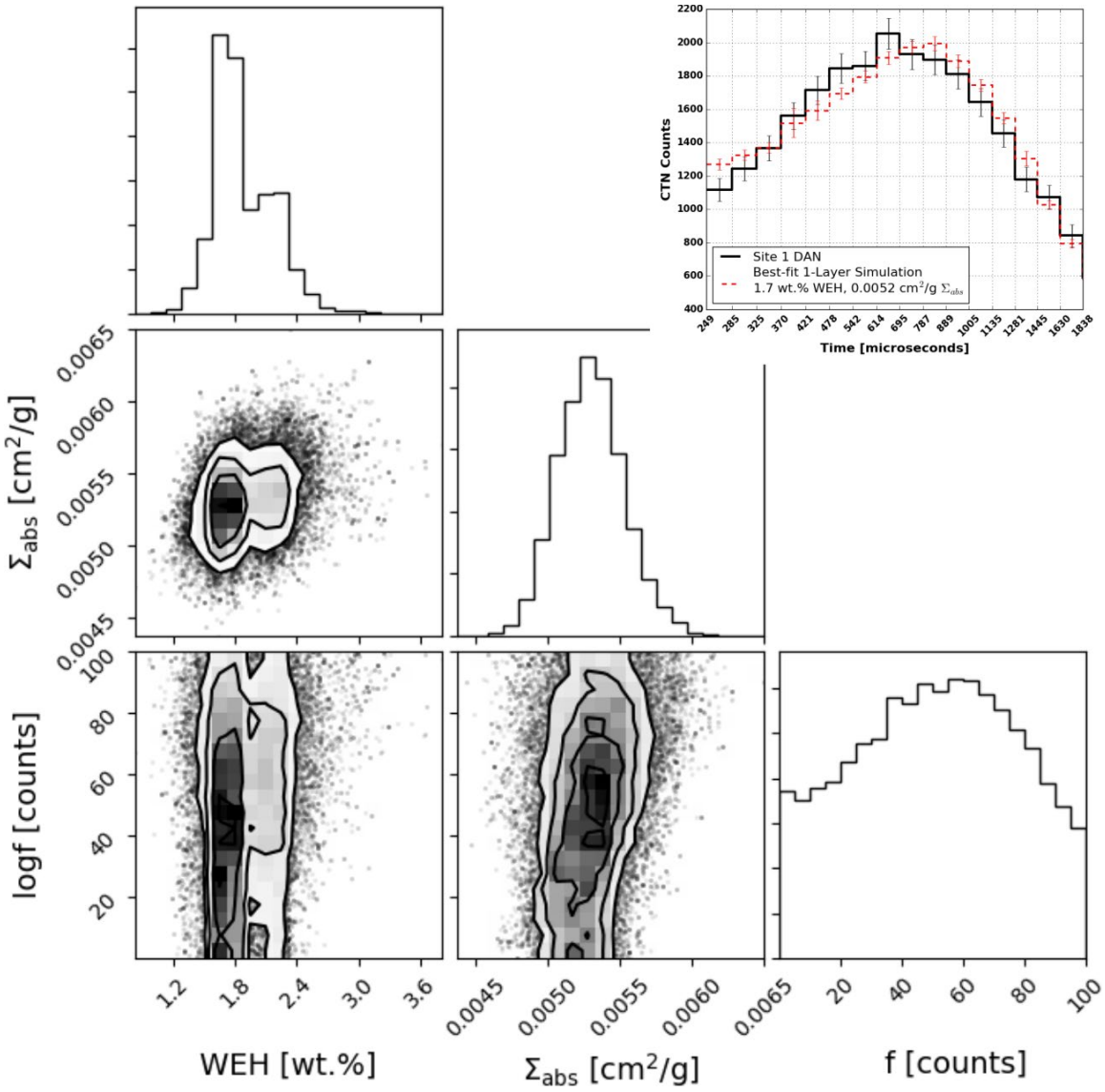

Figure A.1. Corner plot showing MCMC results of Site 1 DAN active measurement compared to model grid 1. Plotted at upper right are the Site 1 DAN die-away curve and best-fit simulation die-away curve. The f histogram trends toward a non-zero value. Taken with the shifted peak position shown in the inset data-model comparison plot, this suggests that the assumptions of this model grid don't exactly reflect the subsurface characteristics of this site. At this location, the rover was on a talus slope with aeolian sand, Stimson and Murray rubble, and Murray bedrock within the surface footprint of DAN. These complexities, which could not be accurately modeled, are likely responsible for the less-than-ideal model precision. Numerical results with uncertainties are summarized for all sites in Table 2.3 (Chapter 2).

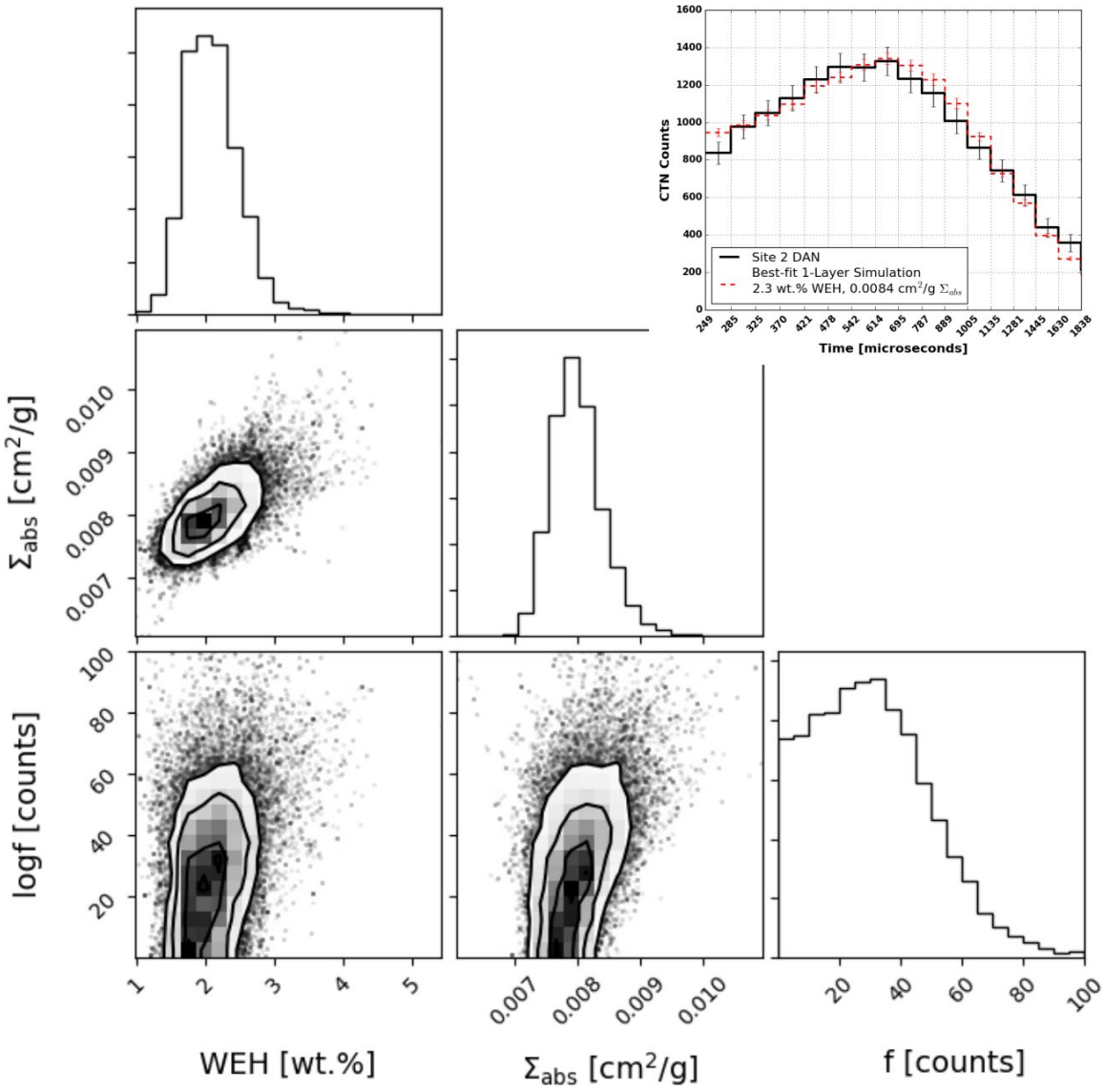

Figure A.2. Corner plot showing MCMC results of Site 2 DAN active measurement compared to model grid 1. Plotted at upper right are the Site 2 DAN die-away curve and best-fit simulation die-away curve. Numerical results with uncertainties are summarized for all sites in Table 2.3 (Chapter 2).

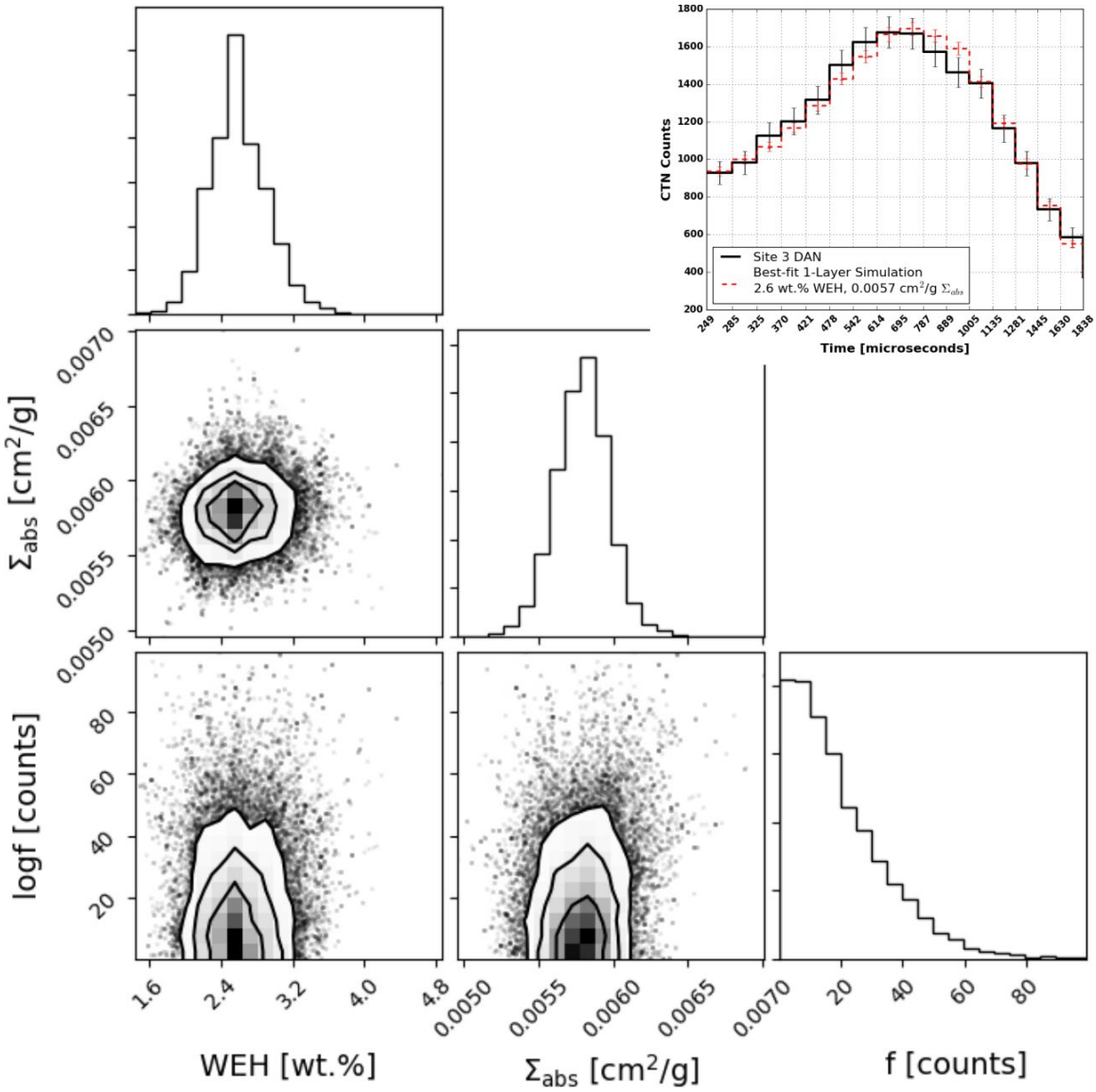

Figure A.3. Corner plot showing MCMC results of Site 3 DAN active measurement compared to model grid 1. Plotted at upper right are the Site 3 DAN die-away curve and best-fit simulation die-away curve. Numerical results with uncertainties are summarized for all sites in Table 2.3 (Chapter 2).

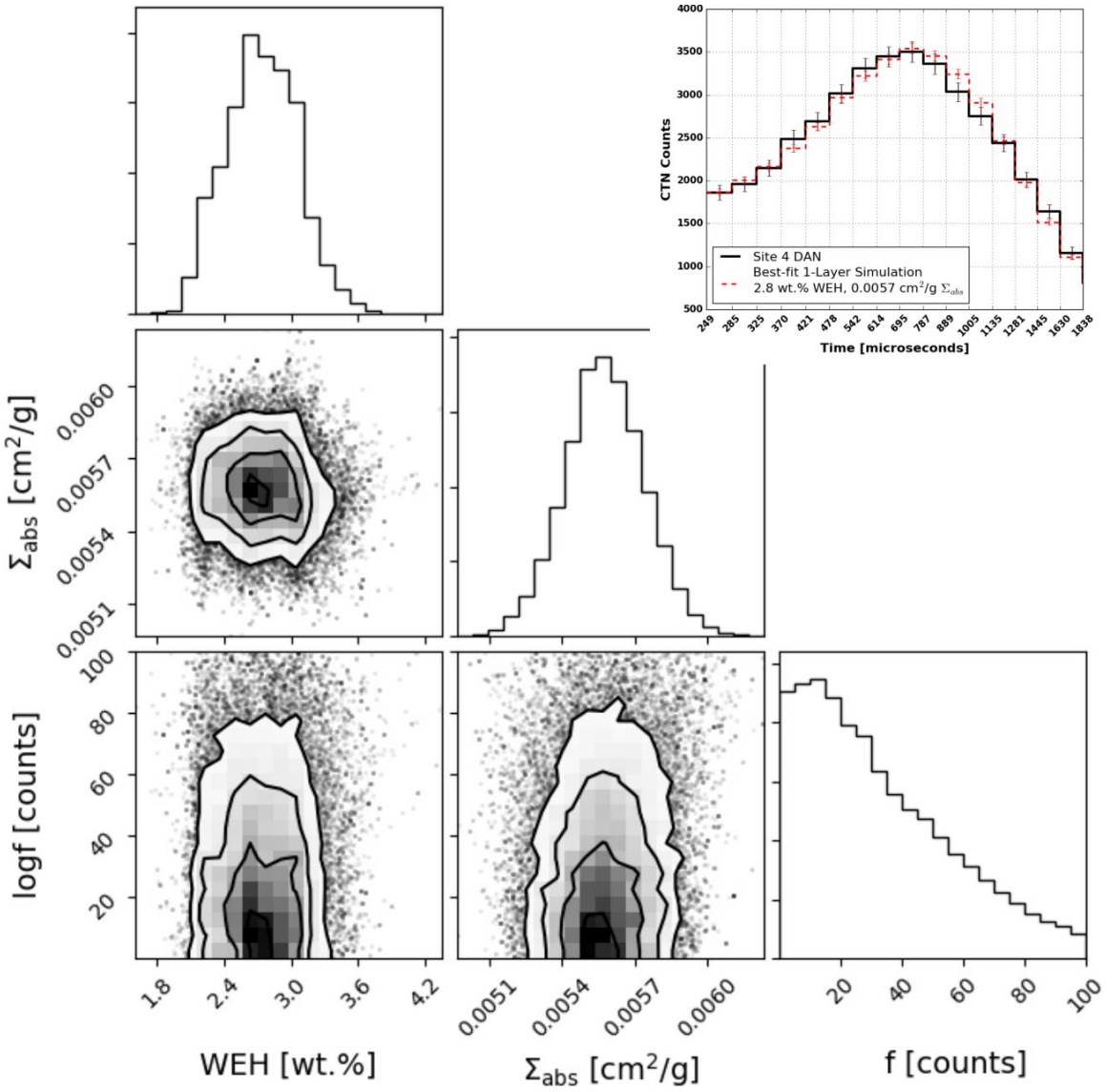

Figure A.4. Corner plot showing MCMC results of Site 4 DAN active measurement compared to model grid 1. Plotted at upper right are the Site 4 DAN die-away curve and best-fit simulation die-away curve. Numerical results with uncertainties are summarized for all sites in Table 2.3 (Chapter 2).

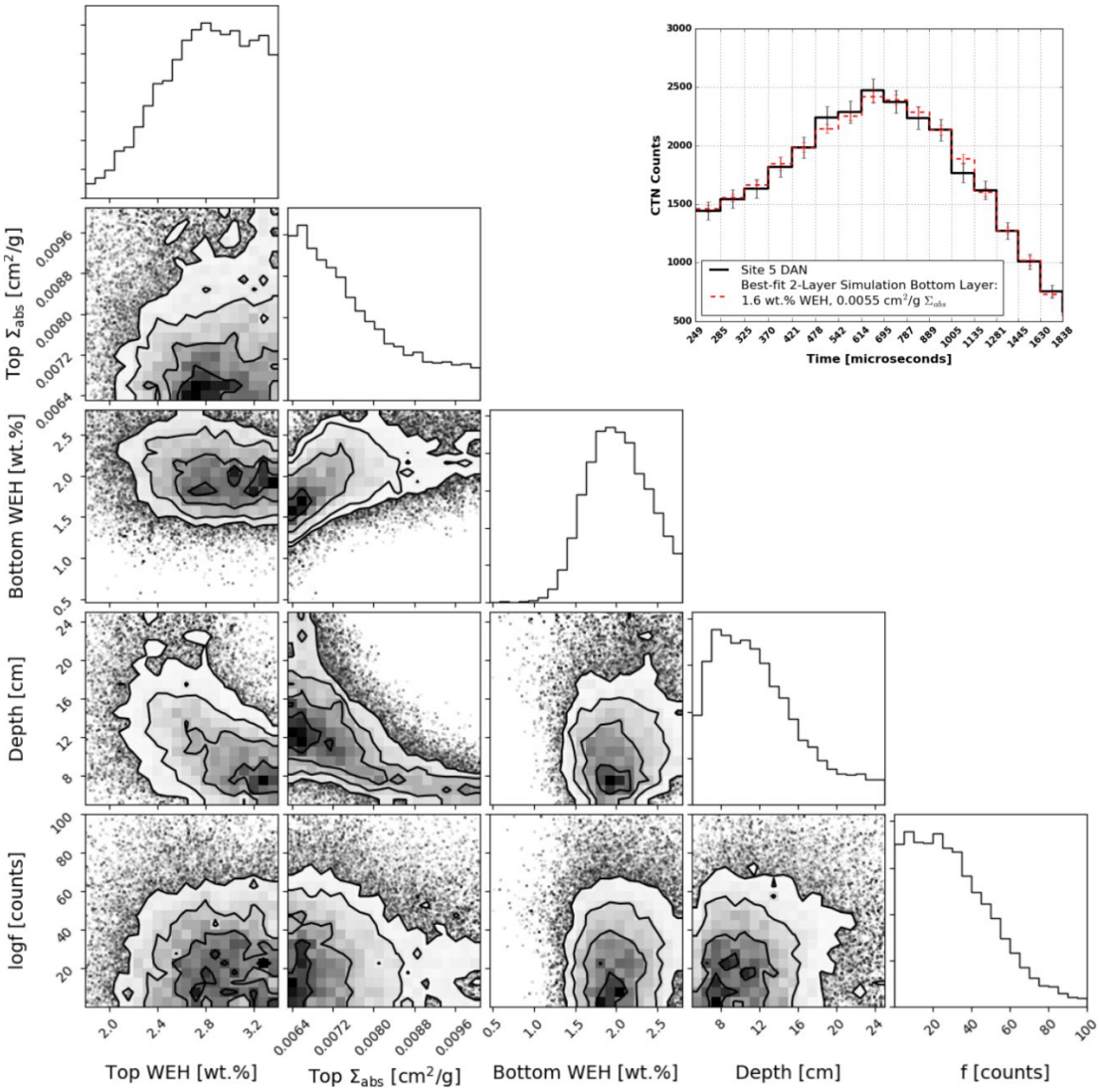

Figure A.5. Corner plot showing MCMC results of Site 5 DAN active measurement compared to model grid 2B. Plotted at upper right are the Site 5 DAN die-away curve and best-fit simulation die-away curve. Numerical results with uncertainties are summarized for all sites in Table 2.3 (Chapter 2).

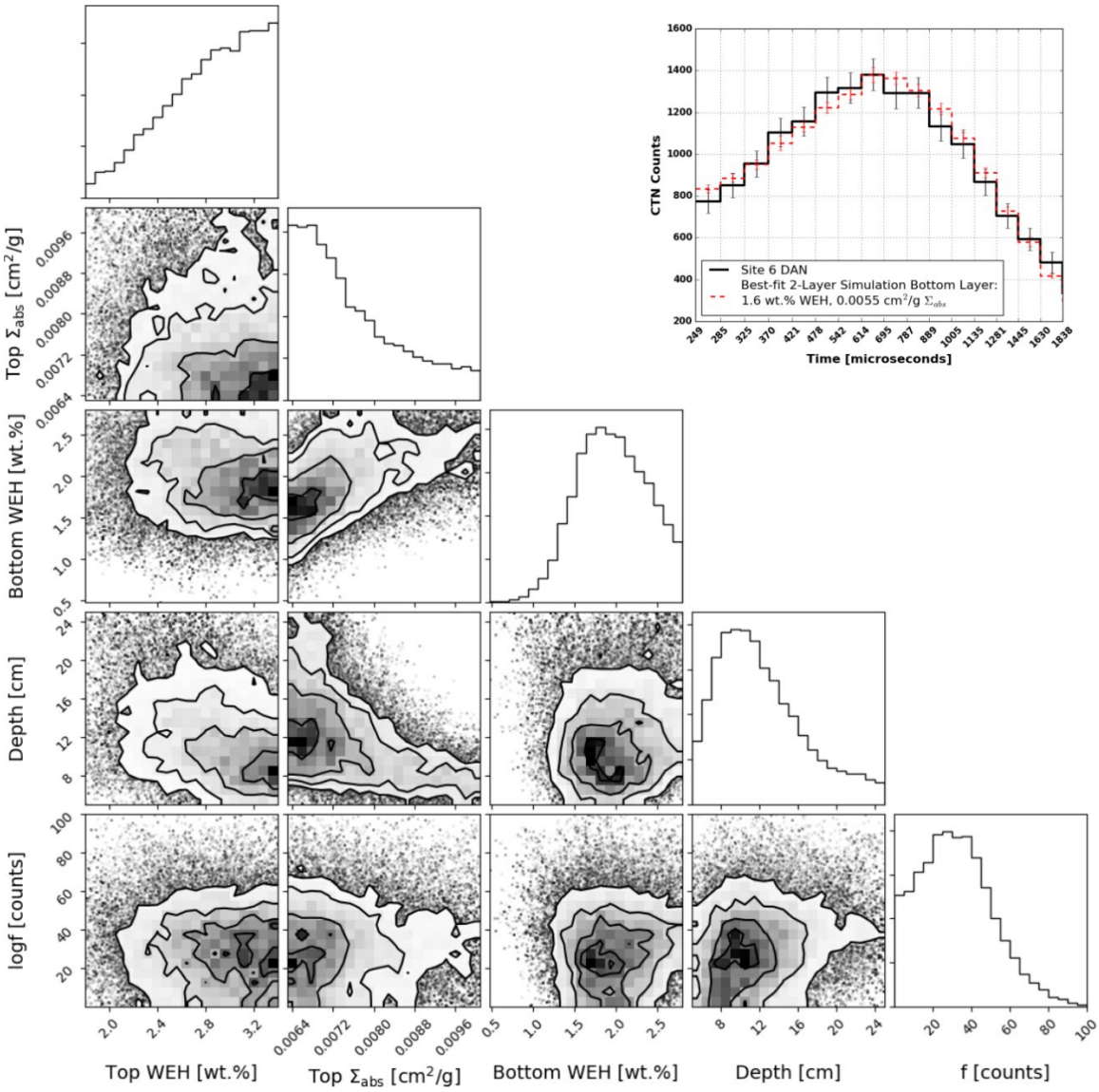

Figure A.6. Corner plot showing MCMC results of Site 6 DAN active measurement compared to model grid 2B. Plotted at upper right are the Site 6 DAN die-away curve and best-fit simulation die-away curve. Numerical results with uncertainties are summarized for all sites in Table 2.3 (Chapter 2).

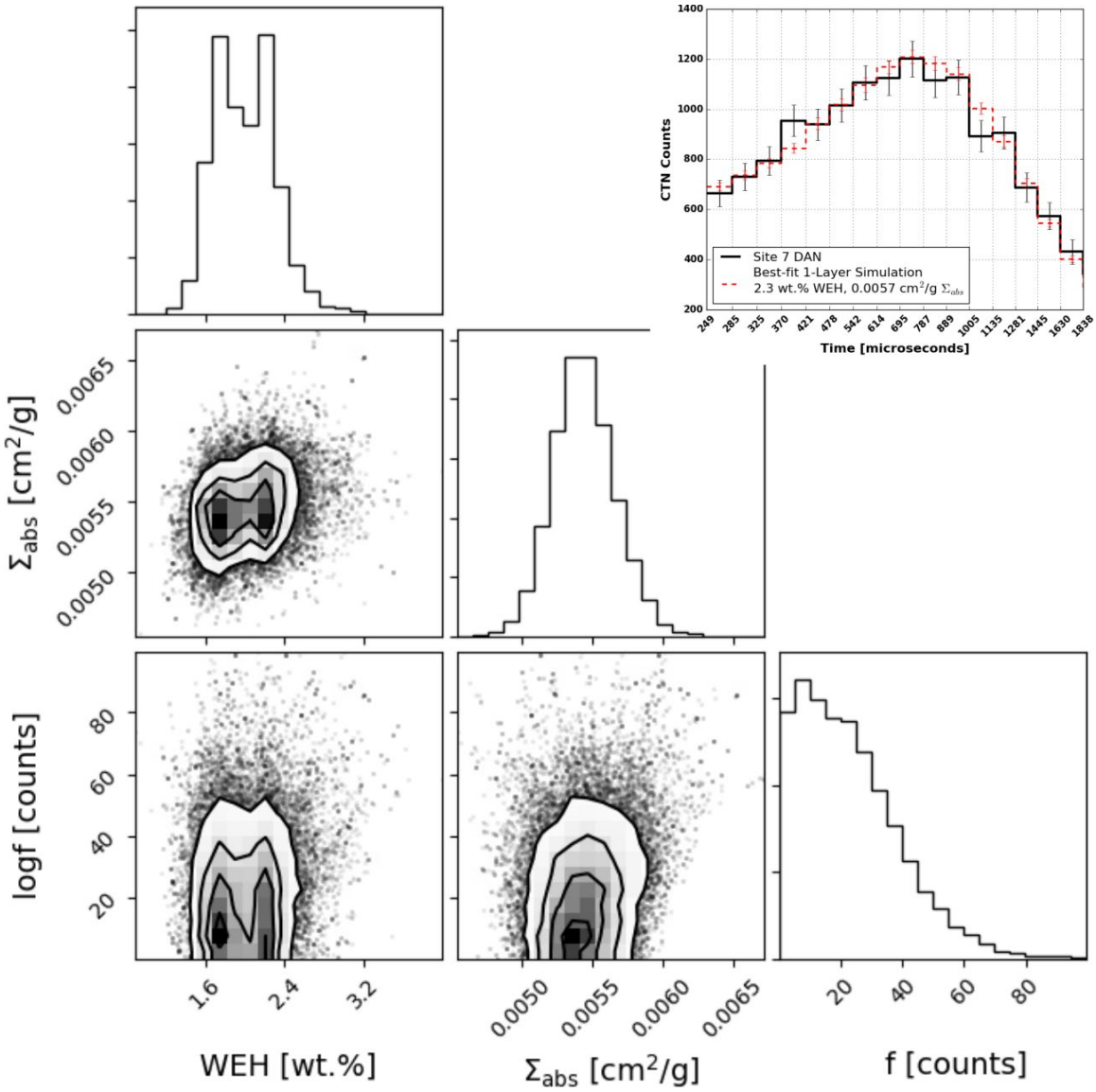

Figure A.7. Corner plot showing MCMC results of Site 7 DAN active measurement compared to model grid 1. Plotted at upper right are the Site 7 DAN die-away curve and best-fit simulation die-away curve. Numerical results with uncertainties are summarized for all sites in Table 2.3 (Chapter 2).

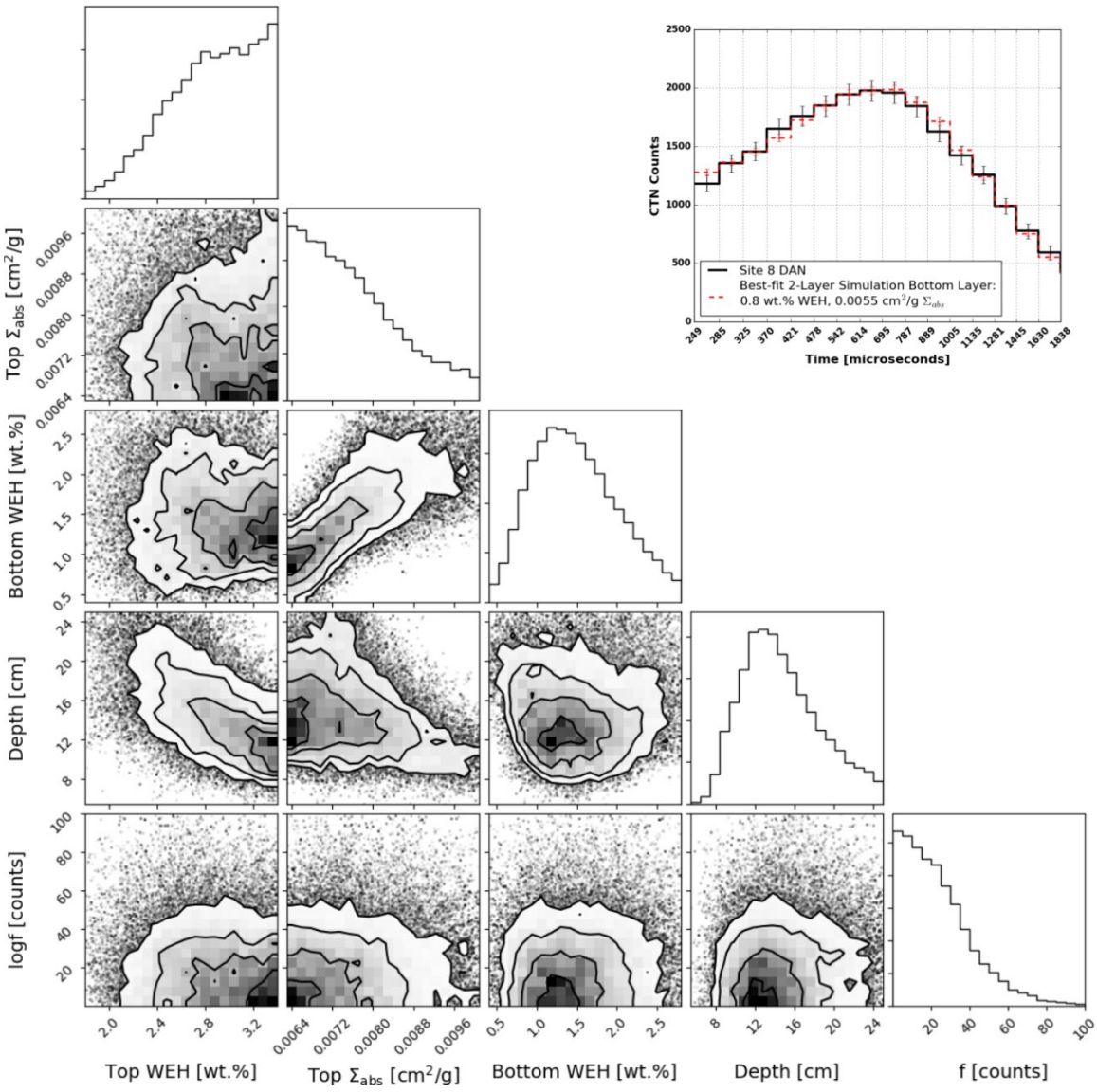

Figure A.8. Corner plot showing MCMC results of Site 8 DAN active measurement compared to model grid 2B. Plotted at upper right are the Site 8 DAN die-away curve and best-fit simulation die-away curve. Numerical results with uncertainties are summarized for all sites in Table 2.3 (Chapter 2).

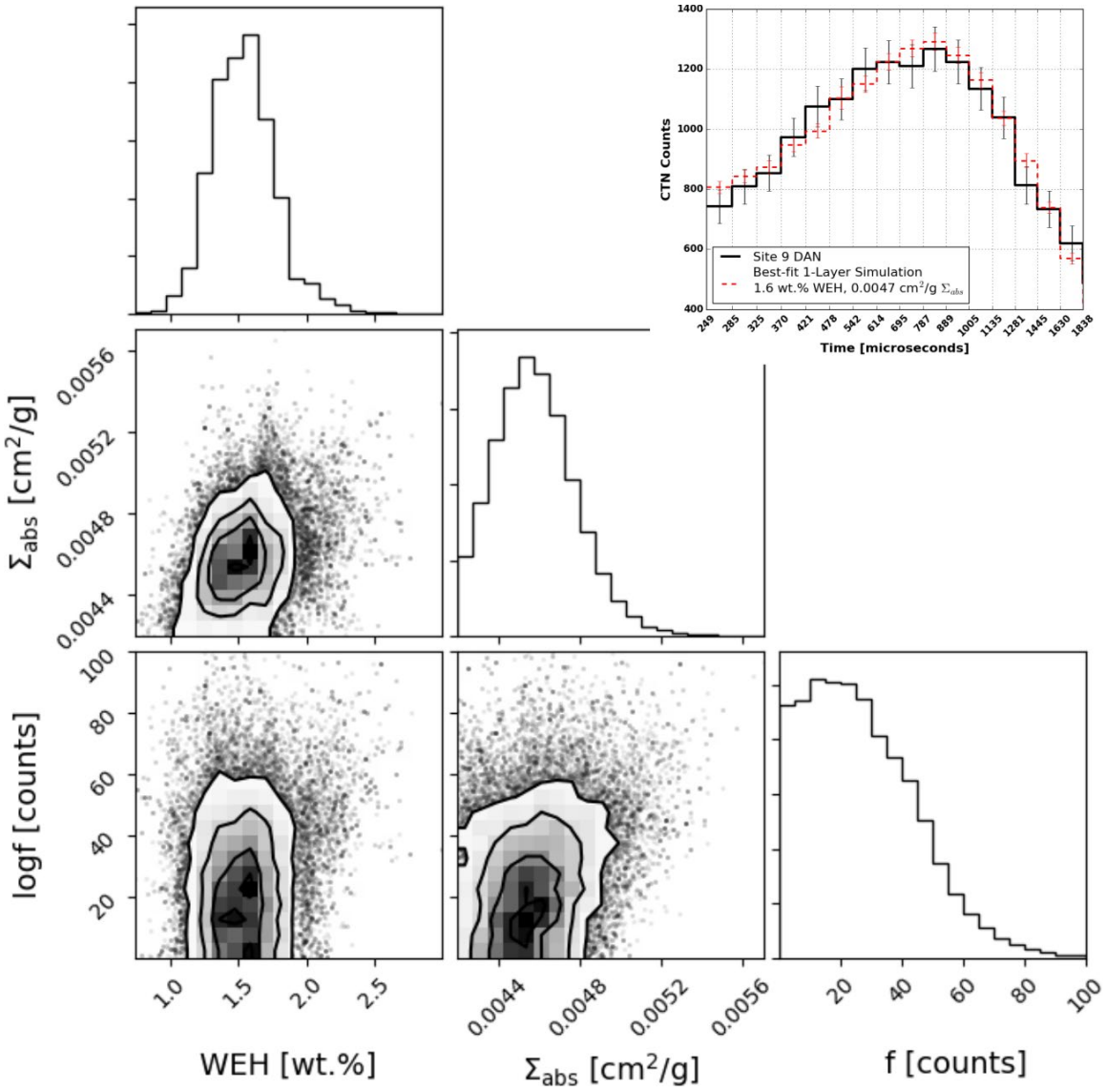

Figure A.9. Corner plot showing MCMC results of Site 9 DAN active measurement compared to model grid 1. Plotted at upper right are the Site 9 DAN die-away curve and best-fit simulation die-away curve. Numerical results with uncertainties are summarized for all sites in Table 2.3 (Chapter 2).

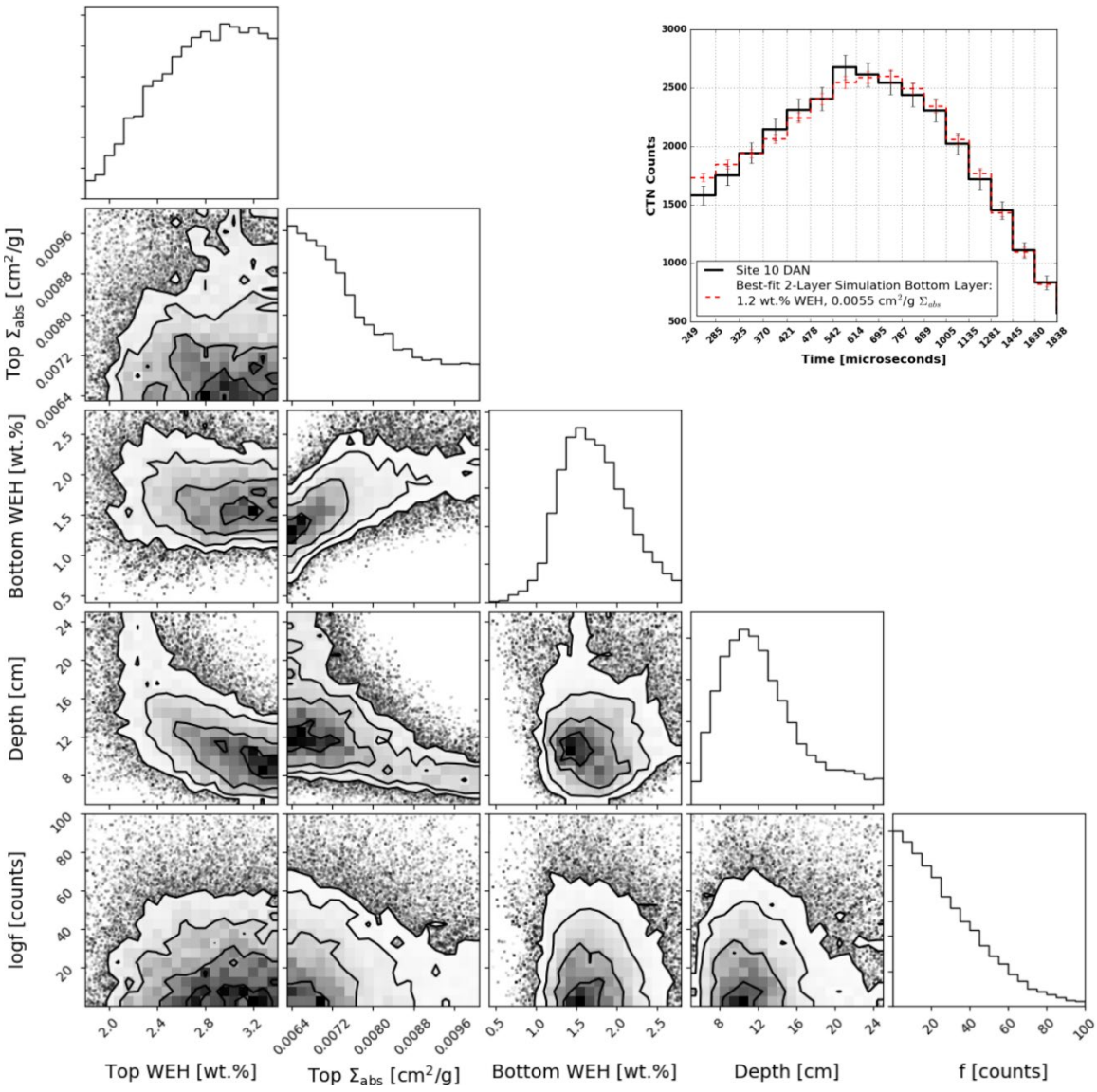

Figure A.10. Corner plot showing MCMC results of Site 10 DAN active measurement compared to model grid 2B. Plotted at upper right are the Site 10 DAN die-away curve and best-fit simulation die-away curve. Numerical results with uncertainties are summarized for all sites in Table 2.3 (Chapter 2).

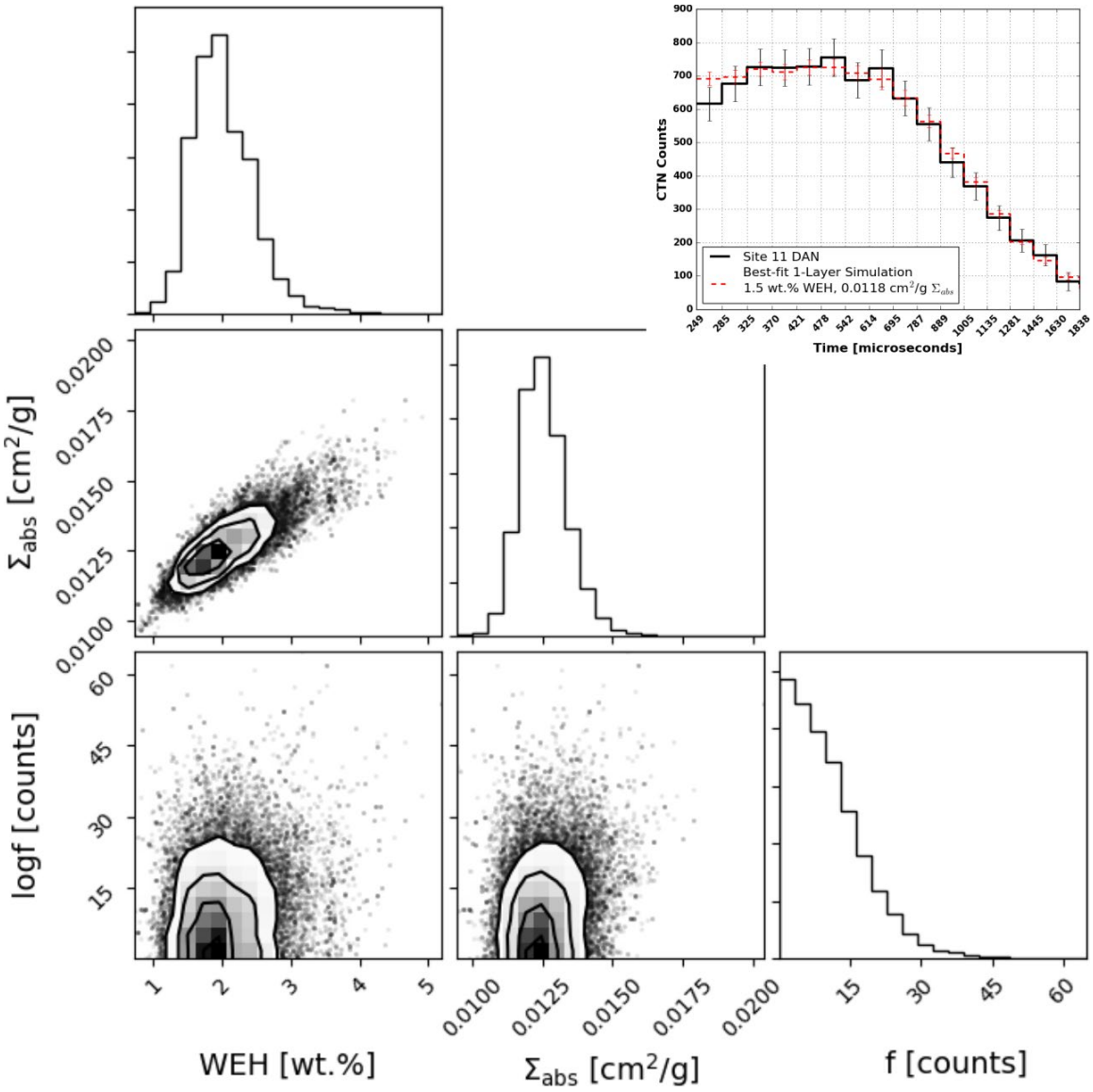

Figure A.11. Corner plot showing MCMC results of Site 11 DAN active measurement compared to model grid 1. Plotted at upper right are the Site 11 DAN die-away curve and best-fit simulation die-away curve. Numerical results with uncertainties are summarized for all sites in Table 2.3 (Chapter 2).

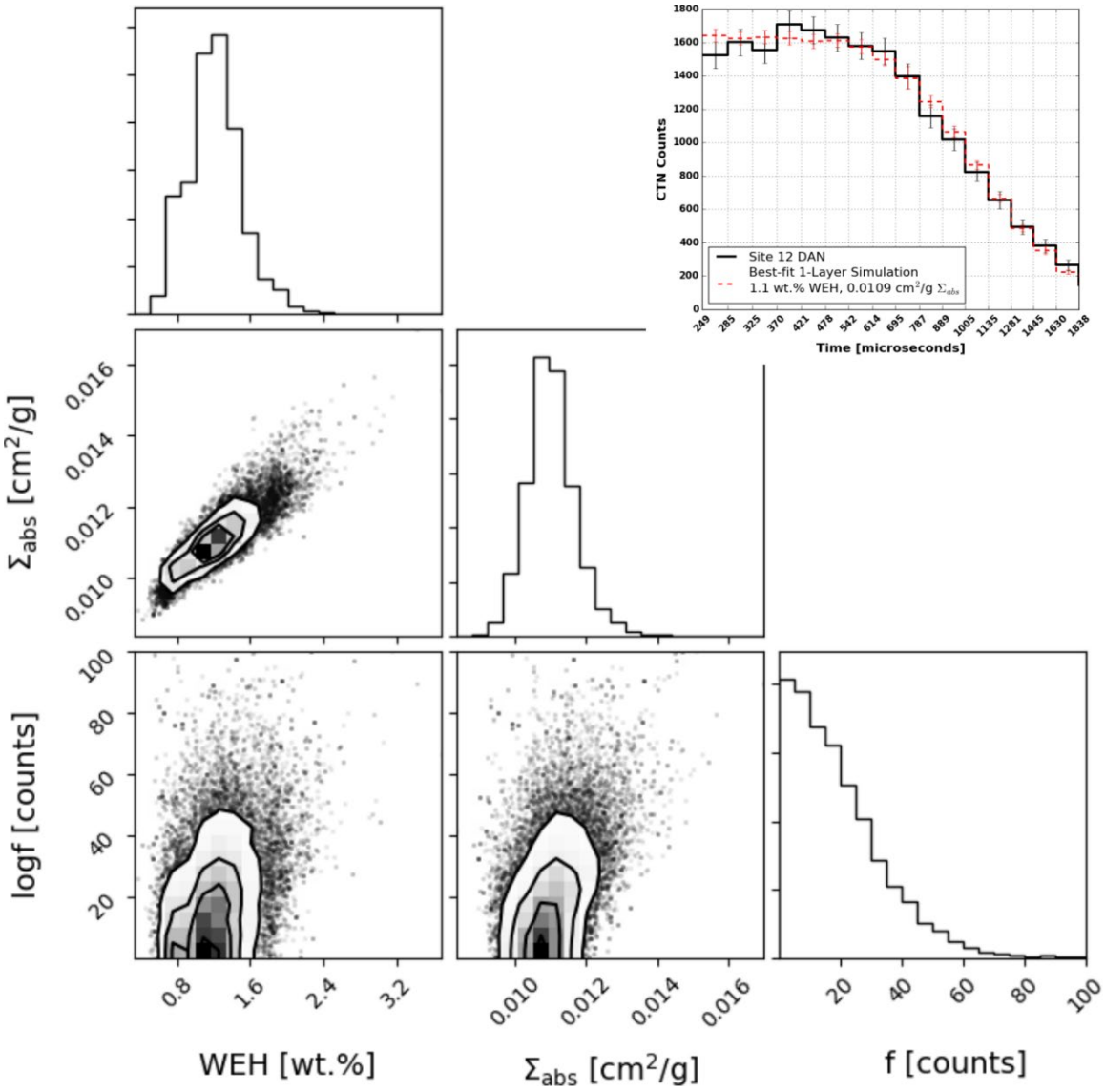

Figure A.12. Corner plot showing MCMC results of Site 12 DAN active measurement compared to model grid 1. Plotted at upper right are the Site 12 DAN die-away curve and best-fit simulation die-away curve. Numerical results with uncertainties are summarized for all sites in Table 2.3 (Chapter 2).

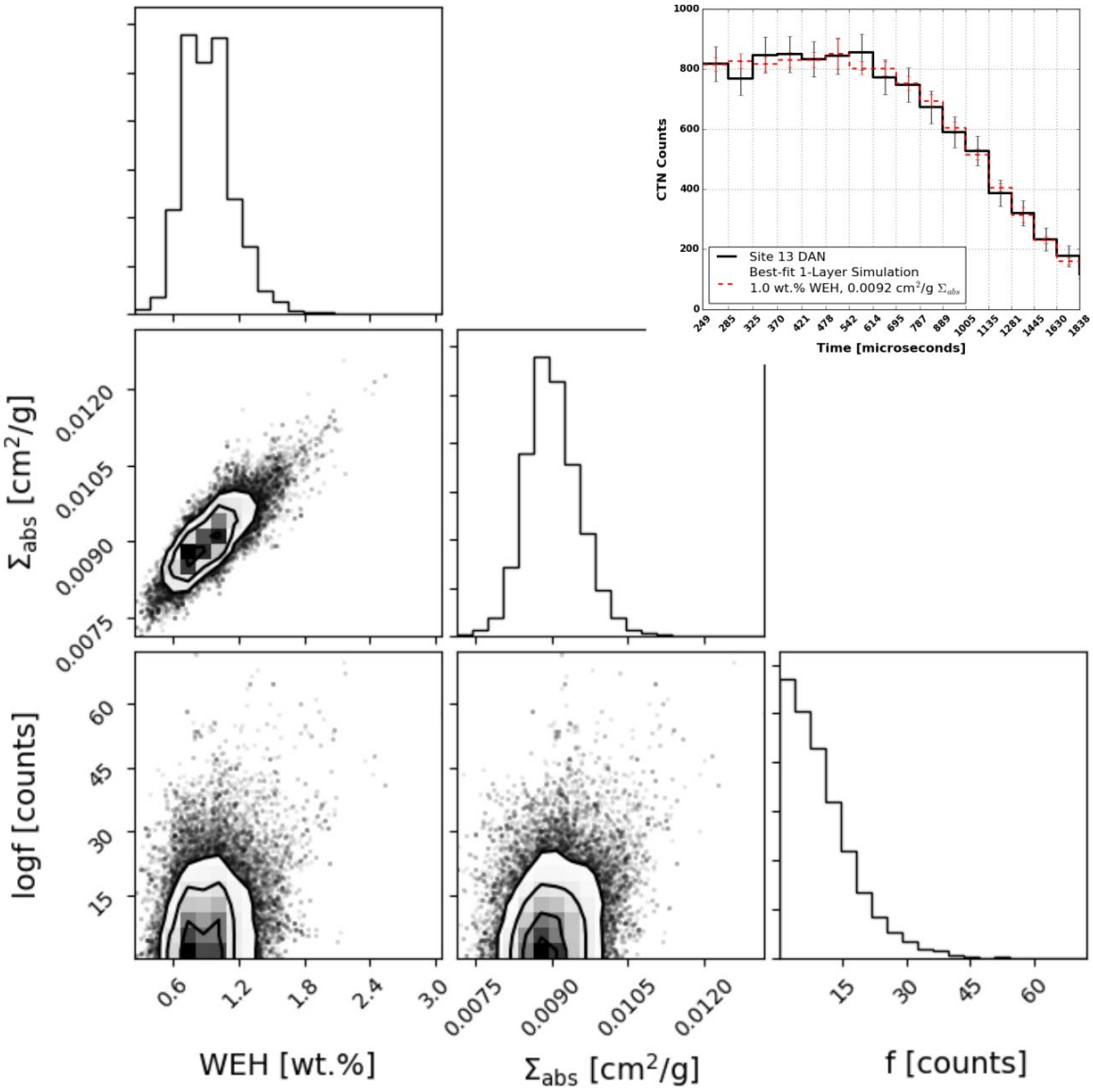

Figure A.13. Corner plot showing MCMC results of Site 13 DAN active measurement compared to model grid 1. Plotted at upper right are the Site 13 DAN die-away curve and best-fit simulation die-away curve. Numerical results with uncertainties are summarized for all sites in Table 2.3 (Chapter 2).

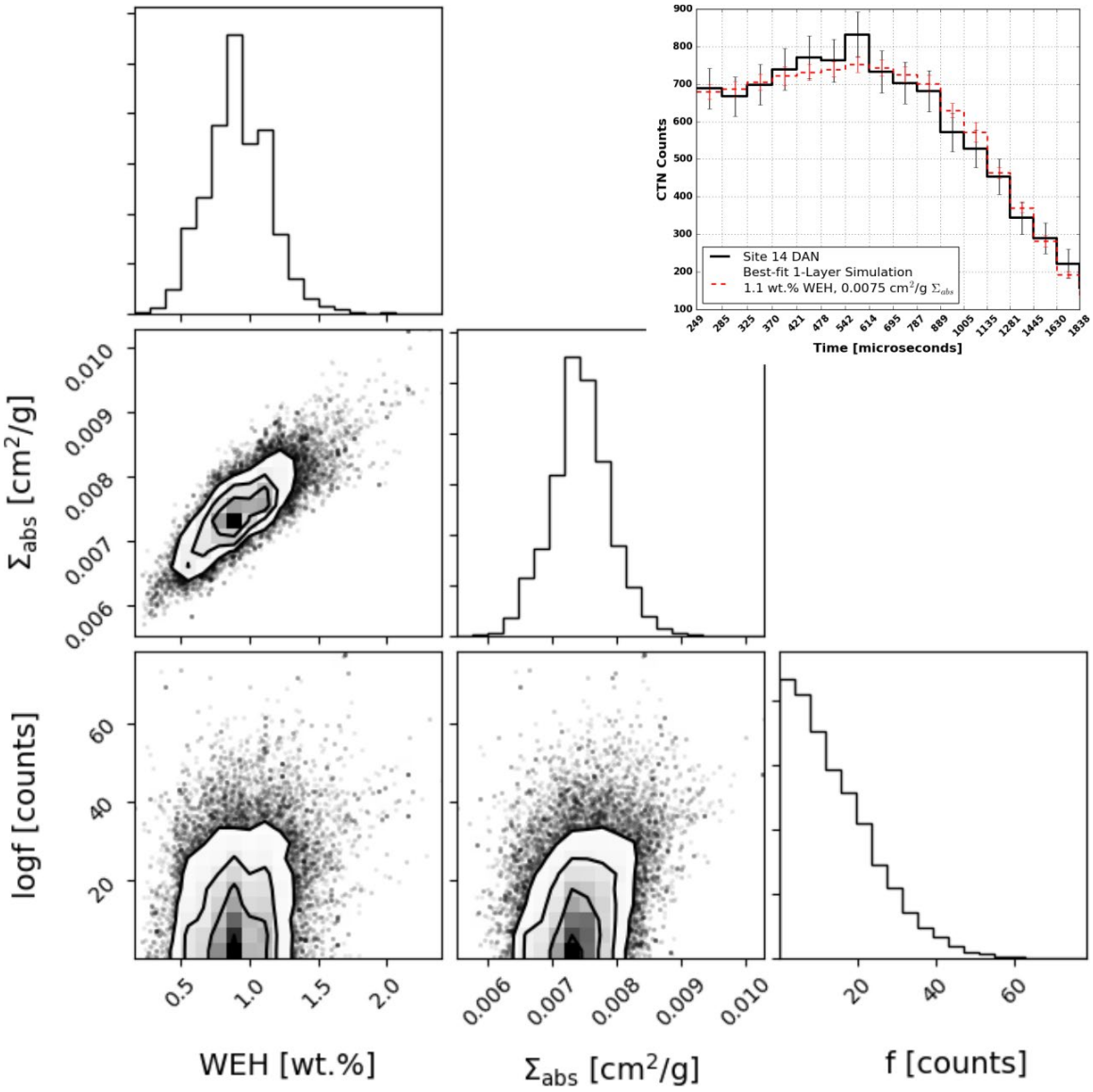

Figure A.14. Corner plot showing MCMC results of Site 14 DAN active measurement compared to model grid 1. Plotted at upper right are the Site 14 DAN die-away curve and best-fit simulation die-away curve. Numerical results with uncertainties are summarized for all sites in Table 2.3 (Chapter 2).

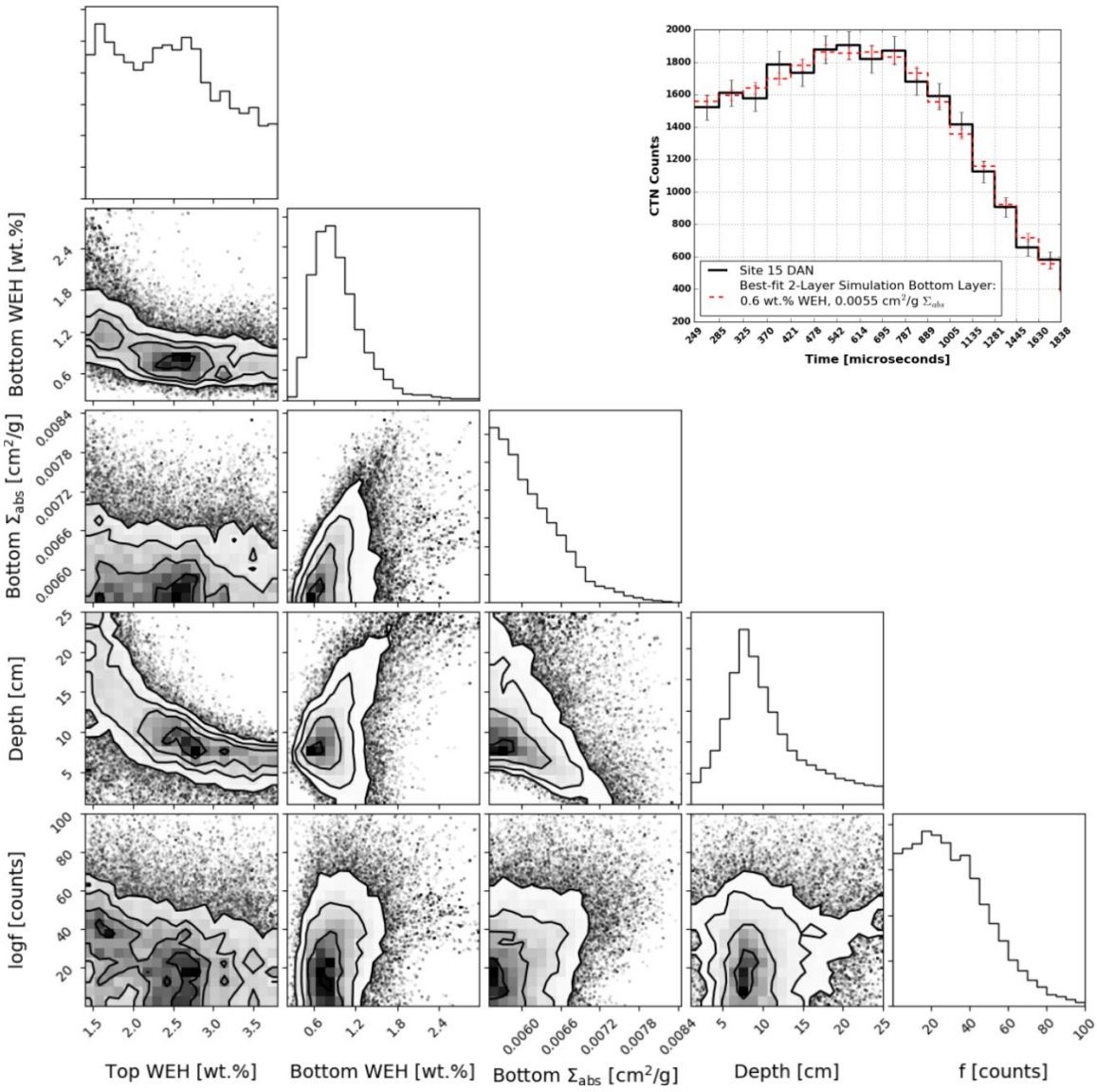

Figure A.15. Corner plot showing MCMC results of Site 15 DAN active measurement compared to model grid 2A. Plotted at upper right are the Site 15 DAN die-away curve and best-fit simulation die-away curve. Numerical results with uncertainties are summarized for all sites in Table 2.3 (Chapter 2).

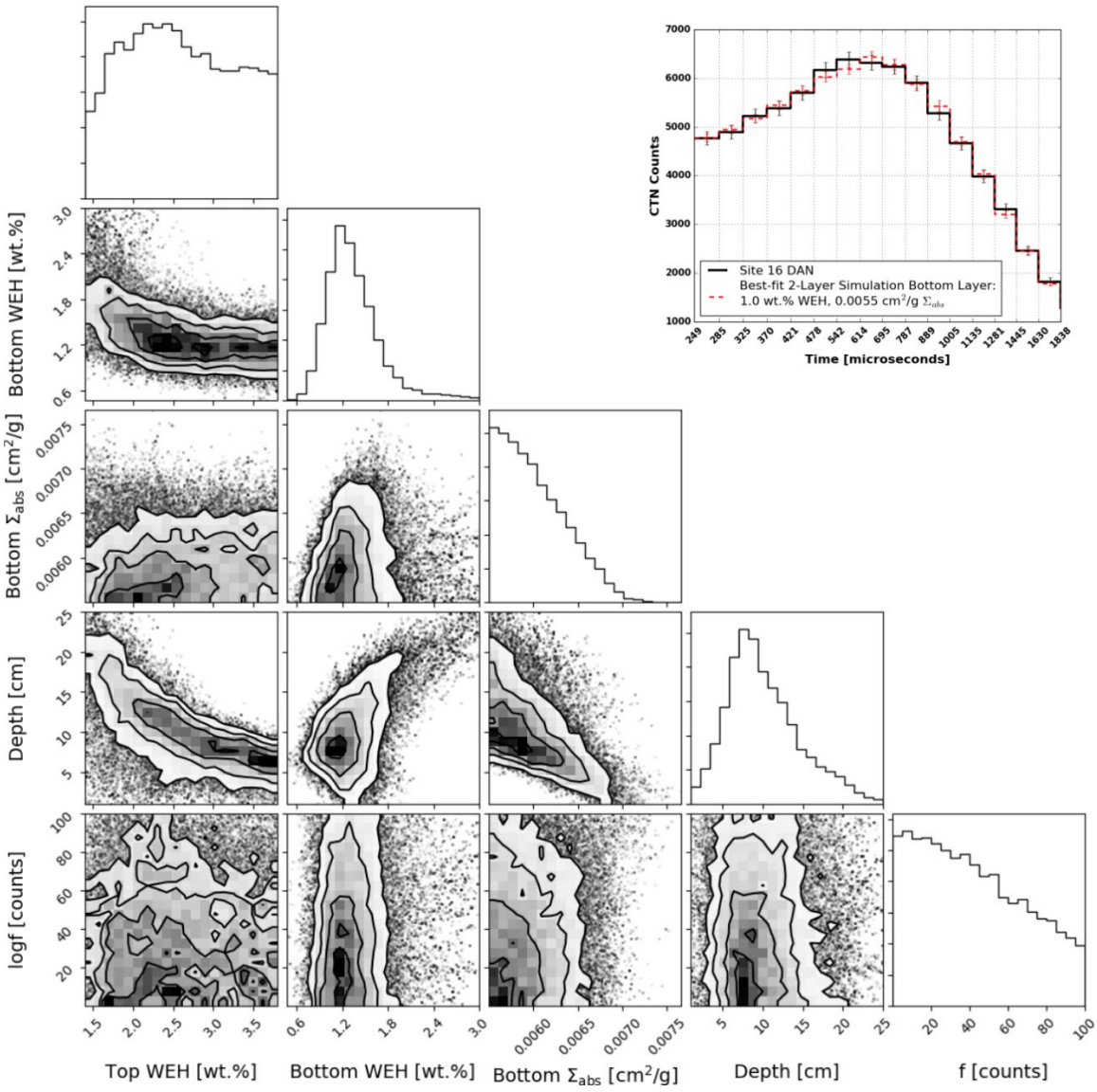

Figure A.16. Corner plot showing MCMC results of Site 16 DAN active measurement compared to model grid 2A; reprinted from Figure 2.6 (Chapter 2) without annotation. Plotted at upper right are the Site 16 DAN die-away curve and best-fit simulation die-away curve. Numerical results with uncertainties are summarized for all sites in Table 2.3 (Chapter 2).

APPENDIX B

PERMISSION STATEMENT FROM CO-AUTHORS FOR CHAPTER 2: "IDENTIFICATION AND DESCRIPTION OF A SILICIC VOLCANICLASTIC LAYER IN GALE CRATER, MARS, USING ACTIVE NEUTRON INTERROGATION"

This chapter was originally published in Journal of Geophysical Research: Planets in 2020 (see reference entry below). It has been reformatted to comply with the ASU Graduate College format manual, and is reproduced here with the permission of the following coauthors: Craig Hardgrove, Patrick Gasda, Travis Gabriel, Mason Starr, Melissa Rice, Jens Frydenvang, Roger Wiens, William Rapin, Sergei Nikiforov, Denis Lisov, Maxim Litvak, Fred Calef, Hallie Gengl, Horton Newsom, Lucy Thompson, and Suzanne Nowicki.

Czarnecki, S., Hardgrove, C., Gasda, P. J., Gabriel, T. S. J., Starr, M., Rice, M., et al. (2020). Identification and description of a silicic volcaniclastic layer in Gale crater, Mars, using active neutron interrogation. *Journal of Geophysical Research: Planets*, 125, e2019JE006180. https://doi.org/10.1029/2019JE006180

APPENDIX C

SUPPLEMENTAL INFORMATION FOR CHAPTER 3: "HYDRATION OF A CLAY-RICH UNIT ON MARS, COMPARISON OF ORBITAL DATA TO ROVER DATA"

Table C.1. DAN Markov-Chain Monte Carlo (MCMC) results used in Chapter 3. Material classifications are those from Figure 3.11 (Chapter 3). Coadded measurements (*) list the sol range within which the coadded measurements were acquired. All coadded measurements are from the same rover location. The sol 1659 measurement is from a sand dune encountered prior to the main study area (Gabriel et al., 2018). This data is also archived on Zenodo (Czarnecki et al., 2022). PPm = Pettegrove Point member, Jm = Jura member, KHm = Knockfarril Hill member, Gm = Glasgow member, Sf = Stimson formation, VRR = Vera Rubin ridge, GT = Glen Torridon, WEH = Water-equivalent hydrogen, Σ_{abs} = Macroscopic thermal neutron absorption cross section

Sol	Coadded Sols	WEH [wt.%]	WEH Error [wt.%]	Σ_{abs} [10^{-3} cm^2/g]	Σ_{abs} Error [10^{-3} cm^2/g]	Unit	Material
1659		0.6800	0.1500	N/A	N/A	Bagnold	sand
1814*	1814-1815	3.1251	0.4995	11.8	0.6	PPm/VRR	bedrock
1819*		3.2780	0.5326	11.7	0.5	PPm/VRR	bedrock
1822*	1822-1826	3.4005	0.5754	13.5	0.7	PPm/VRR	bedrock
1827		3.3915	0.6370	13.5	0.9	PPm/VRR	bedrock
1828		2.8028	0.5499	11.5	0.7	PPm/VRR	bedrock
1830*	1830-1833	3.6019	0.5426	13.6	0.7	PPm/VRR	bedrock
1834		3.2493	0.5285	10.8	0.5	PPm/VRR	bedrock
1837		4.1399	0.7006	12.8	0.6	PPm/VRR	bedrock
1843		3.4183	0.7272	13.2	0.9	PPm/VRR	bedrock
1846		2.7563	0.4751	12.4	0.8	PPm/VRR	bedrock
1848*	1848-1849	3.5311	0.5701	12.3	0.5	PPm/VRR	bedrock
1850		1.6952	0.3763	9.5	0.6	PPm/VRR	bedrock
1864		3.5412	0.8783	12.5	1.0	PPm/VRR	bedrock
1867		2.4350	0.5136	10.0	0.7	PPm/VRR	bedrock
1869*	1869-1870	2.7116	0.4236	11.5	0.6	PPm/VRR	bedrock
1871		2.1060	0.3696	10.0	0.6	PPm/VRR	bedrock
1877		2.2455	0.4198	11.2	0.7	Jm/VRR	regolith
1894		2.4342	0.4203	12.7	0.8	Jm/VRR	regolith
1903*	1903-1905	4.1560	0.9890	18.7	1.2	Jm/VRR	regolith
1905		2.4464	0.6741	18.2	1.8	Jm/VRR	regolith
1910		2.8617	0.7418	15.8	1.6	Jm/VRR	regolith
1923		2.6680	0.4910	13.9	0.9	Jm/VRR	regolith
1928		2.6167	0.5262	14.6	1.2	Jm/VRR	regolith
1930*	1930-1934	3.5359	0.6724	16.6	1.0	Jm/VRR	bedrock
1944		3.2797	0.5708	12.6	0.7	Jm/VRR	regolith
1946		3.3545	0.6510	11.5	0.6	Jm/VRR	regolith
1949		3.7739	0.7138	14.0	0.9	Jm/VRR	regolith
1950*	1950-1957	3.6335	0.7936	18.1	1.4	Jm/VRR	regolith
1962*	1962-1983	3.3234	0.6324	16.4	1.1	Jm/VRR	regolith
1998		2.1831	0.3940	11.7	0.8	Jm/VRR	regolith
1999		3.4606	0.7294	12.1	0.8	PPm/VRR	regolith

Sol	Coadded Sols	WEH [wt.%]	WEH Error	Σ_{abs} [10^{-3} cm^2/g]	Σ_{abs} Error	Unit	Material
2003		3.0914	0.5824	11.7	0.7	PPm/VRR	regolith
2009		2.7412	0.4985	11.7	0.8	PPm/VRR	regolith
2012		1.9562	0.4310	10.0	0.7	PPm/VRR	regolith
2017*	2017-2018	3.5172	0.7917	13.6	1.0	Jm/VRR	regolith
2020		2.9051	0.5358	10.0	0.6	PPm/VRR	regolith
2023		2.8226	0.5428	11.9	0.7	PPm/VRR	regolith
2027		2.8416	0.5534	12.4	0.8	PPm/VRR	regolith
2039		3.5818	0.7102	12.9	0.7	PPm/VRR	bedrock
2040		3.4435	0.5738	11.7	0.6	PPm/VRR	bedrock
2044		2.6187	0.4595	11.9	0.7	PPm/VRR	bedrock
2157*	2157-2161	2.6693	0.5308	12.5	0.7	Jm/VRR	regolith
2163*	2163-2166	2.9325	0.4418	14.2	0.6	Jm/VRR	regolith
2222*	2222-2245	3.4170	0.6417	16.6	0.9	Jm/VRR	regolith
2298		2.3431	0.4321	12.7	0.9	Jm/VRR	regolith
2299		3.6957	0.7016	12.3	0.7	KHm/VRR	regolith
2300		3.0275	0.5253	11.6	0.7	KHm/VRR	regolith
2302		3.9058	0.7454	11.4	0.6	Jm/GT	regolith
2304		3.7999	0.6520	11.6	0.6	Jm/GT	regolith
2306		4.4788	0.7255	11.3	0.5	Jm/GT	regolith
2309		4.6738	0.7022	11.1	0.5	Jm/GT	regolith
2311		3.2511	0.6093	11.2	0.6	Jm/GT	regolith
2313		3.8153	0.5949	11.6	0.5	Jm/GT	regolith
2316*	2316-2319	3.9237	0.6303	12.5	0.5	Jm/GT	regolith
2320*	2320-2333	3.6896	0.5877	10.5	0.4	Jm/GT	regolith
2338		4.4807	0.7256	10.4	0.5	Jm/GT	regolith
2350		3.6186	0.6312	10.9	0.5	Jm/GT	regolith
2352		3.5262	0.6318	11.1	0.6	Jm/GT	regolith
2354		4.7177	0.9166	11.4	0.7	Jm/GT	regolith
2357		3.3409	0.5986	11.2	0.6	Jm/GT	regolith
2359		4.7483	1.0368	11.3	0.7	Jm/GT	regolith
2361		4.3778	0.8494	11.8	0.6	Jm/GT	regolith
2364		4.0449	0.6671	11.8	0.6	Jm/GT	regolith
2381*	2381-2404	3.4663	0.6009	12.5	0.6	Jm/GT	regolith
2407*		2.9144	0.4984	10.6	0.6	Jm/GT	regolith
2408*	2408-2411	4.1042	0.5640	10.4	0.4	Jm/GT	regolith
2412		3.9219	0.7534	10.8	0.6	Jm/GT	regolith
2413		2.7169	0.4855	9.9	0.6	Jm/GT	regolith
2414		4.2123	0.7585	10.7	0.6	Jm/GT	regolith
2416		5.0451	0.8907	12.0	0.7	Jm/GT	regolith
2429		4.5659	0.7640	12.1	0.6	Jm/GT	regolith
2432		3.0435	0.5739	10.4	0.6	Jm/GT	regolith

Sol	Coadded Sols	WEH [wt.%]	WEH Error [wt.%]	Σ_{abs} [10^{-3} cm^2/g]	Σ_{abs} Error [10^{-3} cm^2/g]	Unit	Material
2435		3.9870	1.0528	12.3	0.9	Jm/GT	regolith
2436		3.8765	0.8213	11.4	0.7	Jm/GT	regolith
2439*	2439-2446	4.5512	0.7604	12.8	0.5	Jm/GT	regolith
2448		3.4458	0.6660	11.4	0.7	Jm/GT	regolith
2454*	2454-2458	3.5143	0.6220	13.1	0.7	KHm/GT	regolith
2459		3.0712	0.6335	11.1	0.7	KHm/GT	regolith
2463*	2463-2466	3.6440	0.7130	13.2	0.8	KHm/GT	regolith
2466		4.9327	0.8934	13.7	0.7	KHm/GT	regolith
2468*	2468-2472	4.5631	0.7751	15.1	0.7	KHm/GT	regolith
2473		3.5926	0.6381	12.0	0.7	KHm/GT	regolith
2475		4.2469	0.8214	12.2	0.7	KHm/GT	regolith
2476		4.1791	0.6687	10.7	0.5	KHm/GT	regolith
2480		4.5637	0.7795	12.3	0.6	KHm/GT	regolith
2555		3.6697	0.7271	11.3	0.7	KHm/GT	regolith
2556*	2556-2559	3.8909	0.5081	11.3	0.4	KHm/GT	regolith
2559*	2559-2562	3.9992	0.5951	10.3	0.5	KHm/GT	regolith
2565*	2565-2568	4.2902	0.8018	14.5	0.7	KHm/GT	regolith
2577*	2577-2579	3.0270	0.5695	12.0	0.8	KHm/GT	bedrock
2595*	2595-2601	4.2561	0.8326	15.2	0.8	KHm/GT	regolith
2618*	2618-2631	2.8526	0.4834	11.6	0.7	Gm/GT	bedrock
2633*	2633-2636	2.7050	0.6307	13.2	1.2	Gm/GT	bedrock
2639*	2639-2641	2.5886	0.4690	12.8	0.6	Gm/GT	bedrock
2643*	2643-2645	3.4271	0.5400	13.6	0.6	Gm/GT	bedrock
2645*	2645-2647	3.6508	0.7886	14.5	1.1	Gm/GT	bedrock
2657		3.6807	0.7727	12.4	0.8	Gm/GT	bedrock
2661*	2661-2663	2.3403	0.5685	15.6	1.2	Gm/GT	regolith
2664*	2664-2684	3.2533	0.6019	15.2	0.9	Gm/GT	regolith
2693*	2693-2695	3.0207	0.7524	12.7	1.0	Gm/GT	regolith
2702*	2702-2725	1.6890	0.5410	15.1	1.6	Sf/GP	regolith
2732*	2732-2733	3.6232	0.9316	18.1	1.5	Sf/GP	regolith
2734*	2734-2736	1.5945	0.3408	10.2	0.7	Gm/GT	regolith
2783*	2783-2784	4.5722	1.0574	14.4	1.0	Gm/GT	bedrock
2804*	2804-2811	3.9252	0.7498	11.4	0.7	Gm/GT	bedrock
2817*	2817-2819	4.7179	0.8529	13.3	0.6	KHm/GT	regolith
2830*	2830-2902	4.1787	0.5213	13.0	0.4	KHm/GT	bedrock
2904*	2904-2916	4.1019	0.5861	12.2	0.5	KHm/GT	bedrock
2944*	2944-2947	4.3316	0.7885	12.4	0.6	KHm/GT	bedrock
2967*	2967-2970	3.9712	0.7993	14.3	0.7	Gm/GT	bedrock
2972*	2972-2976	4.8809	0.8387	16.2	0.9	Gm/GT	bedrock
2995*	2995-2998	3.2074	0.6325	12.0	0.7	Gm/GT	bedrock
3000*	3000-3001	5.3329	1.1843	18.1	1.4	Gm/GT	bedrock

Sol	Coadded Sols	WEH [wt.%]	WEH Error [wt.%]	Σ_{abs} [10^{-3} cm^2/g]	Σ_{abs} Error [10^{-3} cm^2/g]	Unit	Material
3005*	3005-3007	4.2747	0.8557	14.0	0.8	Gm/GT	bedrock
3008*	3008-3009	3.7151	0.6437	13.6	0.8	Gm/GT	bedrock
3015*	3015-3017	4.1857	0.8568	14.3	0.9	Gm/GT	bedrock
3018*	3018-3019	3.6103	0.7031	13.2	0.7	Gm/GT	bedrock
3022*	3022-3025	3.8655	0.6393	11.0	0.6	Gm/GT	bedrock
3028*	3028-3032	3.3891	0.8167	13.4	1.0	Gm/GT	bedrock
3032*	3032-3034	3.3881	0.9110	14.2	1.2	Gm/GT	bedrock
3042*	3042-3044	4.6798	2.4509	13.3	1.9	Gm/GT	bedrock
3049*	3049-3052	4.9745	1.3460	16.8	1.5	Gm/GT	bedrock
3052*	3052-3069	4.0276	0.7260	15.9	0.9	Gm/GT	bedrock

APPENDIX D

PERMISSION STATEMENT FROM CO-AUTHORS FOR CHAPTER 3: "HYDRATION OF A CLAY-RICH UNIT ON MARS, COMPARISON OF ORBITAL DATA TO ROVER DATA"

This chapter was originally published in Journal of Geophysical Research: Planets in 2023 (see reference entry below). It has been reformatted to comply with the ASU Graduate College format manual, and is reproduced here with the permission of the following coauthors: Craig Hardgrove, Ray Arvidson, Maddie Hughes, Mariek Schmidt, Thomas Henley, Luz Maria Martinez Sierra, Insoo Jun, Maxim Litvak, Igor Mitrofanov, and Jack Lightholder

Czarnecki, S., Hardgrove, C., Arvidson, R. E., Hughes, M. N., Schmidt, M. E., Henley, T., et al. (2023a). Hydration of a clay-rich unit on Mars, comparison of orbital data to rover data. *Journal of Geophysical Research: Planets*, 128: e2021JE007104. https://doi.org/10.1029/2021JE007104

APPENDIX E

SUPPLEMENTAL INFORMATION FOR CHAPTER 4: "CONSTRAINING THE HYDRATION OF CLAY MINERALS AND ABUNDANCES OF AMORPHOUS PHASES IN GALE CRATER, MARS"

Text E.1. Error Estimations for Amorphous Fractions of CheMin Data

Abundances of X-ray amorphous materials in drill samples are determined via FULLPAT analysis of Chemistry and Mineralogy instrument (CheMin) X-ray diffraction (XRD) patterns. FULLPAT uses linear least-squares minimization with a library of individual XRD patterns from crystalline and amorphous materials to fit a CheMin XRD pattern (Chipera & Bish, 2002; 2013). To facilitate quantitative analysis of CheMin patterns, individual phases spiked with an internal standard (beryl or corundum) were measured on a lab version of CheMin to determine their reference intensity ratios. Measuring library patterns on a flight-like CheMin instrument allows for the removal of instrumental and sample-related effects during FULLPAT analysis. Library patterns include silicate minerals (e.g., plagioclase and potassium feldspars, clinopyroxene, orthopyroxene, olivine, quartz, smectite, illite), oxides and hydroxides (e.g., magnetite, hematite, goethite), sulfates (e.g., gypsum, starkeyite), carbonates (e.g., calcite, siderite), phosphate (fluorapatite), and X-ray amorphous materials (basaltic and rhyolitic glasses, opal-A, opal-CT, ferrihydrite, allophane, amorphous Mg-sulfate, and Fe-Si and Al-Si gels).

The 2σ errors (i.e., 95% confidence level) on mineral abundances determined from FULLPAT have already been determined as ± 3.4 wt.% (Chipera & Bish, 2002), but the errors associated with the amorphous abundance have not been well constrained. The 2σ errors on amorphous abundances determined from FULLPAT analyses of Mars Science Laboratory (MSL) CheMin patterns are typically reported as 50% of the total modeled amorphous content. For example, if the amorphous content was modeled as 50 wt.%, the 2σ error would be reported as ± 25 wt.% (e.g., Rampe et al., 2020b). This value is based on experience from Dr. Steve Chipera, a co-creator of FULLPAT and a Co-Investigator on the CheMin team.

To better quantify errors associated with the amorphous component, we used a laboratory version of CheMin to acquire XRD patterns of physical mixtures of basaltic igneous minerals and silica glass in known quantities, then performed FULLPAT analyses on these XRD patterns. Basaltic igneous minerals in these mixtures included plagioclase feldspar (40 wt.% of the basaltic mineral fraction), diopside (40 wt.%), and olivine (20 wt.%). Silica glass from a crushed borosilicate glass slide was added to the basaltic mineral mixture in the following amounts: 10 wt.%, 20 wt.%, 40 wt.%, 60 wt.%, 70 wt.%, 80 wt.%, 85 wt.%, and 90 wt.%. Particle sizes were <150 μm. These mineral-glass mixtures and the basaltic mineral mixture and glass end members were measured on the CheMin IV instrument at NASA Johnson Space Center. CheMin XRD patterns were analyzed using the FULLPAT program tailored for the MSL CheMin instrument. The end member library included phases typically used to analyze MSL CheMin patterns (i.e., plagioclase, sanidine, clinopyroxene, orthopyroxene, olivine, magnetite, hematite, clay minerals, Ca-sulfate, carbonate, basaltic glass, rhyolitic glass, and ferrihydrite).

Modeled amorphous abundances were compared to actual abundances to derive absolute and relative errors (Table E.1, Figures E.1 and E.2). The highest absolute and relative errors are associated with high (90 - 100 wt.%) and low (0 - 10 wt.%) amorphous abundances. FULLPAT analyses of CheMin patterns typically identify ~30 - 70 wt.% amorphous materials (e.g., Rampe et al., 2020b), suggesting an actual amorphous abundance of ~20 to 80 wt.%. In this range, absolute and relative errors are typically <5 wt.% and <5%, respectively. As such, for this manuscript, we assume a 5% relative error for CheMin amorphous abundances.

Acknowledgement: We are grateful to Dr. Michael Rowe for providing mineral and amorphous mixtures on which to test errors associated with amorphous abundances in FULLPAT analyses.

Text E.2. Assumptions Regarding Chemistry of Phases in Section 4.2.5

We assume a 1:1 ratio of OH:Cl in akaganeite by default because this ratio is unconstrained by CheMin and at least one sample is consistent with Cl in the structure (Rampe et al., 2020a). We assume apatite in all samples is fluorapatite because although CheMin is not always able to identify the specific variety of apatite, it has never identified hydroxylapatite or chlorapatite, but has sometimes identified fluorapatite (Rampe et al., 2017; Rampe et al., 2020a). We assume that opal-CT is hydrated at 6.3 wt.% water-equivalent hydrogen (WEH), the same abundance used for opal-A, and note that only three samples (TP, BK, OU) in this study have opal-CT bulk abundances > 5 wt.%. For all but one sample in Table 4.1 (Chapter 4), CheMin and Sample Analysis at Mars instrument (SAM) studies have been most consistent with a specific clay mineral. But the clay mineral phase in the MJ sample is unconstrained. In this case, we use the mean structural WEH abundance (4.57 wt.% WEH) of other clay minerals in Gale crater samples (saponite, montmorillonite, nontronite) and illite, a clay mineral suggested as a possible fit for the MJ diffraction pattern. We note that the range of possible structural WEH abundances in these clay minerals is relatively small (3.71 – 4.97 wt.%) and that the clay mineral bulk abundance of MJ is also small (5 wt.%).

We do not include some minor/trace elements (Cl, Ti, Cr, Mn, P) in our analyses, despite being reported in the literature, because these elements could be unrealistically concentrated in the amorphous fraction during amorphous chemistry calculations, and could be in the crystalline fraction (Rampe et al., 2020b; Smith et al., 2021). Although perchlorates are likely contributors to the reported amorphous chemistry, SAM results indicate that their abundances are low (Sutter et al., 2017).

Candidate amorphous phase chemistries are reported in Table 4.2 (Chapter 4). Our rhyolitic glass composition is a mean Chassigny martian meteorite glass inclusion composition from Varela et al. (2000), and our basaltic glass composition comes from Filiberto et al. (2008), which is based on a Gusev crater, Mars basaltic material (as in Gabriel et al., 2018). Our Fe-sulfate is ferric with hydration based on Sklute et al. (2015) as in Gabriel et al. (2018). Our Mg-sulfate hydration is based on Vaniman et al. (2004) as in Gabriel et al. (2018). Our opal-A uses a mean Gale crater opal-A hydration value from Rapin et al. (2018). We use a hisingerite composition from the Mars analog Duluth Complex in Minnesota (Evans et al., 2017), and allophane and ferrihydrite compositions from Rampe et al. (2016). Glass, allophane, hisingerite, and ferrihydrite hydration are from Gabriel et al. (2018) and references therein. We use a relative uncertainty of 30% for oxides in glass, allophane, and hisingerite. Relative uncertainties for oxides in Fe- and Mg-sulfate, opal-A, and ferrihydrite are 30% of the WEH abundance for that phase.

The very low abundance or absence of some cations in the amorphous chemistry of some samples requires the adjustment or removal of some candidate amorphous phases from our models. Rather than modeling unusual compositions (e.g., basaltic glass with no Mg), we do not include a glass phase in some cases. For MB (no Mg), we do not model basaltic glass, Mg-sulfate, or "excess" Mg, and remove Mg from rhyolitic glass and hisingerite. For MJ and OU (no Ca), we do not model basaltic glass or "excess" Ca, and remove Ca from rhyolitic glass and hisingerite. For CH (no K), we remove "excess" K and remove K from rhyolitic and basaltic glass. For BK (no Al and K), we do not model allophane or "excess" K and remove Al and K from rhyolitic and basaltic glass. Although an Al-free rhyolitic glass is unusual, the low-WEH/high-silica BK composition limits the maximum abundance of the more hydrated opal-A (see Section 4.3.2 of the main text). Of the candidate amorphous phases, only rhyolitic glass is a suitable fit for the BK silica.

Table E.1. Quantification of X-ray amorphous uncertainties. Actual and modeled abundances in mixtures, and absolute and relative errors of modeled abundances.

Actual Amorphous Abundance [wt.%]	Modeled Amorphous Abundance [wt.%]	Absolute Error [wt.%]	Relative Error [%]
0	4.9	4.9	-
10	21.2	11.2	112.0
20	26.5	6.5	32.5
40	39.3	0.7	1.8
60	59.5	0.5	0.8
70	68.8	1.2	1.7
80	74.1	5.9	7.4
85	80.4	4.6	5.4
90	82.4	7.6	8.4
100	88.2	11.8	11.8

Table E.2. Dynamic Albedo of Neutrons instrument (DAN) data products used in Chapter 4. Data are available on the PDS (Mitrofanov, 2013). Markov-Chain Mone Carlo (MCMC) corner plots are provided in Figures E.3 – E.23 below. WEH results for each sample site are listed in Table 4.1 (Chapter 4).

Sample(s)		DAN Data Products	Distance to Drill
JC	John Klein & Cumberland	DNB_423679520EAC02950060094_____M2	Over drill hole
		DNB_423680770EAC02950060112_____M2	Over drill hole
CH	Confidence Hills	DNB_464342017EAC07530421020_____M1	~4 meters
		DNB_465594567EAC07670421020_____M1	~4 meters
MJ	Mojave	DNB_469140928EAC08070441432_____M1	~4 meters
TP	Telegraph Peak	DNB_467990524EAC07940440568_____M1	~4 meters
		DNB_471625260EAC08350442336_____M1	~4 meters
		DNB_477664541EAC09030450450_____M1	~4 meters
		DNB_478647287EAC09140450450_____M2	~4 meters
BK[a]	Buckskin	DNB_490974595EAC10530482518_____M1	~4 meters
		DNB_491242423EAC10560482542_____M1	~4 meters
OU	Oudam	DNB_517961251EAC13570542280_____M1	~3 meters
MB	Marimba	DNB_523287221EAC14170561236_____M2	~3 meters
QL	Quela	DNB_526666616EAC14550572798_____M1	~3 meters
SB	Sebina	DNB_529508126EAC14870581986_____M2	~2 meters
ST	Stoer	DNB_586766657EAC21320721316_____M1	~3 meters
		DNB_587470297EAC21400721316_____M1	~3 meters
		DNB_587978084EAC21460721316_____M1	~3 meters
		DNB_588177033EAC21480721316_____M1	~3 meters
		DNB_588184978EAC21480721316_____M1	~3 meters
		DNB_588248470EAC21490721316_____M1	~3 meters
		DNB_588266275EAC21490721316_____M1	~3 meters
		DNB_588297294EAC21490721316_____M1	~3 meters

HF	Highfield	DNB_571667399EAC19620680580_____	M1	~4 meters
		DNB_572891265EAC19760680580_____	M1	~4 meters
		DNB_573537718EAC19830680580_____	M1	~4 meters
		DNA_594754184EAC22220730550_____	M1	~3 meters
		DNA_595369115EAC22290730550_____	M1	~3 meters
		DNA_596172040EAC22380730550_____	M1	~3 meters
		DNA_596813232EAC22450730550_____	M1	~3 meters
RH	Rock Hall	DNA_597857175EAC22570731206_____	M1	~3 meters
		DNA_597960327EAC22580731206_____	M1	~3 meters
		DNA_598039783EAC22590731206_____	M2	~3 meters
		DNA_598090406EAC22600731206_____	M1	~3 meters
		DNA_598575706EAC22650731206_____	M1	~3 meters
		DNA_599551815EAC22760731206_____	M1	~3 meters
		DNA_600145740EAC22830731206_____	M1	~3 meters
		DNA_600770507EAC22900731206_____	M1	~3 meters
		DNA_601065704EAC22930731206_____	M1	~3 meters
AK	Aberlady & Kilmarie	DNB_607358079EAC23640751350_____	M1	~5 meters
		DNB_608872674EAC23810751398_____	M1	~3 meters
		DNB_609348049EAC23860751398_____	M1	~3 meters
		DNB_609395029EAC23870751398_____	M1	~3 meters
		DNB_609944021EAC23930751398_____	M1	~3 meters
		DNB_610473902EAC23990751398_____	M1	~3 meters
		DNB_610924911EAC24040751398_____	M1	~3 meters
		DNB_611268106EAC24080751564_____	M1	~6 meters
		DNB_611345891EAC24090751564_____	M1	~6 meters
		DNB_611450120EAC24100751564_____	M1	~6 meters
		DNB_611537695EAC24110751564_____	M2	~6 meters
GE	Glen Etive 1 & Glen Etive 2	DNB_617659029EAC24800762930_____	M1	~5 meters
GG	Glasgow	DNB_641365366EAC27470792008_____	M1	~3 meters
		DNB_641719479EAC27510792008_____	M1	~3 meters
		DNB_642339247EAC27580792008_____	M1	~3 meters
		DNB_642965098EAC27650792008_____	M1	~3 meters
		DNB_643584447EAC27720792008_____	M1	~3 meters
MA	Mary Anning 1 & Mary Anning 3	DNB_655308354EAC29040822188_____	M1	~3 meters
		DNB_655736279EAC29090822188_____	M1	~3 meters
		DNB_656179711EAC29140822188_____	M1	~3 meters
		DNB_656253883EAC29150822188_____	M1	~3 meters
		DNB_656371191EAC29160822188_____	M1	~3 meters

[a]The WEH value for BK was published in Czarnecki et al. (2020) using the listed data products.

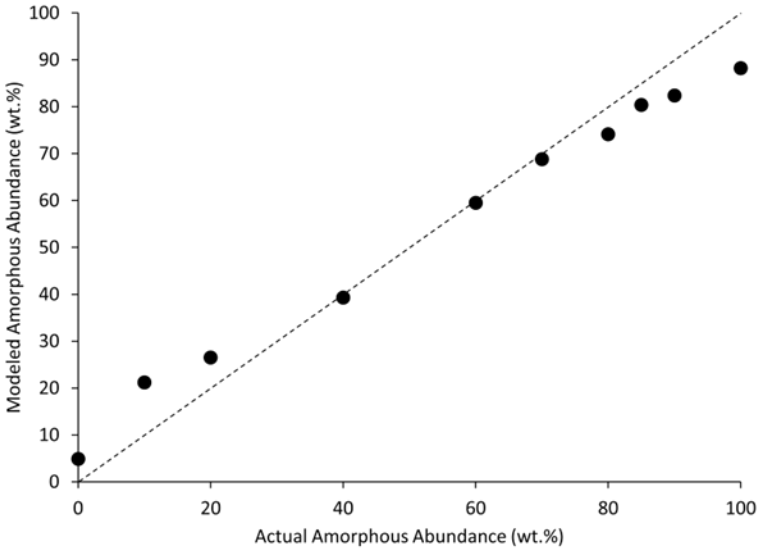

Figure E.1. Modeled amorphous abundances from FULLPAT analyses compared to actual amorphous abundances in the mixtures. The dashed line is a 1:1 line, where points closer to the line represent more accurate models.

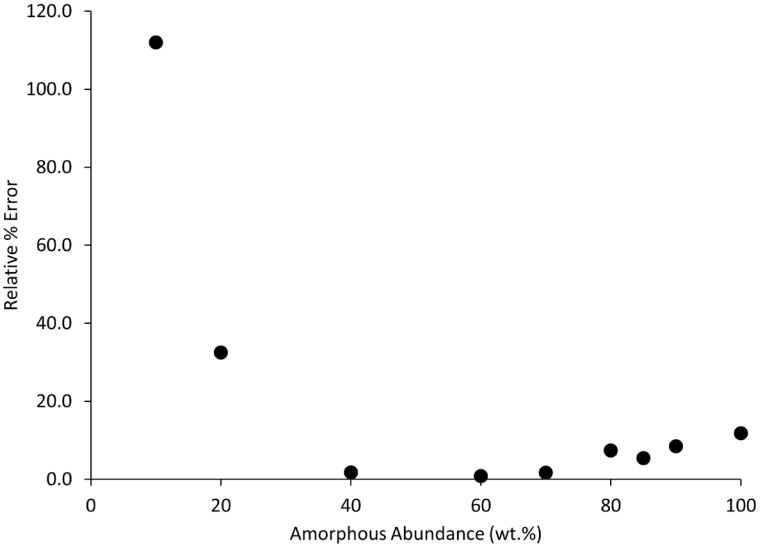

Figure E.2. Relative percent errors of amorphous abundances from FULLPAT analyses compared to the actual amorphous abundances in the mixtures. The most accurate models have the lowest relative percent error.

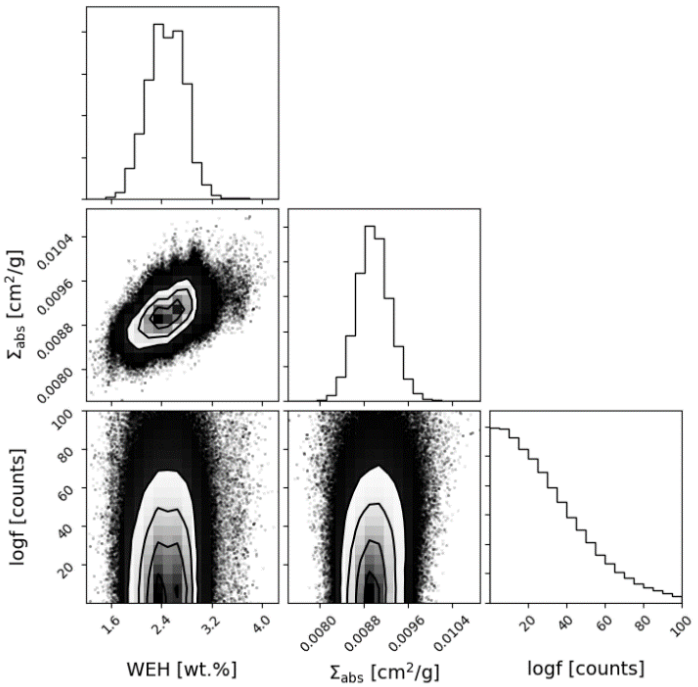

Figure E.3. Dynamic Albedo of Neutrons (DAN) Markov-Chain Monte Carlo (MCMC) results for John Klein/Cumberland (JC) measurement
DNB_423679520EAC02950060094_____M2

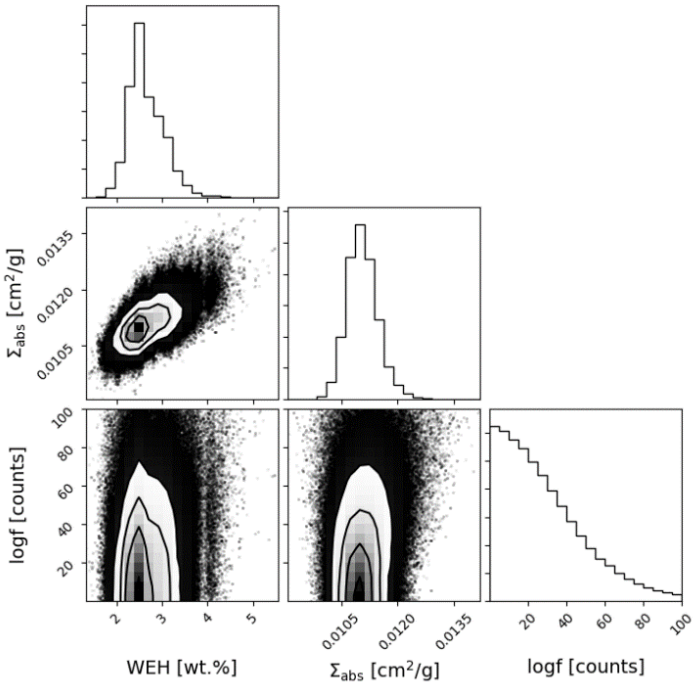

Figure E.4. DAN MCMC results for John Klein/Cumberland (JC) measurement
DNB_423680770EAC02950060112_____M2

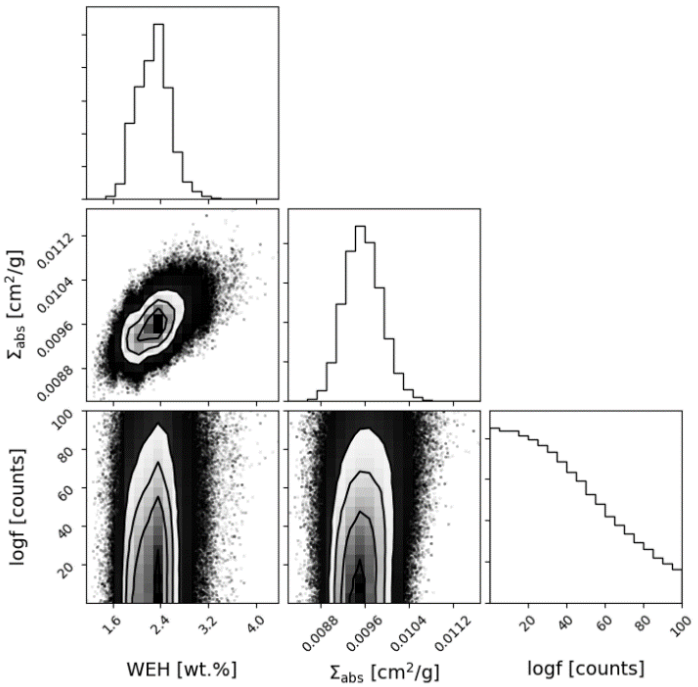

Figure E.5. DAN MCMC results for Confidence Hills (CH) coadded measurements DNB_464342017EAC07530421020_____M1, DNB_465594567EAC07670421020_____M1

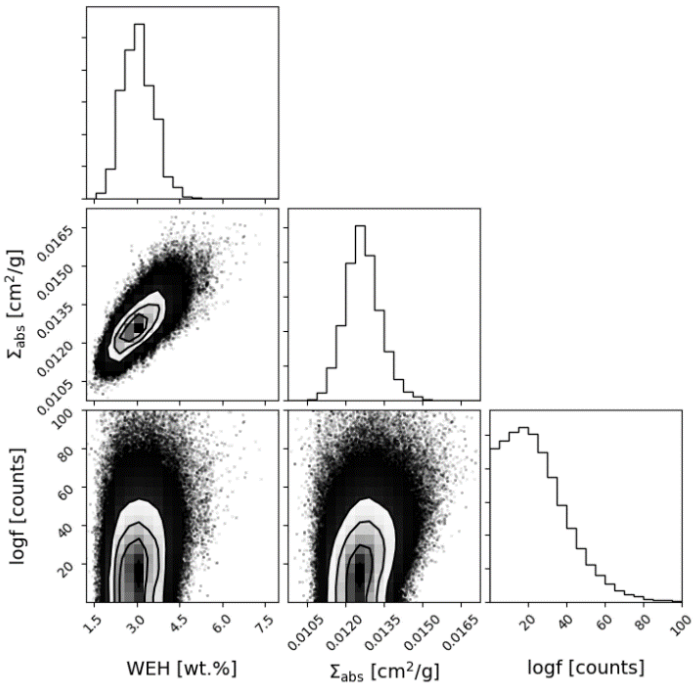

Figure E.6. DAN MCMC results for Mojave (MJ) measurement DNB_469140928EAC08070441432_____M1

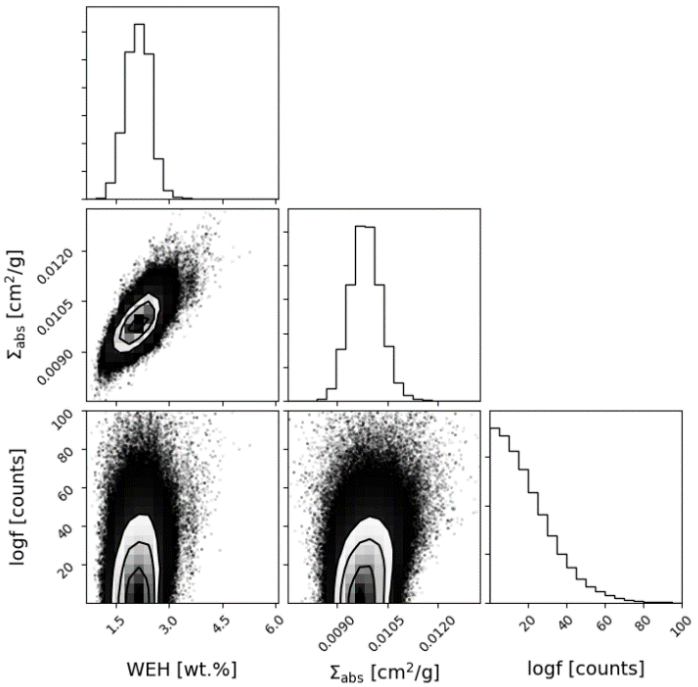

Figure E.7. DAN MCMC results for Telegraph Peak (TP) measurement DNB_467990524EAC07940440568_____M1

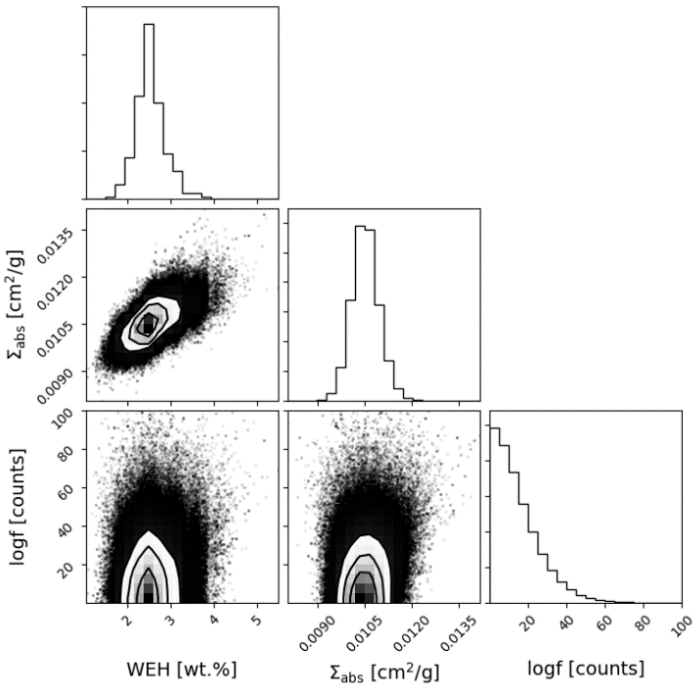

Figure E.8. DAN MCMC results for Telegraph Peak (TP) measurement DNB_471625260EAC08350442336_____M1

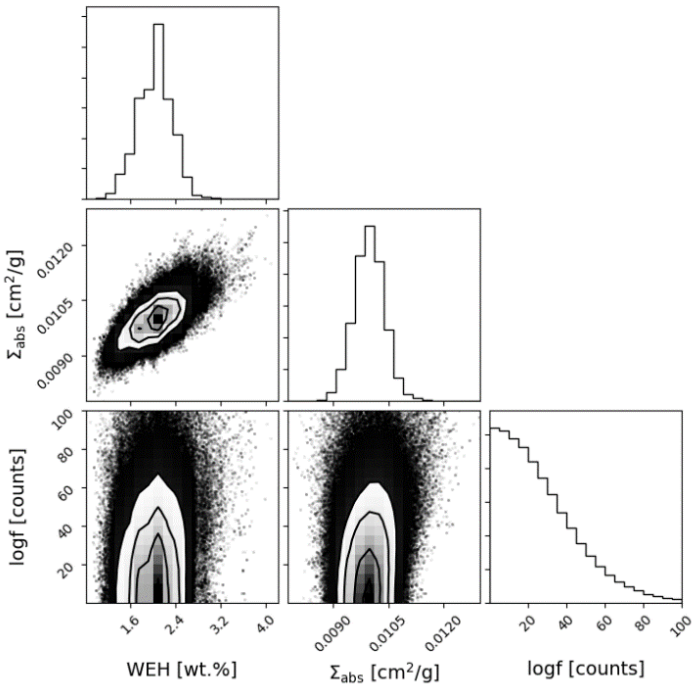

Figure E.9. DAN MCMC results for Telegraph Peak (TP) coadded measurements DNB_477664541EAC09030450450_____M1, DNB_478647287EAC09140450450_____M2

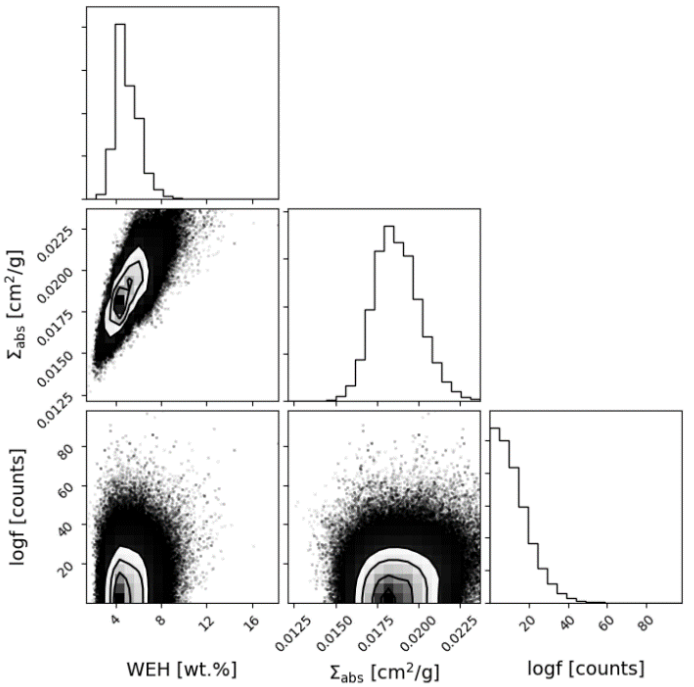

Figure E.10. DAN MCMC results for Oudam (OU) measurement DNB_517961251EAC13570542280_____M1

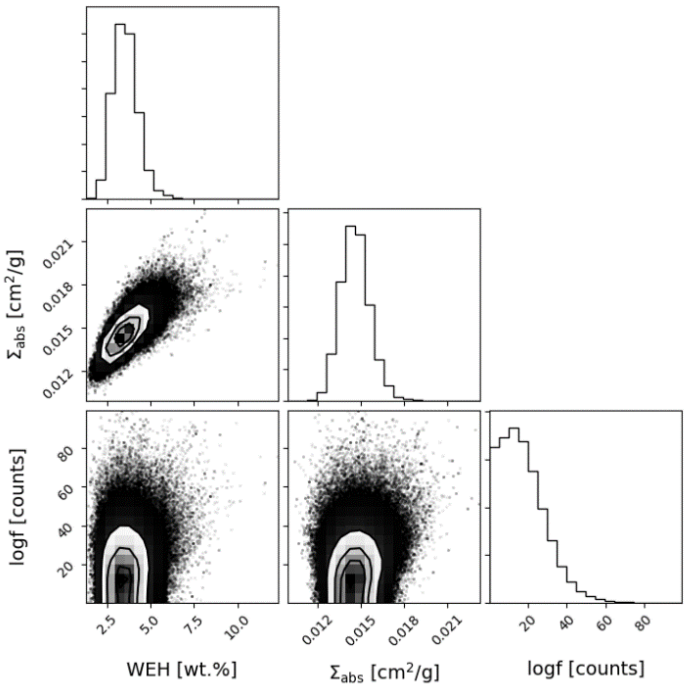

Figure E.11. DAN MCMC results for Marimba (MB) measurement DNB_523287221EAC14170561236_____M2

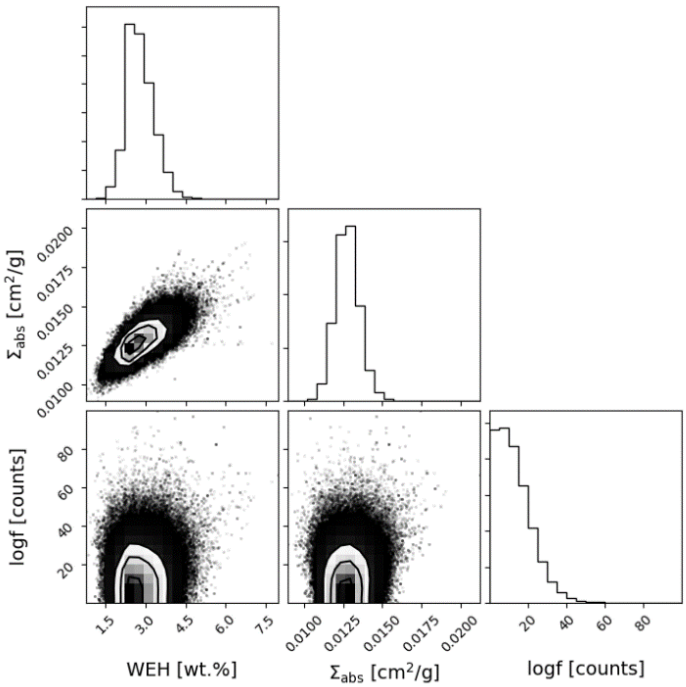

Figure E.12. DAN MCMC results for Quela (QL) measurement DNB_526666616EAC14550572798_____M1

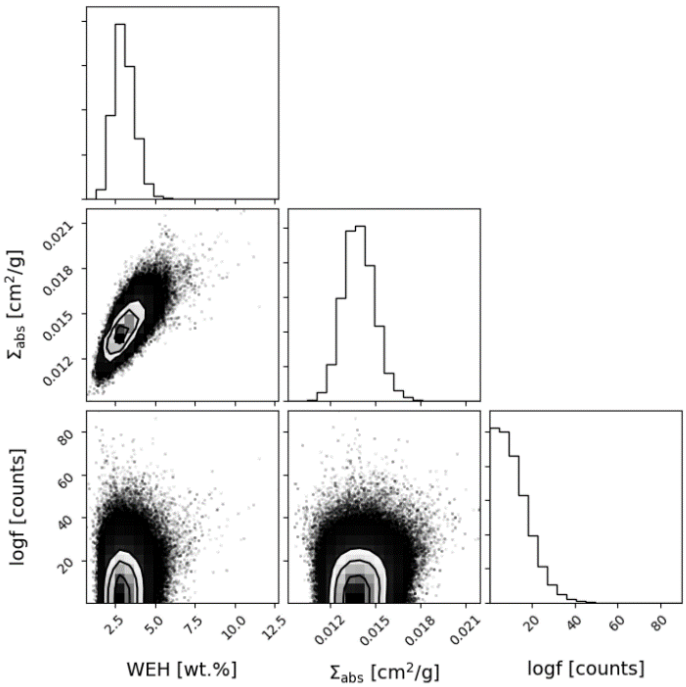

Figure E.13. DAN MCMC results for Sebina (SB) measurement DNB_529508126EAC14870581986_____M2

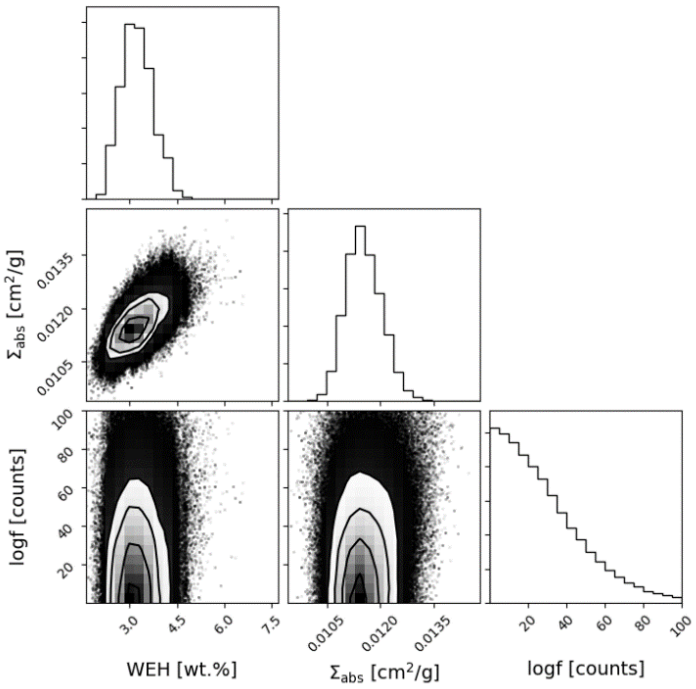

Figure E.14. DAN MCMC results for Stoer (ST) coadded measurements DNB_586766657EAC21320721316_____M1, DNB_587470297EAC21400721316_____M1, DNB_587978084EAC21460721316_____M1, DNB_588177033EAC21480721316_____M1, DNB_588184978EAC21480721316_____M1, DNB_588248470EAC21490721316_____M1, DNB_588266275EAC21490721316_____M1, DNB_588297294EAC21490721316_____M1

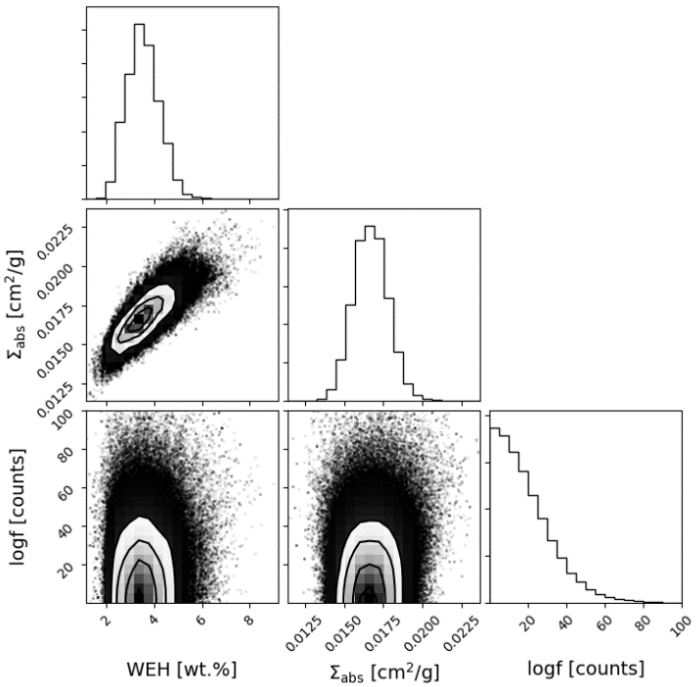

Figure E.15. DAN MCMC results for Highfield (HF) coadded measurements DNB_571667399EAC19620680580_____M1, DNB_572891265EAC19760680580_____M1, DNB_573537718EAC19830680580_____M1

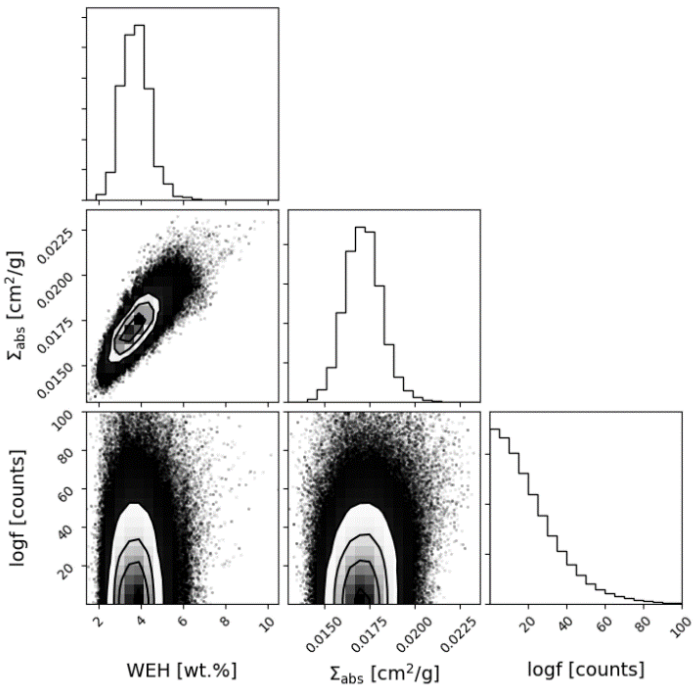

Figure E.16. DAN MCMC results for Highfield (HF) coadded measurements DNA_594754184EAC22220730550_____M1, DNA_595369115EAC22290730550_____M1, DNA_596172040EAC22380730550_____M1, DNA_596813232EAC22450730550_____M1

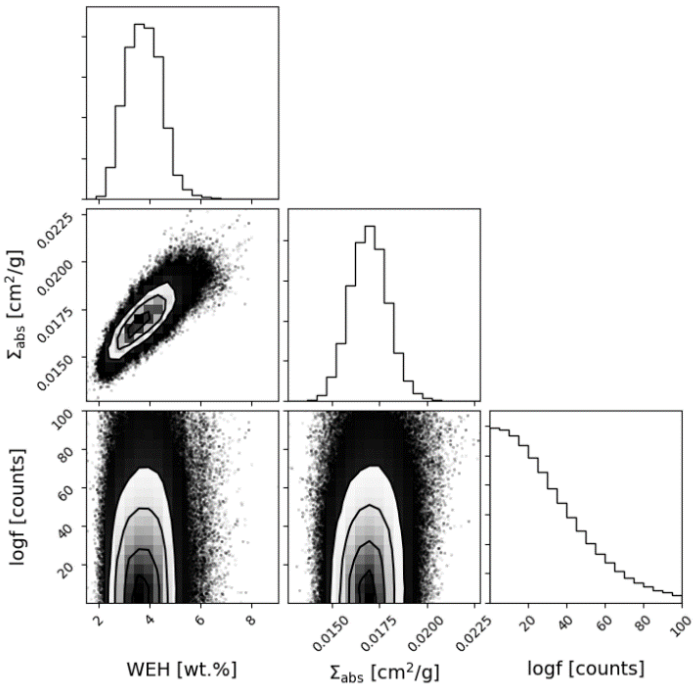

Figure E.17. DAN MCMC results for Rock Hall (RH) coadded measurements DNA_597857175EAC22570731206_____M1, DNA_597960327EAC22580731206_____M1, DNA_598039783EAC22590731206_____M2, DNA_598090406EAC22600731206_____M1, DNA_598575706EAC22650731206_____M1, DNA_599551815EAC22760731206_____M1, DNA_600145740EAC22830731206_____M1, DNA_600770507EAC22900731206_____M1, DNA_601065704EAC22930731206_____M1

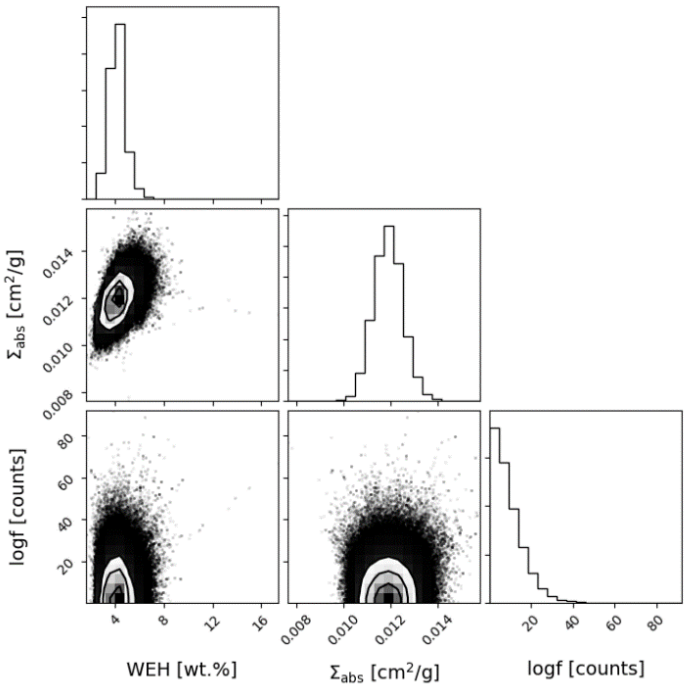

Figure E.18. DAN MCMC results for Aberlady/Kilmarie (AK) measurement DNB_607358079EAC23640751350_____M1

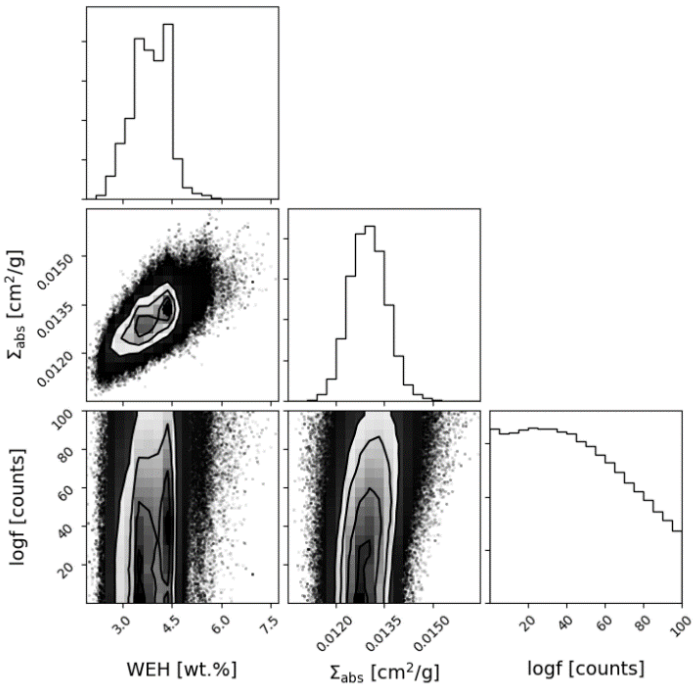

Figure E.19. DAN MCMC results for Aberlady/Kilmarie (AK) coadded measurements DNB_608872674EAC23810751398_____M1, DNB_609348049EAC23860751398_____M1, DNB_609395029EAC23870751398_____M1, DNB_609944021EAC23930751398_____M1, DNB_610473902EAC23990751398_____M1, DNB_610924911EAC24040751398_____M1

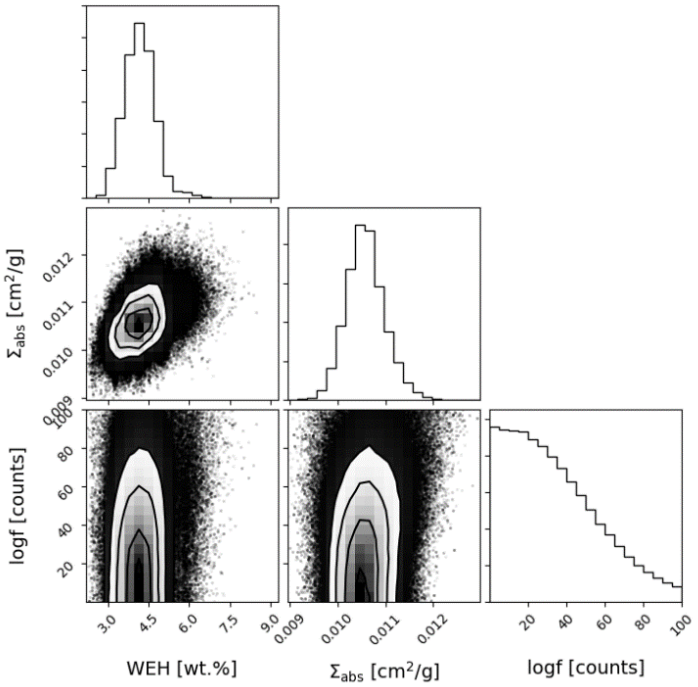

Figure E.20. DAN MCMC results for Aberlady/Kilmarie (AK) coadded measurements DNB_611268106EAC24080751564_____M1, DNB_611345891EAC24090751564_____M1, DNB_611450120EAC24100751564_____M1, DNB_611537695EAC24110751564_____M2

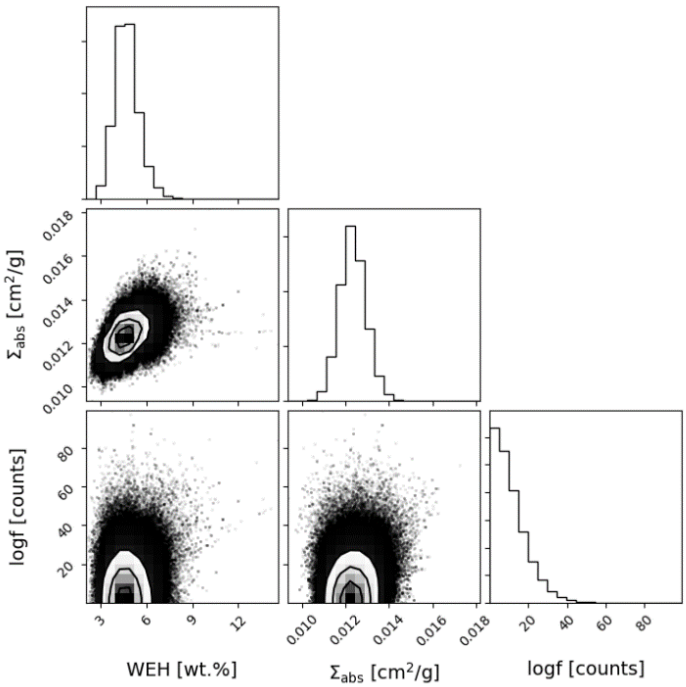

Figure E.21. DAN MCMC results for Glen Etive 1,2 (GE) measurement DNB_617659029EAC24800762930_____M1

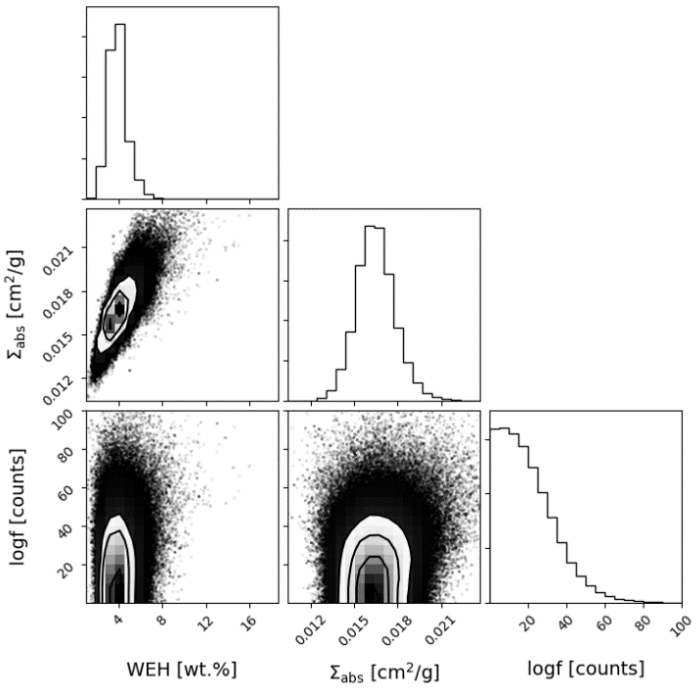

Figure E.22. DAN MCMC results for Glasgow (GG) coadded measurements DNB_641365366EAC27470792008_____M1, DNB_641719479EAC27510792008_____M1, DNB_642339247EAC27580792008_____M1, DNB_642965098EAC27650792008_____M1, DNB_643584447EAC27720792008_____M1

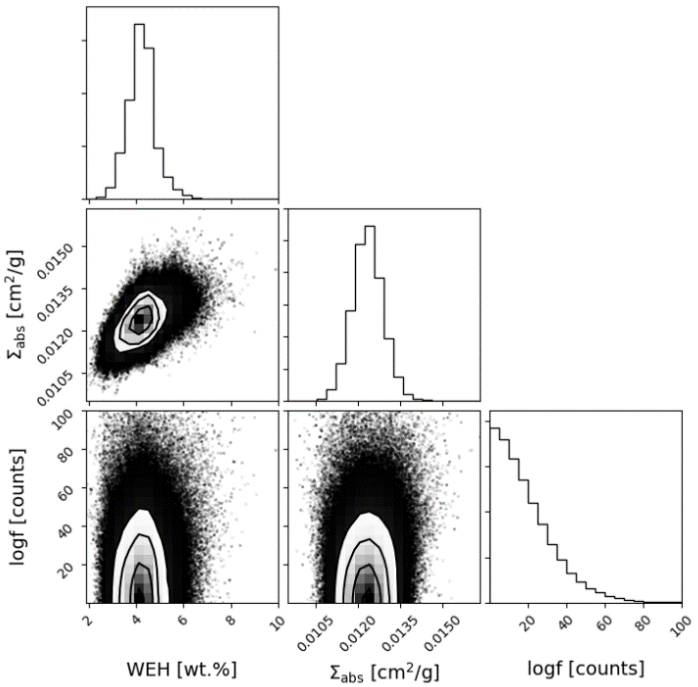

Figure E.23. DAN MCMC results for Mary Anning 1,3 (MA) coadded measurements DNB_655308354EAC29040822188_____M1, DNB_655736279EAC29090822188_____M1, DNB_656179711EAC29140822188_____M1, DNB_656253883EAC29150822188_____M1, DNB_656371191EAC29160822188_____M1

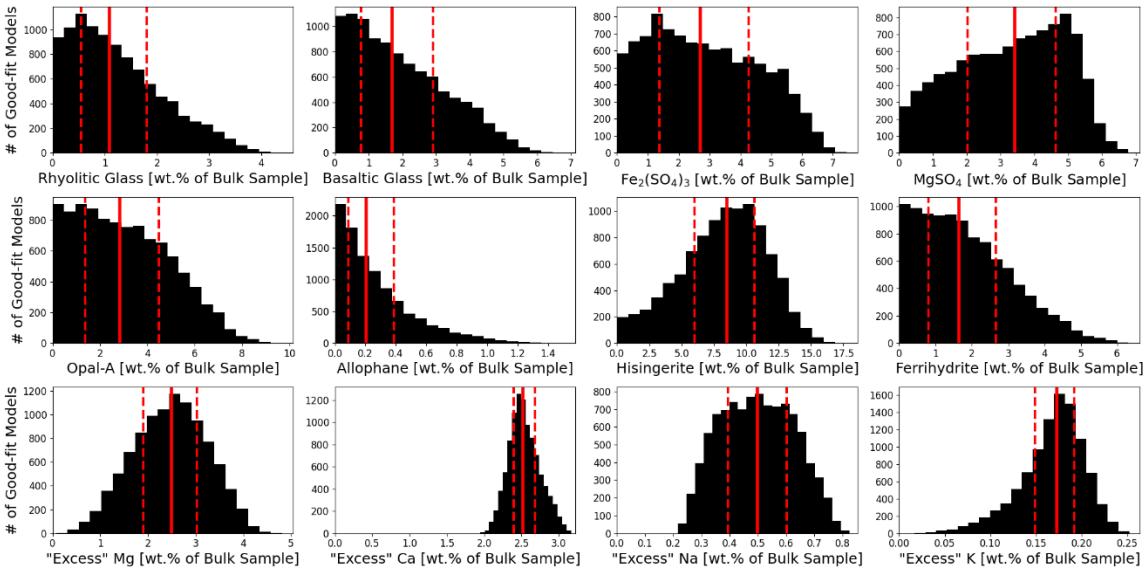

Figure E.24. John Klein/Cumberland (JC) modeled amorphous phase and "excess" cation distributions.

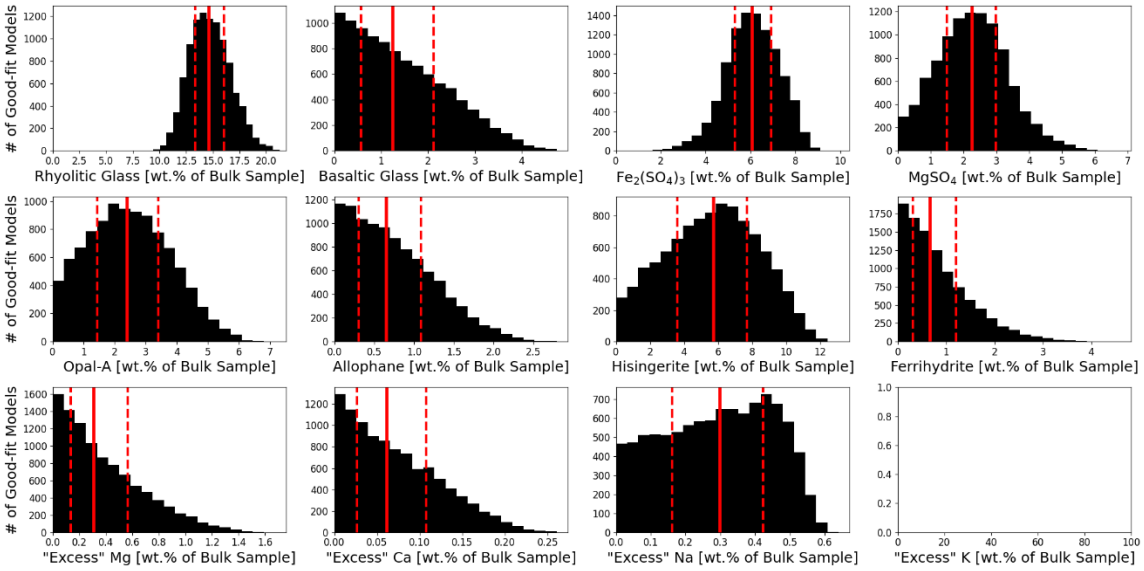

Figure E.25. Confidence Hills (CH) modeled amorphous phase and "excess" cation distributions. CH contained negligible K in the amorphous fraction, so "excess" K was not modeled.

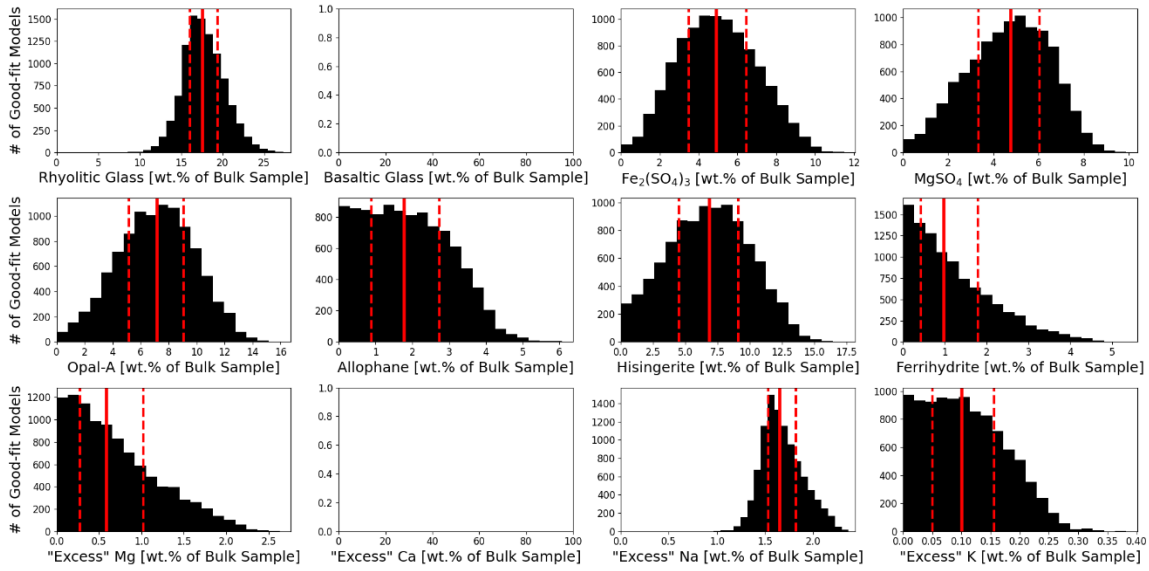

Figure E.26. Mojave (MJ) modeled amorphous phase and "excess" cation distributions. MJ contained negligible Ca in the amorphous fraction, so basaltic glass and "excess" Ca were not modeled.

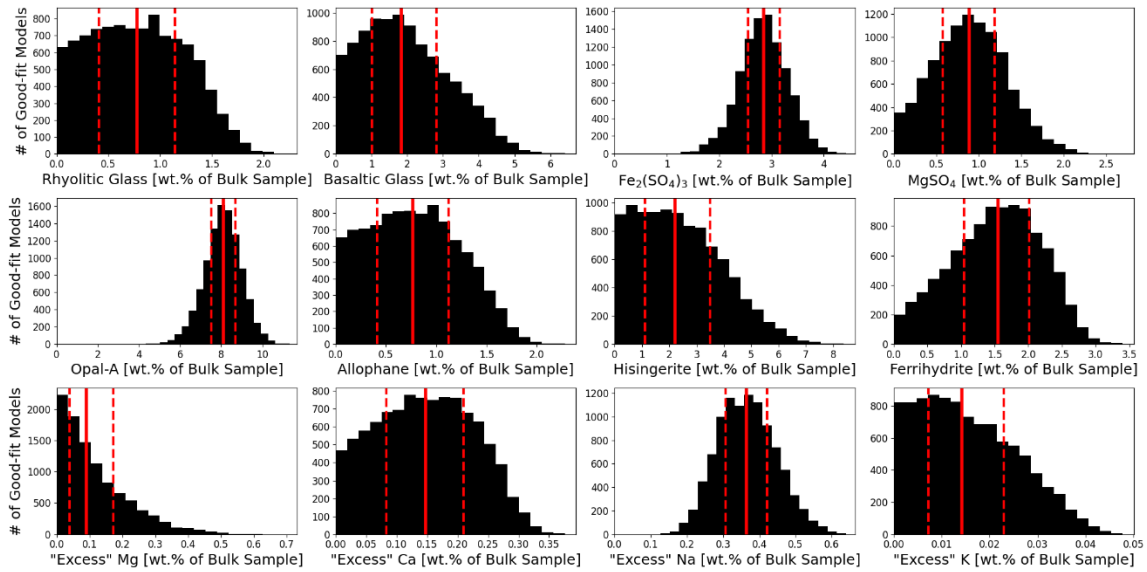

Figure E.27. Telegraph Peak (TP) modeled amorphous phase and "excess" cation distributions.

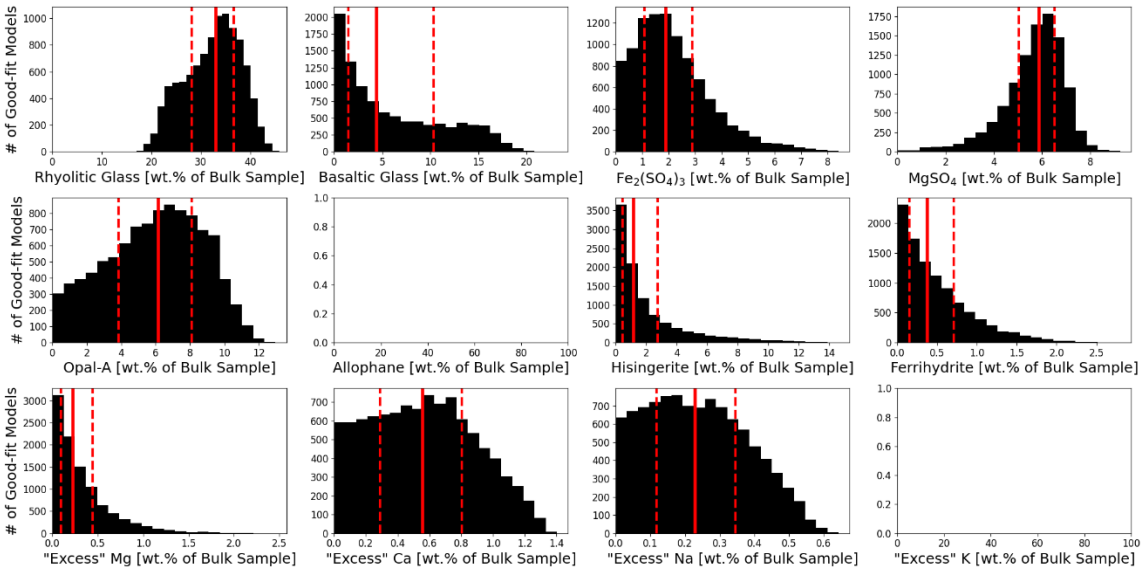

Figure E.28. Buckskin (BK) modeled amorphous phase and "excess" cation distributions. BK contained negligible Al and K in the amorphous fraction, so allophane and "excess" K were not modeled.

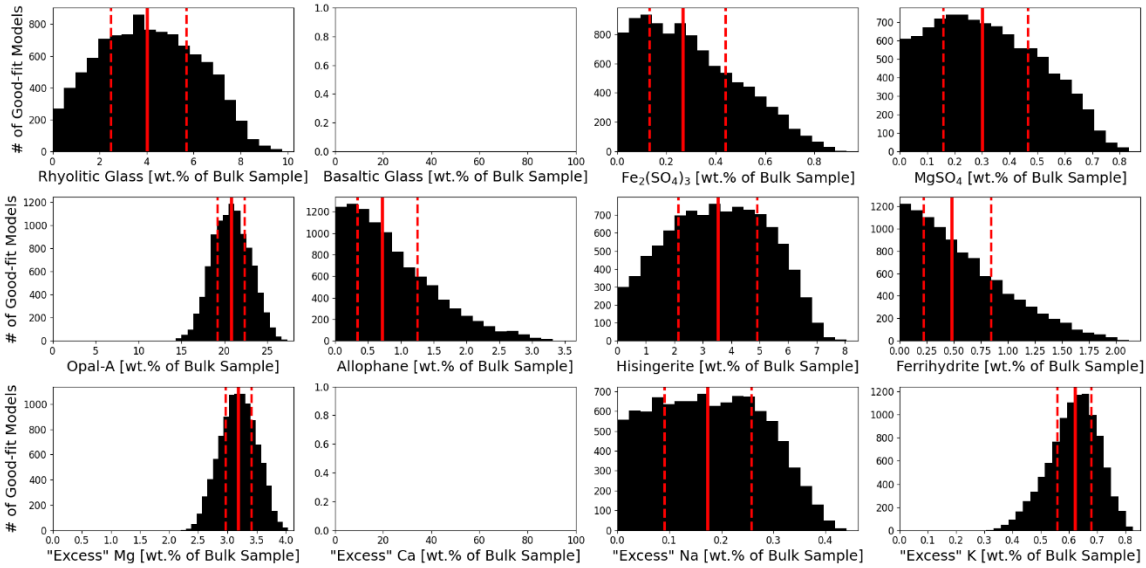

Figure E.29. Oudam (OU) modeled amorphous phase and "excess" cation distributions. OU contained negligible Ca in the amorphous fraction, so basaltic glass and "excess" Ca were not modeled.

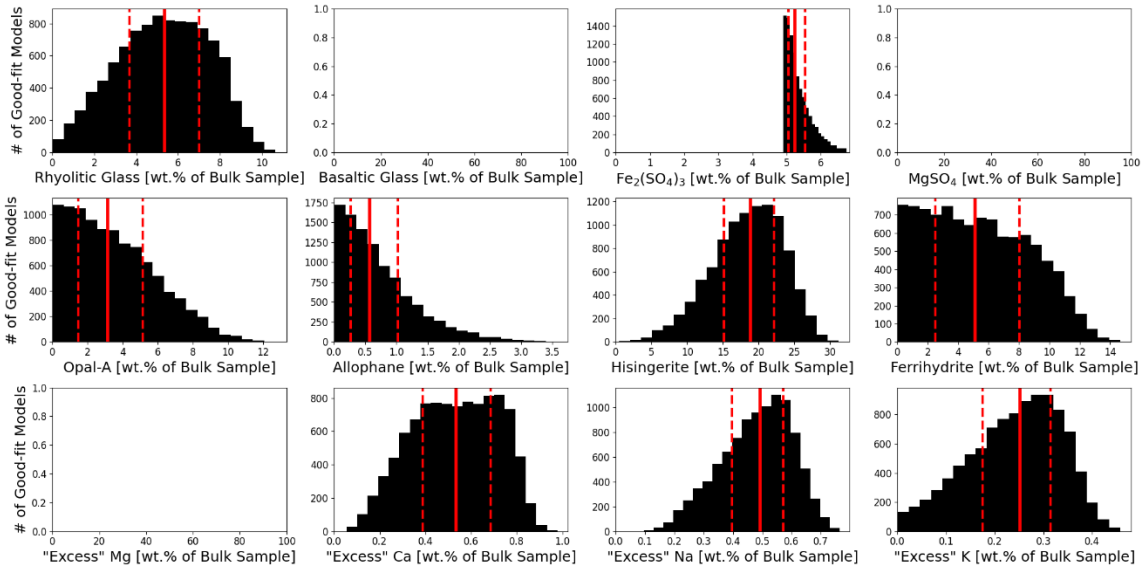

Figure E.30. Marimba (MB) modeled amorphous phase and "excess" cation distributions. MB contained negligible Mg in the amorphous fraction, so basaltic glass and "excess" Mg were not modeled.

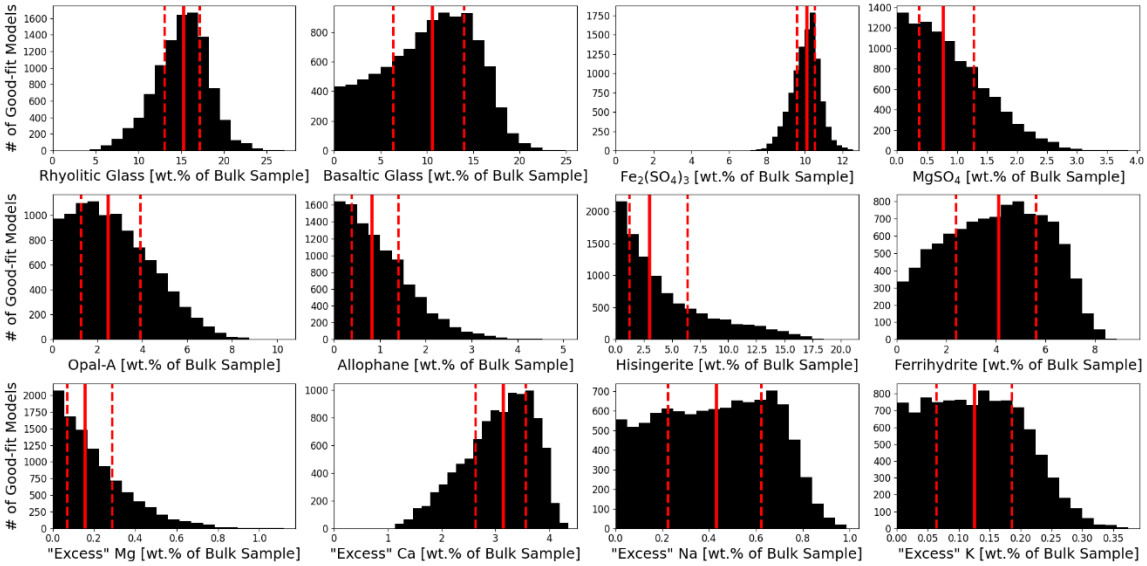

Figure E.31. Quela (QL) modeled amorphous phase and "excess" cation distributions.

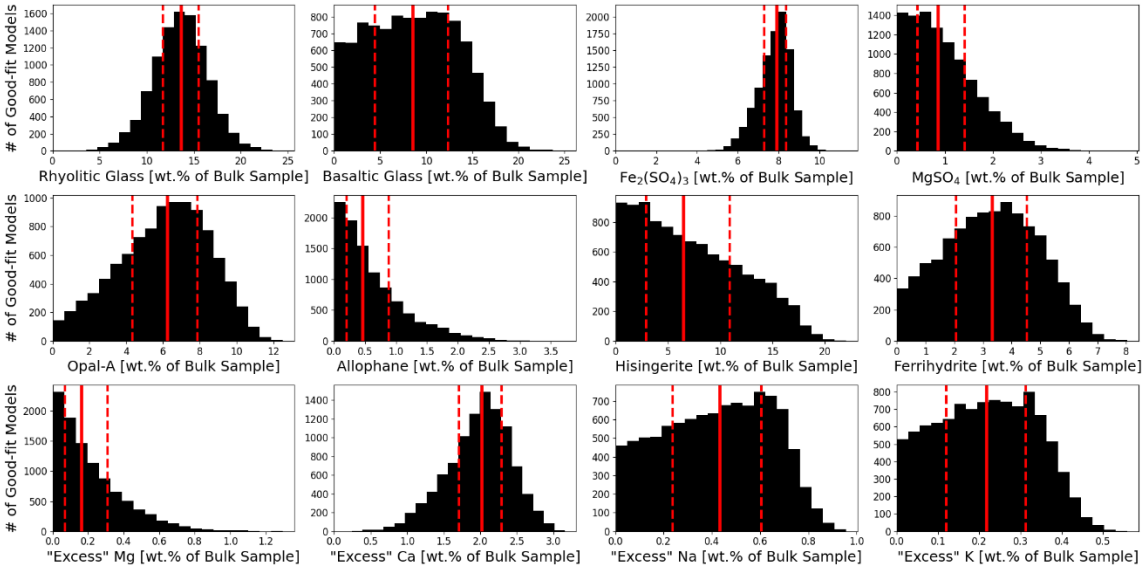

Figure E.32. Sebina (SB) modeled amorphous phase and "excess" cation distributions.

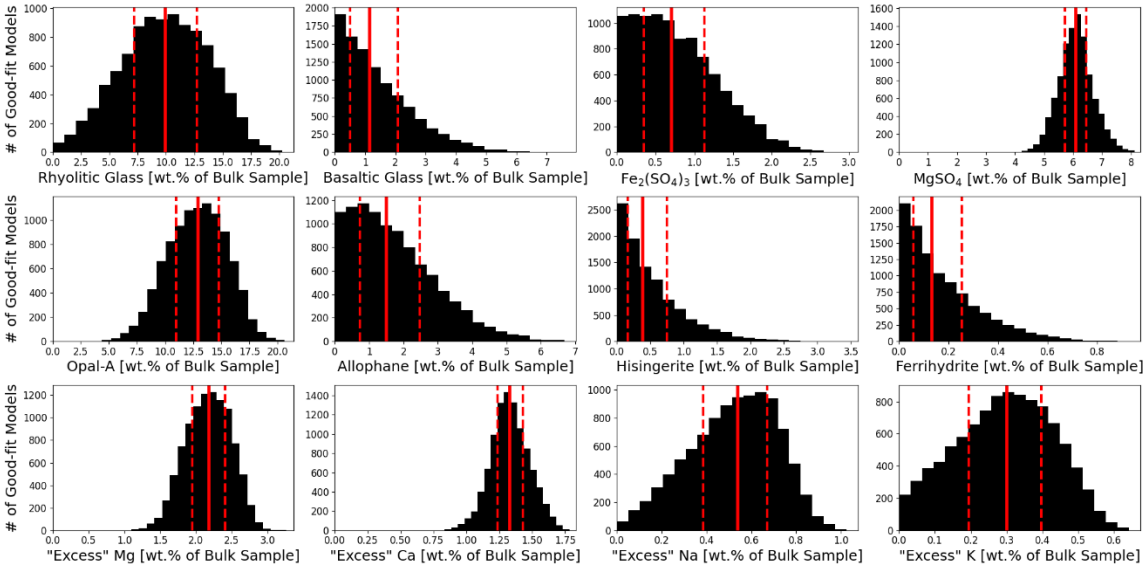

Figure E.33. Stoer (ST) modeled amorphous phase and "excess" cation distributions.

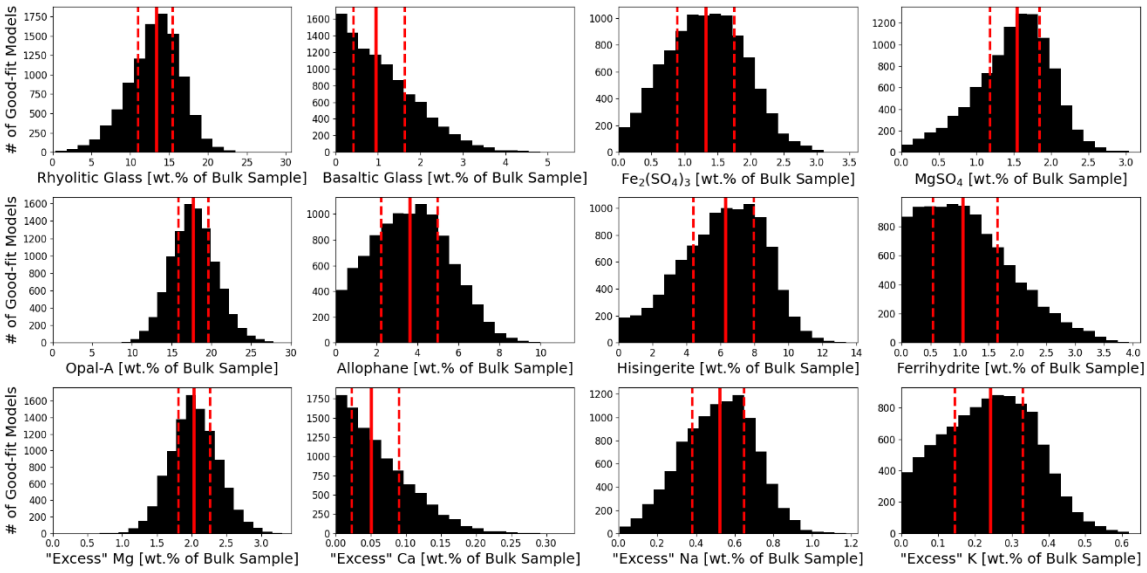

Figure E.34. Highfield (HF) modeled amorphous phase and "excess" cation distributions.

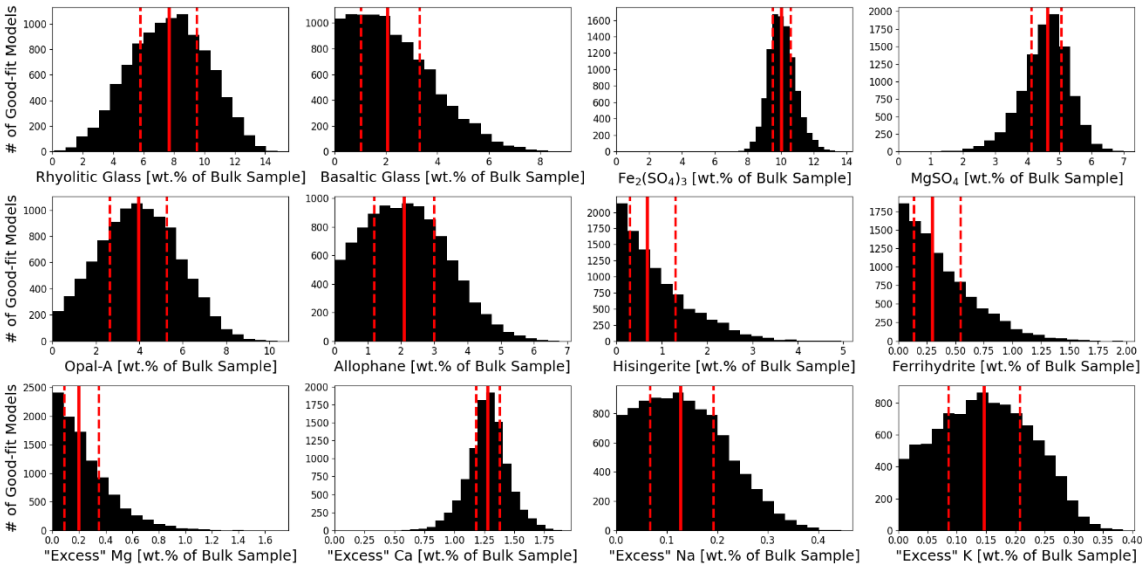

Figure E.35. Rock Hall (RH) modeled amorphous phase and "excess" cation distributions.

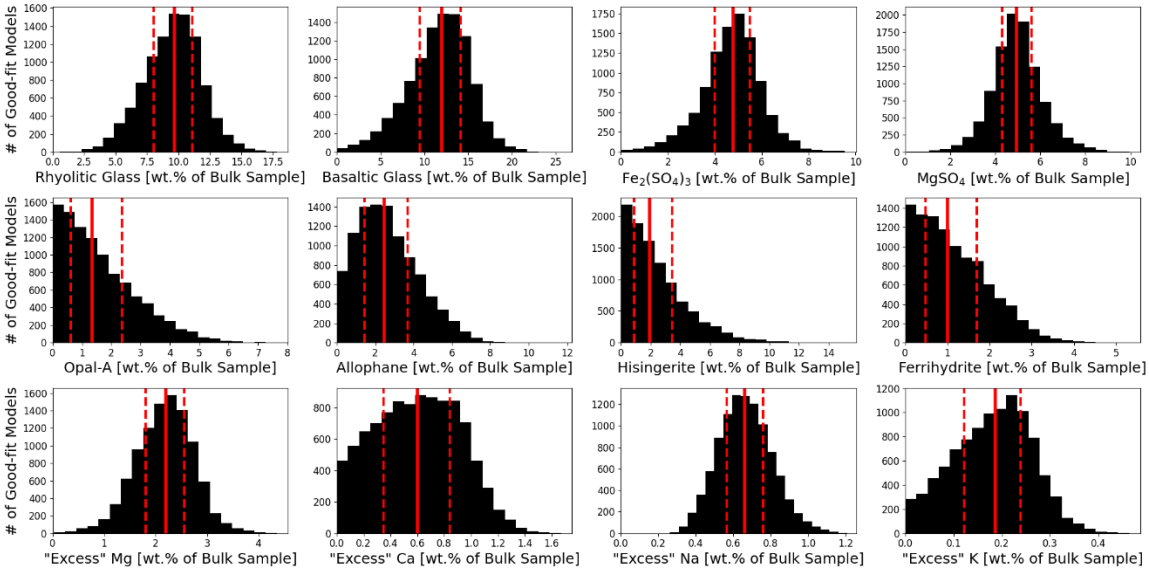

Figure E.36. Aberlady/Kilmarie (AK) modeled amorphous phase and "excess" cation distributions.

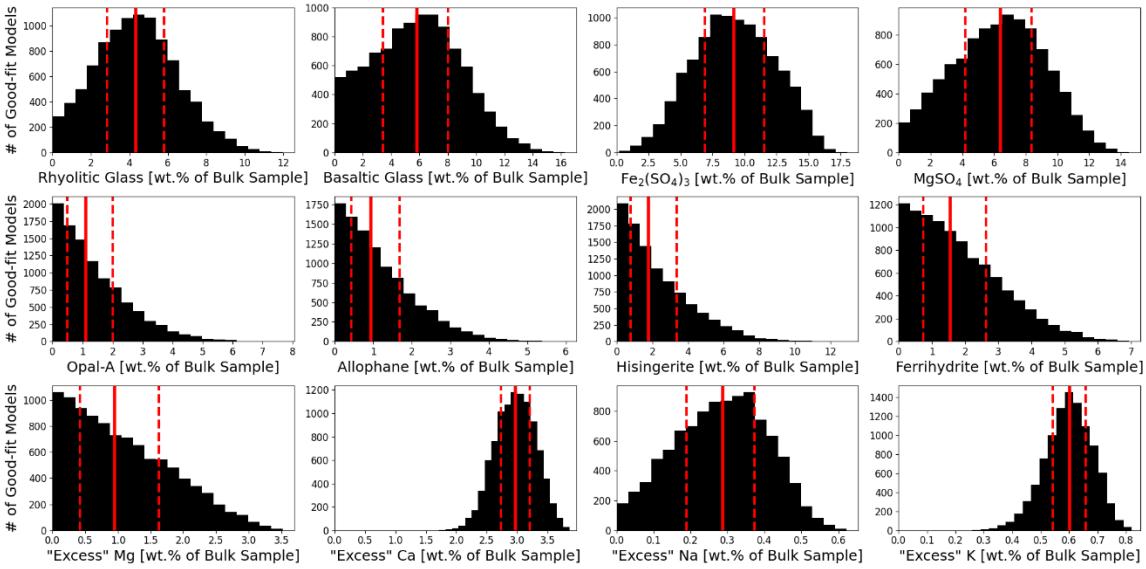

Figure E.37. Glen Etive 1,2 (GE) modeled amorphous phase and "excess" cation distributions.

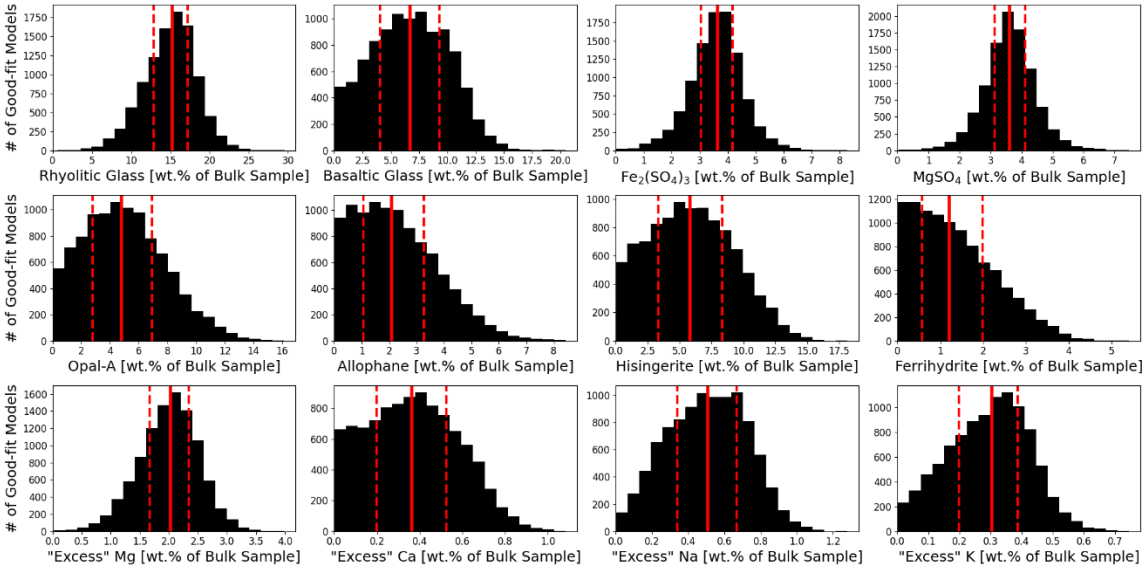

Figure E.38. Glasgow (GG) modeled amorphous phase and "excess" cation distributions.

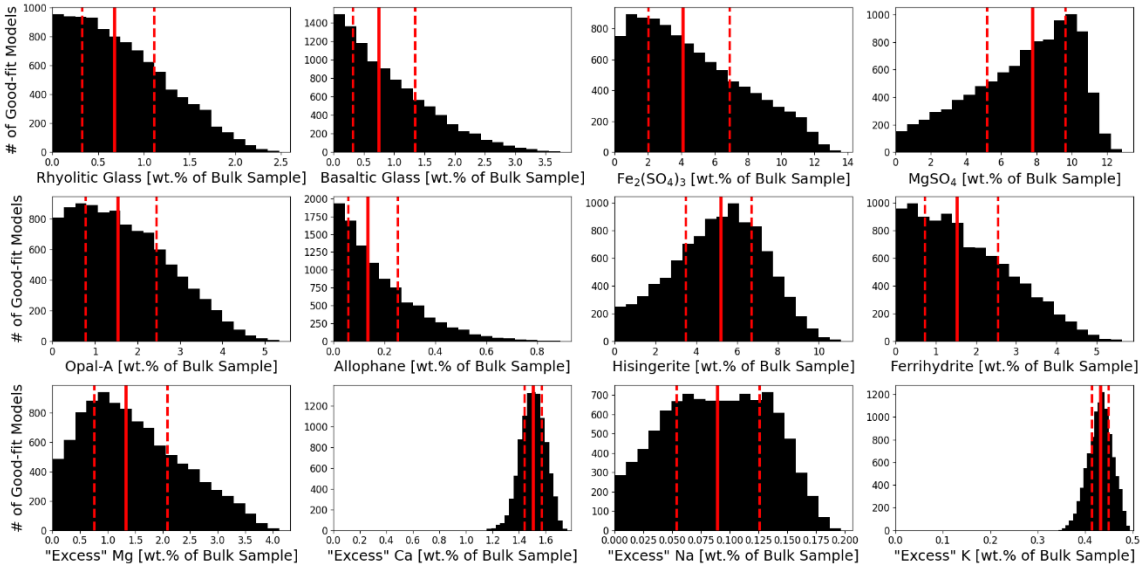

Figure E.39. Mary Anning (MA) modeled amorphous phase and "excess" cation distributions.

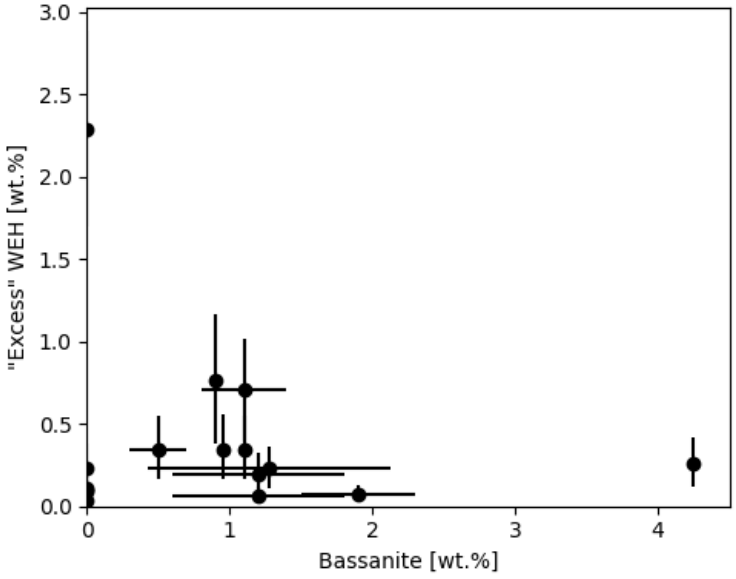

Figure E.40. Bassanite vs. modeled "excess" WEH. No correlation is evident, indicating that if gypsum has dehydrated to bassanite prior to CheMin analyses, this difference is not a significant source of the "excess" WEH modeled here. Bassanite abundances from CheMin XRD (Rampe et al., 2017; Bristow et al., 2018; Rampe et al., 2020a; Thorpe et al., 2022). "Excess" WEH error bars extend from Q_1 to Q_3.

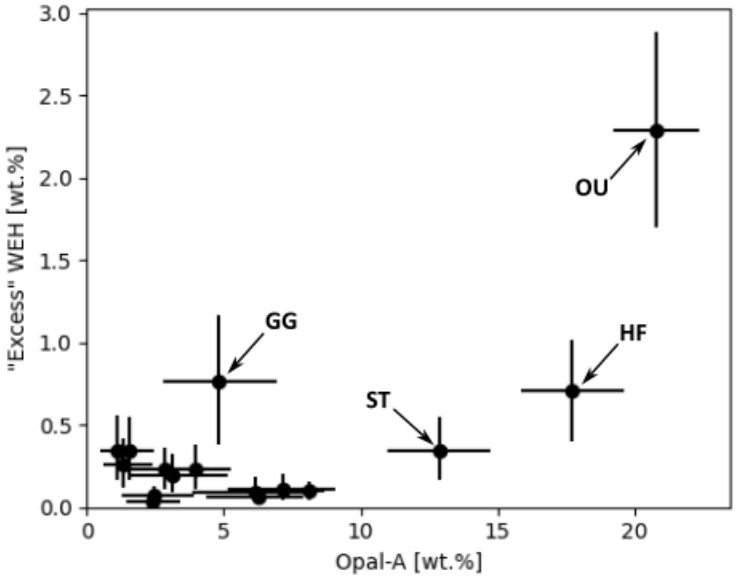

Figure E.41. Modeled opal-A vs. modeled "excess" WEH. OU, ST, and HF have abundant opal-A and "excess" WEH in our models, but contain ferripyrophyllite, a non-expandable clay mineral that cannot accommodate as much "excess" WEH as smectites. GG has higher modeled opal-A and "excess" WEH than other Glen Torridon (GT) samples. "Excess" WEH for OU, ST, HF, and GG may indicate greater opal-A hydration than that used in our models. Error bars extend from Q_1 to Q_3.